Gamma-Ray Bursts observations with Cherenkov telescopes : H.E.S.S. legacy observations and optimisation of follow-up and detection with the Large-Sized Telescop

Mathieu De Bony de Lavergne

UNIVERSITÉ SAVOIE MONT BLANC

THÈSE

Pour obtenir le grade de

Docteur de l'Université Savoie Mont-Blanc

Spécialité : **Physique Subatomique et Astroparticules**

Arrêté ministériel : 25 Mai 2016

Présentée par

Mathieu de Bony de Lavergne

Thèse dirigée par **Gilles Maurin**
et co-encadrée par **David Sanchez**

Préparée au sein du **Laboratoire d'Annecy de Physique des Particules**
et de l'**École doctorale de physique de Grenoble**

Gamma-Ray Bursts observations with Cherenkov telescopes: H.E.S.S. legacy observations and optimisation of follow-up and detection with the Large-Sized Telescope of CTA

Soutenue le **28 Février 2023**,
devant le jury composé de :

Giovanni Lamanna
Laboratoire d'Annecy de Physique des Particules, Président
Heide Costantini
Centre de physique des particules de Marseille, Rapporteuse
Abelardo Moralejo
Institut de Física d'Altes Energies, Rapporteur
Laurent Derome
Laboratoire de physique subatomique et de cosmologie, Examinateur
Loïc Rolland
Laboratoire d'Annecy de Physique des Particules, Examinateur
Fabian Schüssler
Institut de Recherche sur les lois Fondamentales de l'Univers, Examinateur

Gilles Maurin
Laboratoire d'Annecy de Physique des Particules, Directeur de thèse
David Sanchez
Laboratoire d'Annecy de Physique des Particules, Co-Directeur de thèse

Short Abstract

Gamma-Ray Bursts are among the most energetic events in our universe. They emit light across the whole light spectrum, from radio to gamma rays through visible light. They have only recently been detected at very high energies after many years of effort. CTA, a next-generation instrument, should allow to catch more of them. The prototype of a CTA telescope, LST-1, is under commissioning at La Palma. With the data being acquired, we look at methods to increase the chance of detecting such events. Also, by looking at past observations from the H.E.S.S. instrument, we try to understand which GRBs we can detect.

Résumé court

Les sursauts gamma sont parmis les phénomènes les plus énergétiques de l'univers. La lumière qu'ils émettent couvrent l'entiereté du spectre lumineux, allant des ondes radio aux rayon gamma en passant par le visible. Ils ont été détectés récemment à très haute énergie après des années de recherches. CTA, l'instrument de nouvelle génération, devrait être capable d'en détecter plus. LST-1, qui est un télescope prototype pour CTA, est actuellement en phase de test à La Palma. Avec les données acquises, il est possible de proposer des méthodes pour améliorer les chances de détections de ces évènements. Il est aussi possible de regarder aux observations passés de l'instrument H.E.S.S. afin de comprend quel sursauts il est possible de détecter.

Abstract

Since the first detection of a Gamma-Ray burst by the Vela satellites in 1967, they have been studied across the whole light spectrum with detection at different wavelengths. They are also one of the first types of objects to be detected with multiple messengers by the codetection of gravitational waves and electromagnetic emission, with GW 170817.

Cherenkov instruments have searched for a counterpart of GRBs at very high energies (above 100 GeV) for a long time. After more than two decades of effort, the H.E.S.S. telescopes achieved the first detection with GRB 180720B quickly followed by MAGIC with GRB190114C. Since these detections, GRBs emission started to be unveiled at VHE with the detection of two other GRBs.

The next generation of Cherenkov telescopes (CTA) is currently being built. GRBs will be one of the key observation targets. LST-1, a prototype of large CTA telescope, is currently under commissioning at La Palma. Thanks to their performance, LST telescopes will be the main contributors of CTA to the detection of GRBs.

A system called the bending model is in charge of the online correction of the pointing of telescopes, which is essential to correct systematic errors linked to the deformation of the lightweight structure. I have entirely developed the code, presented here, during my PhD. It takes care of the data acquisition, interacting with subsystem of the telescope, the data quality, the analysis, and the determination of a deformation model. I have also worked on the integration of the program into the LST software framework.

The observations of GRBs by LST-1 have already started. This was for the occasion to improve the follow-up strategy, especially when the alert comes from instruments with poor localisation accuracy, such as Fermi/GBM. On the analysis side, I have worked on the first background model for LST but also on the improvement of the sensitivity, either by searching for better selection criteria for the events or testing new reconstruction algorithms based on deep learning created at the LAPP.

Finally, H.E.S.S. telescopes, in Namibia, have observed a lot of GRBs since 2004. A catalogue of all these observations and their results is under creation, intending to answer the question of why so many observations were performed without success before the detection of the first GRBs and why the ones detected have been and not the others. I was in charge of the analysis of all the data and the interpretation I made with my colleagues is presented here.

Résumé

Depuis les premières détection de sursaut gamma par les satellites Vela en 1967, ils ont été largement étudié sur l'ensemble du spectre lumineux avec des détection à différentes longeurs d'onde. Ils ont été aussi un des premiers types d'objets detectés en astronomie multimessager avec la détection simultanée en ondes gravitationelles et ondes lumineuse de GW 170817.

Les télescopes Cherenkov ont cherché une contrepartie aux sursauts gamma à très haute énergie (au delà de 100 GeV) depuis longtemps. Après des années d'effort, les télescopes H.E.S.S. ont effectué la première détection avec GRB 180720B rapidement suivi par la détection de GRB 190114C par MAGIC. Depuis ces détections, l'émission de ces objets à très haute énergies a commencé à être dévoilé notamment avec l'aide de la détection de deux autres sursauts.

La prochaine génération de télescopes Cherenkov, appelés CTA, est actuellement en cours de construction. Les sursauts gamma seront parmis les principales cibles d'observation. LST-1, qui est un télescope prototype pour CTA, est actuellement en phase de test à La Palma. Avec leur performance, les télescopes LST seront parmis les principaux contributeurs à la détection de sursauts pour CTA.

Un système appelé bending model est en charge de la correction du pointé des télescopes durant les observations : il est en effet essentiel de corriger les erreurs systématiques de pointé du télescope, lié à la déformation de la structructure légère. J'ai entièrement développé le code, présenté ici, durant ma thèse. Il s'occupe de prendre les données, interagir avec les différents systèmes du télescope, de vérifier la qualité des données, de les analyser et de déterminer le modèle de déformation. J'ai également travaillé à l'intégration du programme au sein du système logiciel pour le contrôle du LST.

Les observations de GRBs avec LST-1 ont déjà commencé. Cela est l'occasion d'améliorer les stratégies pour le suivi d'évènements, en particulier pour les alertes venant d'instruments avec des localisations peu précises comme Fermi/GBM. Du coté de l'analyse, j'ai travaillé sur les premiers modèles de fond du LST ainsi que à une amélioration de la sensibilité, soit en cherchant des meilleurs critères de sélections des évènements, ou en testant les nouveaux algorithemes de reconstruction utilisant le deep learning créé au LAPP.

Finalement, H.E.S.S., installé en Namibie, à observé de nombreux sursauts depuis 2004. Un catalogue des observations et de leur résultats est en cours de création, avec comme objectif de répondre à la question de pourquoi autant de sursauts ont été observés sans succès avant les premières détections. J'étais en charge de l'analyse des données, et j'ai également travaillé à l'interprétation des données avec mes collègues dont les résultats sont présenté dans ce manuscript.

Remerciements

Je souhaiterai tout d'abord remercier David pour son encadrement tout le long de cette thèse mais également pour la liberté et le soutien à travers les nombreux projets que j'ai pu mener. Merci également à Gilles pour avoir co-dirigé cette thèse et toutes les suggestions bien utiles venues à travers nos discussions.

Je souhaiterai également remercier Armand pour toute son aide sur le `Bending Model`. Merci également à Thierry et Jean-Luc pour leur aide et expertise technique afin d'intégrer le `Bending Model` au sein de l'ensemble des infrastructures du LST.

Merci à Thomas pour toutes ces explications sur le fonctionnement des analyses Cherenkov et la possibilité d'avoir pu travailler sur le projet Gammalearn.

Merci à Pierre, sans qui bien des projets aurait été beaucoup plus complexes sans tout ses conseils pour réaliser des codes et les optimiser. Et merci également à Frédérique pour l'aide apportée afin de faire tourner ces codes sur les infrastructures de calcul.

Merci à Corinne et Caroline pour leur aide sur les nombreuses démarches administratives.

Merci également à Sylvain, Romain, Damir et Jayesh pour ces joyeux midi du temps où l'on avait accès à une cantine. Je souhaiterai également remercier l'ensemble de l'équipe H.E.S.S./CTA et notamment Sami, Enrique, Vincent, Céline et Estelle pour toutes ces discussions intéressantes autour d'un repas ou d'un café.

Merci à Aurel pour m'avoir introduit au suite de Sobol.

Et finalement merci à Guillaume, Bastien et Adrien, pour ces joyeuses soirées sur Discord malgré les confinements et couvre-feux ainsi que leur soutien tout le long de cette thèse.

Contents

Part I

Introduction

Chapter 1

The history of Cosmic Rays

1.1 Discovery of the Cosmic-Rays

The beginning of astroparticle history is usually attributed to the detection of Cosmic-Rays by Victor Hess in 1912. His experiment aimed to explain the origin of electroscope discharges. The electroscope is composed of two metallic leaves that are connected to an electrode. When this electrode is electrically charged, the leaves also charge and repel each other. However, in the air, the instrument is slowly discharging as a result of the ionisation of the air by energetic particles. Following the discovery of radioactivity in 1896 by Henri Becquerel (Becquerel, 1896), it was quickly proposed that the explanation for this effect would be radiation emitted from the ground.

To test this hypothesis, Theodore Wulf measured the discharge rate at the bottom of the Eiffel Tower and the top (Wulf, 1910). He found that the discharge rate was decreasing but at a slower rate than expected. Finally, Victor Hess proved that radiations come from outer space with his balloon experiment going up to 5300 m (Fig. 1.1) (Hess, 1912). He measured a slight decrease in the discharge rate up to an altitude of 1000 m, followed by a significant increase in the discharge rate at higher altitudes. The discharge rate doubled at its highest measurement point of 5300 m compared to the ground measurement (Fig. 1.2). The principal explanation for this result is that charged particles arrive from space and are partially absorbed by the atmosphere, causing an attenuation of the signal on the ground compared to higher altitudes. The slight increase of signal at ground level compared to low altitude could be explained by a contribution of radioactivity from the ground. These measures, confirmed later by other experiments, were clear evidence of cosmic-rays' existence. Victor Hess received a Nobel Prize in 1936 for this discovery.

After the discovery of the cosmic-rays, the question of the nature of the particles composing them arose. Two main possibilities were foreseen : charged particles defended by physicists like Compton and γ photons supported by physicists like Milikan. In 1927, Clay showed a dependency of the flux with latitude (Clay, 1927). This effect was confirmed by Pierre Auger and Louis Leprince-Ringuet using the coincidence between Geiger-Müller counters for detecting cosmic-ray events and roughly determining their direction using the alignment of the detectors (Leprince-Ringuet, L. and Auger, P., 1934). They confirmed Clay's finding but also showed that more cosmic-rays come from the west than from the east at the equator. It was interpreted as the result of the interaction of particles with the Earth's geomagnetic field, yielding the conclusion that cosmic-rays particles must be charged.

Similar experiments, but with counter-spread horizontally, led to the discovery of showers of particles. In these first experiments, the technical limitation of the instrumentation did not allow the measurement of the spread of the showers to be greater than one metre. Pierre Auger perfected the method and measured the existence of coincidence up to a 300 m spread, establishing that the showers are not local phenomena but wide ones, and they are developing through the entire atmosphere. He also showed that primary particles could go at least up to 1×10^{15} eV (Auger et al., 1939).

Particle physics started relying on the study of the cosmic-ray induced showers as they were providing high-energy particles, impossible to produce at the time due to technical limitations. This

Figure 1.1: Hot air balloon of Victor Hess after one of his flights (1912)

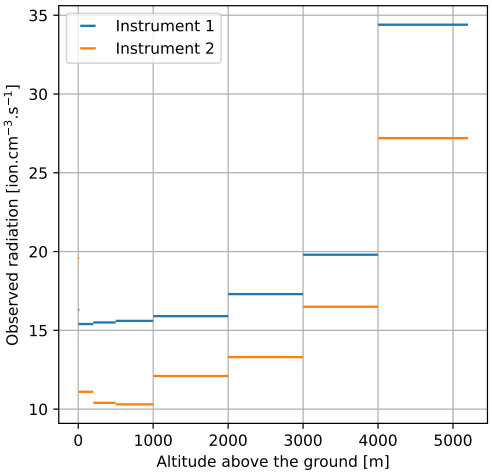

Figure 1.2: Average measure of the radiation obtained by Victor Hess across its seven balloon flights. Data are taken from Hess (1912)

allowed for the discovery of several particles, such as the positron in 1932 by Anderson, who studied tracks in a cloud chamber (Anderson, 1933), the muon in 1936 by Neddermeyer and Anderson (Neddermeyer and Anderson, 1937), the pion π^+ and π^- in 1947 by C. Powell, C. Lattes, and G. Occhialini, and later the strange particles Λ, Ξ, and Σ.

Later in the 1950s, the first accelerators started to provide high-energy particles, and particle physics started to separate from the astrophysics and study of cosmic-rays. A better understanding of particle physics also helps to improve the experiments studying the astrophysics origin of cosmic rays. This put the domains of astroparticles at the frontier of particle physics, astrophysics, and cosmology.

1.2 Properties of the Cosmic-Rays

1.2.1 Cosmic-Rays spectra

The spectrum of cosmic-rays has been well-studied since their discovery, and it is currently known for more than 12 orders of magnitude in energy and 32 in flux. Most of the spectrum could be approximated by a simple power law $dN/dE \propto E^{-\Gamma}$ with a spectral index $\Gamma \sim 2.7$ (Fig. 1.3).

Despite this quite regular aspect of the spectra, some features could be observed in it :

- Below 1×10^9 eV, the flux drops due to the solar modulation. This is caused by the solar magnetic field that deviates from the charged particles composing the cosmic-rays and prevents them from reaching the Earth. The sun's magnetic field varies by cycles of 11 yr, so the flux of low energies cosmic-rays also changes on the same time scale.

- Above 1×10^{15} eV, the flux decrease is slightly softer with a spectral index of $\Gamma \sim 3.1$ instead of $\Gamma \sim 2.7$ at the lower energies. This feature is called the knee of the spectrum. It is believed to come from the transition of cosmic-rays originating from the galaxy at low energies and cosmic-rays from outside the galaxy at higher energies.

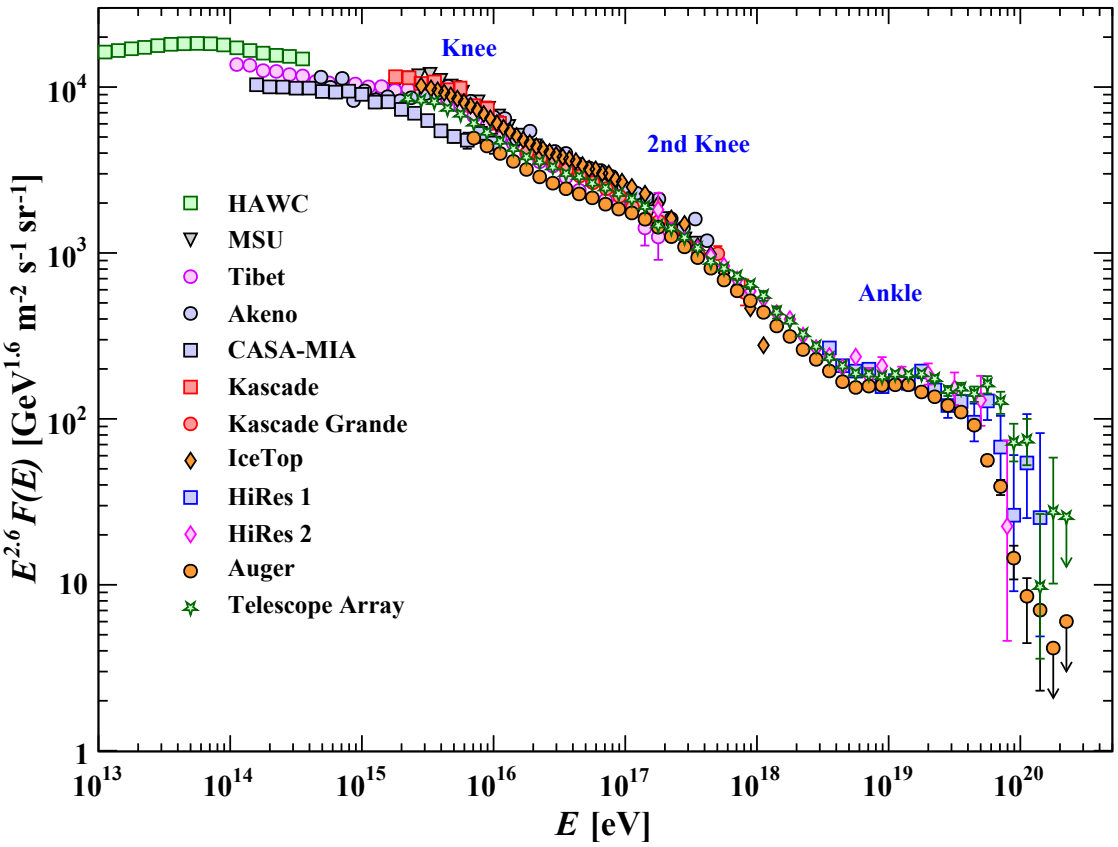

Figure 1.3: The energy spectrum of all cosmic-rays. Figure from Particle Data Group et al. (2022)

- Above 1×10^{17} eV, a second knee appears with a small steepening of the spectrum
- Above 6×10^{18} eV, the spectra hardened to reach a spectral index of $\Gamma \sim 2.7$, probably due to the domination of the extragalactic cosmic-rays.
- At energies above 5×10^{19} eV, the flux dropped quickly, likely due to the Greisen–Zatsepin–Kuzmin limit (GZK limit). This effect was predicted in 1966 (Zatsepin and Kuz'min, 1966) (Greisen, 1966). Above this energy, cosmic-rays start interacting with the cosmic microwave background (CMB) and are absorbed during the travel between the source and the observer. Pierre Auger Observatory has confirmed the existence of a drop in the flux at these energies, but it remains to determine whether it is due to the GZK limit (Abraham et al., 2008).

1.2.2 Cosmic-Rays composition

The cosmic-rays are composed mainly of nucleons ($\sim 99\%$) and electrons ($\sim 1\%$), with a tiny fraction of gamma-ray photons. Most nucleons are protons ($\sim 89\%$) and helium nuclei ($\sim 10\%$). The overall chemical composition is not too far from the chemical composition of the solar system (Fig. 1.4), even if some differences could be spotted. One of the most important ones is the overabundance of Lithium, Beryllium, and Boron. It is due to their secondary origins, as they are produced by the spallation process of heavier nuclei.

However, the composition across the energy spectrum is still not well known, except for the lower energies. At higher energies, due to the low flux, in order to be able to have a large effective area, cosmic-rays are observed from the ground by detecting the atmospheric showers they create. The results of these experiments about the composition of particles around the knee differ a lot according

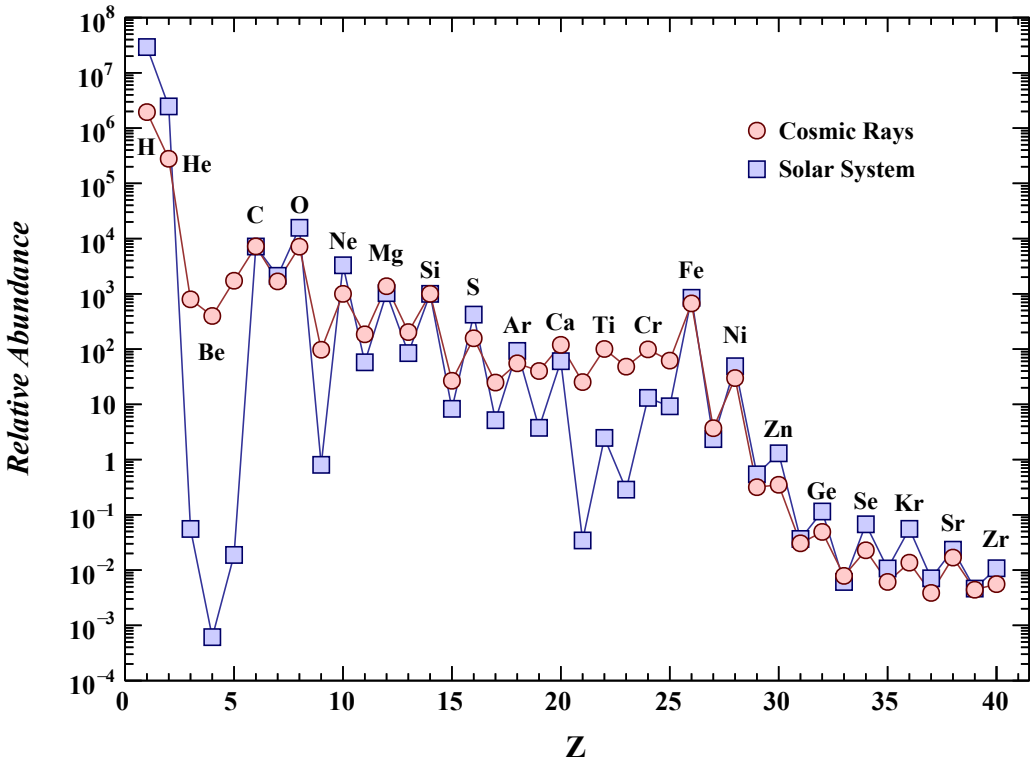

Figure 1.4: Relative abundance of the different nuclei in the solar system (blue) and the cosmic-rays (red). Figure from Particle Data Group et al. (2022)

to the experiments and the interaction model used to reconstruct the original particle that created the shower (Di Sciascio, 2022).

1.3 Origin of the Cosmic-Rays

1.3.1 Acceleration mechanism

The power-law spectra of the cosmic-rays and their very high energies point to acceleration by non-thermal processes. Several processes can explain the acceleration of particles at such energies, depending on the source type.

1.3.1.1 Fermi accelerations

Enrico Fermi proposed in 1949 a model to explain the acceleration of cosmic-rays (Fermi, 1949) which has been called second-order Fermi acceleration. In this model, the medium has multiple moving magnetic clouds, each with a uniform and constant magnetic field, without any correlation between the different clouds. When a particle enters a magnetic cloud, it will be deviated and exit the cloud in a different direction (Fig. 1.5a). If the collision is head-on, the particles will gain energy, otherwise, it will lose energy. The average energy gain at each collision could be approximated by the equation:

$$\left\langle \frac{\Delta E}{E} \right\rangle \simeq \frac{4}{3}\beta^2$$

with β defined as $\frac{v}{c}$, with v the speed of the particle, and c the speed of light,

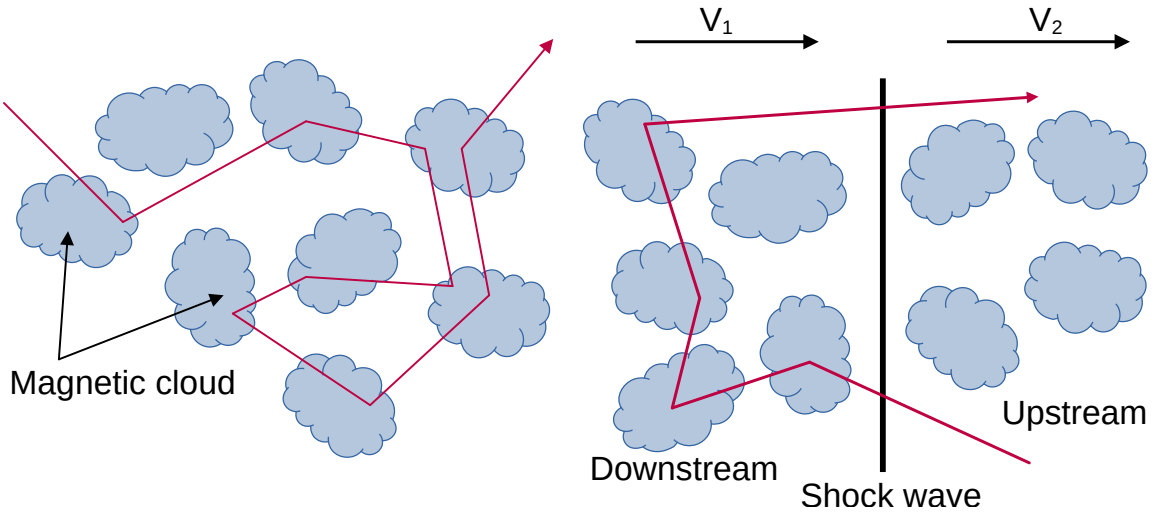

(a) Principle of the second-order Fermi acceleration (b) Principle of the first-order Fermi acceleration

Figure 1.5: Principle of Fermi acceleration. Figure inspired from Brun (2011).

Due to the dependency on β^2, the process is inefficient. Nevertheless, the overall idea of multiple diffusion on magnetic clouds is the base of many acceleration models. The first-order Fermi acceleration was proposed to solve the issue of inefficient acceleration in order to properly explain the cosmic-rays spectrum (Fermi, 1954). In this case, a non-relativistic shock wave propagates through the medium. A particle from the upstream interacts with magnetic clouds downstream before being directed toward the upstream again (Fig. 1.5b). This will cause mainly head-on entry in magnetic clouds, improving the efficiency of the process with an energy gain at each cycle given by the equation:

$$\left\langle \frac{\Delta E}{E} \right\rangle \simeq \frac{4}{3}\beta$$

The dependency is in β instead of β^2, making the process much more efficient than the second-order Fermi acceleration.

For the acceleration of the highest energy cosmic-rays, relativistic shock waves are often considered (Gallant, 2002). In that case, at each cycle of particles going from upstream to downstream and upstream again, the particle's energy gains are in the same order of magnitude as the initial energy.

All the different types of Fermi acceleration predict power law spectra for the accelerated particles in accordance with the measured spectra of cosmic-rays.

1.3.2 Origin of Cosmic-Rays

The question of the origin of the cosmic-rays is still open, even if some pretty big hints have been unveiled during the last 100 years. In this section, several astrophysical objects will be presented that are candidates for being acceleration sites of cosmic-rays. This is a non-exhaustive list of objects that are also detected in gamma-rays.

1.3.2.1 Extragalactic or galactic

The existence of the knee in the spectra is interpreted as a transition between cosmic-rays originating from the galaxy to outside of the galaxy. As cosmic-rays are charged, they are deviated by magnetic fields. The Larmor radius R gives the gyration radius of particles in a magnetic field which in the relativistic case is given by the formula 1.1, where m is the mass of the particle, β is defined as $\frac{v}{c}$

with v the speed of the particle, and c the speed of light, γ is the Lorentz factor defined as $\frac{1}{\sqrt{1-\beta^2}}$, Z and the atomic number of the particles, e the elementary charge and B the magnetic field.

$$R = \left| \frac{\gamma m \beta c}{ZeB} \right| \tag{1.1}$$

$$R[pc] \approx \frac{E[PeV]}{ZB[\mu G]} \tag{1.2}$$

In the ultra-relativistic case ($\beta \approx 1$), the formula could be approximated as 1.2 where R is the gyration radius in pc, E is the energy of the particles in PeV, and B is the magnetic field in µG. If the gyration radius is smaller than the size of the galaxy for a typical galactic magnetic field, then the cosmic-rays will be confined. This is the case for cosmic-rays with an energy below the knee ($\sim 5 \times 10^{15}$ eV).

Above this energy, cosmic-rays emitted within the galaxy are no longer confined, so the flux drops with a softer index. Above the ankle, the flux hardens again, which can be interpreted as a new component that becomes dominant. This component is believed to be from extragalactic origin.

Determining the exact acceleration sites of cosmic-rays is difficult as there are deviates along the path between the source and the observer. So, the direction from which they arrive does not correspond to the direction where the emission source is in the sky. At the highest energies, cosmic-rays' deviation could start to be relatively small, so it is possible to search for a privileged direction of the source. Auger observatories have detected large-scale anisotropy of the cosmic-rays at the highest energies (above 8 EeV) (The Pierre Auger Collaboration et al., 2017). This anisotropy points far away from the galactic centre or the galactic plane (Fig. 1.6), and the analysis by the Auger collaboration has shown that galactic origin is not favoured (Abreu et al., 2022a). Recently, the Auger collaboration reported a hint of excess at higher energy (39 EeV), possibly associated with starburst galaxy (Aab et al., 2018). Nevertheless, no clear association with a given source has been made so far.

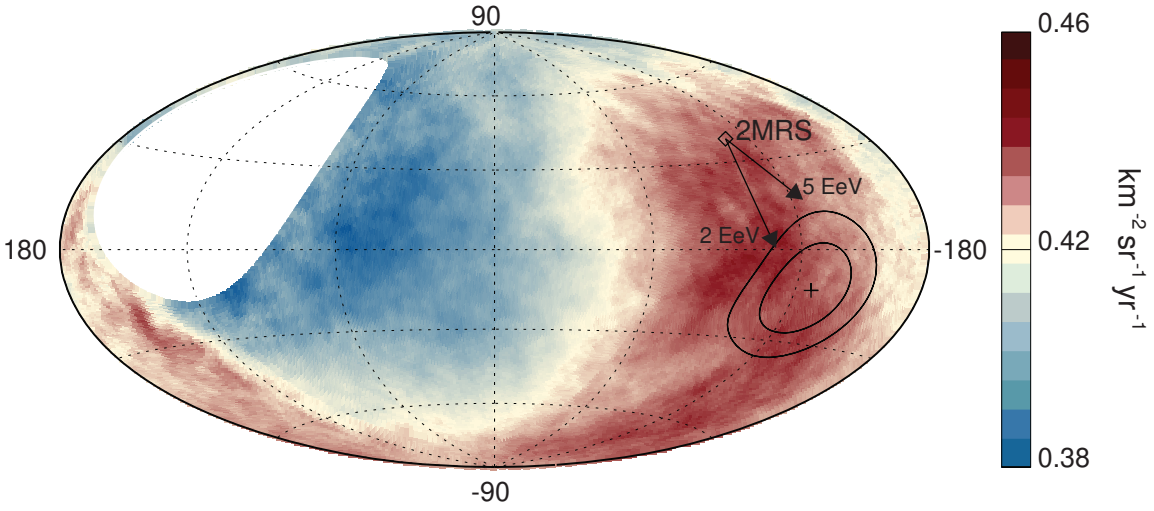

Figure 1.6: Cosmic-ray flux observed by Auger Observatory above 8 EeV (galactic coordinates). The arrows show the expected deviation due to magnetic field for cosmic-rays of the given energies. The Pierre Auger Collaboration et al. (2017)

At lower energies, such analysis is impossible as the deviation by magnetic field makes the arrival direction almost isotropic. In order to study the origin of cosmic-rays, the best way is to use another non-charged messenger, such as neutrinos or photons. Neither will deviate along the path to the observers. So by observing them, we can determine the source that emitted them. The presence

of accelerated charged particles will lead to the production of both photons and neutrinos. Some emission processes for photons will be described later.

Neutrino astronomy is challenging due to the limited sensitivity of the detectors caused by the tiny cross-section of interactions of neutrinos with matter. Up to now, only two neutrino sources have been detected, the Sun (Hirata et al., 1989) and SN 1987A (a supernova in the Great Magellanic Cloud) (Hirata et al., 1987). Another significant result of neutrino astronomy is the hint for an association of a flare from the blazar TXS 0506+056 detected across the electromagnetic spectrum and a single neutrino high energy detected by IceCube (IceCube Collaboration et al., 2018). We could hope for more detections in the future with the construction of several new detectors (KM3Net, Baikal-GVD, Hyper-Kamiokande, ...) or the upgrade of current detectors like Super-Kamiokande and IceCube.

Gamma-ray astronomy started in the 60's with satellite observations. Since then, thousands of sources have been detected with several instruments at different energies. More details will be provided in Chapter 2.

1.3.2.2 Identification of the potential acceleration sites

Potential sources for accelerating cosmic-rays could be determined as a function of the maximal energy they could accelerate. For this, the Larmor radius could be used again (Eq. 1.2). For a particle to continue accelerating, it needs to stay confined in the sources. Consequently, it will depend on the source's size and the intensity of the magnetic field within the source.

On figure 1.7 is represented by the so-called Hillas plot (Hillas, 1984) that represents the size and intensity of the magnetic field for each type of source. The maximal energy that could be reached is represented by a power law of index -1. Some sources will only be able to produce low-energy cosmic-rays like solar flares, others could only accelerate up to the knee like the supernova remanent, and others, like Gamma-Ray Bursts and Active Galactic Nuclei, could go up to the highest energies observed.

1.3.2.3 Galactic sources

As discussed before, acceleration sites within our galaxy are likely to explain the cosmic-ray below the knee and are mainly linked to stars or their remains.

Supernova remanent The most massive stars (above 8 $M_\odot$) spectacularly end their lives. As most of the hydrogen in the core has been fused to make helium, the fusion of helium will start. The core will start to contract and heat up, allowing the fusion of heavier elements, first carbon, then neon, then oxygen, and then silicon. At each step, the core will continue to contract and heat up, and the fusion reactions happen faster. With the fusion of silicon into iron, the star reaches the point where fusion cannot produce any more energy, as fusion in heavier elements is endothermic. The iron core collapses under gravitational pressure. The exterior shell of the stars will also collapse and bounce onto the core creating a gigantic explosion called a supernova. This explosion creates a shock wave that propagates outside of the star. The remainder of the core transforms into a neutron star or, if it is too massive, into a black hole.

Another type of supernova also exists, the supernova of type Ia, originating from a different process. White dwarfs are the remains of the core of a lighter star that had flushed its outer layer. The remaining core is a dense object composed of degenerated matter. In case this star is accreting matters, it will gain mass, and there is a critical mass called the Chandrasekhar mass ($\sim 1.4\ M_\odot$). When reached, the star collapses and creates a thermonuclear explosion that destroys all the remains of the star. These supernovae are highly used in cosmology to measure distance as their luminosity is always the same due to the explosion always happening at the same mass.

Supernova remanents (also called SNR) originate from supernovae. It is the exterior shell that has been expelled, forming a shock wave that propagates through space (Fig. 1.8). Particles could be accelerated here through the Fermi 1st-order acceleration mechanism. They are among the best candidates for explaining cosmic-rays below the knee. Gamma-ray observations confirmed the

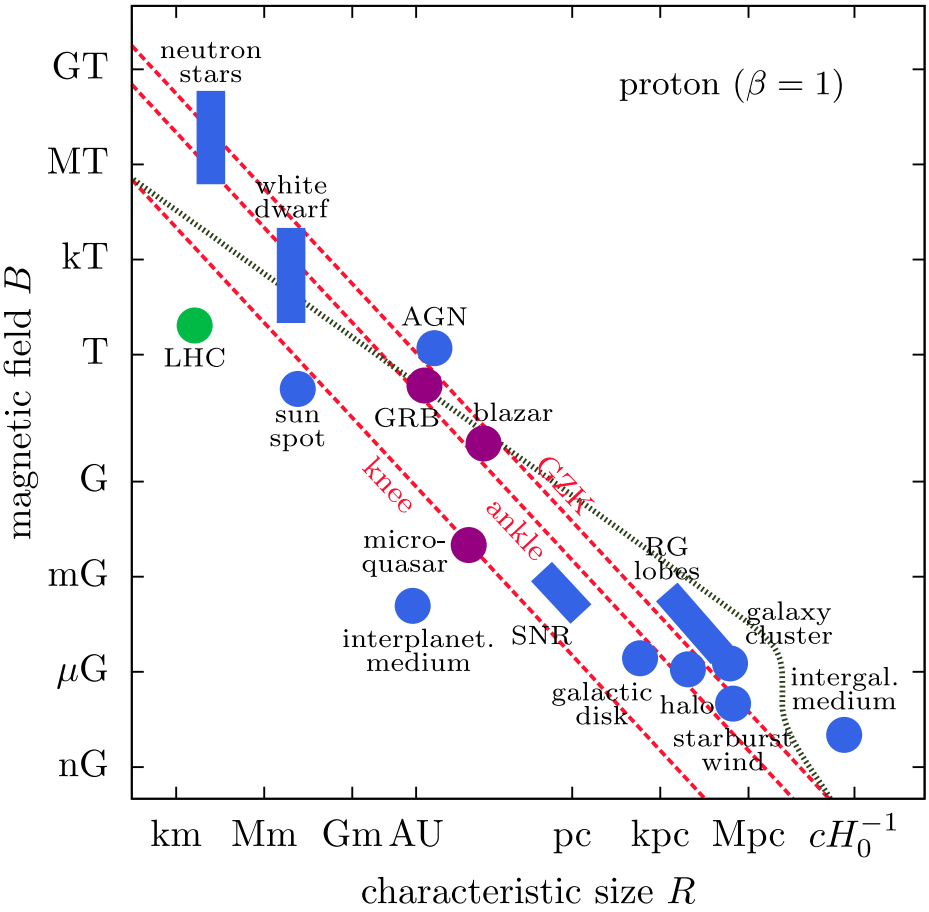

Figure 1.7: Represent the maximum energies of the cosmic-rays protons accelerated for each type of source. Coloured regions indicate the typical possible values for each source, and the dashed lines represent the typical energies that could be reached for a given magnetic field and size. Figure extracted from Aartsen et al. (2018).

presence of high-energy electrons in this type of source. Detecting neutrinos from this kind of source would help pinpoint cosmic-ray production to these sources.

Pulsars As mentioned above, after a supernova, a neutron star can be formed if the core of the star is not heavy enough to form a black hole. These objects are compact, with a typical size of around 10 km for a mass above 1 $M_\odot$. The physics of these objects remains mainly unknown, but they are composed of neutrons formed by the fusion of electrons and protons. As the angular momentum was conserved during the collapse, neutron stars rotate extremely fast with periods between a few milliseconds to a few seconds. Their magnetic fields are very strong, going from 1×10^4 T to 1×10^{11} T for the strongest ones, called magnetars. This magnetic field induces collimated emission along the magnetic poles. Most of the time, the magnetic poles are not aligned with the rotation axis. It makes a beam of light that acts like a lighthouse. This causes a pulsated emission which gives the name of pulsars to these objects. The first detection of a pulsar was performed in Radio by Jocelyn Bell in 1967 (Hewish et al., 1968). Since the first detection, thousands of pulsars have been detected in radio, and some emissions for a few pulsars have been detected in X-Ray and γ-rays.

The exact state of the matter composing the neutron stars is still unknown. Several models predict the acceleration of particles (mainly leptons) in the direct environment of the neutron stars,

[1] Credit: NASA, ESA, and Z. Levay (STScI), https://commons.wikimedia.org/wiki/File:Sn_1006.jpg
[2] Credit: B. Saxton, NRAO/AUI/NSF, https://public.nrao.edu/gallery/parts-of-a-pulsar/

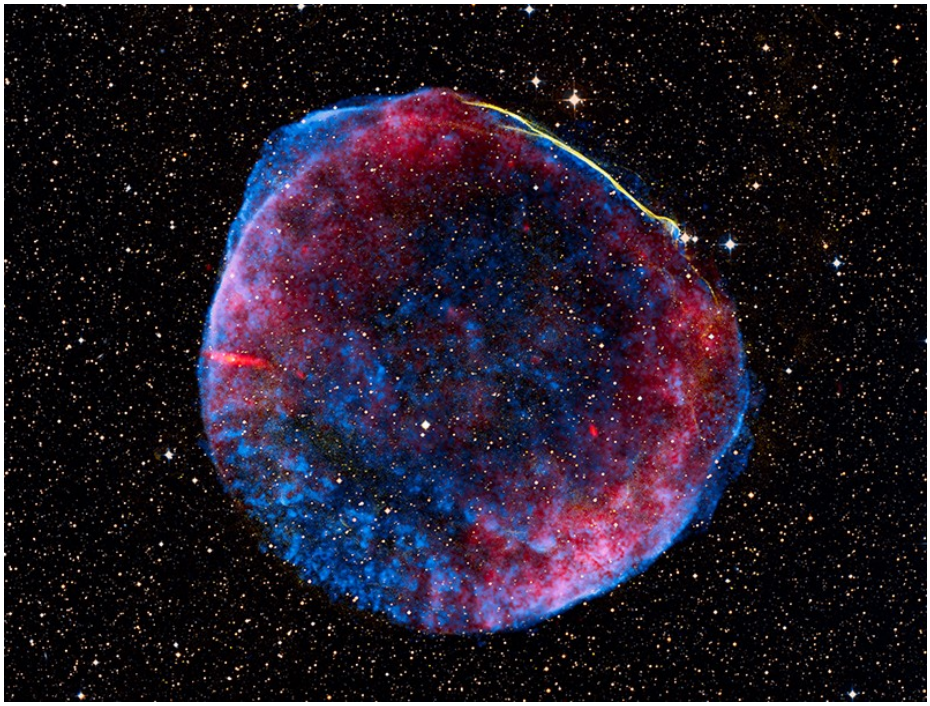

Figure 1.8: Composite image of the supernova remanent of SN 1006 (supernova of type Ia). This is a composite image of optical (yellow), radio (red), and X-Ray (blue) data. The shell caused by the propagation of the shock wave is easily visible[1].

which could explain the emission of light detected from these objects. Consequently, pulsars could be one of the main contributors to the leptonic part of the galactic cosmic-rays.

Pulsar Wind Nebulae The accelerated particles escaping from the pulsar environment form the wind of the pulsar. The particles encounter the gas ejected during the supernova and form a stationary shock wave. This shock wave allows acceleration of the particles at larger energies through the first-order Fermi acceleration process. They differ from supernovae remanent by continuous injection of energy from the pulsar, while supernovae remanent energy only comes from the initial injection by the supernova.

Binary system A binary system is a system where two stars orbit around each other. This is quite common, as it is estimated that at least 70% of the stars are part of a multiple system (two or more stars).

One particular case of binary systems are the ones with one of the objects that is compact (a black hole or a neutron star) and the other companion is a star close to the compact object. The compact object is the remain of a previous massive star that has already made supernovae.

When the compact object is a black hole and the companion star is close enough, the black hole could start to accrete matter that forms an accretion disk and a jet. Due to some similarity of this process with quasars, these systems are often called microquasars.

Novae Novae are thermonuclear explosions at the surface of white dwarfs. This phenomenon is due to the accretion at the surface of hot gas composed of a major part of hydrogen. This often happens when the white dwarf is a member of a binary system with a giant star close by. As the giant star size increases, the external layer of the star is accreted by the white dwarf (Fig. 1.10). The recent detection of gamma-rays at TeV from the recurrent novae RS Ophiuchi put in evidence

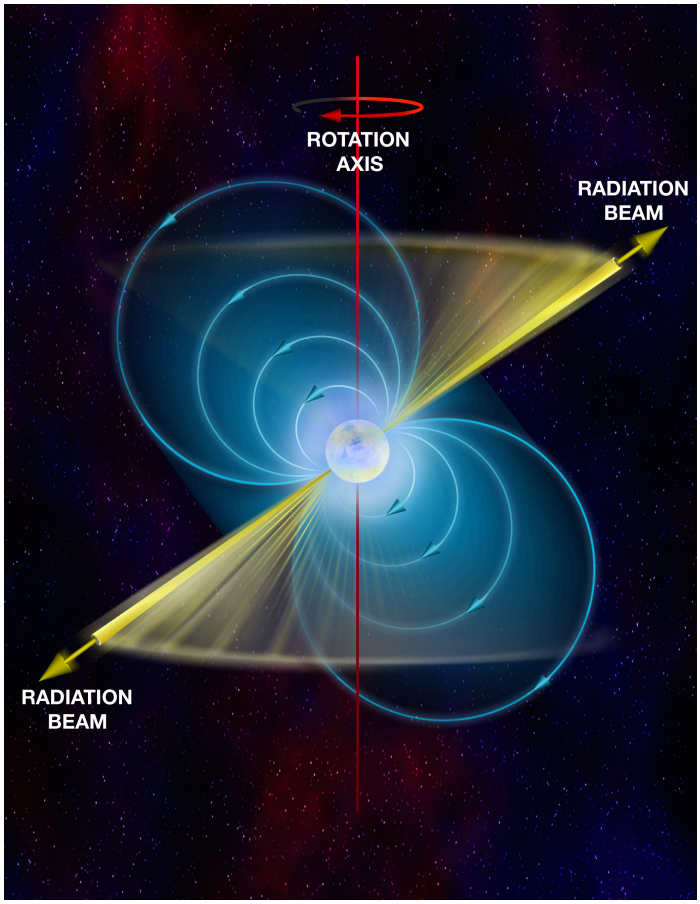

Figure 1.9: Schema of the structure of a pulsar. The neutron star is at the centre with a fast rotation on itself. The radiation beam is aligned with the magnetic axis, which could be different from the rotation axis, causing the pulsation effect from the observer's point of view.[2]

that protons are accelerated in the process (H. E. S. S. Collaboration et al., 2022) (Acciari et al., 2022).

1.3.2.4 Extragalactic sources

To search for the origin of the cosmic-rays at the highest energies, we need to look for phenomena that are among the most energetic in the universe and occur outside our galaxy.

Active galactic nuclei Nearly all galaxies have in their centre a supermassive black hole (10^6 - 10^9 $M_\odot$), but only 10% of the galaxies are active, called Active Galactic Nuclei (AGN). The AGNs are called active due to the light emission linked to their high accretion rate of matter, forming a bright accretion disk. In some cases, bipolar relativistic jets could be formed. The light emitted by this disk and the potential jet could be brighter than all the light emitted from the other part of the galaxy. When there is a jet, and if this one is aligned with the line of sight, it is called a blazar. With the help of the doppler boosting of the jet, this forms a very bright object that allows them to be detected at a very long distance, making them among the furthest ever detected astrophysical sources (Fig. 1.11).

[3]Credit : superbossa.com / MPP, https://www.mpg.de/18529322/0412-phys-nova-outbursts-a-new-source-for-cosmic-rays-151955-x

[4]Credit : NASA and The Hubble Heritage Team (STScI/AURA), https://hubblesite.org/contents/media/images/2000/20/968-Image.html

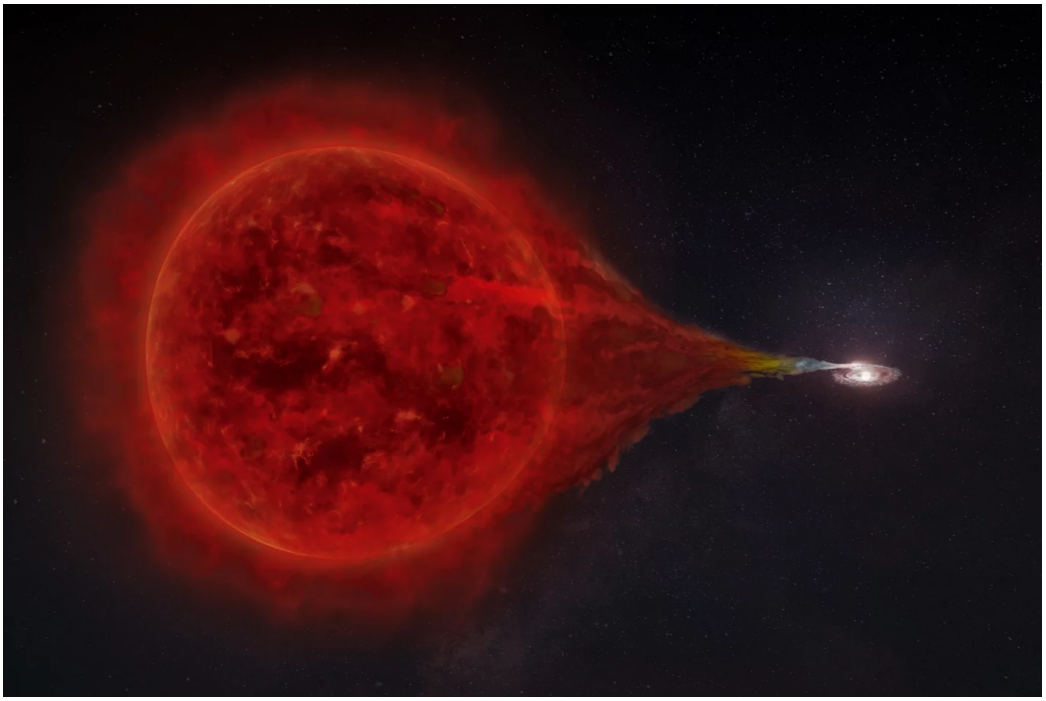

Figure 1.10: Artistic view of binary system that could create nova. The external layer of the red giant on the left is accreted by the white dwarf on the right.[3]

Gamma-ray bursts Gamma-ray bursts (GRB) are among the most energetic phenomena in the universe. A massive amount of energy is released in a very short timescale (a few tens of milliseconds to a few hundred of seconds). Following this first emission, a more lasting one emerges that could be detected up to a few months after the burst in radio. Due to their brightness, these phenomena could be detected from very far. With their ultra-relativistic jets and the associated shock waves created, GRBs are among the candidates to explain the cosmic-rays at the highest energies. More details on GRBs can be found in chapter 3.

1.4 Emission process of photons

The accelerated particles can emit light through various processes. In this part, the main ones used to explain the emission of objects studied at gamma-ray energies are presented.

1.4.1 Synchrotron process

Any charged particles in a magnetic field emits light called synchrotron. The Lorentz force applies to a charged particle of mass m, charge q, of speed $\vec{v}$ in a magnetic field $\vec{B}$; expressed as :

$$\frac{d}{dt}(\gamma m\vec{v}) = \frac{q}{c}\vec{v} \times \vec{B}$$

where c is the speed of light, $\gamma = \frac{1}{\sqrt{1-\beta^2}}$ the Lorentz factor, and $\beta = \frac{v}{c}$.

The total power emitted through the synchrotron process P is given by the equation 1.3 with σ_T the Thomson cross-section. The maximum energy of the photons emitted is given by the equation 1.4.

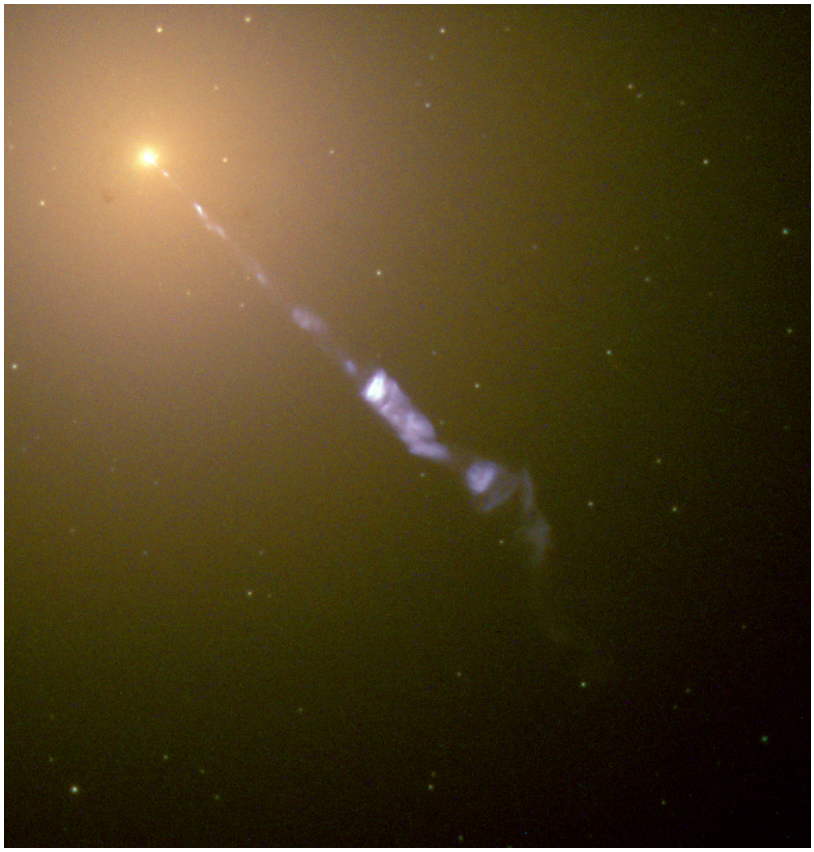

Figure 1.11: The blazars M87. This composite images allow an easy visualization of the central part and the associated jet. The data are from the WFC2 camera of Hubble.[4]

$$P = \frac{4}{3}\sigma_T c\beta^2\gamma^2\frac{B^2}{8\pi} \tag{1.3}$$

$$E_\gamma = 0.45\frac{qB\hbar}{m}\gamma^2 \tag{1.4}$$

P is dependent on the mass of the charged particle. As a consequence, protons will produce a significantly less powerful synchrotron emission than lepton at the same energy. In astrophysics sources, the synchrotron emission is mainly caused by electrons and explains emission from radio up to X-rays.

One marker of the synchrotron process is the polarization of the emitted light (Rybicki and Lightman, 1979). The spectrum of the synchrotron light emitted by particles following a power law spectrum of index p is a power law of index $\alpha = (p-1)/2$ (Blumenthal and Gould, 1970).

1.4.2 Inverse Compton process

A particle can transfer part of its energy to a photon through the inverse Compton scattering process. There are two different regimes :

- Thomson regime : in this regime, the energy of the photon, in the rest frame of the particle, is small in with respect to the mass energy of the particles ($E_\gamma \ll mc^2$). Only a part of the energy is transferred to the photon, and the total power radiated for an isotropic photon field is $P_{IC} = \frac{4}{3}c\gamma^2\beta^2\sigma_T U_{ph}$ with U_{ph} the energy density of the seed photon field. The spectra of

the emitted light from particles with a power spectra of index p is a power law spectra of index $\alpha = (p+1)/2$ (Blumenthal and Gould, 1970).

- Klein-Nishina regime : in this regime, the energy of the photon, in the rest frame of the particle, is large compared to the mass energy of the particles ($E_\gamma \gg mc^2$). All the energy of the particle is transmitted to the photons, and the cross-section of interaction with the photon will become smaller as the energy of the photon goes higher. This will cause a softer spectra of the emitted light. In the case of particles with a power spectra of index p, the radiated spectra will be a power law spectra of index $\alpha = (p+1)$ (Blumenthal and Gould, 1970).

The seed photons for inverse Compton scattering could be external photons from the CMB, diffuse emission from the galaxy, ... Or they could be internal to the source (thermal or synchrotron emission. If seed photons are emitted by synchrotron and then boosted at higher energies by the same electron population thanks to inverse Compton, we call it a Synchrotron Self-Compton (SSC) emission.

1.4.3 Bremsstrahlung

The Bremsstrahlung or braking radiation is the radiation emitted by charged particles when they are in the electric field of a nucleus or ion. In the case of electrons, the process could be very efficient, creating photons with an energy of the same order of magnitude as the electron. The efficiency of the process will also depend on the ionisation. The electrons surrounding the nucleus will screen a part of the electric field and worsen the efficiency of the process. The maximum efficiency will be obtained in a fully ionized medium. The total power radiated P_{Brem} through this process in a fully ionized medium composed of N different species of ions of density n_i is given by the equation :

$$P_{Brem} = \frac{e^6}{16\pi^3 \epsilon_0^3 m^2 c^4 \hbar} \sum_i^N n_i Z_i \left(Z_i + 1\right) E \left(\ln 2\gamma + \frac{1}{3}\right)$$

with e the elementary charge, Z_i the charge of the ions of species i and E the energy of the particles (Rybicki and Lightman, 1979).

The spectra radiated by an electron population with a power law spectra of index p is also a power law spectra of index $\alpha = p$ (Longair, 2011).

1.4.4 Pion Decay

All of the processes above are mainly relevant for leptons, but processes involving protons, called hadronic emission, must be considered.

The production of pion happens during an inelastic collision of two protons (Eq. 1.5). The π_0 created is unstable and disintegrates in two photons with a half-life of $\sim 8 \times 10^{-17}$ s (Eq. 1.6). The π^+ and π^- particles also decay in muons and neutrinos.

$$p + p \longrightarrow \pi^0 + \pi^+ + \pi^- \tag{1.5}$$

$$\pi^0 \longrightarrow \gamma + \gamma \tag{1.6}$$

The diffuse high-energy gamma-rays emission of the galaxy is explained through this process by the initial interaction of cosmic-rays with gas clouds in the galaxy. As this process will also create neutrinos, detecting neutrinos is a marker of the hadronic process taking place inside the source.

Chapter 2

Gamma-ray astronomy

Contents

Production of gamma-rays is linked to the most violent and rapid phenomena, and gamma-ray astronomy allows us to probe such phenomena in the Universe. Of course, identifying sources is of paramount importance in astronomy, but the angular resolution is often limited in such energy range compared to other wavelengths. This fact always gave an important role in the multiwavelength aspect of this field. At these energies, the low photon fluxes are also an important constraint on the detectors and their capabilities.

2.1 Constraints of the gamma-ray astronomy

The most energetic part of the electromagnetic spectrum is called the gamma-ray domain. There is no universal convention for the separation between X-Ray and gamma-ray, but it is usually defined around a few hundred keV. As for the upper limit, absorption phenomena in the source or during the travel from the source to the observer limit the possibility of detection at the highest energies. The highest energy gamma-rays have been recorded by LHAASO with photons up to 1.4 PeV (Cao et al., 2021).

At these energies, it is impossible to make an optic system that works with gamma-rays, even with Wolter mirror[1]. The detection systems are inspired by particle physics, yielding to what is called astroparticle physics. Direct detection of gamma-rays is not possible from the ground, as there are absorbed by the atmosphere. Consequently, balloon or satellite experiments are used for direct detection. Indirect detection can be achieved with a ground-based system to increase the effective area at the highest energies.

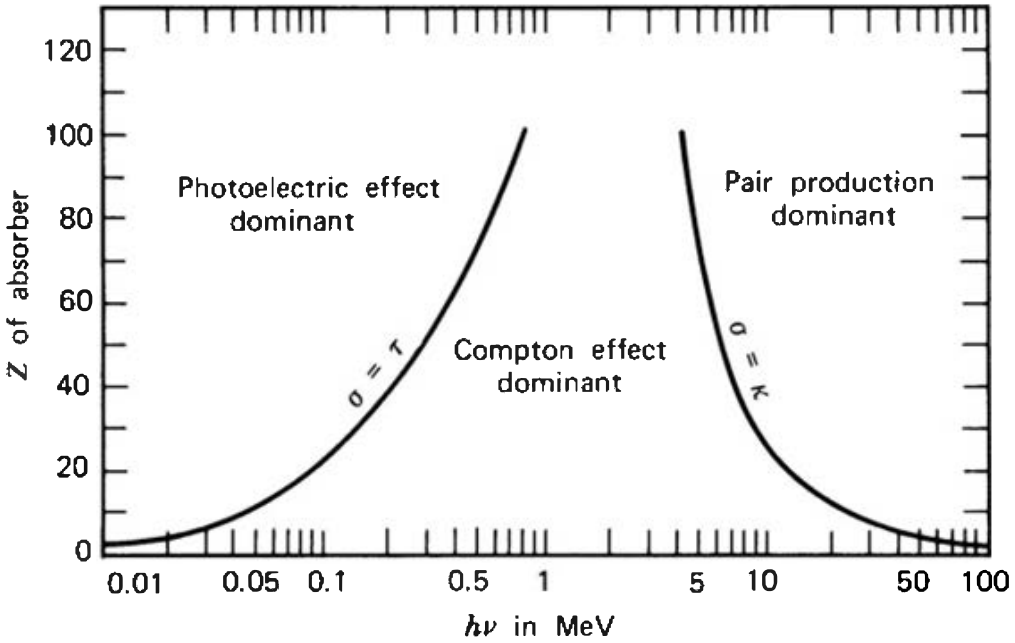

Figure 2.1: Dominant interaction of gamma-rays with matters in function of the energy $h\nu$ of the gamma-rays (horizontal axis) and the atomic number Z of the material used (vertical axis). An interaction will be considered dominant when its cross-section of interaction is larger than the ones of the other's interaction. Figure from Knoll (2010)

In the gamma-ray energy range, light-matter interactions dramatically change with energy, which has a massive impact on the design of the detector. At the lowest energies, starting from X-rays up to the MeV range, the interaction would mainly be due to photoelectric effects (Fig. 2.1). Above and up to few MeV, Compton scattering dominates. Finally, pair creation is the interaction process at the highest energies.

2.2 The firsts gamma-ray experiments

At the end of the fifties and early sixties, several balloon experiments tried to detect gamma-rays amongst the cosmic rays. The experiment by Thomas Cline in 1960 showed some hint of the existence of gamma-rays of cosmic origin, but the atmospheric background was limiting the sensitivity of the instruments (Cline, 1961). The satellite Explorer 11, launched on the 27th of April 1961, was the first space gamma-ray telescope and detected gamma rays from space origin, but was not sensitive enough to detect any source (Kraushaar and Clark, 1962).

In March 1967, the OSO-3 satellite was launched. Among the numerous instruments onboard, there was a high-energy gamma-ray detector. The experiment detected the emission from the galactic

[1]Wolter mirror is the type of mirror mainly used in X-Ray astronomy. This idea has been first proposed by Hans Wolter, who gave its name to the concept (Wolter, 1952). It consists of a series of concentric glancing-incidence mirrors that will focus the incoming photons. As the energy of the X-Ray increases, it becomes harder to make these kinds of mirrors as the maximum incidence angle becomes smaller. NuSTAR telescope is the one reaching the highest energy with a Wolter mirror, up to 79 keV (Harrison et al., 2013).

plane and the galactic centre above 50 MeV, making it the first detection of gamma-ray sources (Kraushaar et al., 1972).

These results were confirmed by the SAS-2 satellite launched in 1972. The experiment also discovered emissions from the first galactic sources with the Crab, Vela, and Geminga regions. SAS-2 measured that a part of the emission from the Crab was pulsated, making it the first detection of a pulsar in gamma-ray (Fichtel et al., 1975). In 1975 was launched the COS-B satellite. Its longer mission duration allowed the identification of 25 sources (Swanenburg et al., 1981). It was also the first experiment to detect an extra-galactic source with the blazar 3C 373 (Swanenburg et al., 1978).

2.3 The CGRO era

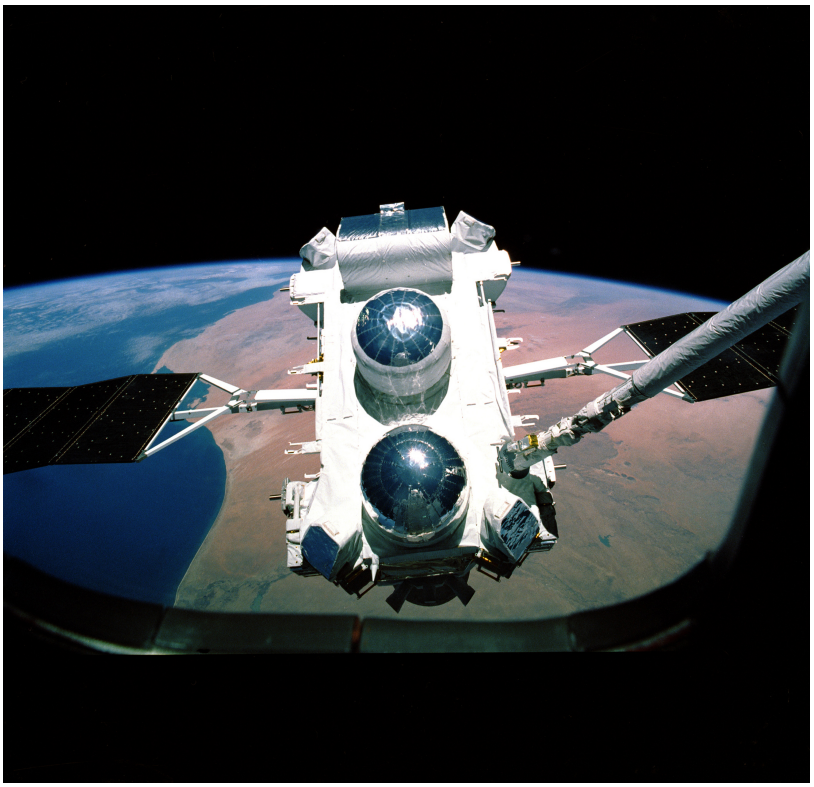

Figure 2.2: Deployment of the CGRO satellite from the space shuttle on the 5th April 1991 [2]

In the eighties, NASA started to work on the programme of the Great observatories. The objective of this programme was to launch four major astronomy missions, each dedicated to a given wavelength. The four missions were the Hubble Space Telescope for optical light, Spitzer Space Telescope for infrared, Chandra X-ray Observatory for X-Ray and finally, Compton Gamma-Ray Observatory (CGRO) for gamma-rays.

CGRO was launched by a space shuttle in 1991 and was the heaviest satellite ever flown with a mass of 17 t (Fig. 2.2). The satellite hosted four different instruments, each dedicated to a specific energy range and with different scientific objectives :

- BATSE, height module of scintillation detectors dedicated to detecting gamma-ray bursts
- OSSE, a spectrometer working between 100 keV and 10 MeV
- COMPTEL, a Compton telescope working between 1 MeV and 30 MeV

[2] Credit : NASA/MSFC, https://www.nasa.gov/centers/marshall/history/cgro140404.html

- EGRET, a pair production telescope working between 20 MeV and 30 GeV

CGRO, with its wide energy range, the increase in sensitivity compared to previous experiments, and its long mission time, led to numerous scientific results. Among them, there is the sky map of Aluminium 26 using the gamma-ray emissions caused by the radioactivity decay allowed by COMPTEL (Diehl et al., 1995), the galactic map of candidate positron sources by OSSE (Purcell et al., 1997), the detection and localisation of more than 2500 gamma-ray bursts by BATSE (Paciesas et al., 1999) or the detection of 271 high energy sources by EGRET (Fig. 2.5a) (Hartman et al., 1999). Among the sources detected and identified by EGRET, there were 66 blazars, five pulsars, and one radio galaxy. Most of the sources detected by EGRET were unassociated to a counterpart in other wavelengths due to the limited angular resolution of the instrument.

2.4 The modern era of gamma-rays space telescope

The INTErnational Gamma-Ray Astrophysics Laboratory (INTEGRAL) is part of the astrophysical programme Horizon 2020 of the European Space Agency. The objective was to create a telescope with at least one order of magnitude of improvement in sensitivity in the soft gamma-rays band compared to previous telescopes. The spacecraft was launched in 2002 on board of a Proton rocket (Fig. 2.3). The spacecraft is equipped with two main instruments, the spectrometer SPI, which works between 20 keV and 8 MeV, and the imager IBIS between 15 keV and 10 MeV.

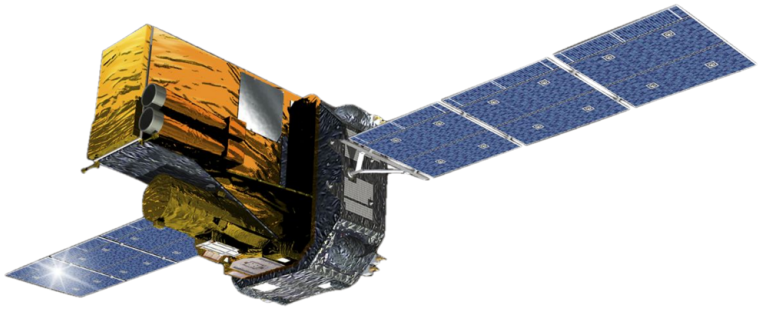

Figure 2.3: Artist rendering of the INTEGRAL spacecraft [3]

Its lifetime has been extended many times, and the satellite should stay in orbit until 2029. With several hundreds of detected sources, INTEGRAL has significantly extended the low-energy gamma-rays catalogue. It has already provided numerous significant results, such as the detection of a new class of X-Ray binaries (Walter et al., 2003) or several results to help unveil the nucleosynthesis process by mapping the distribution of several radioactive elements (Harris et al., 2005) (Diehl et al., 2006) (Renaud et al., 2006).

At higher energy, thinking on the successor of EGRET started shortly after the end of CGRO. The goal was to increase the sensitivity by one order of magnitude and also improve the angular resolution in order to associate sources with counterparts at other wavelengths. This was especially important for the large number of sources in the galactic plane. The spacecraft named *Fermi* was launched in 2008 with two instruments onboard (Fig. 2.4). The LAT (Large Area Telescope), the main instrument, observes radiation between 100 MeV and 1 TeV. A second instrument, GBM (Gamma-ray Burst Monitor), detects and localises gamma-ray bursts. The mission is still active and performs a complete sky survey every 3 h.

Compared to the predecessor EGRET, *Fermi/LAT* greatly increased the number of detected sources, with 5064 sources in the last version of the catalogue (Fig. 2.5b) (Abdollahi et al., 2020)

[3] Credit : NASA, https://science.nasa.gov/get-involved/toolkits/spacecraft-icons
[4] Credit : NASA, https://science.nasa.gov/get-involved/toolkits/spacecraft-icons
[5] Credit: NASA, https://heasarc.gsfc.nasa.gov/docs/cgro/images/egret/EGRET_All_Sky.jpg
[6] Credit: NASA/DOE/Fermi LAT Collaboration, https://svs.gsfc.nasa.gov/14090

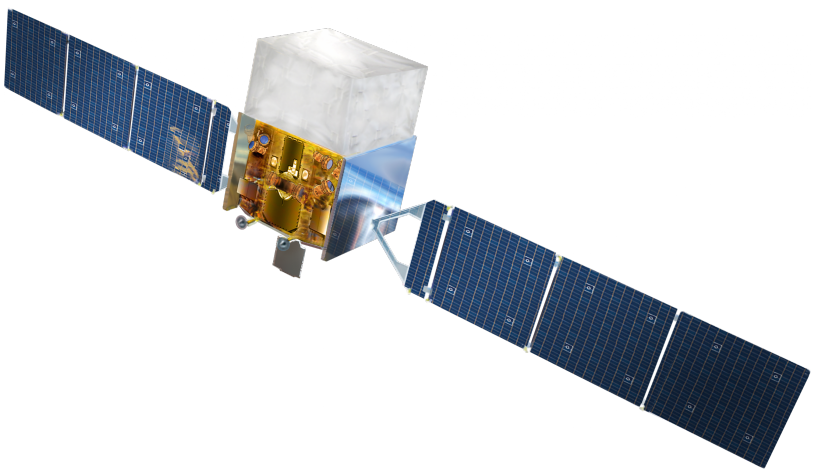

Figure 2.4: Artist rendering of the *Fermi* spacecraft [4]

with only 1336 sources unassociated with counterparts in other wavelengths (63 % of the sources were unassociated in EGRET catalogue). The number of detected sources should continue to increase with observation time. One of the most significant results of *Fermi/LAT* is the discovery of the *Fermi* Bubbles, two giant lobes around the galactic centre, believed to be the relic of the past activity of the galactic nucleus (Su et al., 2010). On his side, *Fermi/GBM* detected more than 3000 GRBs up to now, with more than 2000 of them in the 10 years catalogue (von Kienlin et al., 2020). This vast number of detections associated with the great instrument performance has significantly helped to understand GRBs' emissions.

Space gamma-rays telescopes have been efficient at detecting signals up to a few tens of GeV, but their size and weight are limited by rocket technology. As a consequence, the detection area could hardly exceed $1\,m^2$. However, the higher the energy of the photons, the smaller the photon flux, so a larger detection area is needed to detect a signal. Consequently, spatial experiments are not well suited for very high-energy gamma-rays.

2.5 Ground gamma-ray telescopes

In order to study very high-energy gamma-rays, ground experiments are needed to benefit from a large effective area. While gamma-rays do not reach the ground, it is still possible to run experiments at these energies. When very high energies gamma-rays enter the atmosphere, they interact with it and create electromagnetic showers. In the air, the light speed is slightly lower than in vacuum, allowing the particles of the showers to exceed it. A phenomenon analogous to a sonic boom occurs and light is emitted, mainly in the blue band. This effect is called the Cherenkov effect, on which ground-based experiments are based. Ground-based experiments have the main advantage of allowing for a much larger detection area to explore the highest energies. One of the main drawbacks is that cosmic rays also create atmospheric showers, and separating these cosmic-ray-induced showers from the gamma-ray showers is a complicated task. Most of the time, satellites use anti-coincidence shields to reject cosmic rays. This anticoincidence shield detects the passage of charged particles allowing the detector to reject an event originating from cosmic-rays. But in the case of a ground experiment, it is impossible to install such shields, as they would need to be very high in the atmosphere. So the best way to reject the background caused by these showers is to rely on the different properties of the showers. A detailed explanation is given in the chapter 5.

Zatsepin and Chudakov first proposed a detection method in the early sixties (Zatsepin and Chudakov, 1961), based on the detection of the Cherenkov light emitted by the atmospheric showers. The first attempt at detecting gamma rays from the ground started with the Crimean telescope in 1960 with a design-led by Chudakov (Fig .2.6). The experiment operated up to 1963 but could not

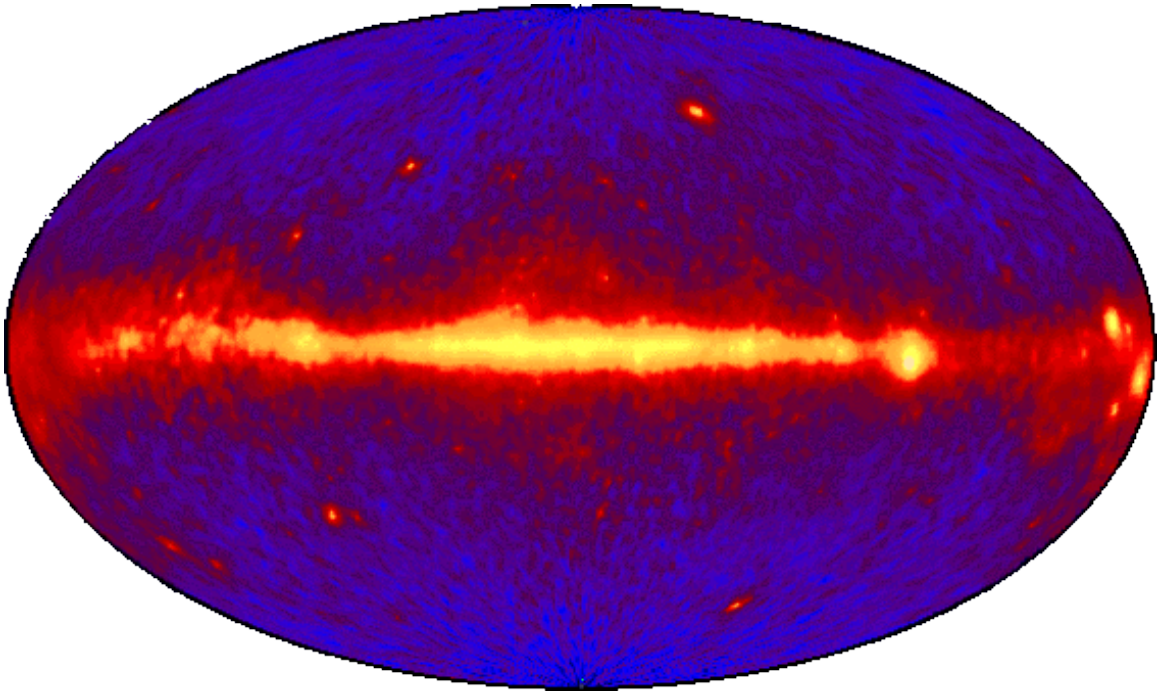

(a) Sky map of all the photons above 100 MeV observed by EGRET during it's nine years of operation[5]

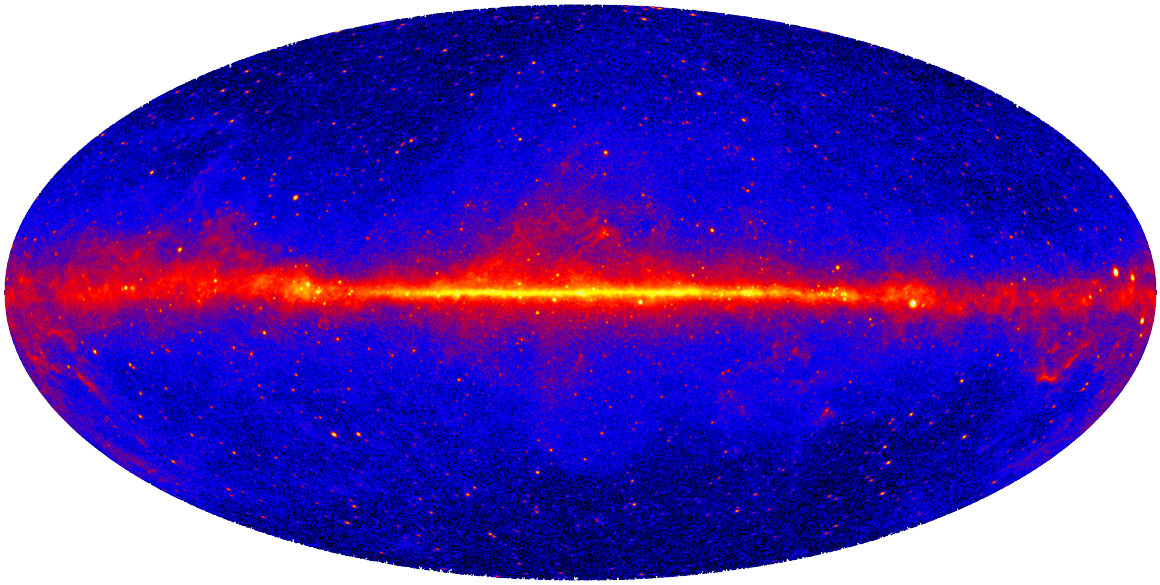

(b) Sky map of all the photons above 1 GeV observed by *Fermi/LAT* for the first twelve years of observations[6]

Figure 2.5: Sky seen at high energy by two different instruments, EGRET and *Fermi/LAT*

detect any signal (Chudakov et al., 1964). Several other experiments, such as Baksan, Durham, or Akeno, tried to detect signals, but failed to do so (Chudakov, 1989).

The Whipple telescope (Fig. 2.7) installed in Arizona innovated in several aspects, a large reflector of 10 m in diameter, a time resolution capability at the nanoseconds levels, a camera with imaging capability using 37 pixels, and a new analysis technique so-called Hillas method to use the information contained in these images (Hillas, 1985). All these elements packed together in a single experiment allowed for the improvement of the background rejection and the energy and direction reconstruction of the photons. In consequence, the sensitivity of the instrument was greatly

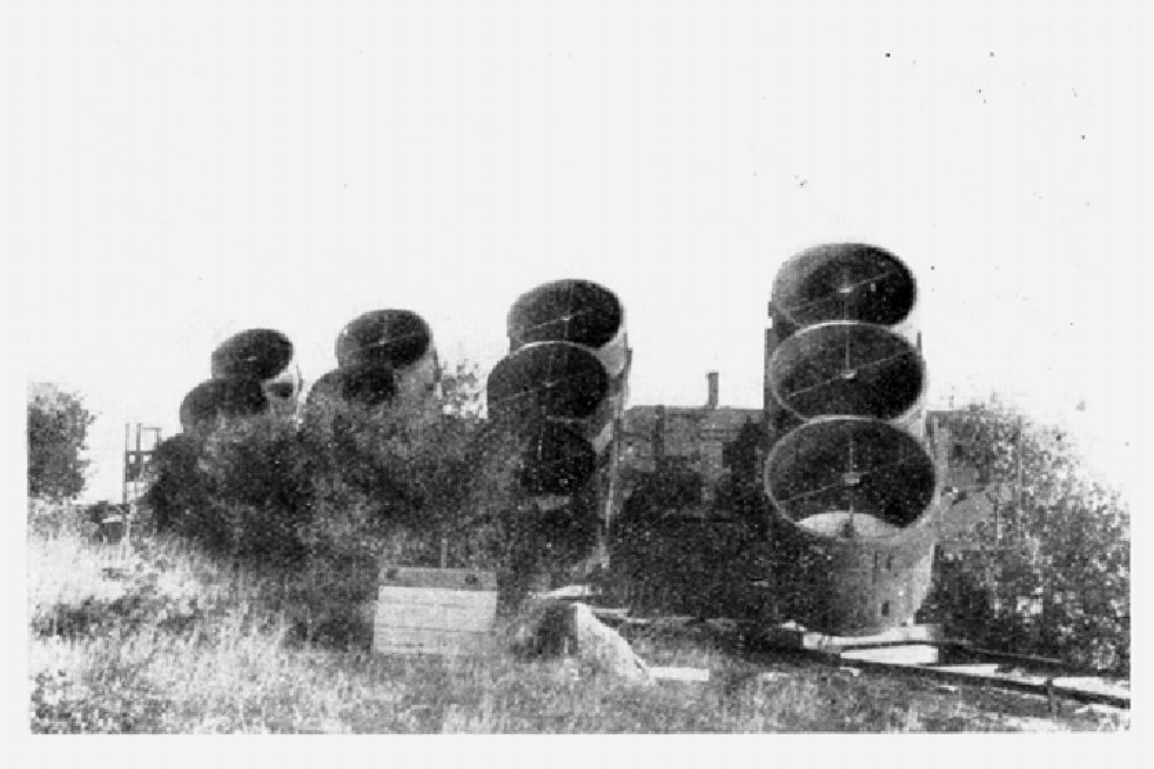

Figure 2.6: The first Cherenkov gamma-ray telescope installed in 1960 in Crimea.

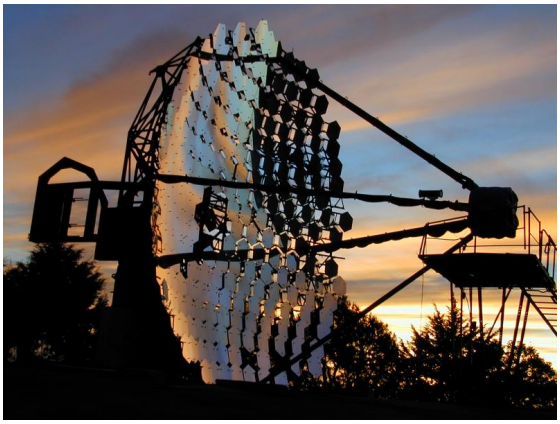

Figure 2.7: The Whipple telescope installed at the Fred Lawrence Whipple Observatory in Arizona

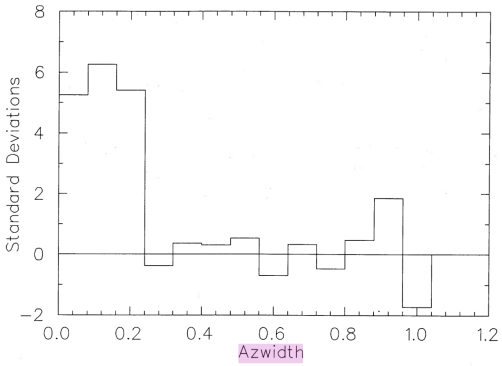

Figure 2.8: First detection of the Crab Nebulae by the Whipple telescope. The figure represents different values of the azimuthal width parameters of the shower images, the standard deviation of the on region centred on the Crab compared to an off region used to estimate background. Gamma-rays-induced showers have smaller azimuthal widths than proton-induced showers, showing, in this case, a significant gamma excess at the source position. Figure from Weekes et al. (1989)

improved, allowing the first detection of a source (the Crab Nebulae) at very high energies (Fig. 2.8) (Weekes et al., 1989).

Following this detection, Whipple detected in 1992 the blazar Markarian 421, the first extra-galactic source (Punch et al., 1992). After these first successes, Whipple was upgraded, and a new generation of IACTs was built. Among them, HEGRA brought a new major improvement, stereoscopical observations. The idea is to use multiple telescopes for the observations, allowing atmospheric showers to be observed from multiple points of view, improving the overall sensitivity (Daum et al., 1997). These new instruments detected a dozen of sources.

In the decade 2000, the third generation of instruments was built with the experiments H.E.S.S., MAGIC, and VERITAS. The design of these experiments used all the knowledge acquired in the previous by using multiple telescopes for stereoscopy with fast imaging cameras composed of hundreds of photo-multipliers (PM). This new generation of instruments can detect flux in the order of a few percent of the Crab Nebulae[7]. This generation of instruments allowed the detection of more than two hundred sources (Fig. 2.9). Several new classes of sources were detected, like novae (H. E. S. S. Collaboration et al., 2022) (Acciari et al., 2022), GRBs (Abdalla et al., 2019) (MAGIC Collaboration et al., 2019a), or pulsars (Aliu et al., 2008).

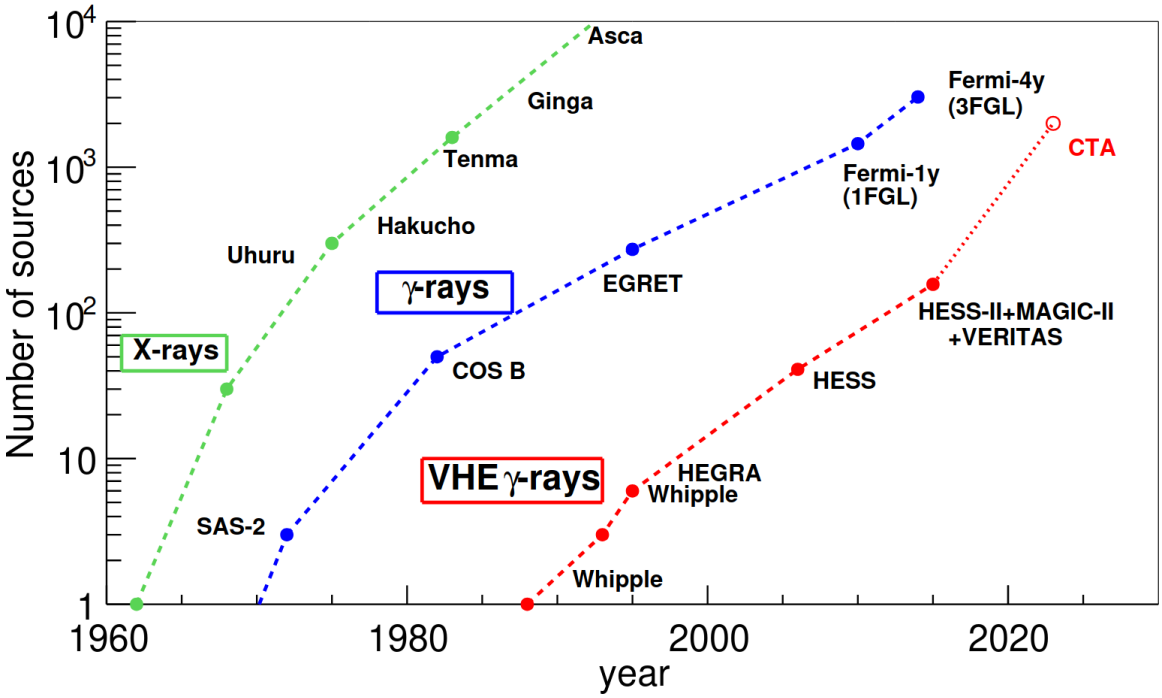

Figure 2.9: So-called Kifune plot showing for different wavelengths the evolution of the number of sources detected as a function of time. The CTA point is a projection made in 2015. Figure from de Naurois and Mazin (2015)

Recently, the next-generation instrument, the Cherenkov Telescope Array (CTA), has started to be built. The construction should last up to the end of the decade 2020. This new instrument will have an extended energy range compared to current experiments and a much better sensitivity, up to one order of magnitude. For this, the observatory will be built across two sites in each hemisphere to cover the whole sky.

More details about the working principle of these instruments and the experiment H.E.S.S. and CTA can be found in the chapters 6 and 7.

Cherenkov telescopes have proved to be great for detecting gamma-rays above a few hundred GeV, with great background rejection capacity, huge effective area, and relatively good energy and direction reconstruction. Among the main inconvenience are the telescopes can only be operated

[7]The Crab Nebulae is the brightest source at VHE. It is also a stable source and is the standard candle for most experiments at VHE or UHE.

during dark night (duty cycle $\sim 10\%$) and have a small Field of View (FoV), typically a few degrees. These limitations cause large limits on the possible exposure in a specific direction of the sky.

2.6 Toward the highest energies

For energies above 10 TeV, even the large effective area of the Cherenkov telescope starts to be limited. Combined with a small field of view and a small duty cycle, it is hard to detect any signal due to the very small flux. To overcome these limitations, other techniques could be used. Instead of detecting the Cherenkov light from the shower, the idea is to directly detect the particles composing the showers using a water tank or scintillator, similar to the ground-based cosmic observatory. This solution allows for a much greater exposure time and a large FoV, at the expense of background rejection capability, energy, angular resolution, and an increased energy threshold.

One of the first experiments of this kind was Milagro. The experiment was composed of a single pond of 5000 m^2 with more than seven hundred photo-multipliers distributed across the whole surface (Atkins et al., 2004). Milagro performed one of the first surveys at VHE of the northern sky, even if the sensitivity was minimal.

The HAWC, High-Altitude Water Cherenkov Observatory experiment, a successor of Milagro, uses three hundred tanks of water with 4 PMTs in each tank instead of using a single pond. The performances are more than one order of magnitude better than Milagro, allowing for a survey with a much higher sensitivity. HAWC detected 65 sources at more than 1 TeV (Fig. 2.10) (Albert et al., 2020) with a majority of galactic sources.

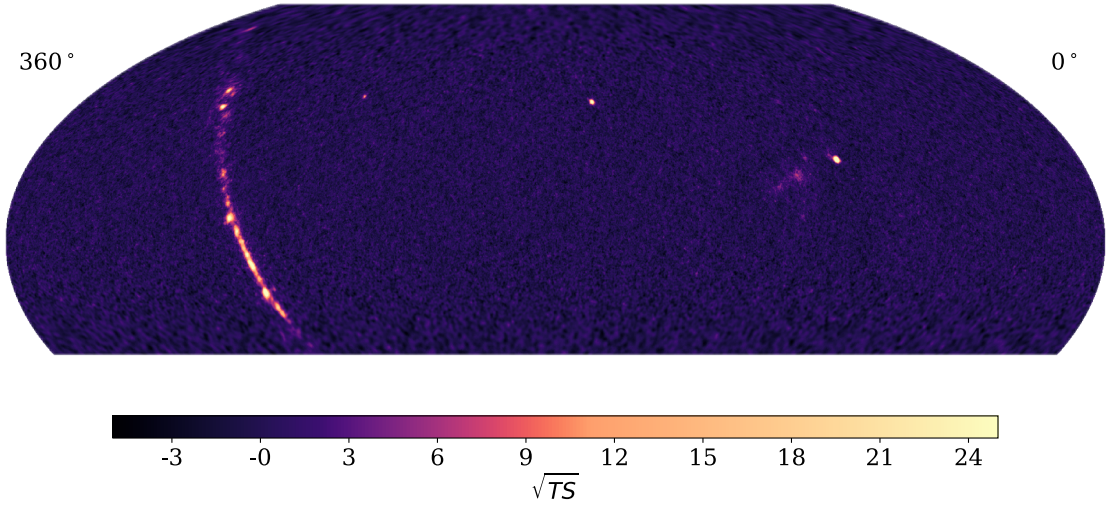

Figure 2.10: Significance map of the whole sky visible by HAWC. The emission from the galactic plane on the left of the figure is easily visible, along with the emission from the Crab on the right and the two blazars Markarian 421 and 501 in the middle of the figure. Figure from Albert et al. (2020)

At higher energies, Tibet AS Gamma, which uses plastic scintillators instead of a Cherenkov water tank, detected for the first time a source above 100 TeV in 2019 (Amenomori et al., 2019). The LHAASO experiment, which used a combination of scintillators, muon detectors, and water tanks, detected the first source above 1 PeV in 2021 (Cao et al., 2021).

LHASSO uses the combination of multiple detectors to improve instrument performances (Ma et al., 2022). This trend is developing in these experiments, as it greatly improves the overall performance of the instrument. For example, the HAWC Eye upgrade will add a small Cherenkov detector (Serna-Franco et al., 2022).

For even higher energies, instruments more focused on cosmic-rays study like the Pierre-Auger

observatory, have searched gamma-ray in their data but have not detected any signal up to now (Abreu et al., 2022b).

2.7 Absorption phenomena

The Universe is not transparent for very high energy gamma-rays. They could be absorbed through the interaction with photons of lower energies, creating an electron-positron pair. The presence of these low energy optic and infrared background light is quickly supposed after the discovery of the cosmic microwaves background (Gould and Schréder, 1967). The light that will interact with VHE photons is the Extra-galactic Background Light (EBL) with a wavelength between 0.1 µm and 100 µm. There are two components in the EBL (Fig. 2.11). The Cosmic Optical Background Light (COB) originates from the light of the galaxies and population III stars, stars of the early universe (Kashlinsky et al., 2005). Cosmic Infrared Background (CIB), on the other hand, is caused by the thermal emission of dust heated by nearby stars (Stecker et al., 1977). Gamma-rays of above 100 TeV will interact with the much more intense Cosmic Microwaves Background (CMB), reducing even more the horizon at these energies.

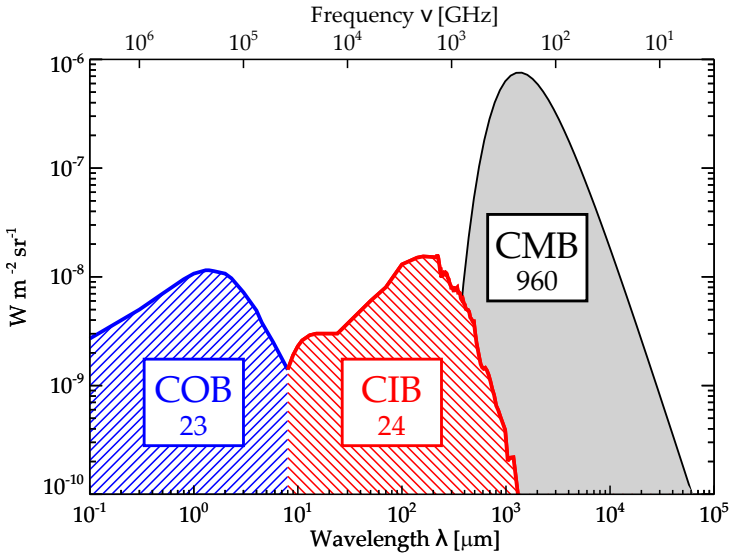

Figure 2.11: Schematic representation of the most important background light. Figure extracted from Dole et al. (2006)

The observed spectra on the earth F_{Obs} is linked to the intrinsic spectra of the source F_{Int} by the formula :

$$F_{Obs}\left(E_\gamma\right) = e^{-\tau(E_\gamma,z))} F_{Int}\left(E_\gamma\right)$$

with E_γ the energy of the photons and τ the optical depth that depends of the photon energy but also the redshift.

The effective attenuation for different redshifts could be seen on the figure 2.12. As it could be seen even for a redshift of z=4, the impact on the spectra at HE will be moderated and so this effect will mainly impact VHE and UHE observatories. A good knowledge of the effect is then important to be able to study the intrinsic properties of the sources. The probe of EBL absorption at VHE could also be a way to improve the constraint on the EBL models. Franceschini (2021) is a detailed review of the phenomena and the actual constraints.

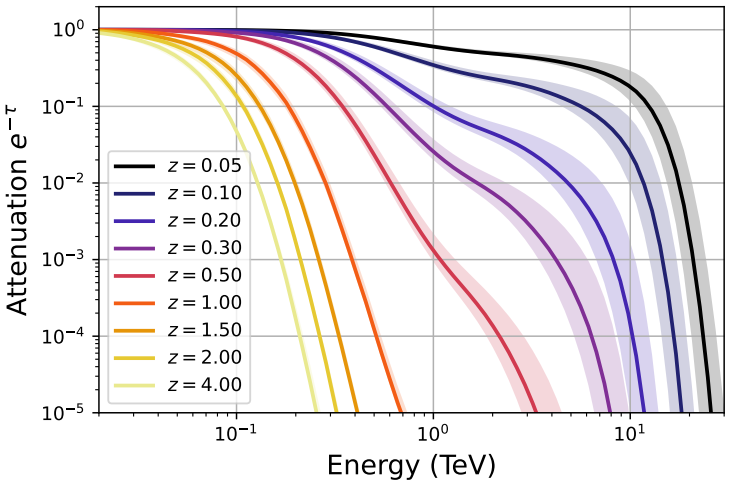

Figure 2.12: The attenuation of a signal due to interaction with the EBL as a function of the energy for various redshifts. The model used is Domínguez et al. (2011)

Chapter 3

Gamma-Ray Burst

Contents

3.1 Discovery of GRBs

Following the Cuban Missile Crisis in 1962, the Soviet Union, the United Kingdom, and the United States signed the Partial Nuclear Test Ban Treaty on the 5th of August, 1963. This treaty banned all nuclear tests not performed underground, with the aim of slowing nuclear proliferation and the arms race.

To ensure that the Soviet Union followed treaty guidelines, the United States developed the Vela project. In particular, a series of spacecrafts dedicated to detecting and locating nuclear explosions were built. Figure 3.1 presents two satellites before the launch. The first pair of satellites was launched on the 17th of October 1963 and equipped with X-Ray, neutrons, and gamma-ray detectors. A total of six pairs of satellites were launched with the evolution of their instruments over time.

On the 2nd of July 1967, Vela satellites recorded a bright burst of gamma rays lasting a few seconds. This burst was not exhibiting the signature of a nuclear bomb explosion. Therefore, some investigations started at the laboratory of Los Alamos to understand the nature of the detected signal. The launch of the satellites 5A&B in 1969 and 6A&B in 1970 allowed the detection of several similar bursts with their more sensitive instrumentation. The discovery was published in 1973 (Klebesadel et al., 1973), and figure 3.2 shows the light curve of this event. Using the detection by multiple satellites, they were able to determine a rough localisation in the sky of some of these events ruling out a solar or lunar origin, but also rejecting a possible association with a known supernova or nova event.

Those events are now called Gamma-Ray Bursts (GRB).

[1] Credit : Los Alamos National Laboratory, https://heasarc.gsfc.nasa.gov/Images/vela5b/vela5b_2.gif
[2] https://heasarc.gsfc.nasa.gov/grbcat/about.html

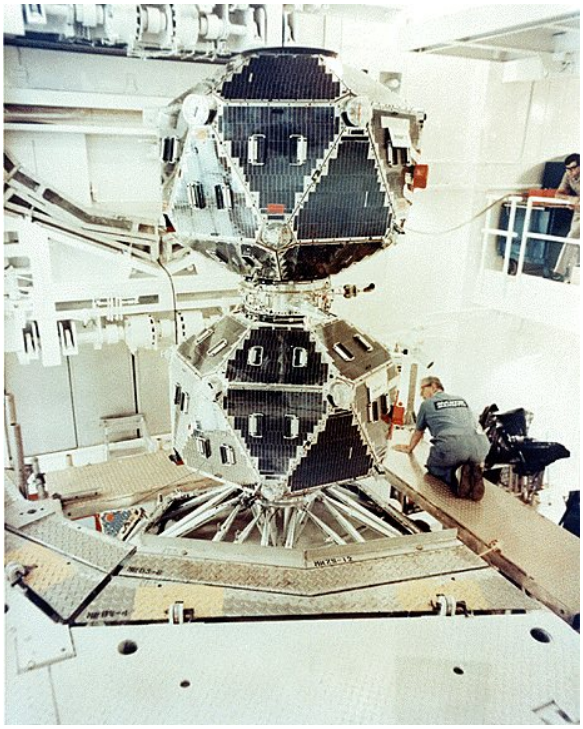

Figure 3.1: Image of the pair of satellites Vela 5A and Vela 5B[1]

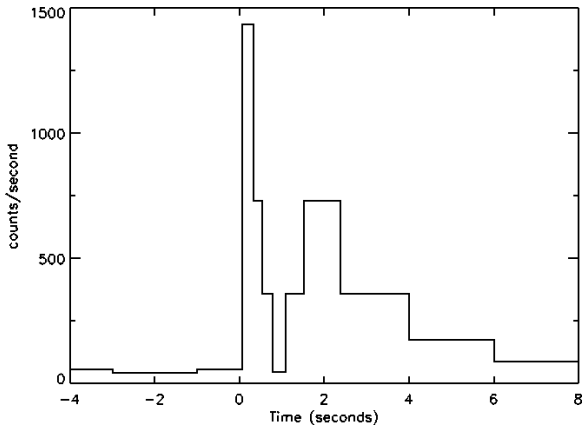

Figure 3.2: Signal registered by Vela satellite 4A and 4B of GRB 670702, the first GRB detected[2]

3.2 The start of the hunt for GRBs

To study the origin and nature of the bursts, localising them is important as it could provide a hint of the provenance and point towards a possible counterpart in other wavelengths. If close-by objects caused the bursts, their positions would correlate with known stars or another close object. In the case of a broader galactic origin, they should be mainly seen within the galactic plane, correlation with the local structures will point towards an origin in the close universe, and finally, in the case of sources at a cosmic scale, the distribution of sources should be isotropic.

To improve the localisation, either better timing information or greater distance between satellites should be used. In the '70s, lots of probes were sent across the solar system, and often a detector sensitive to gamma-rays was present onboard. In 1976, the Interplanetary Network (IPN) was created to gather data from these instruments and compute the gamma-ray burst localisation. The

first version of this network integrated Helios-2, the Pioneer Venus Orbiter probes, Venera 11, Venera 12, and the satellites SIGNE 3 and Prognoz 7. Several bursts were detected and localised with this method (Klebesadel et al., 1982) but no counterpart was identified. IPN is still running today, with 32 missions taking part or took part in the network. A timeline of the IPN with the different missions is given in figure 3.3.

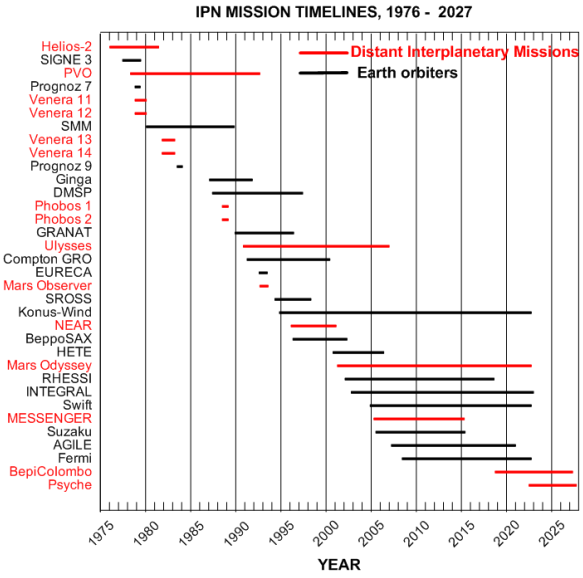

Figure 3.3: Timeline of the participation of space missions in the Interplanetary Network

3.3 BATSE and its legacy

An important milestone was achieved on the 5th of April 1991, with the launch of the CGRO satellite by the space shuttle Atlantis. Onboard the Burst and Transient Source Experiment (BATSE) was dedicated to detecting and studying gamma-ray bursts. The instrument was composed of eight modules placed at each corner of the satellite. Each module was composed of two different scintillation counter detectors. The first one, the Large Area Detector (LAD), has the detection and localisation of bursts as its main objectives. The second one, the Spectroscopy Detector (SD), is much smaller and thicker, giving a better energy resolution. Their main objective is to provide precise spectral information about the burst (Paciesas et al., 1989). BATSE was sensitive to gamma-rays between 20 keV and 1 MeV. The triggering system searched for a rate increase of duration from 64 ms to 1024 ms allowing for the detection of very short bursts. The wide field of view of each detector allows any part of the sky that is not blocked by the Earth to be seen by at least four detectors. The difference in signal between the detectors allows for the localisation of a burst within a few degrees (Preece et al., 2000).

Among the reasons for the lack of detection of counterparts to GRBs with IPN was the delay for the localisation information. Today, a delay of a few days is typical for getting this information from IPN, and could be even more important at the time. BATSE was able to give localisation information on its own without the need to cross-match the information with another instrument. To allow any instrument to have a fast response to GRBs, as soon as the detection of a GRB started by BATSE, data were transmitted to Earth via a ground station if available, otherwise through the communication satellite network Tracking and Data Relay Satellite (TRDS). The data were then processed, and the information was transmitted through the BATSE Gamma-Ray Burst Coordinates Distribution Network (BACODINE). This whole system allowed for the coordinates to be distributed with a time delay as low as 5.5 s, improving the delay by 5th to 6th order of magnitude compared to the previous system (Barthelmy et al., 1994). The BACODINE system

evolved to support other instruments and became the GRB Coordinates Network (GCN). GCN is today one of the cornerstones for the GRB community to perform follow-ups, and most of the instruments able to detect GRB transmit their alert through this system.

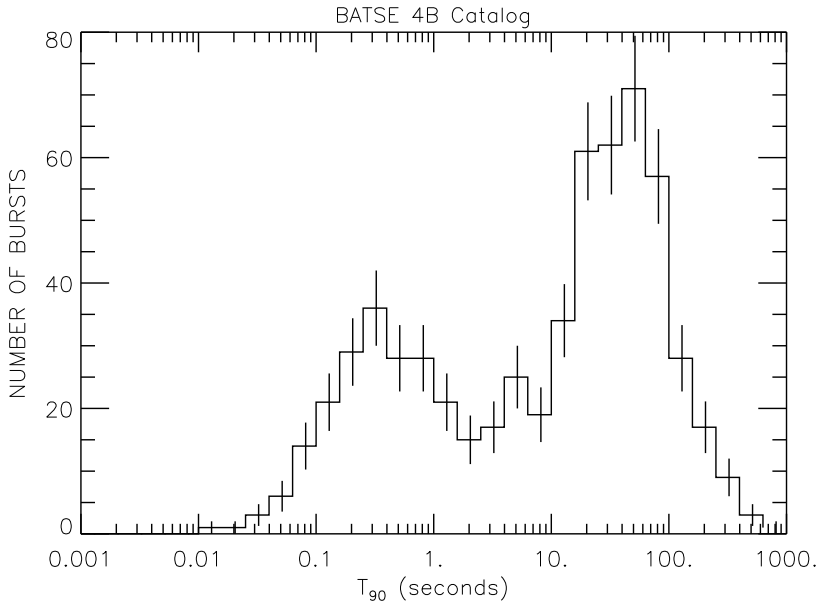

Figure 3.4: Distribution of the T_{90} duration for BATSE observed GRBs. Figure from (Paciesas et al., 1999)

BATSE has led to numerous discoveries and has significantly helped to better understand gamma-ray bursts. One of them is the existence of two subcategories of GRBs based on their duration. To estimate the duration, the T_{90}[3] parameter was used. The first category is called short GRB, with a duration of less than 2 s, and the second long GRB, with a duration of more than 2 s (Fig. 3.4) (Kouveliotou et al., 1993)). With its good sensitivity and wide field of view, BATSE has detected a total of 2704 GRBs in nine years of operation. BATSE has, in this way, also helped to unveil the wide variety of GRBs light curves (Fig. 3.5).

Another important result is the distribution in the sky of the GRBs observed by BATSE. With the first 193 days of data, BATSE has shown that the burst distribution was isotropic with high confidence (Meegan et al., 1992) pledging in favour of sources at a cosmological distance. One implication is that GRBs are among the most energetic phenomena of the Universe as they are bright and distant. This result was reinforced across the life of the experience and the detection of more GRBs (Fig. 3.6) (Paciesas et al., 1999).

Onboard of CGRO, along with BATSE, there was the instrument EGRET, which observed gamma-rays at higher energies compared to BATSE. On the 3rd of May 1991, EGRET detected nine photons coherent both spatially and temporally with BATSE detection of a burst. With the highest energy detected of 200 MeV, this significantly extended the energy spectra of gamma-ray bursts (Schneid et al., 1992). GRB 930131 was also detected by EGRET, this time up to 1 GeV (Sommer et al., 1994). In 1994, the very bright GRB 940217 was detected by EGRET with energies up to 18 GeV and for 90 minutes (Hurley et al., 1995). This emission lasted much longer than the BATSE emission, which lasted only 180 s. This was the first indication of the existence of a long-lasting emission, called afterglow, as opposed to the short ones detected previously and called prompt emission.

[3]The T_{90} is the duration for the burst to emit 90% of its total fluence starting at a time when 5% has been emitted.
[4]Credit : Daniel Perley, https://fr.m.wikipedia.org/wiki/Fichier:GRB_BATSE_12lightcurves.png
[5]Credit : NASA, https://heasarc.gsfc.nasa.gov/docs/cgro/cgro/batse_src.html

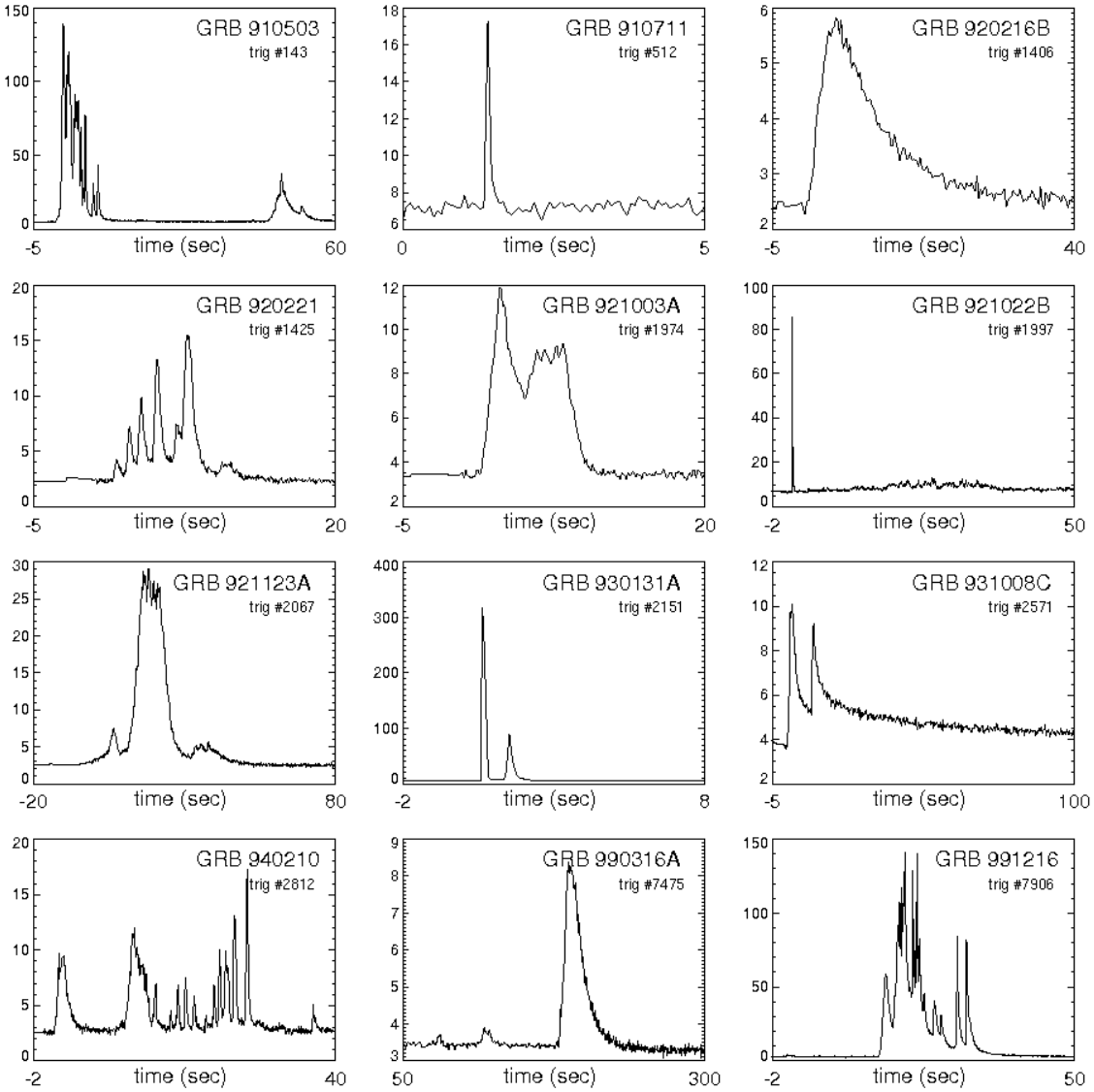

Figure 3.5: Light curves of twelve bright GRBs recorded by BATSE[4]

3.4 Rising of GRBs follow-ups

Despite all the improvements broad by BATSE, no detection of a counterpart at lower energy was achieved. BATSE with the BACODINE system solved the issue of the delay, but the localisation had an uncertainty of a few degrees, much larger than the field of view of most low-energy instruments.

In 1996, the space agency of Italy (ASI) and the Netherlands (NISR) launched the Beppo-SAX X-Ray satellite. The six onboard instruments allowed an energy coverage from 0.1 keV to 300 keV. Among them, two were of special interest. The anti-coincidence shield of the Phoswich Detector System (PSD) instrument could be used to detect GRBs with a rough localisation. However, Beppo-SAX was also equipped with two Wide Field Camera (WFC) observing X-Ray between 2 keV and 30 keV, with a field of view of 20 deg. This instrument was equipped with a coded mask that allowed source localisation determination up to a few arcminutes.

GRB 970228 was successfully detected by WFC instrument. The Beppo-SAX team performed a follow-up 8 h after the burst using the onboard soft X-Ray LECS and MECS instruments and successfully detected a new fading X-Ray source (Frontera et al., 1998). Following this detection,

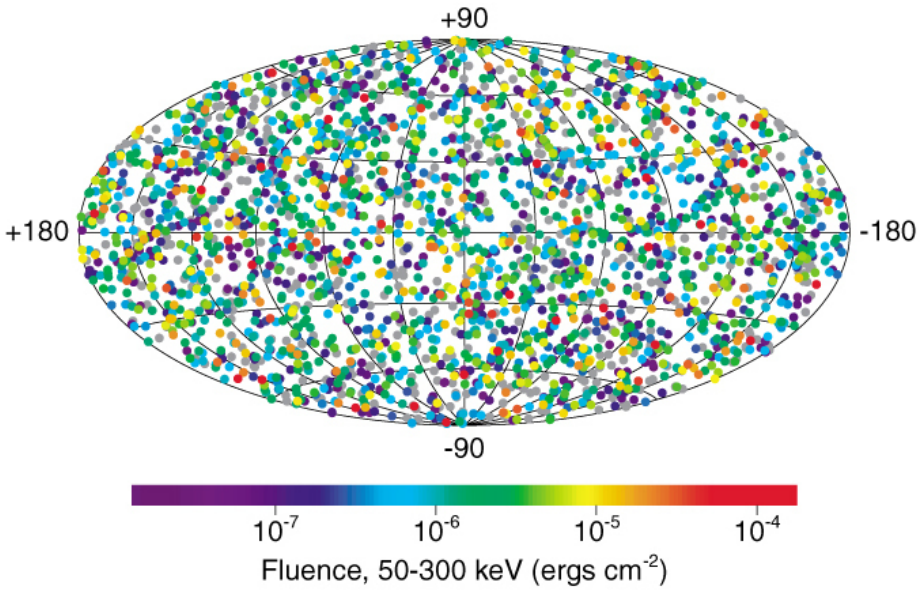

Figure 3.6: Skymap of the position of the 2704 burst detected by BATSE during its nine years of operation. The colour scale represents the fluence of the burst.[5]

the William Herschel Telescope observed the burst with a delay of 20 h and detected a new optical source (van Paradijs et al., 1997). This was the first clear detection of an afterglow at energies lower than gamma-rays. Later observations of the Hubble Space Telescope allowed for the detection of the host galaxy of the burst with the afterglow still visible (Fruchter et al., 1999). The position of the burst on the side of the galaxy (see Fig 3.7) ruled out models linking GRBs and Active Galaxy Nuclei (AGNs).

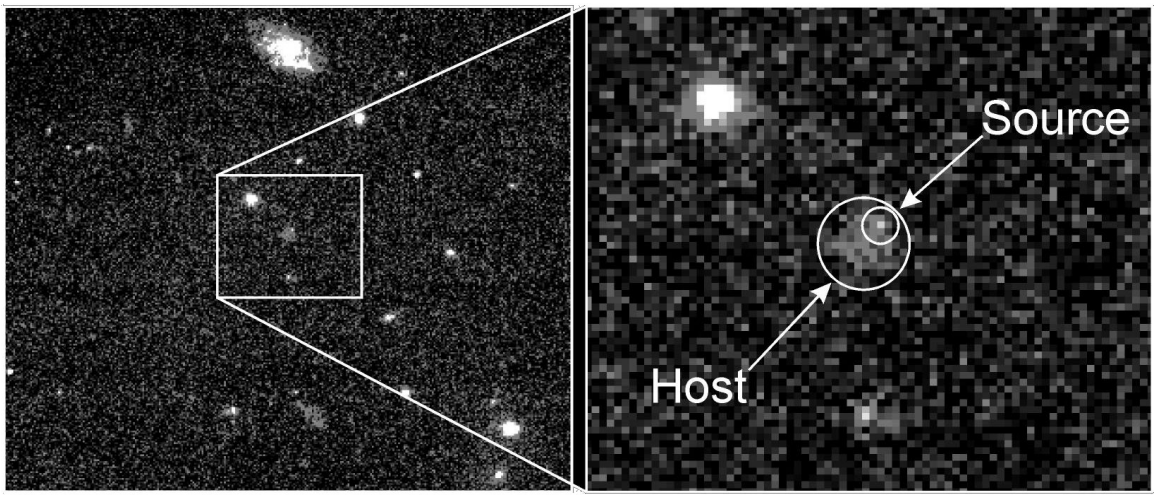

Figure 3.7: Observation of GRB 970228 by the Hubble Space Telescope. The afterglow of the GRB could be identified alongside with the host galaxy.[6]

Just a few months later, GRB 970528 was detected by WFC, an instrument onboard of Beppo-Sax. The afterglow was detected in X-Ray and optical like 970228. The Keck II telescope acquired spectroscopic data and was able to determine the redshift of the GRBs at z=0.835 (Metzger et al.,

[6]Credit : Andrew Fruchter (STScI), Elena Pian (ITSRE-CNR), and NASA/ESA, https://esahubble.org/images/opo9730a/

1997). This burst was also the first burst with afterglow detection in radio by VLA[7] (Frail et al., 1997). This measure helped to confirm the hypothesis that GRBs emissions were linked to relativistic jets.

In 1998, the supernova SN 1998 BW was detected within the uncertainty region of GRB 980425 (detected by Beppo-SAX). This supernova presents atypical spectral behaviour, especially in radio, indicating an expansion at relativistic speed. The supernova peaked approximately two weeks after the GRB (Galama et al., 1998). Despite the very low chance of this event being a coincidence, it was not possible to firmly link the supernova and the GRB at the time.

High Energy Transient Explorer 2 (HETE-2) was the first mission whose primary goal was to study GRBs. HETE-2 was launched in 2000 by NASA as a replacement for the HETE satellite, which was lost due to a launch failure in 1996. The instruments onboard HETE-2 were very close to the ones onboard HETE. It was equipped with three wide fields of view instruments, FREGATE a gamma-ray detector (6 keV-400 keV) with a 3 sr FoV, SXC a soft X-Ray camera (0.5 keV-14 keV) with a FoV of 0.9 sr and WXM an X-Ray detector (2 keV-25 keV) with a FoV of 1.6 sr. Any burst could be localised with a precision of up to $30''$. HETE-2 also adopted a pointing strategy that ensures that the instruments always points in the direction of the night sky for ground-based instruments, increasing the possibility of follow-ups.

Among the GRBs detected by HETE 2, GRB 030329 was the first clear association of a supernova with a gamma-ray burst. Multiple acquisitions of optical spectra of the events have shown the evolution of the spectra from a GRB afterglow-like to a supernova-like (Hjorth et al., 2003). This discovery allowed us to link long GRBs to the death of the stars.

3.5 The modern era of GRB detector

Today, two instruments provide most of the GRBs alert, *Swift* and *Fermi*. It is still important to mention other instruments: ISGRI (part of the IBIS instrument) and the anti-coincidence shield of the SPI instrument, both onboard INTEGRAL, launched in 2002. There is also a pair of GECAM satellites launched by the Chinese space agency in 2020.

The *Swift* spacecraft was launched in 2004 by NASA. The primary objectives of this mission are the study of GRBs as a successor of the HETE-2 mission. The spacecraft hosts three instruments :

- Burst Alert Telescope (BAT) : a hard X-Ray coded mask telescope with a dynamic range of 15 keV to 150 keV and a large FoV of 2 sr. The instrument is devoted to detecting and studying the prompt phase of GRBs. Its good angular resolution of a few arcminutes make it one of the best instrument to perform follow-up from the ground.
- X-Ray Telescope (XRT) : a soft X-Ray telescope (0.2 keV - 10 keV) designed to detect the afterglow of a burst to determine its spectra and light curve. The provided localisation is also better with an uncertainty of a few arcseconds.
- UltraViolet/Optical Telescope (UVOT) : This instrument has six different filters (between 170 nm and 650 nm), and its main objective is to study the optical afterglow and especially the early phase. It could also refine the localisation to a precision below the arcsecond.

When *Swift*/BAT detect a GRB, the spacecraft slew in order to have the two other narrow field of view instruments be able to observe the GRB. It is also performing frequent observations on previously detected GRBs for a certain time to determine more long-term light curves.

Swift was the first to detect the afterglow of a short GRB and to identify the host galaxy (Gehrels et al., 2005). The farthest GRBs, GRB 090423, with a redshift of 8.1 (Salvaterra et al., 2009) has been detected thanks to *Swift*. Another GRB, GRB 090429B, was measured with a photometric redshift of 9.4 (Cucchiara et al., 2011), but the measure suffers from large uncertainties. The detection of these very high redshift GRBs could be an indirect way to study the stars of the early Universe and the reionisation phase.

The other major space mission for GRB study is *Fermi* with onboard two instruments :

[7] Very Large Array is an array of radio antenna installed in the state of New Mexico in the United States.

- Large Area Telescope (LAT) : this is a pair production telescope dedicated to the observation of high energy gamma-rays (100 MeV-2 TeV). With its large FoV of 2 sr, it performs a complete survey of the sky every 3 hours.

- Gamma Burst Monitor (GBM) : the instrument is composed of 14 Scintillation detectors. Twelve of the detectors are focused on the low energy (5 keV-1 MeV). The detectors are placed all around the satellite, allowing full coverage of the sky that is not occulted by the earth. The last two detectors are focused on the detection of higher energies (300 keV-30 MeV). The overall design allowed for a wider energy range than BATSE for a similar spectral resolution, but at the expanse of the effective area.

The follow-up of GBM alert is difficult due to the large uncertainty on the localisation, so contrary to bursts detected by *Swift*, most GBM bursts do not benefit from ground follow-up. Nevertheless, GBM is a great instrument to study the prompt phase, with more than 3300 bursts detected up to date. LAT is able to detect some bursts at high energy, improving the localisation provided by GBM. However, it is only for the brightest burst due to the very low sensitivity of LAT on short timescales and with a significant delay as data need to be ground processed. GBM currently has the record of the most energetic burst with the detection of GRB 080916C and a total isotropic equivalent energy of 8.8×10^{54} erg. The burst redshift was z = 4.35 (Abdo et al., 2009).

Another important discovery of GBM is the detection of the short GRB 170817A 1.7 s after the detection of the merger of neutron stars GW 170817 by the gravitational waves interferometers LIGO and Virgo (Abbott et al., 2017). Ground and space follow-up allowed for the detection of the afterglow from radio to X-ray. These results are the confirmation of the link between neutron star merger and short GRBs and one of the first examples of multi-messenger astronomy.

3.6 GRBs at VHE

The first detection of GRBs at HE energy has been performed by EGRET with GRB 910503 and the first afterglow with GRB 940217. The observation of bursts at HE is now with *Fermi*/LAT quite common, with the detection of more than 200 bursts.

The search for a signal at VHE has already started with the first Cherenkov telescopes but also with particle detectors on the ground. Detection of a prompt phase at VHE has never been achieved despite the fact that few bursts happened in the FoV of a Cherenkov Telescope (Aharonian et al., 2009b) and the high exposure time and wide FoV of detectors such as Milagro and HAWC. *Fermi*/LAT detected GRB 130427A with photons close to 100 GeV at the end of the prompt/early afterglow phase and photons with energy of 95 GeV a few minutes after the prompt phase. The detection of these photons showed emission very close to the VHE domain.

The first detection of an afterglow at VHE was a long-awaited result and required hundreds of unsuccessful follow-ups by Cherenkov experiment (Aharonian et al., 2009a) (Longo et al., 2022). The first detection was performed by H.E.S.S. on GRB 180720B (Fig. 3.8) (Abdalla et al., 2019). The signal was detected during 2 h of observation with a delay of 10.1 h. Following this detection, MAGIC detected the early afterglow of GRB 190114C up to 1 TeV (MAGIC Collaboration et al., 2019a). More intriguing is the detection of the nearby GRB 190829A up to 56 h after the burst by H.E.S.S. (H. E. S. S. Collaboration et al., 2021). Finally, MAGIC detected GRB 201216C, with a redshift of z=1.1. This is the farthest VHE source ever detected (Fukami et al., 2022).

3.7 The standard model for GRB emission

Numerous models have first been proposed to explain gamma-ray bursts. The discoveries of BATSE and the discoveries and study of afterglow allowed by Beppo-Sax have rejected most of them.

As seen previously, there are two sub-categories of GRBs, short and long GRBs, both with distinct progenitors. Observations have allowed us to link short GRBs to neutron star mergers and long GRBs to supernovae.

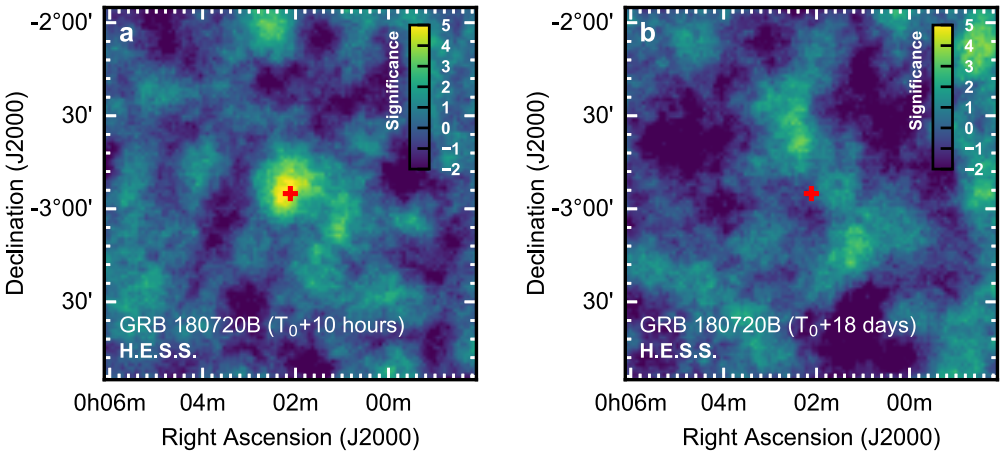

Figure 3.8: Observation of the field of GRB 180720B by H.E.S.S. On the left is a significance map of the observation performed with a 10 hour of delay, and on the right, is the one with 18 days of delay. The red cross is the position of the GRB measured in optic. Figure from (Abdalla et al., 2019).

3.7.1 Formation of the central engine and relativistic jet formation

The actual model for GRB emission is called the fireball internal-external shock model (Fig. 3.9).

The first step of the model is the creation of the central engine composed of a forming black hole and an accretion disk. In the case of short GRBs, these conditions and the matter in the disk are provided by the merger of two neutron stars. In the case of the long GRBs, this is the core collapse at the end of the life of a rapidly rotating massive star that is the cause of the creation of this central engine. The very high accretion rate of the central engine causes the emission and acceleration of an ultra-relativistic jet. This acceleration model is called the fireball (Cavallo and Rees, 1978).

3.7.2 The prompt emission

The prompt emission is explained by the presence of an internal shock (Rees and Meszaros, 1994). The rapid evolution of the central engine caused important variations in the physical parameters that will significantly impact the Lorentz factor of the matter ejected in the jet. The various shells of matter travel at different speeds inside the jet and form a shock between each other. As seen in a previous chapter, shocks allow for the acceleration of particles at very high energies. The accelerated particles could then emit light through the synchrotron process or inverse Compton. The multiple peaks of emission that could be seen during the prompt phase could be interpreted as multiple shocks of multiple layers of matter.

3.7.3 The afterglow emission

The GRB environment is never completely empty. The jet formed will encounter the interstellar medium, and two shock waves will form (Meszaros and Rees, 1993). The first one is the reverse shock, which will travel back in the jet and mainly contribute to the early phase of the afterglow. The second one is called the forward shock travel and creates a more long-lasting emission. Both shocks could accelerate particles that could then emit light through the synchrotron or inverse Compton process. As the matter from the jet travels in the interstellar medium, it loses energy, causing the

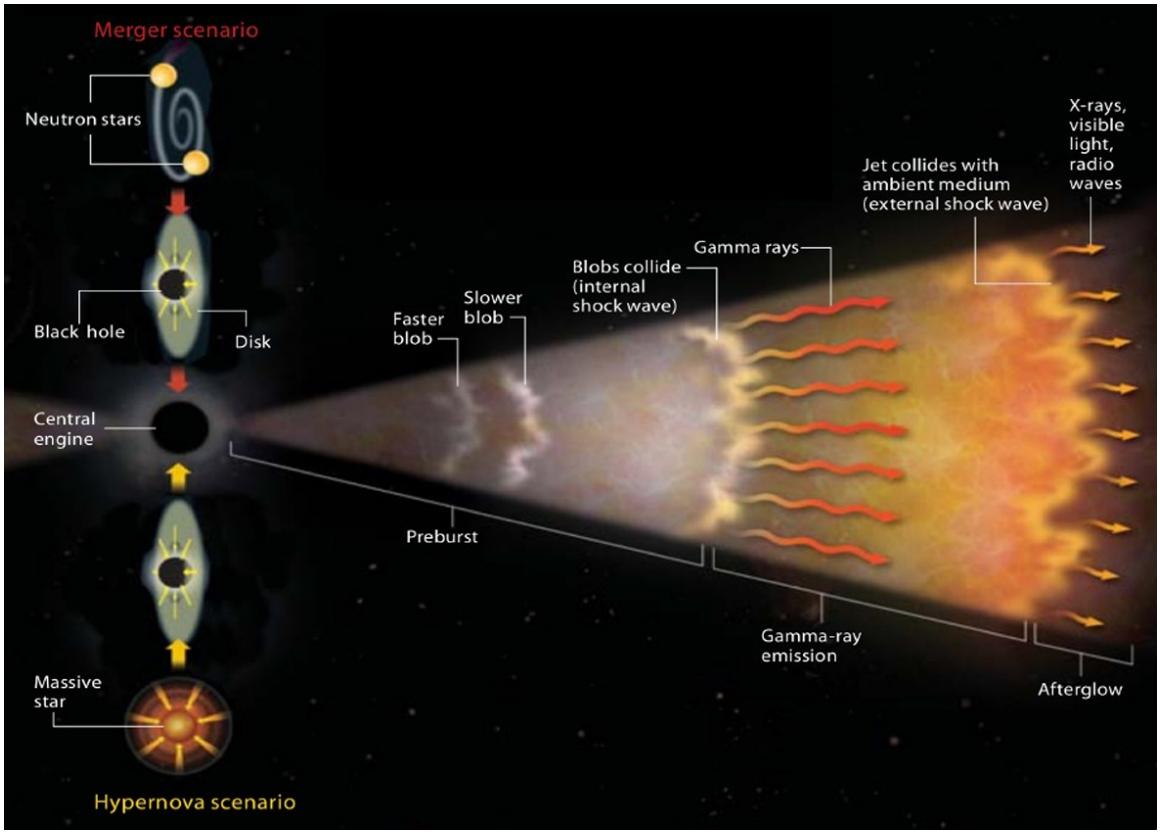

Figure 3.9: Artistic view of the standard model for the emission of gamma-ray burst. Figure from (Piron, 2016)

afterglow's brightness to decrease across time. This emission can be detected in radio and X-Ray more than a year after the burst in some cases (Kangas and Fruchter, 2021) (Troja et al., 2019).

3.8 More than two classes of GRBs ?

3.8.1 GRB 200415A, a giant magnetar flare ?

The short GRB 200415A triggered the GBM instrument onboard of *Fermi*. IPN network using data from several instruments was able to localise the burst in Sculptor (NGC 253), a nearby galaxy located only at 3.5 Mpc. The light curves recorded by several instruments show some similarity to giant magnetar flares recorded in our galaxy (Svinkin et al., 2021). Magnetars belong to a special class of highly magnetised neutron stars (B $>1 \times 10^{14}$ G) and might be the source of the Soft Gamma-Ray Repeaters, which are series of bursts in X-ray or gamma-ray originating from the same object. They are believed to sometimes cause giant flares such as SGR 1806-20 in 2004 (Terasawa et al., 2005). GRB 200415A was also detected by *Fermi*/LAT with three gamma-rays of energy up to 1.7 GeV. The hard spectrum is similar to the one measured for short GRBs by *Fermi*/LAT, indicating the presence of ultra-relativistic outflow (Fermi-LAT Collaboration et al., 2021). This detection opens the question whether a fraction of the short GRBs are not neutron star mergers but magnetar giant flares.

3.8.2 The ultra-long GRBs, a separate class of GRBs ?

The prompt phase of a long GRB has a mean duration of $\sim$40 s, and a duration of a few hundreds of seconds is not exceptional. Some GRBs have lasted for a very long time, like GRB 111209A with

a duration of ∼25 ks (Gendre et al., 2013). It has been proposed that these GRBs are a special class with progenitors that will be different from the long GRBs (Levan et al., 2014) (Boër et al., 2015). This question is still open, and the very limited number of bursts detected complicates the task of answering it.

3.8.3 The low luminosity GRBs case

In the luminosity distribution of long GRBs, a separate population seems to appear at low luminosity (Liang et al., 2007). These GRBs might have jets with a low Lorentz factor or with a jet that does not point towards Earth (Daigne and Mochkovitch, 2007). Several authors have proposed that the emission processes could be completely different and caused by a failed jet (Bromberg et al., 2011) (Nakar and Sari, 2012).

3.9 GRB 221009

At the time of writing these lines, GRB 221009 has very recently been detected by GBM. It is the brightest burst ever detected by a GRB instrument (Veres et al., 2022). The X-Shooter instrument installed on one of the VLT telescopes measured the redshift at $z = 0.151$ with an isotropic equivalent energy of 2×10^{54} erg (de Ugarte Postigo et al., 2022). This places the GRB at the high end of the energy distribution and the low end of the redshift distribution, explaining its exceptional brightness. However, since GBM instruments suffer from a huge saturation effect, the isotropic equivalent energy could be underestimated (Lesage et al., 2022). It is worth noting that the burst was so bright that perturbation of the ionosphere was detected with perturbation of the propagation of very low frequency radio waves used for marine communication (Guha and Nicholson, 2022) (Hayes and Gallagher, 2022).

Another important announcement related to this GRB is the detection by LHAASO of more than 5000 VHE photons with a maximum energy of 18 TeV (Huang et al., 2022). If this announcement is confirmed, it would be the first detection of a prompt phase at VHE. Also if the detection of these 18 TeV photons is confirmed with a good energy resolution, it will be very hard to explain it with the actual models of absorption by EBL.

This exceptional burst is under a massive follow-up campaign by numerous instruments. It will likely help to improve our understanding of these events and, if the LHASSO experiment announced are confirmed, bring some major breakthrough for the GRB field and VHE astronomy.

3.10 Open question and perspective

Even if our understanding of the GRBs progressed a lot compared to the very confused picture at the launch of CRGO in 1991, many open questions remain. In this part will be discussed some of them and their perspectives.

As discussed above, the categorisation of GRBs in Short-Long GRB is maybe too restrictive, and new categories of GRBs could emerge in the coming years. As the classification relies mainly on the T_{90}, it could cause some misclassification as the separation between the two classes is not very strong. For example, GRB 200826A with a T_{90} of 1.13 s measured by GBM would be easily classified as a short GRB, but optical follow-ups have shown that it is very likely a collapsar scenario, so a long GRB (Ahumada et al., 2021). Another issue of classification based on the T_{90} is that this parameter could be affected by the instrument's sensitivity and the energy range, which vary from one instrument to another. A proposition has been made to transform the two classes, Type I GRB (for a merger of neutron star) and Type II GRB (for the collapse of the core of a massive star), and to add other parameters to the separation of GRBs in this two-class (Zhang, 2011).

Long GRBs have been connected to supernovae, especially of type Ib and Ic, but only a small portion of the observed supernovae have been connected to the emission of GRB. The beamed emission of GRB could explain part of this difference, but another element is needed to fully determine the criteria that make a massive star become a GRB or not (Guetta and Della Valle, 2007).

To study the exact relation of neutron star merger with short GRBs, the future increased rate of gravitational wave signals will likely help. Furthermore, the detection of mergers of neutron stars and black holes by LIGO/VIRGO (Abbott et al., 2021) could open the question of whether they could also be the progenitors of GRBs (Zhang, 2011).

The way in which particles are accelerated in GRBs is far from being solved, and several scenarios are still open to explain it, among them shock, magnetised shock, or even magnetic reconnection (Gomboc, 2012) (Zhang, 2011).

The radiation mechanism of the prompt phase is still unclear, either concerning the type of particles that caused the emission (electrons or protons) or the main process of emission (synchrotron, synchrotron self Compton, inverse Compton diffusion on thermal photons). The high energy emission seen during some prompt phases by *Fermi*/LAT is also causing debate about its origin, another component of the main emission or emission from a different region(Gomboc, 2012).

The composition of the GRB ejecta remained unknown. The proportion of lepton and proton but also the intensity of the magnetic field remain unclear. These questions have a very strong impact on the GRBs being the main contributor to the Ultra High Energy Cosmic Rays and high energy neutrino background (Zhang, 2011).

The modelisation of the afterglow emission seen by IACT at VHE energy has proven to be challenging. For these few events, the VHE emission seems closely related to the behaviour of the X-Ray (MAGIC Collaboration et al., 2019a) (H. E. S. S. Collaboration et al., 2021). In the case of GRB 190114C, a Synchrotron Self Compton model has worked quite well (MAGIC Collaboration et al., 2019b). In the case of GRB 1908298A, an SSC modelisation allows a good description of the low energies but a quite imperfect one of the VHE emission (Salafia et al., 2022). Some authors have argued that a single synchrotron component is able to describe the data. Nevertheless, it requires an unknown process to very efficiently accelerate electrons at energy approaching multi-PeV energies or an unknown process that causes a major difference in the strength of the magnetic field between the acceleration and radiation sites.

The sample of GRBs observed at VHE is very small. The detection of more GRB at VHE would likely help to have a broader and less biased vision of GRB at VHE and help solve a few open questions. All the bursts detected currently were bright bursts, so the improvement in sensitivity brought by CTA could lead to a significant increase in the detection rate of GRBs.

Although still not achieved at VHE, the detection of the prompt phase could also be very important to understand better the question of the HE emission and the radiation process of the prompt phase. Detectors like HAWC or LHASSO, with a very good duty cycle and a large FoV, have a limited short time scale sensitivity and a high energy threshold, limiting their detection capability to bright and close GRBs. A solution to this issue could come from gravitational-wave detectors. For the O4 observation runs, a pre-alert could be sent in some cases. This alert would allow repointing instruments like IACTs on the position and to wait for the burst to happen. In a more distant future eLISA mission, a space-based GW detector could alert days or even months earlier of the merger events.

Chapter 4

Résumé de la partie 1

Contents

4.1 Les rayons cosmiques

L'histoire des rayons cosmique à commencé en 1912 avec la détection de ceux-ci par Victor Hess. Il a montré à l'aide de mesures en montgolfière qu'un flux de particules chargés arrivait de l'espace. Depuis cette découvertes, ceux-ci ont été longuement étudiés. Le spectre en énergie est maintenant connu depuis une énergie de quelque GeV jusqu'à la centaine de EeV, avec un flux s'étalant sur plus de 30 ordres de grandeurs (Fig. 4.1). Ce rayonnement est principalement composé de protons mais de manière plus marginale est aussi composé d'une grande variétés de particules, dont des ions de nombreuses espèces, des électrons ou encore des positrons.

De nombreux points restent à éclaircir sur le rayonnement cosmique, notamment les sources de ces rayonnements et les mécanismes d'accélération pour les particules les plus énergétiques. De nombreux types de sources ont été identifiées comme candidats potentiels à l'explication d'une partie du spectre de rayonnement cosmique. Cependant la détection directe du rayonnement cosmique ne permet pas d'identifier les sources. Du fait des champs magnétiques présents dans notre galaxie, ces particules sont déviées et l'information de l'origine est perdue lors de leur détection.

Pour étudier les sources potentielles et évaluer leur capacité d'accélération, il est nécessaire de se baser sur des messagers neutres qui ne seront pas déviés lors de leur voyage entre la sources et l'observateur. Des neutrinos sont émis lors de nombreux processus hadronique, et devrait être

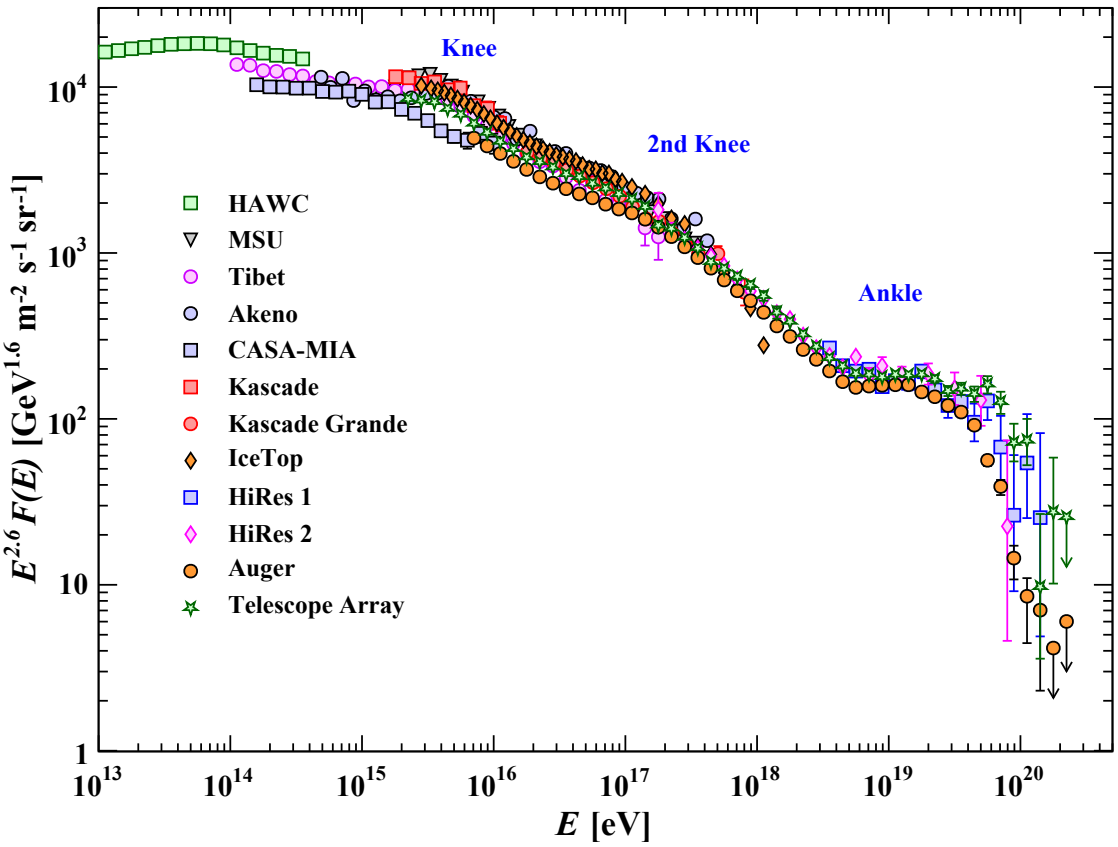

Figure 4.1: Le spectre en énergie de l'ensemble des rayons cosmiques. Figure issue de Particle Data Group et al. (2022)

émis depuis les zones d'accélération de hadron, qui compose l'essentiel du rayonnement cosmique. Cependant leur détection est très compliqué du fait de leur très faible section efficace, et seul deux sources astrophysiques sont connus actuellement, le soleil et la supernova SN 1987A. L'autre messager possible est le photon. Ceux-ci peuvent être émis par un nombre variés de mécanisme dans les sites d'accélération de particules chargés. On peut s'attendre notamment à des émission en rayonnement gamma via un processus synchrotron, inverse Compton, Bremsstrahlung, ou encore la désintégration de pions.

4.2 L'astronomie gamma

L'astronomie gamma est née au début de l'ère spatiale. En effet, l'intégralité du rayonnement gamma étant absorbée par l'atmosphère, il a fallu attendre d'être capable d'envoyer des instruments au delà de celle-ci. OSO-3, satellite lancé en 1967 par la NASA, fut la première expérience à détecter une source astrophysique de rayonnement gamma. Les satellites successifs ont permis de détecter de plus en plus de sources gamma de haute énergies, avec actuellement *Fermi/LAT* qui a détecté plus de 5000 sources (Fig. 4.2).

Cependant la surface efficace des satellites étant limitée, il est nécessaire de revenir au sol pour observer des photons gamma de plus haute énergies. Pour cela il est possible de les détecter indirectement à l'aide de la gerbe atmosphérique créé par les photons interagissant avec l'atmosphère. Il est soit possible de détecter le passage des particules composant la gerbes ou de détecter la lumière Cherenkov qu'elles émettent. C'est à l'aide de cette dernière méthode que la toute première source gamma de très haute énergie, la nébuleuse du Crabe, a été détectée par le télescope Whipple en

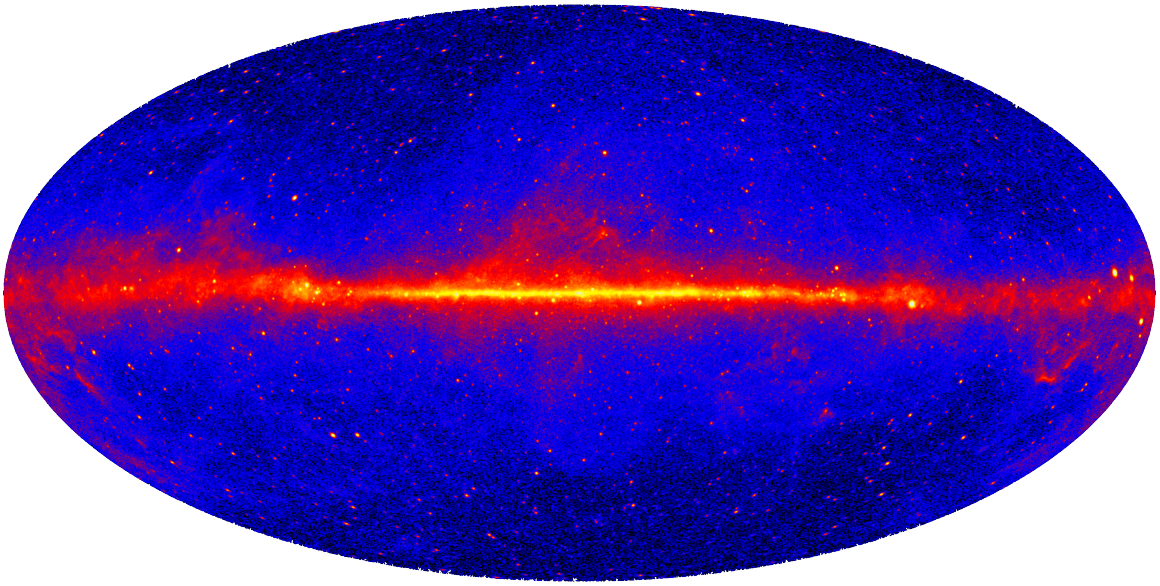

Figure 4.2: Carte du ciel de tout les photons de plus de 1 GeV détectés par *Fermi/LAT* lors des douze premières années d'observations

1989. La génération actuelle d'instruments, composée de trois expériences, H.E.S.S., MAGIC et VERITAS à permis la détection de près de 300 sources.

Les expériences détectant directement le passage des particules composant les gerbes atmosphérique ce sont développées plus récemment. Ces expériences par leur design sont capable d'observer une large portion du ciel et cela tout au long de la journée. Le temps d'exposition important qui en découle à permis d'augmenter progressivement l'énergie maximale détectée, aboutissant aux premières détections de sources à UHE et à la détection par LHASSO de sources émettant à plus de 1 PeV en 2021.

La propagation du rayonnement gamma de très haute énergie est affectée par un phénomène d'absorption, causé par l'interaction des photons gamma avec le fond diffus optique et infrarouge appelé EBL lors de leur trajet entre la source et l'observateur. Cela affecte la capacité de détection des sources extra-galactiques (Fig. 4.3).

4.3 Les sursauts gamma

4.3.1 Les premières observations

La première détection d'un sursaut gamma (aussi appelé GRB) a été effectuée en 1967 par les satellites espions américains Vela. Celui-ci consistait en une brève bouffée de rayons gamma (Fig. 3.2). Vela permit de déterminer que le signal provenait bien d'une source non terrestre qui n'était pas le Soleil, la Lune, ou encore des supernova connues. Ceci est le point de départ d'une longue traque pour chercher l'origine des ces sursauts.

L'instrument BATSE à bord du satellite CGRO, lancé en 1991 par la NASA, permit de lever un certain nombre de mystères, en déterminant notamment que les sursauts gamma avait une origine extra-galactique. L'expérience a mis aussi en avant l'existence de deux populations de sursauts caractérisées par leur durée (Fig 4.5). Ces deux catégories sont simplements appelés sursauts gamma longs et sursauts gamma courts.

La détection d'une contrepartie dans une autre longueur d'onde fut longtemps attendue. Il était très rare à l'époque d'avoir une localisation précise disponible rapidement. Le satellite Beppo-SAX avec notamment ces instruments en rayons X à large champs de vue permis de résoudre ce problème. Ainsi en 1997, Beppo-SAX détecte GRB 970228. Les informations fournies par le satellite permettent

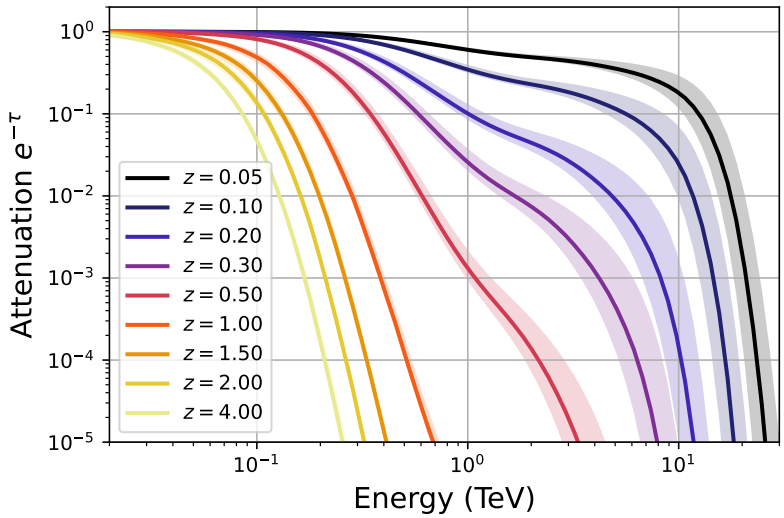

Figure 4.3: Atténuation du signal dû à l'interaction avec l'EBL en fonction de l'énergie pour des sources à différents redshift. Le modèle utilisé provient de Domínguez et al. (2011)

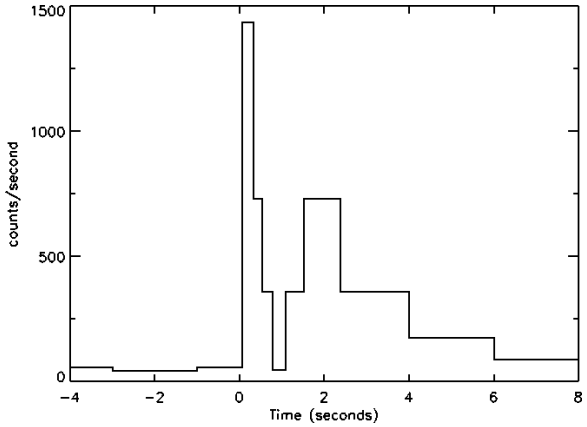

Figure 4.4: Signal provenant de GRB 670702 enregistré par les satellites Vela 4A et 4B. Ce signal est la première détection d'un sursaut gamma.

une détection d'une contrepartie en optique et rayon X. Quelques mois plus tard, pour GRB 970528, sera également détectée une contrepartie radio.

La détection d'une émission rémanente avec les instruments modernes, est un chose commune pour les GRBs avec une localisation précise. Celle-ci peut être détectée sur une période allant de quelques heures après le sursaut initial jusqu'à plusieurs années après celui-ci particulièrement en radio.

4.3.2 Modèle de sursaut gamma

L'ensemble des observations de sursaut gamma à permis de déterminer un modèle pour le sursaut gamma, appelé modèle de la boule de feu avec choc interne-externe (Fig. 4.6) (Cavallo and Rees, 1978) (Rees and Meszaros, 1994). Le début de scénario du modèle part d'un trou noir en formation avec un disque d'accrétion autour. Cet ensemble est appelé moteur central. Afin d'arriver à ce scénario, il y a un progéniteur différent pour chacune des deux catégories de sursaut gamma. Les sursauts gamma courts sont issus de la fusion d'étoile à neutron tandis que les sursauts gamma longs

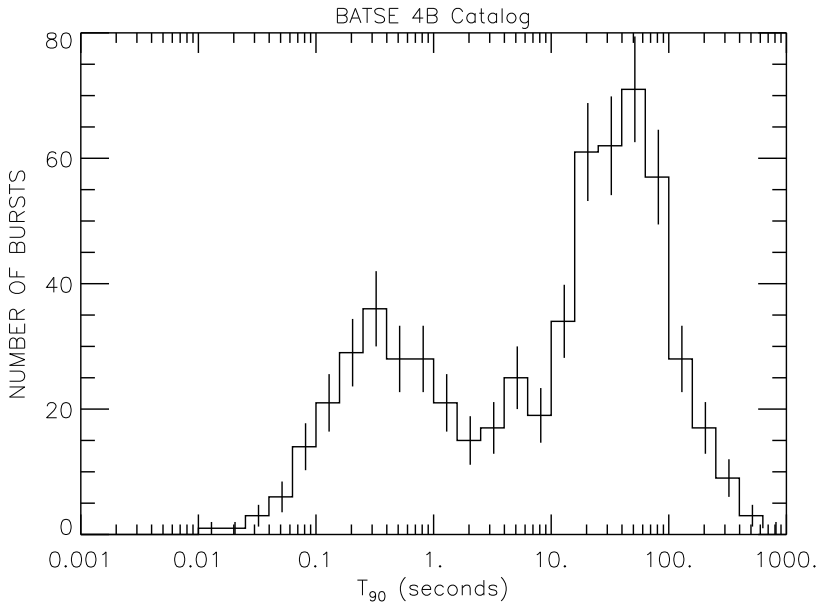

Figure 4.5: Distribution de la durée des sursauts gamma (T_{90}) observés par BATSE. Figure issue de (Paciesas et al., 1999)

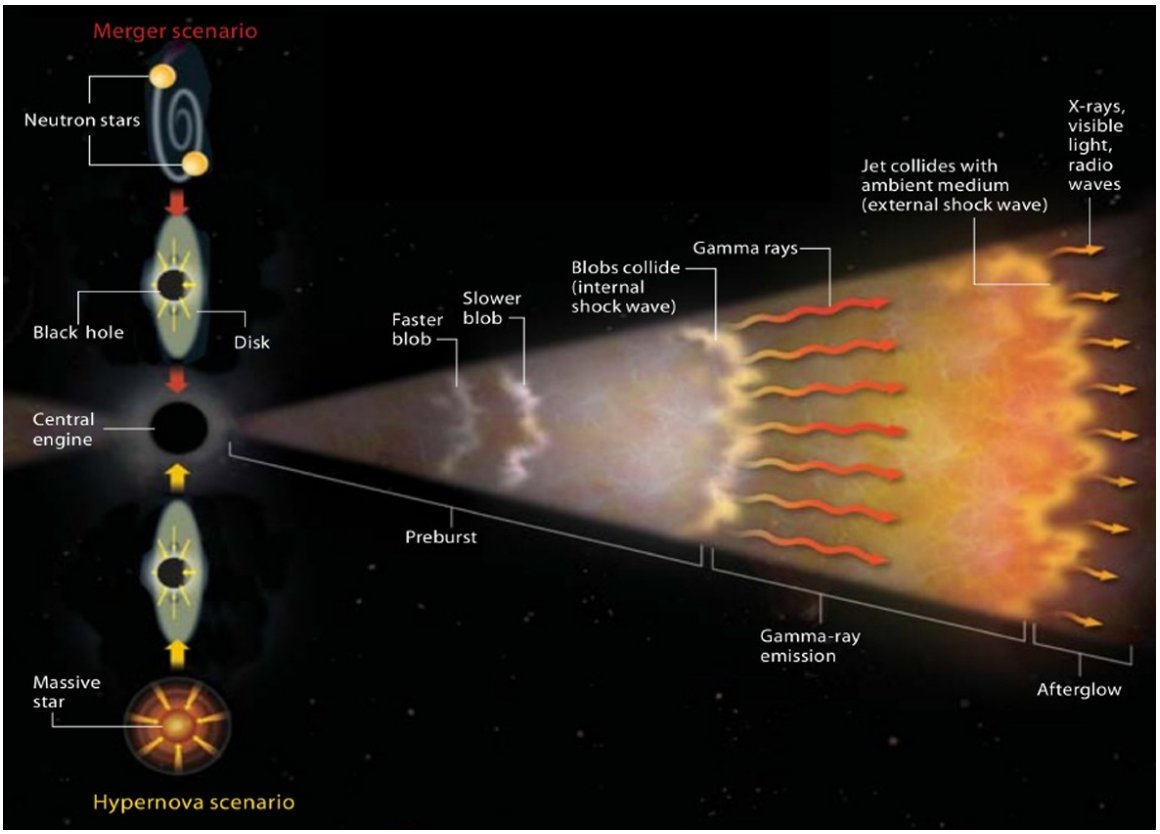

Figure 4.6: Vue artistique du modèle standard pour les sursauts gamma. Figure issue de (Piron, 2016)

sont issus du collapse du coeur d'étoile massive en rotation rapide.

Le taux d'accrétion élevé permet la formation de jet ultra-relativiste. Au sein de ces jets, différentes couches de matière se déplacent à des vitesses différentes. La collision entre ces différentes couches est la cause de l'émission initiale appelé prompte. Le jet rentre ensuite en collision avec le milieu entourant le ou les astres à l'origine du sursaut. Cela est à l'origine de la seconde émission qui dure plus longtemps, appelé rémanente.

4.3.3 L'émission des sursauts à très haute énergie

Dès les prémices de l'astronomie gamma à très hautes énergies, une contrepartie au sursaut gamma a été recherchée. Il aura cependant fallu attendre plusieurs dizaines d'années pour les premières détections avec GRB 180720B par H.E.S.S. et GRB 190114C par MAGIC. Depuis, 3 autres GRBs ont été détectés. GRB 19014C au tout début de la phase rémanente, tandis que GRB 190829A a été détecté jusqu'à 56h après la phase prompte ouvrant la voie à une émission dépassant largement le cadre du simple début de la phase rémanente.

4.3.4 Questions ouvertes sur les sursauts gamma

La première détection d'un sursaut gamma remonte à plus de 50 ans mais de très nombreuses inconnues restent sur ce phénomène, notamment quel est le mécanisme d'accélération des particules, quels sont les mécanismes d'émission ou encore s'ils contribuent de manière notable au rayons cosmiques de ultra haute énergies. Les observations de sursauts à très haute énergies peuvent contribuer à répondre à ces questions.

Part II

Imaging Atmospheric Cherenkov Telescope

Chapter 5

The Imaging Cherenkov Technic

Contents

5.1 Atmospheric showers

A gamma-ray entering the atmosphere interacts to create an electron-positron pair. The produced leptons could then interact through the Bremsstrahlung process to create new gamma-rays, which could then again create new electron-positron pairs. This process would continue as long as there are enough energies to create new pairs. What we call an electromagnetic shower composed of electrons, positrons and gamma-rays is then created. The figure 5.1, left panel, shows a simulation of a gamma-ray induced shower from the side (top) and the bottom. The shower is regular and the particles do not have a large longitudinal momentum.

The problem is that cosmic-rays (Hadron and Leptons) entering the atmosphere also create atmospheric showers. If the shower is induced by a hadron, it will be composed of protons, pions, muons, or other particles. Figure 5.1, right panel, shows a simulated shower for a hadron. Already, it is visible that the shower has subshowers and large transverse momentum with more erratic behaviour.

The differences mentioned above between the two types of showers are the basis of discrimination between particle types in the Cherenkov Technic.

Several instruments such as LHASSO and HAWC detect directly the particles reaching the ground. However, one of the drawbacks is the high energy threshold due to the need for particles to reach the ground. To be able to reach smaller energies, Imaging Atmospheric Cherenkov Telescope (IACT) rely on the indirect detection of atmospheric showers. In fact, such detectors detect blue light from the showers...

5.2 The Cherenkov light

Due to the very high energy of the charged particles in the showers, they will travel faster than the speed of light in the atmosphere. The atmosphere being a dielectric medium, the incoming particule excites the atomic electrons to form a coherent wave-front. The resulting electromagnetic shock

wave led to the emission of light called Cherenkov light (Fig. 5.2), in the name of the physicist who discovered it, Pavel Cherenkov, in 1934.

The light emitted in a light cone with an opening angle of $2\theta_C$ given by the expression 5.1 with n the refractive index of the medium and $\beta = \frac{v}{c}$.

$$\theta_C = \sin^{-1}\left(\frac{1}{n\beta}\right) \tag{5.1}$$

Most of the Cherenkov light is emitted close to the maximum development of the showers (altitude at which there are the most particles in the shower). For a shower with a maximum development at 10 km, the opening angle is ∼1.2°, and so the ground surface that will receive Cherenkov light is a disk of ∼120 m. Most of the light is emitted in the UV or blue with wavelength going from ∼300 nm to from ∼600 nm. The Cherenkov flash seen at ground level is very short (a few nanoseconds).

The number of Cherenkov photons N emitted by wavelength λ and track length x of the charged particle is given by the equation 5.2 with α the fine-structure constant and θ_C the half opening angle of the emitted Cherenkov light.

$$\frac{\mathrm{d}^2 N}{\mathrm{d}\lambda \mathrm{d}x} = 2\pi\alpha \frac{\sin^2\theta_C}{\lambda^2} \tag{5.2}$$

The quantity of Cherenkov light is proportional to the track length of particles, and the track length is proportional to the energy of the particles as the first approximation. Consequently, the amount of Cherenkov light emitted is a reasonable estimate of the energy of the particles that have created the shower.

The atmosphere is not perfectly transparent to UV and blue light, so the light could be absorbed by ozone or diffused by Mie or Rayleigh diffusion through its track across the atmosphere.

As a consequence, for detecting gamma-rays using Cherenkov light, a good knowledge of the atmosphere is useful as this is the calorimeter but also the medium of propagation of the Cherenkov light. This uncertainty is typically one of the important sources of systematic errors in Cherenkov experiments.

5.3 Imaging Atmospheric Cherenkov Telescope

The objective of IACT is to take an image of the very short and faint flash of Cherenkov light created by the atmospheric shower. As a result, these kinds of experiments could only be observed during dark nights with good weather conditions. This limiting factor reduces the duty time of the experiments to 1000 h per year or ∼10% of the time. Some experiments have started to observe with moderated moonlight to increase the duty cycle at the expense of degraded performance, especially at low energies. The multiple experiments that have been conducted so far have highlighted several of the important features needed for achieving good performance.

- A large reflector, here a segmented mirror dish to collect an important amount of light. The larger the mirror, the lower the instrument's energy threshold.
- A camera with fine pixelisation to capture small details of the showers. This will help to improve angular and energy resolution as well as background rejection.
- A very fast electronic to record the fast Cherenkov flash lasting a few nanoseconds but also to avoid capturing too much night sky background light.
- A large field of view to catch the whole extension of the showers at high energy, improving the effective area, energy and angular resolution.
- Multiple telescopes closed enough to make stereoscopic observations of the same shower achieving better background rejection, energy and angular resolution.

The image of the electromagnetic shower, recorded by the instruments, is then used to determine the direction, the energy, and the type of particles that have created the shower. Examples of images of atmospheric showers are given in figure 5.3. A detailed explanation of the reconstruction technique will be given in chapter 12.

The current generation of instruments is composed of three different experiments, H.E.S.S., MAGIC, and VERITAS. They are all arrays of IACTs to benefit from stereoscopy and are composed of telescopes with large mirrors and fast and finely pixelated cameras in order to maximise the performance. More details on H.E.S.S. will be given in chapter 6.

The next generation instrument, Cherenkov Telescope Array (CTA), uses even larger IACT arrays composed of several sizes of telescopes, each optimised for a given energy range. More details on CTA will be given in chapter 7.

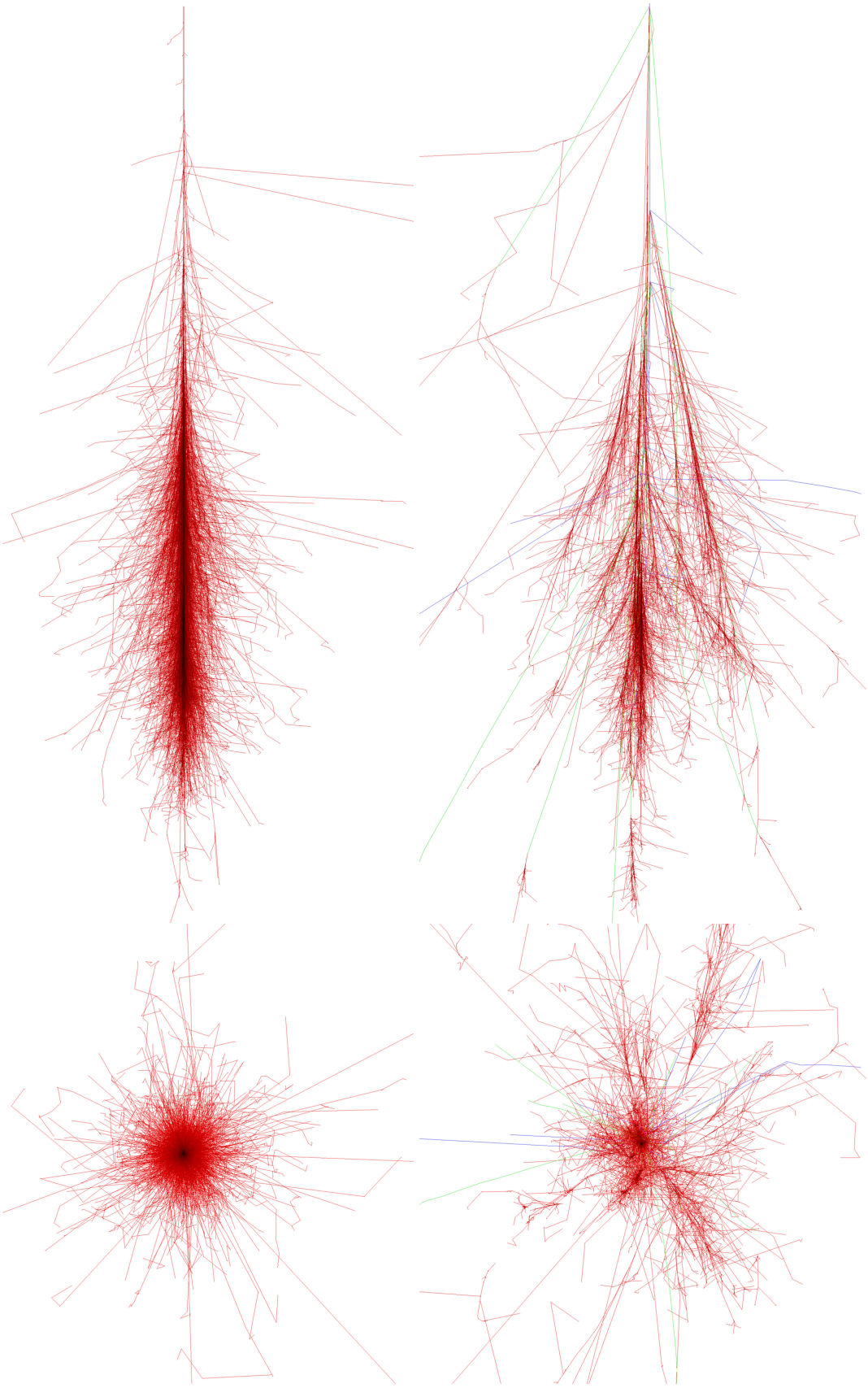

Figure 5.1: Particle tracks of simulated atmospheric showers (at 100 GeV) with the software CORSIKA for a proton (right) and a gamma-ray (left) induced shower. Each shower is shown from the side and the bottom. Credit : CORSIKA.

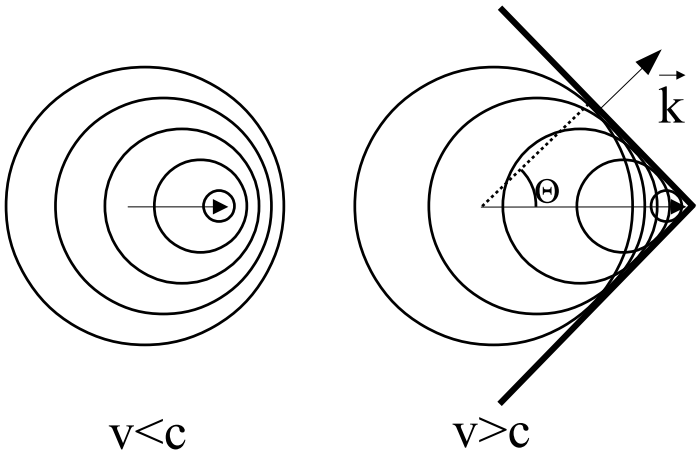

Figure 5.2: On the left, is a case of electromagnetic waves associated with a sub-luminic charged particle. On the right, electromagnetic waves with the formation of a shock wave in the case of the supra-luminic charged particle. Figure from de Naurois and Mazin (2015).

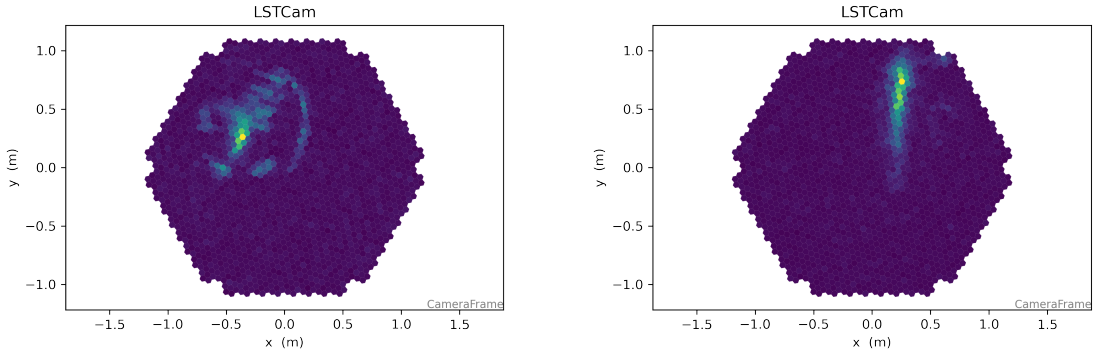

Figure 5.3: Image of a shower induced by a hadron-like (left panel) and gamma-like (right panel) particles seen by LST-1.

Chapter 6

High Energy Stereoscopic System

Contents

The third generation of Imaging Atmospheric Cherenkov Telescope (IACT) is still in operation. The High Energy Stereoscopic System (H.E.S.S.) is one of these experiments, together with MAGIC (La Palma, Canary Islands) and VERITAS (Arizona). H.E.S.S. is celebrating its 20 years of operation and will still take data for several years.

6.1 Location of the H.E.S.S. telescopes

H.E.S.S. is installed in Namibia on the Khomas Highland at 1800 m of altitude. This experiment is 120 km away from the capital Windhoek in a semi-desertic area with a very small population density. The site does not suffer from light pollution and has good weather conditions ensuring a large observation time.

The position in the southern hemisphere allows observation of the centre of the galaxy, where the density of galactic sources is high. Also, the position benefits from a reduced geomagnetic field due to the South Atlantic Anomaly that allows a smaller deviation of the particles composing the shower, easing the reconstruction from the telescope's images.

6.2 The telescopes

The system is composed of five telescopes (Fig. 6.2). Four small telescopes were installed in the first phase of H.E.S.S., and a larger one was installed during the second phase. The success of H.E.S.S. is based on the knowledge obtained from the previous generation of Cherenkov telescopes since it encompasses all of the principles described in section 5.

6.2.1 CT 1-4 telescopes

The first phase of H.E.S.S. (called H.E.S.S. I) has seen the construction of four telescopes with a reflector of 12 m of diameter. These telescopes were equipped with a camera of 960 pixels, made of photomultipliers with good quantum efficiency. The camera (Fig. 6.3) is divided into 60 drawers of 16 pixels each. In front of each pixel is placed a Winston Cone to limit the FoV of the pixel

[1] http://tevcat.uchicago.edu/
[2] Credit : Klepser, DESY, H.E.S.S. collaboration

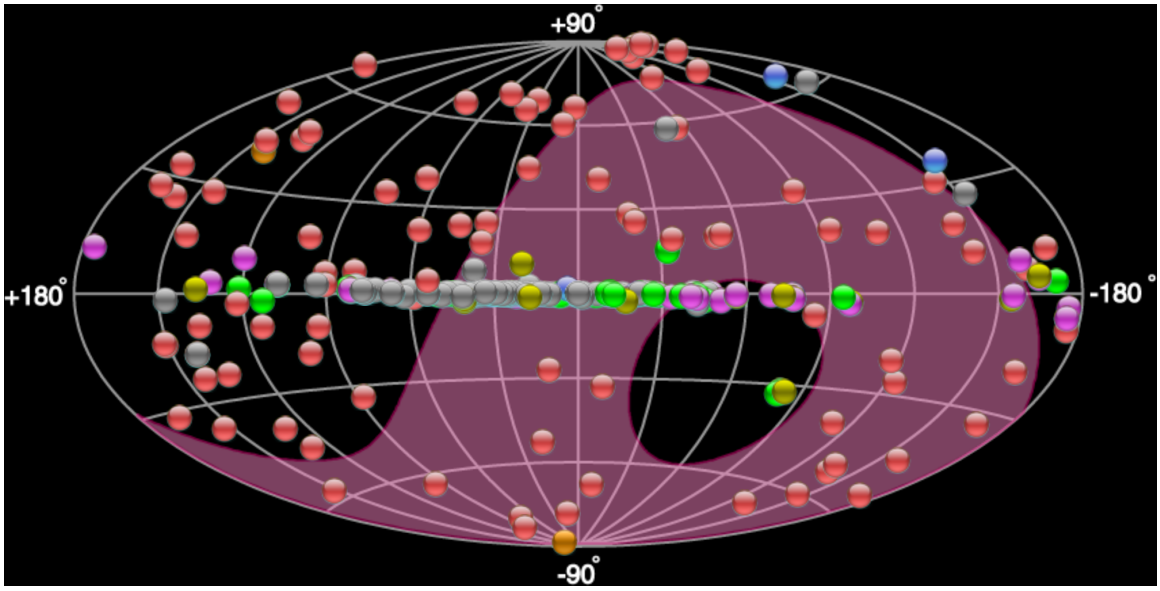

Figure 6.1: The red area shows the accessible sky from the site of the H.E.S.S. experiment. A large part of the Milky Way is visible. The circles represent sources detected at very high energies. Figure generated by TeVCat[1].

Figure 6.2: The site of the H.E.S.S. experiment with the four small telescopes CT 1-4, the big telescope CT 5 and the control room. The photography was taken in September 2012.[2]

(reducing NSB) and maximise light collection coming from the mirror. The camera has a large field of view of 5 deg.

The telescopes are placed in a square configuration with sides of 120 m length. The telescopes are named Cherenkov Telescope 1, 2, 3 and 4 or CT 1-4. This system provides a great sensitivity above 200 GeV up to a few tens of TeV and has allowed for the detection of several tens of sources since the beginning of operation in 2003.

In 2016, the cameras were upgraded for cameras with better and faster electronics, improved data quality, increased trigger rate, and reduced dead time. The dead time is the time during which

Telescope	CT 1-4	CT 5
Mirror dimension	Hexagonal of 12 m of diameter	Rectangular of 32 m by 24 m
Total mirror area	108 m^2	614 m^2
Focal length	16 m	36 m
Optical design	Davies-Cotton	Parabolic
Telescope weight	60 t	580 t
Maximum moving speed	100 deg/min	200 deg/min
Number of pixel	960	1764
Pixel angular size	0.16 deg	0.067 deg
Camera field of view	5.0 deg	3.2 deg
Integration time	16 ns	16 ns
Typical camera trigger rate	500 kHz	3600 kHz

Table 6.1: Comparison between the two different types of H.E.S.S telescopes. The camera information is the ones of the camera installed in 2022.

Figure 6.3: Photography of one of the cameras of CT 1-4 during the installation of Winston cones

the camera cannot acquire a signal due to the digitisation of an image. The trigger rate of the CT1-4 camera was around 100 Hz for the first cameras and around 400 Hz for the upgraded camera. All this improvement allowed for a decrease in the energy threshold. The phase of H.E.S.S. following the installation of these cameras is called H.E.S.S-IU.

6.2.2 CT5 telescope

In 2012 was added at the centre of the squared form by CT 1-4, another telescope called CT 5. This telescope has a much wider mirror of 32 m by 24 m, making it, at the time, the largest optical telescope in the world. The objective was to significantly lower the energy threshold of the system to observe active galaxy nuclei and transients. It also allows reducing the energy gap between H.E.S.S. and *Fermi*LAT.

The camera is composed of 2048 pixels and is also divided into drawers of 16 pixels. Winston cones are also installed. The field of view of the camera is 3.2° only but offers a much better angular size of the pixels (allowing better reconstruction of the small showers seen at low energy). The phase

of H.E.S.S. following the construction of this telescope is called H.E.S.S. II.

In 2019, the camera was exchanged with a preliminary version of the FlashCam, a camera that will equip the telescopes of the next generation of IACT. This camera, called NamCam, is composed of 1764 pixels and is improving data quality, operation reliability, dead time, and trigger rate, allowing for a lower energy threshold.

6.3 Data acquisition

6.3.1 Observation condition

The Cherenkov flash produced by an electromagnetic shower is very short and faint. Observations should then be performed in dark time i.e. astronomical twilight when the sun is 18° below the horizon. For several years, H.E.S.S. has been observing with a crescent moon. Since too bright light can damage the PMT, the voltage is reduced during moon observations.

Observation windows, called run, last for 28 min in H.E.S.S. This is a balance between having stable observation conditions (zenith angle, atmosphere, etc.) and a reasonable data volume per run.

6.3.2 Trigger individual telescope

Each PMT is very sensitive to light and especially to the light coming from the night sky background (NSB, mainly star light). With the aim to reduce this background, the acquisition is only triggered under certain conditions that must be fulfilled at the telescope and array levels.

The first trigger is built at the telescope level. The CT1-4 camera is logically divided into 38 sectors of 64 pixels, which means that sectors are overlapping. A trigger is issued when at least 4 photo-electrons in 3 neighbouring pixels (in a single sector) have been detected in a 1.3 ns windows. This ensures to reject of NSB events. In this case, the telescope trigger is sent to the central trigger. For CT5, the logic is the same, with different thresholds.

6.3.3 Array trigger

Since the detection of background light is a random phenomena, a good way to remove it is to acquire data only when two telescopes have triggered it. This is managed by the central trigger, which has several cases to handle :

- CT5 triggers are recorded and called Mono. Observations with CT5 alone can also be performed (Mono mode). This allows us to reduce the energy threshold.
- CT1-4, also called HESS I Stereo. At least 2 telescopes must be triggered in this case
- CT1-5, this is the HESS II Stereo mode where CT5 and one telescope from CT1-4 have sent triggers.

The figure 6.4 is a cartoon of the different modes of triggers. Once a trigger has been made, the event is recorded.

6.4 Data processing scheme

The H.E.S.S. data reduction follows several steps. Three different analyses are performed: an online analysis, an on-site analysis, which quickly analyses the data, and an offline analysis, performed in Europe several days after the data acquisition.

The online analysis, called Real-Time Analysis (RTA), is used to quickly react to the detection of flaring events or a GRB and helps to decide if observations should be continued or not. The sensitivity of this RTA is reduced compared to the offline analysis.

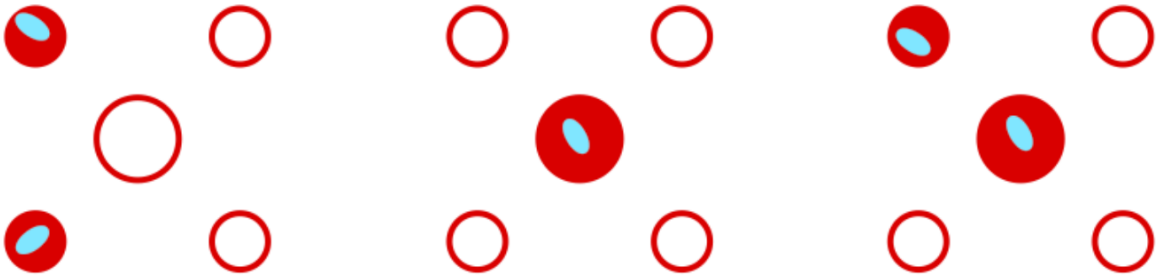

Figure 6.4: The three different trigger configurations for H.E.S.S. Each telescope is represented as a circle, the bigger central circle representing CT5. A filled circle represent a telescope with a trigger due to the detection of Cherenkov light. The left case represents the H.E.S.S.-I stereo trigger where at least two telescopes CT 1-4 telescope are detecting the shower. The middle case is the H.E.S.S.-II Mono trigger, where only CT 5 is triggering. The right case is the H.E.S.S.-II Stereo trigger where CT 5 and at least one of the CT 1-4 telescopes trigger. Figure from Chevalier (2017)

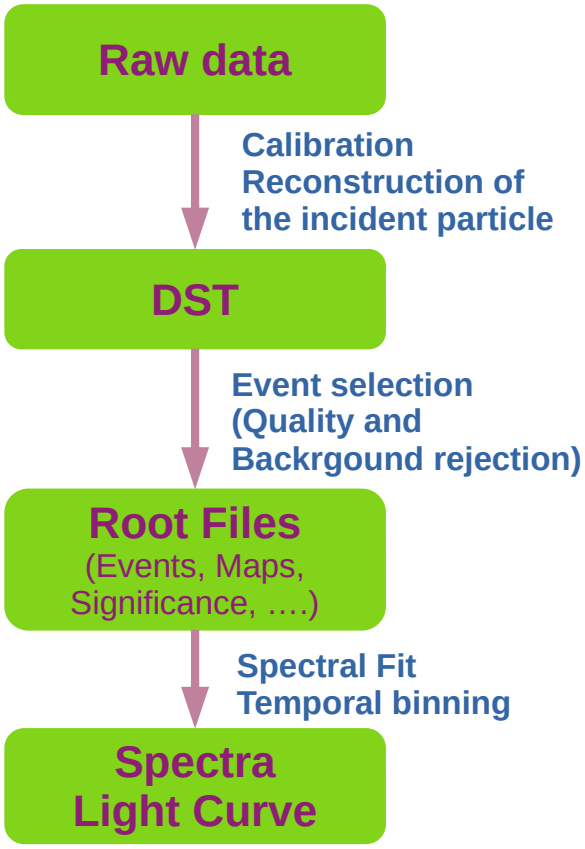

Figure 6.5: Principle of the analysis of H.E.S.S data starting from the raw data with ParisAnalysis

The on-site analysis, also called Next Day Analysis (NDA) is run automatically during the day. The sensitivity of the analysis is only a bit better than RTA, but the results are much more reliable due to better calibration of the data, allowing to confirm results from the Real Time Analysis quickly.

Data are then transferred to Europe (at the CC IN2P3 at Lyon and at the MPIK in Germany) to be analysed by two different chains: `ParisAnalysis, PA` and `HESS Analysis Program, HAP`. Historically, the transfer was done via tape and could have taken several weeks, but now, data can be transferred via internet from the H.E.S.S. site.

Data are then calibrated, which means that the recorded electronic signal is converted into a

number of Cherenkov photons per pixel. This is the basis for the discrimination and reconstruction steps. The calibration takes several inputs and steps :

- Gain of each PMT which is measured in two channels, high and low. The Gains are measured using single PE calibration runs
- Electronic noise, also called as pedestal
- FlatField coefficients, correction of the inhomogeneities between pixels
- Optical efficiency of the system (Mirror, Winston cone, etc) which are measured using the muon rings of the hadronic showers

A detailed explanation can be found in de Naurois (2012). The resulting files are called `DST`. These DSTs can then be used to compute the parameters of the shower based on the calibrated images. Usually, in the `PA` chain, a semi-analytical model call `Model++` (de Naurois and Rolland, 2009) is used, and different selection cuts can be applied (Aharonian et al., 2006).

Finally, maps, spectra, and light-curve or upper-limits can be produced.

Chapter 7

Cherenkov Telescope Array

Contents

7.1 The CTA project

Cherenkov Telescope Array (CTA) is the next-generation instrument of IACTs. Compared to the current generation, the objective is to widen the energy range, improve sensitivity by up to one order of magnitude, and improve angular and energy resolution. The idea of the project started in the mid-2000s, with the letter of intent published in 2007.

The CTA telescope arrays will be made up of three types of telescope, each optimised for a given energy range. To increase sensitivity at low energy, very large telescopes with finely pixelated cameras are important. The Large-Sized Telescopes (LST) with their very large mirror will cover the low energy. On the other hand, to improve high-energy sensitivity, a vast array covering a large surface on the ground is needed. This is achieved with a large number of Small-Sized Telescopes (SSTs) with a large field of view. In the core energy range, performant Middle-Sized Telescopes (SCT and MST), comparable to the current generation in terms of size, will be used.

7.2 Two sites for two arrays

The Cherenkov Telescope Array Observatory (CTAO) will build and operate two arrays of telescopes. The arrays will be located in the northern and southern hemispheres and will consist of several tens of telescopes of different sizes and types. The dual sites allow full coverage of the sky. Figure 7.1 gives the array layouts for the north and south sites, and table 7.1, the number of telescopes per site.

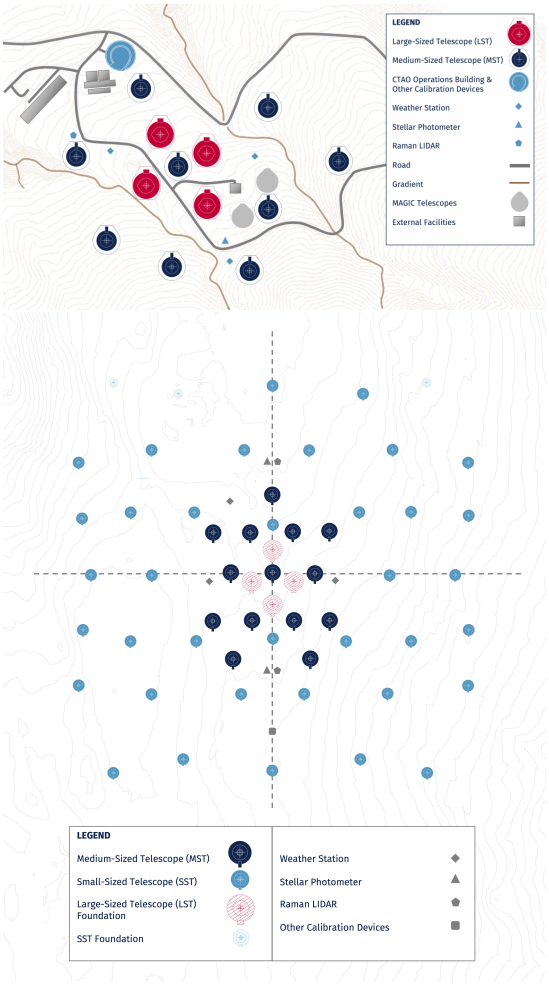

Figure 7.1: Planned layout for the Northen site (top) and Southern site (bottom).

7.2.1 Northern array

The CTAO-North site, located on the island of La Palma in the Canary Islands, Spain, will host four Large-Sized Telescopes (LSTs) and nine Medium-Sized Telescopes (MSTs) equipped with the Nectar Cam camera. LSTs are designed to capture the low-energy sensitivity of CTAO, while MSTs will cover the core energy range. This site has a less suitable view of the Milky-Way than the south site, and then no SST will be built.

The site is already home to a prototype LST, and the array is planned to be fully built by 2027. The observatory is located at an altitude of 2200 meters. It is a famous site for optical telescope observations in the northern hemisphere, with several telescopes, such as the Gran Telescopio Canarias (GTC) and the Telescopio Nazionale Galileo (TNG), already installed there. The MAGIC telescopes, used for very high-energy gamma-ray astronomy, are also located at the site.

Array	Site	LST	MST	SST
North	La Palma, Spain	4	9	0
South	Paranal, Chile	0	14	37

Table 7.1: Current planned telescope configuration for the first phase of CTA

7.2.2 Southern array

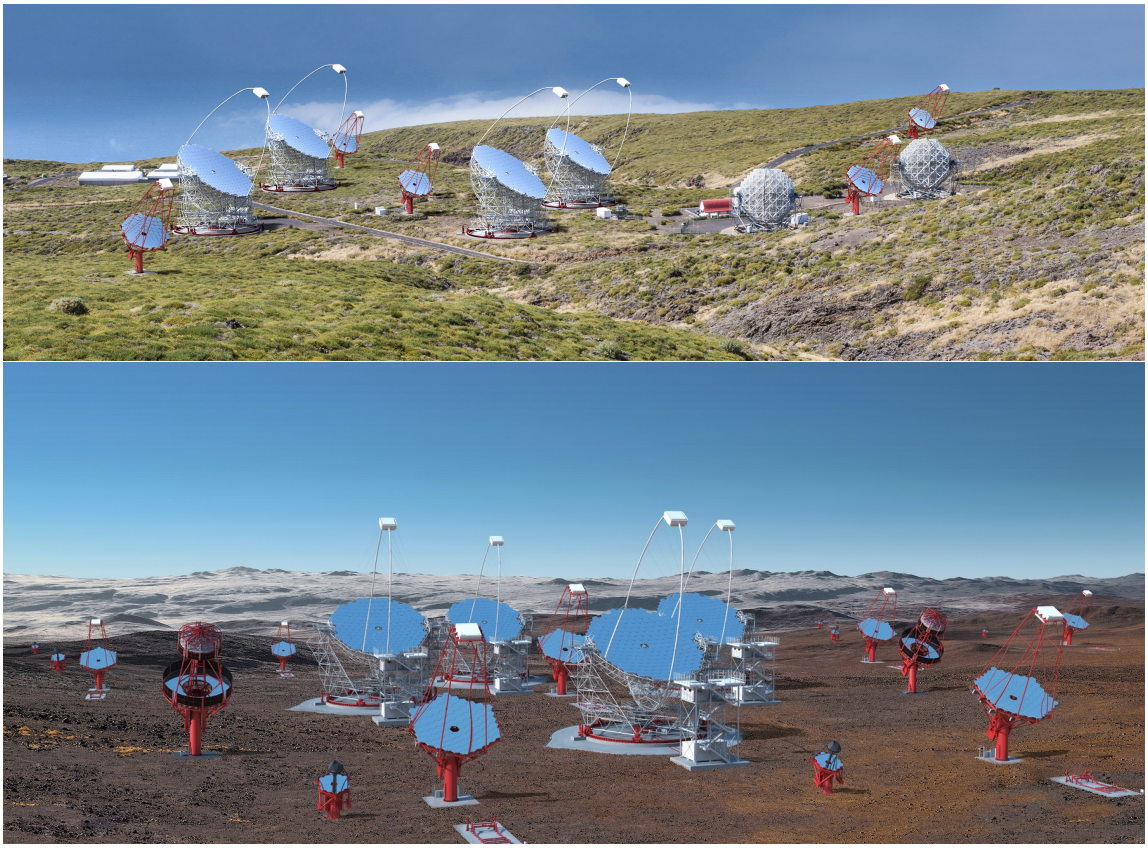

Figure 7.2: Artistic rendering of the CTA North and South array in Paranal. Credit : Gabriel Pérez Diaz, IAC / Marc-André Besel, CTAO

The southern hemisphere array of CTA is also planned to be located at the Paranal Observatory.

The Paranal Observatory is a complex of telescopes located in the Atacama Desert of Chile. It is known for its extremely dry and stable climate, making it an ideal location for telescopes. The observatory is home to the Very Large Telescope (VLT) and soon the Extremely Large Telescope (ELT)

Due to the important view of the Milky-Way, the south array will be optimised for the detection of gamma-ray energies ranging from 150 GeV to 300 TeV, with a focus on studying Galactic targets. The observatory will have 14 Medium-Sized Telescopes (MSTs) equipped with Flash Cam and 37 Small-Sized Telescopes (SSTs). There may also be at least two Large-Sized Telescopes (LSTs) at the observatory.

In the second construction phase, the observatory may also include Single-Mirror Cherenkov Telescopes (SCTs). Infrastructure work for the CTAO at the Paranal Observatory has already started.

7.3 Three sizes of telescopes

The figure 7.3 presents an artistic view of the different sizes of telescopes : The SST prototype, two prototypes of Medium-Sized Telescopes and the LST prototype.

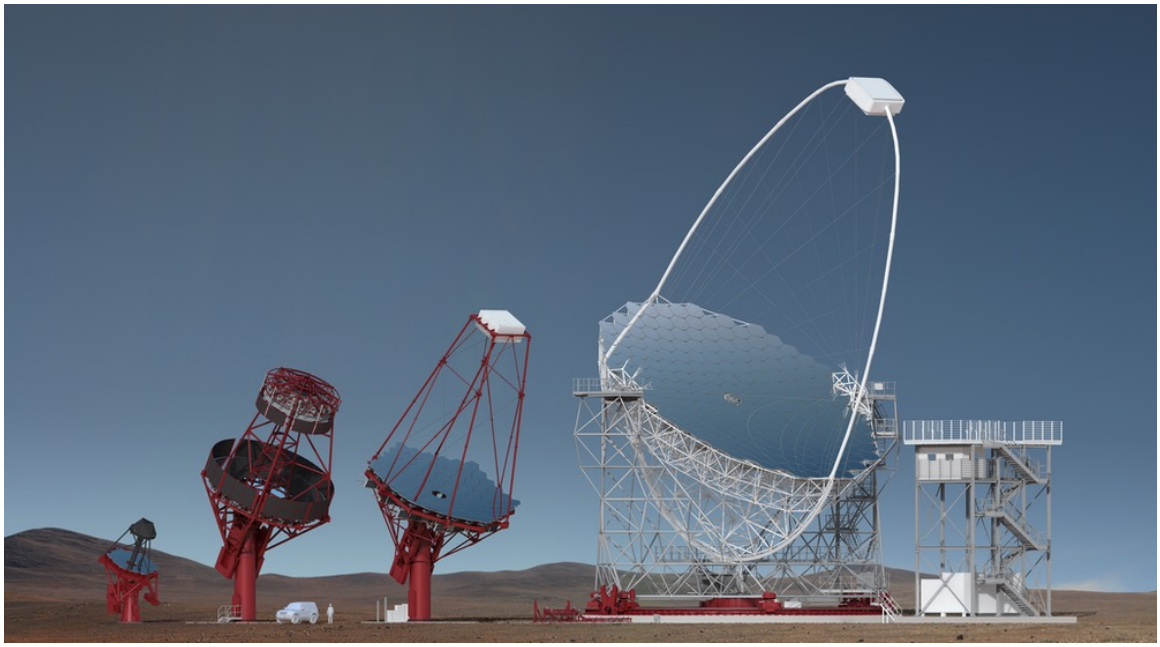

Figure 7.3: Artistic view of all the telescope designs for CTA. From the left to the right, SST, SCT, MST and LST. Credit : Gabriel Pérez Diaz, IAC

7.3.1 Large-Sized Telescopes: LST

The LST have a very large 23 m parabolic mirror and will be the state-of-the-art tool for observing extragalactic sources, transients, or pulsars. Its 400 m^2 reflective surface and low energy threshold of 20 GeV make it an exceptional device. With a weight of around 100 tonnes, it is designed with an aluminium and carbon structure, allowing it to be lightweight yet robust. With its very fast repositioning capabilities, it can make a half-turn in just 20 seconds. The first prototype is currently being tested in La Palma, and three more telescopes will be built in 2024-2025. More details can be found in section 8.

7.3.2 Medium-Sized Telescopes: MST and SCT

The MST is an 11.5m diameter Davies Cotton mirror telescope and is devoted to the core of the CTA energy range. Its size is similar to that of the H.E.S.S. I or VERITAS telescope, but its field of view is much wider, and the energy threshold is lowered to around 80 GeV. The number of telescopes and the area covered have increased compared to the current generation, which will increase the effective area, improving the quality of reconstruction.

There are two different types of cameras, Flash Cam and Nectar Cam, with one type of camera per site. The MST cameras will have a large field of view of about 8 degrees. The first version of the FlashCam is currently installed in the H.E.S.S.-II telescope. A prototype has been built in Berlin and tested with prototypes of both cameras, now disassembled. A new prototype should be constructed in La Palma with a NectarCam before the end of 2024.

Another version of the medium-sized telescope has been developed. The Schwarzschild-Couder Telescope (SCT) is a dual-mirrored version of the MST. Its unique optical support structure is designed to support segmented primary and secondary mirrors, as well as the high angular resolution camera and an improved angular resolution. The camera is equipped with pixels based on silicon photomultipliers (SiPMs). The SCT prototype (pSCT) was inaugurated on January 17, 2019, at the Whipple Observatory.

7.3.3 Small-sized Telescopes: SST

The Small-Sized Telescope (SST), devoted to very the very-high-energy, will be the most numerous telescope, with 37 planned to be spread out over several square kilometres in the southern hemisphere only. Its design is based on the Schwarzschild-Couder aplanatic dual-mirror configuration. The dual-mirror design reduces aberrations at the edges of the field of view. The main mirror is small, with a diameter of 4.3 m, but the field of view is very large, with 10.5 degrees. The camera consists of 2048 silicon photomultiplier pixels. The energy threshold is around 1 TeV. The SST will mainly be useful for the study of galactic sources, as they are not affected by absorption due to interaction with extragalactic background light. Three original designs were proposed, and a prototype was built for each of them. The final design used components from these different designs. One of the original designs, ASTRI, will be used to build an array of 9 telescopes on the island of Tenerife, called ASTRI Mini-Array.

7.4 Science with CTA

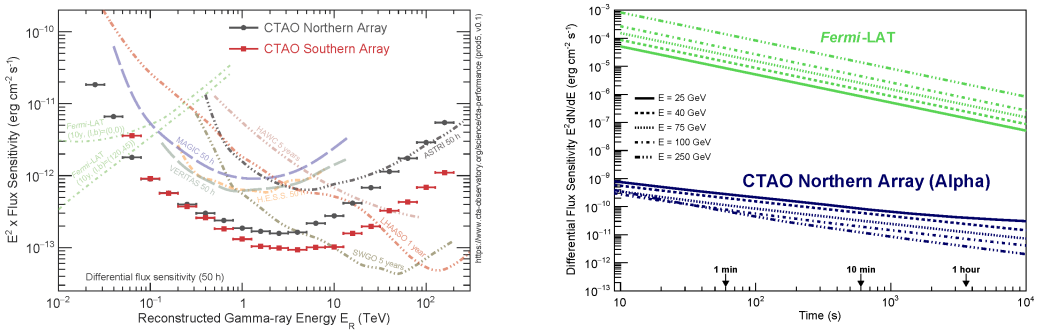

Figure 7.4: Differential sensitivity of the two arrays of CTA compared to several experiments (left). Differential sensitivity at low energy on short timescales of CTA North compared to Fermi/LAT (right).

The CTA is expected to significantly improve upon the performance of current instruments used in VHE astronomy, with an increase in sensitivity, energy resolution, and angular resolution compared to existing instruments. CTA will be able to cover all standard science subjects in VHE astronomy and will have a short time-scale sensitivity that is many orders of magnitude greater than current instruments, particularly at low energies. This will make it particularly powerful for studying transient phenomena, including flaring active galactic nuclei and GRBs. The figure 7.4 presents the performance of CTA compared to the current generation and to the LAT.

CTA will also have a much wider field of view (FoV) in the gamma-ray range than current instruments, which will allow it to more easily search for counterparts to transient alerts with poor localisation, such as gravitational waves (GW), neutrinos, or some gamma-ray bursts (GRBs). The wider FoV will also help the CTA to discover new transient phenomena.

In addition to its capabilities for studying transient phenomena, CTA is expected to carry out a galactic survey that is one order of magnitude deeper than current surveys, which will allow for a better understanding of galactic sources and the origins of cosmic rays. CTA will also conduct the first extra-galactic survey covering 25% of the sky, allowing the first unbiased population study of extra-galactic sources.

Chapter 8

Large-Sized Telescope

Contents

Figure 8.1: Picture of the LST1 prototype[1]

The Larged-Sized Telescopes are the telescopes of CTA focused on low energies and high-speed repointing. Their size makes them the second largest Cherenkov Telescope behind the H.E.S.S. II telescope. A prototype, called LST-1, has been under commissioning since 2019 in La Palma, where the northern array of CTA will be installed (Fig. 8.1).

8.1 Telescope structure

One of the main focuses of the LST is to be able to follow any alert very quickly. The telescope needs to be able to repoint in less than 20 seconds, and then the structure needs to be as light as possible with as minimal deformation as possible. To achieve this, a significant part of the telescope structure is made using composite materials that allow a great strength-to-weight ratio.

The telescope is installed on top of a circular rail of 23.9 m of diameter with an Alt-Az mount (Fig. 8.2). Six bogies are placed at the base of the telescope structure to allow azimuthal movement. A pin is placed at the centre of the rails and is the starting point of the cable chain that goes into the structures for controlling and monitoring the different elements and also transferring the data from the Cherenkov camera. The cooling pipes for the camera come through this path. The overall system allows for a total movement of ∼540 deg. The centre of the cable chain is placed in order to minimise the chance that a track in the sky will need to make a full turn of the telescope to be followed.

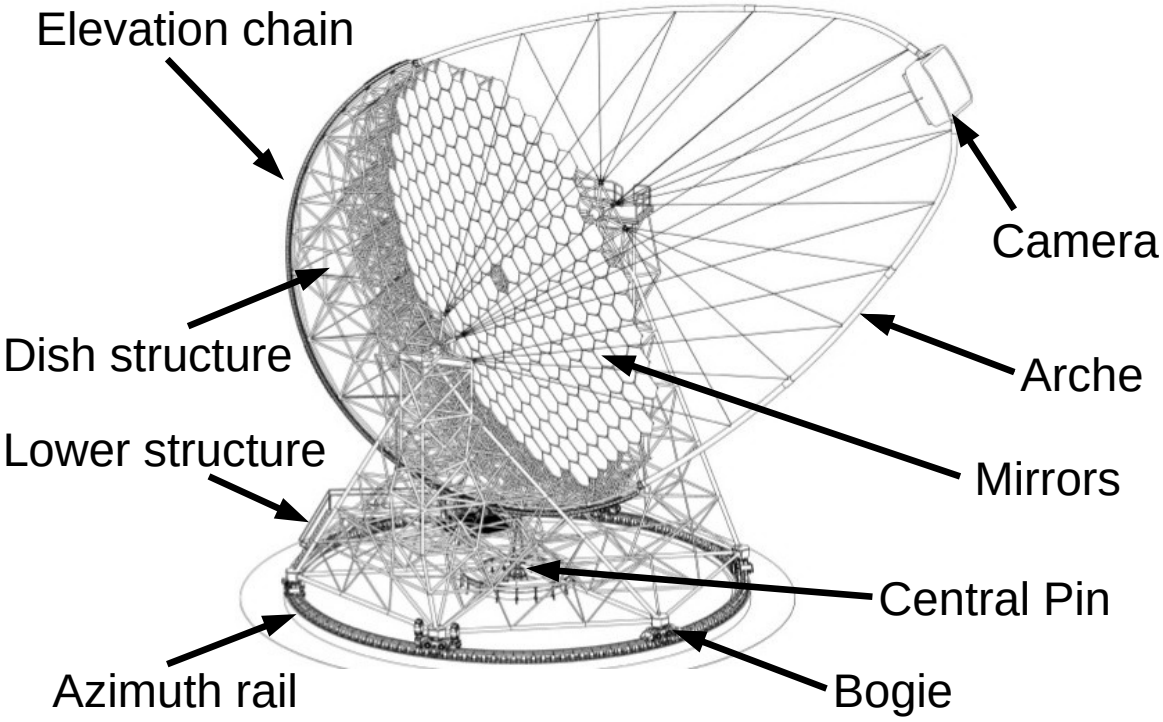

Figure 8.2: Schema of the LST telescope

The bottom part of the structure, which supports the dish, is made of steel tubes, and the part forming the dish where the mirrors are fixed is composed of aluminium and carbon fibre tubes. The dish rotates on an axis, allowing for elevation movement created by two rotation points on each tower of the structure. This movement is transmitted by a chain fixed at the back of the dish that is then driven by a motor placed in the lower structure.

The Cherenkov camera is placed at 28 m, which is the focal point of the dish. Its support frame is at the centre of a carbon fibre arch (see Fig. 8.2). Attached to the bottom and top edges of the

[1] Credit : Tomohiro Inada

dish (Fig. 8.2), the arch is made of several smaller tubular parts that are joined together with the help of a muff. The arch is made by a company named Lorima which specialises in making carbon fibre masts for boats. The use of this technology allowed us to reduce the total weight of the arch to 2.5 t and then the LST only weight 103 t.

Finally, an access tower is placed at the parking position to allow easy access for camera maintenance and is also used to lock the telescope during the day.

8.2 Drive system

The movement of the LST is ensured by the drive system, which is designed for precise tracking of a source for a long time with an error of less than 30″ while allowing for fast re-pointing with the objectives to reach any target in the sky in less than 30 s.

Two electrical motors are placed on two opposite bogeys of the azimuthal rail, and another one is placed at the centre of the lower telescope structure and connected to the chain on the back of the dish, allowing it to move on the elevation axis.

To provide the energy needed for the fast repointing (the motors could need up to 360 kW of power), a flywheel is installed at the base of the camera tower. The motors are controlled by a Programmable Logic Controller and use variators and sensors on the motors axis, but also on the telescope movement axis.

8.3 Optical system

The LST is equipped with a single parabolic reflector of 28 m of focal length and 23 m of diameter composed of 198 hexagonal mirrors of 1.5 m of width. The total effective area, including shadowing due to the structure, is 368 m^2. The individual facet is composed of a sandwich of glass with an aluminium honeycomb inside and a reflective coating on top. This honeycomb structure allows for a lightweight mirror of ∼47 kg per facet. The reflective coating is optimised for wavelengths between 300 nm and 550 nm corresponding to the typical wavelength of Cherenkov light with an average reflection of 92%.

Each mirror is attached to the dish using a three points system. Two of the points are actuators, while the last one is fixed. This design allows each mirror to move independently. As the structure will deform depending on the pointing of the telescope, each mirror position needs to be adjusted to maintain an optimised reflector shape. This ensures achieving the requirement for the optical angular resolution and pointing precision. The system in charge of adapting the mirror position is called Active Mirror Control (AMC). To be able to determine the correction to be applied, each mirror is equipped with a CMOS camera that looks at a laser target close to the Cherenkov camera. Two Optical Axis References Lasers (OARL) are emitted from the centre of the dish and are considered fixed. This allows the AMC system to correct the position of the mirrors (Hayashida et al., 2015).

8.4 The camera

The LST camera is made of 1855 photomultiplier tubes. On top of the photomultipliers, Winston cones are placed. As for other Cherenkov cameras, they allow to collect the light that will otherwise fall in between the circular shape PMTs and limit the vision angles of the PMTs to reduce the night sky background (Okumura et al., 2017). The overall field of view of the camera is 4.5 deg. The figure 8.3 shows an image of the focal plane of the telescope.

Seven PMTs are connected to a single electronic module. The fast electronic in the module allows for a sampling rate of the PMTs signal of 1 GHz. The camera is composed of a total of 265 modules. The trigger system of the camera is a three-level system.

The first level is the individual pixel that triggers when the charge exceeds a given value. The second one is at the module level. When there are a pixel trigger, the module will determine if

[2]Credit : Tomohiro Inada

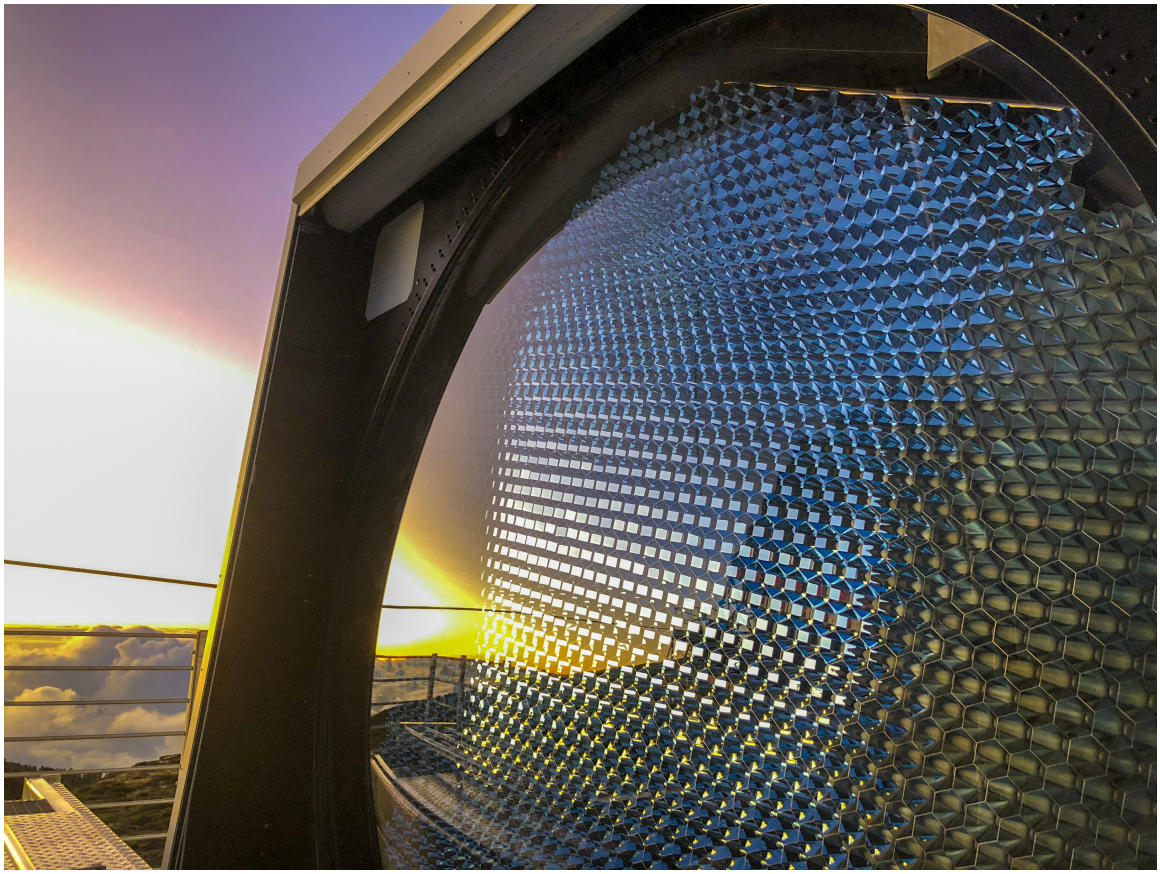

Figure 8.3: Photography of the focal plane of the camera[2]

the total signal in the module exceeds a given level. Then, if multiple contiguous module triggers (currently three), the camera will trigger, and the data will be saved.

The PMT signal is not integrated in time by the camera, but the entire waveform made of 38 samples of 1 ns is transferred. During normal operations, the camera operates at a typical trigger rate of 9 kHz. There are also two other triggers that will be run in parallel during the operation for calibration purposes. The first one is a random 100 Hz trigger with the objective of recording data without any light caused by atmospheric showers to estimate the pedestals of PMTs. The other one is also a random 100 Hz trigger, but synchronous with a calibration laser fired from the centre of the dish in the direction of the camera. The purpose of these data is to measure the gain of the PMTs.

The overall camera structure as a dimension of 2.8 m × 1.9 m × 1.15 m with a total weight of 2 t. The camera is closed thanks to a shutter, and acrylic glass is placed on the front of the PMTs to protect them from dust, humidity, etc... The camera is cooled with the help of a water-cooling system, itself cooled using a chiller at the base of the telescope.

8.5 Auxiliary devices

In the camera around the detector plane, twelve LEDs are placed on a circle of radius 1.3 m and 4 additional ones on one side. These LEDs allow different instruments placed at the centre of the dish to determine the precise position of the Cherenkov camera.

A white imaging target, called the Start Imaging Screen (SIS), could be automatically moved in the centre of the camera. This screen is placed at the focal point of the reflector to allow for the observation of stars (while PMTs are placed to observe the showers at several kilometres in the

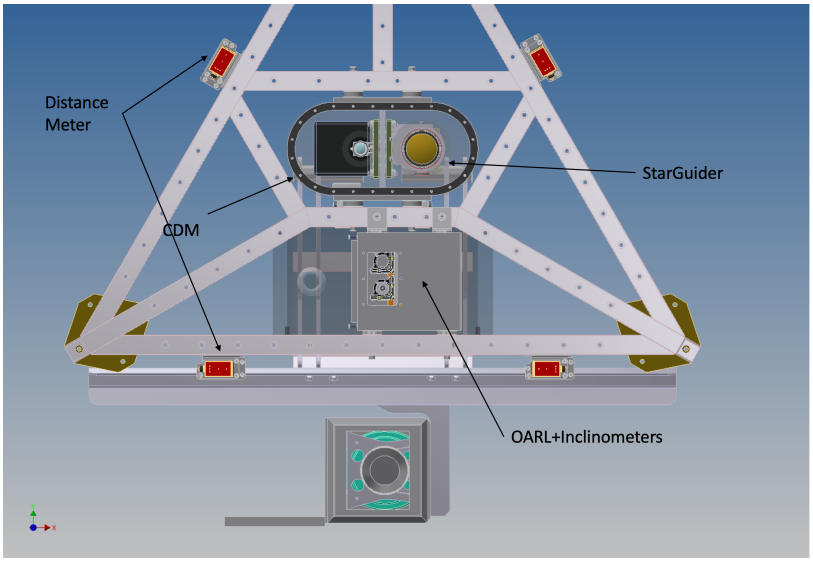

Figure 8.4: Equipment at the centre of the dish of LST-1.

atmosphere). The SIS is used to allow the determination of the optical Point Spread Function[3] (PSF) but also during measurement of the bending of the LST (see chapter 10).

Reflecting targets are placed at each corner of the camera to allow four distance metres (DM) to measure the distance of the main camera to the centre of the dish.

Finally, as mentioned already, another imaging target is placed below the camera frame to image the position of the OARL. The two lasers are installed at the centre of the dish, where no mirror is installed, together with other instruments. Figure 8.4 presents a drawing of this part of the telescope.

In this position could be found the calibration box that fires a laser used to calibrate the PMTs and also a cooled CCD camera called PSF camera. Its main role is to allow for the alignment of the mirrors and the monitoring of it. There are also two cameras used for online and offline pointing corrections. Figure 8.5 shows their hood at the centre. The Camera Displacement Monitor (CDM) is a CMOS camera used to monitor the displacement of the Cherenkov Camera at a frequency of 10Hz. The second camera is a CCD named StarGuider which observes a star field to determine the exact pointing of the camera. More information on pointing correction can be found in chapter 10.

There are also two inclinometers that allow measuring the inclination on two different axes of the telescope.

8.6 Scientific perspective for the Large-Sized Telescope

The LSTs, with their large reflector, provide the low-energy sensitivity of CTA and will provide the ability not only to increase the sensitivity but also to reduce the energy threshold compared to the current IACT generation. This ability will allow us to observe AGNs and GRBs at higher redshift than with current instruments. At the moment, the record for the furthest AGN detected is PKS 0346-27 at a redshift of z=0.991 (Wagner et al., 2021), while the farthest GRB is GRB 201216C at a redshift of 1.1 (Fukami et al., 2022). It has been estimated that CTA could detect AGN up to a redshift of 2 and GRB up to a redshift of 4.

This will allow us to detect sources at an earlier age of the universe, but also to study extragalactic background light at further redshift or to also explore new physics like a violation of the Lorentz invariance or testing the existence of axions-like particles (Amelino-Camelia et al., 1998).

Fermi/LAT already covers this part of the spectrum, but the sensitivity on short-time scales of the LSTs will be several orders of magnitude better, making LSTs a *transient machine* for AGNs

[3]The PSF is the shape of the image of a punctual object like a star through the optical system

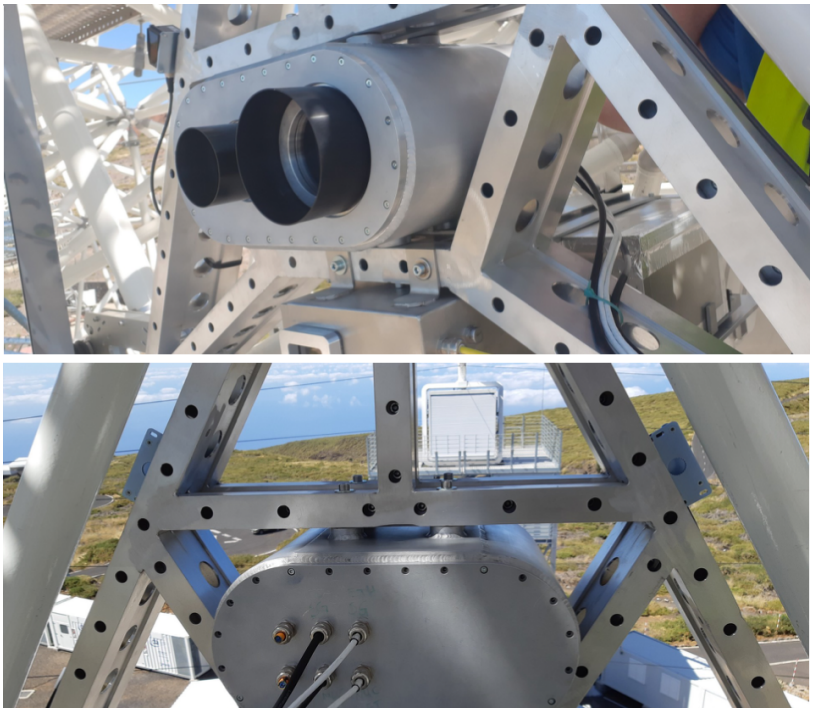

Figure 8.5: Pictures of the centre of the dish of LST-1 from the front and behind. The start-guider and the CDM and in the box.

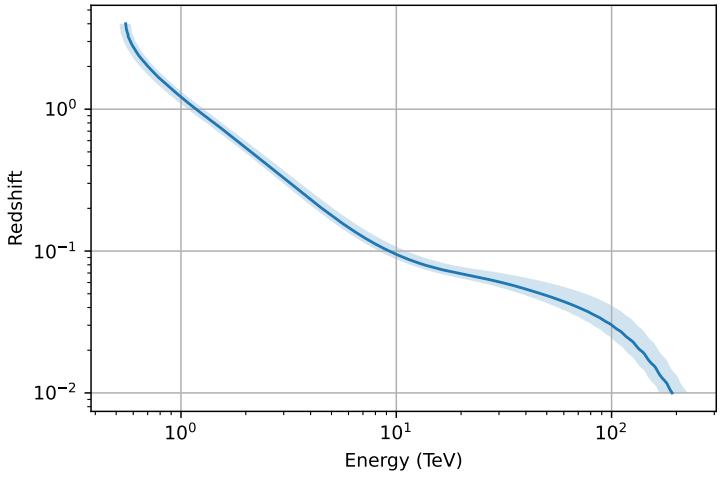

Figure 8.6: Redshift corresponds at the optical depth in function of energy. The model used for EBL is Domínguez et al. (2011)

flares or GRBs. For fast transients like GRBs, the very fast repositioning capabilities of the LSTs could help to catch the end of prompt emission from long GRBs and the very early stage of the afterglow.

Chapter 9

Résumé de la partie 2

Contents

9.1 Principe de fonctionnemment des télescopes Cherenkov

9.1.1 Les gerbes atmosphériques

Les photons gamma de très hautes énergies entrant dans l'atmosphère interagissent en créant une paire électron-positron. Les leptons produits interagissent alors par le processus de Bremsstrahlung pour créer de nouveaux photons gamma, qui peuvent à leur tour créer de nouvelles paires électron-positron. Ce processus se poursuit tant qu'il y a suffisamment d'énergie pour créer de nouvelles paires. C'est ce que nous appelons une gerbe atmosphérique composée d'électrons, de positrons et de photons gamma. La figure 9.1, sur le panel de gauche, montre la trajectoire des particules obtenues lors de la simulation d'une gerbe atmosphérique créée par un photon gamma.

Cependant les particules du rayonnement cosmique créent elles aussi des gerbes atmosphériques. Celles créées par des hadrons seront composées d'une vaste variété de particules avec notamment des protons, des pions ou des muons. Le panel de droite de la figure 9.1 montre la trajectoire des particules obtenues lors de la simulation d'une gerbe atmosphérique créée par un proton.

Les gerbes créées par hadrons présentent des différences notamment de formes par rapport à celles créées par un photon gamma. Celles créées par un photon seront plus régulières et leur structure pourra s'éloigner d'une symétrie radiale. Celles créées par des hadrons auront des structures plus complexes, avec des sous-ensembles et généralement une plus grande extension latérale. Ces différences permettront de distinguer les gerbes dues aux photons de celles dues aux hadrons lors de l'analyse des données.

9.1.2 L'effet Cherenkov

En raison de leur très grande énergie, les particules chargées des gerbes atmosphériques voyagent plus vite que la vitesse de la lumière dans l'atmosphère. L'atmosphère étant un milieu diélectrique, la particule entrante excite les électrons atomiques pour former un front d'onde cohérent. L'onde de choc électromagnétique qui en résulte conduit à l'émission d'une lumière appelée lumière Cherenkov (Fig. 9.2), du nom du physicien qui l'a découverte, Pavel Cherenkov, en 1934.

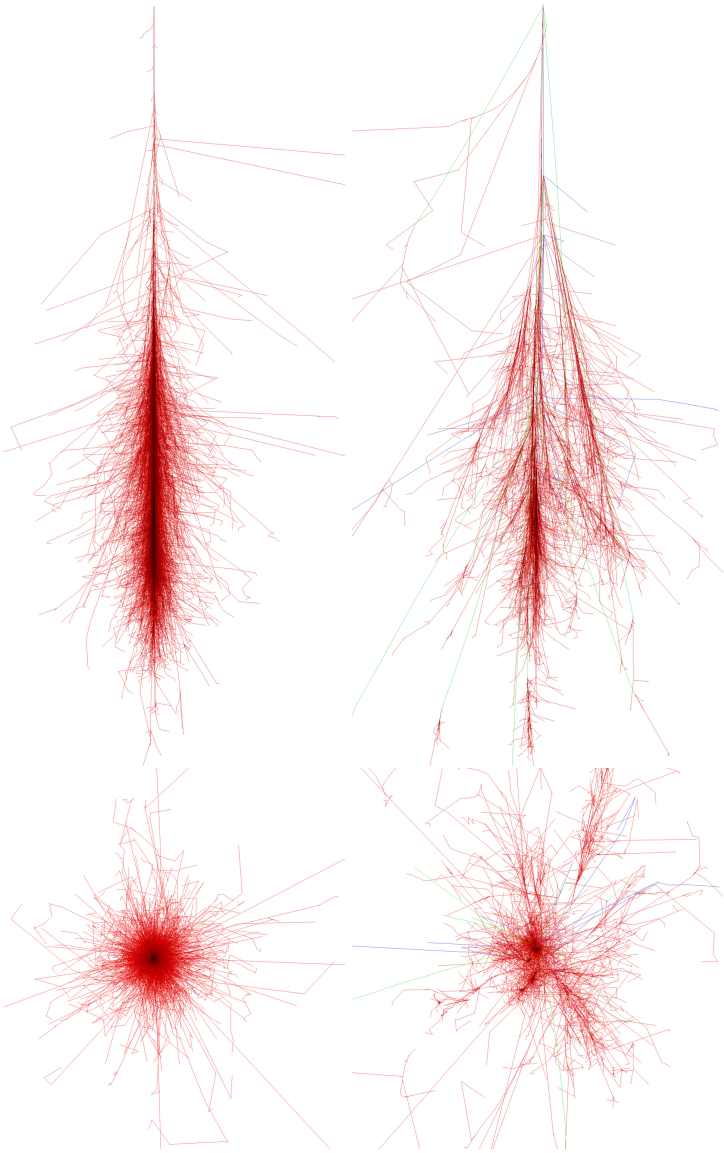

Figure 9.1: Trajectoires des particules dans une simulation de gerbes atmosphériques (énergie de 100 GeV) réalisée à l'aide du logiciel CORSIKA pour des gerbes créeé par un proton (panel de droite) et un photon gamma (panel de gauche). Chaque gerbe est présentée par le coté et par dessous. Crédit : CORSIKA.

9.1.3 Les télescopes à effet Cherenkov atmosphérique

Finalement, cette lumière Cherenkov est captée par les télescopes utilisés, appelés télescopes à effet Cherenkov atmosphérique (Imaging Astmospheric Cherenkov Telescope ou IACT en anglais). Plusieurs générations de télescopes Cherenkov ont permis de mettre en avant les caractéristiques importantes pour les performances de ces derniers. On peut notamment citer :

- Un large miroir, pour collecter le plus possible de lumière provenant des gerbes.
- Une caméra avec une pixélisation fine afin de capturer les détails de la gerbe.
- Une électronique rapide afin d'enregistrer seulement le flash de lumière Cherenkov (durée de seulement quelques nanosecondes).

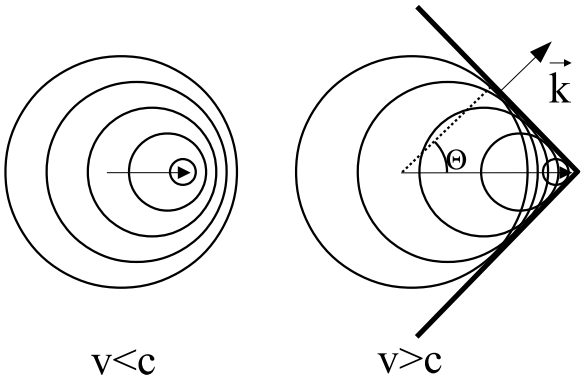

Figure 9.2: Sur le panel de gauche, des ondes électromagnétiques associées à une particule chargée sub-luminique. Sur le panel de droite, des ondes électromagnétiques associées à une particule chargée supra-luminique avec la formation d'une onde de choc. Figure issue de de Naurois and Mazin (2015).

- Un large champ de vue pour être capable de voir l'entièreté de l'extension de la gerbe atmosphérique.
- Plusieurs télescopes suffisamment proches pour voir la gerbe sous plusieurs angles.

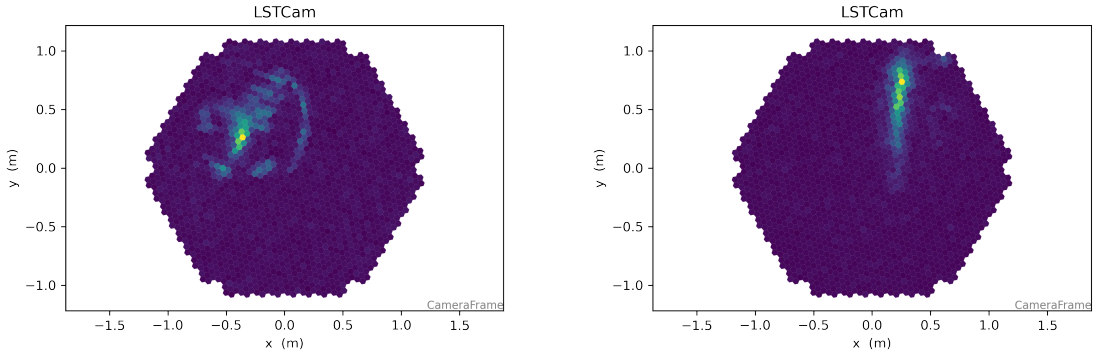

Figure 9.3: Image d'une gerbe probablement produite par un hadron (panel de gauche) et produite par un photon (panel de droite) vue par le LST-1.

La figure 9.3 montre deux exemples d'images de gerbes vues par un IACT (LST-1 ici). L'enjeu de l'étape de reconstruction sera, à partir de ces images, de déterminer la direction d'origine, l'énergie et le type de particule qui a créé la gerbe.

La génération actuelle d'instruments se compose de trois expériences : H.E.S.S., MAGIC et VERITAS. La génération suivante sera quant à elle principalement composée de l'expérience CTA, qui reprend les élément ayant fait le succès de la génération actuelle, mais en étendant notamment la taille du réseau ou le nombre de télescopes le composant.

9.2 L'expérience H.E.S.S.

L'expérience H.E.S.S. est installée sur le plateau Khomas à une altitude de 1800 m en Namibie. Son placement dans l'hémisphère Sud lui permet d'observer une part importante du plan galactique dont le centre galactique.

L'expérience est composée de cinq télescopes à effet Cherenkov atmosphérique (Fig. 9.4). Les quatre premiers télescopes, CT 1-4, ont été installés durant la première phase de l'expérience, qui a commencé en 2004. Le cinquième, CT 5, a été installé par la suite et à rejoint le réseau lors du

Figure 9.4: Photographie du site d'installation de l'expérience H.E.S.S. On peut voir les quatre petits télescopes CT 1-4, et le gros télescope CT 5 ainsi que la salle de contrôle. La photographie a été prise en septembre 2012.

début de la seconde phase en 2013. Il possède un miroir nettement plus large afin de descendre le seuil en énergie. Les caméras des petits télescopes ont été mises à jour en 2016 et celle de CT 5 en 2019. Les principales caractéristiques des télescopes sont rassemblées dans le tableau 9.1.

Télescope	CT 1-4	CT 5
Dimension du miroir	Hexagonal de 12 m de diamètre	Rectangulaire de 32 m par 24 m
Surface totale du miroir	108 m^2	614 m^2
Distance focale	16 m	36 m
Design optique	Davies-Cotton	Parabolique
Masse d'un télescope	60 t	580 t
Vitesse de rotation maximale	100 deg/min	200 deg/min
Nombre de pixels	960	1764
Taille angulaire d'un pixel	0.16 deg	0.067 deg
Champs de vue de la caméra	5.0 deg	3.2 deg
Temps d'intégration	16 ns	16 ns
Taux de déclenchement	500 kHz	3600 kHz

Table 9.1: Comparaison entre les deux types de télescopes de H.E.S.S. Les informations sur les caméras correspondent à celles installées en 2022.

Les observations de H.E.S.S. sont découpées en runs de 28 minutes. Les observations ont principalement lieu pendant la nuit sans Lune, mais depuis 2019, des observations ont aussi lieu avec la Lune quand sa phase est proche de la nouvelle Lune.

Une des particularité de H.E.S.S. par rapport aux expérience passées ou actuelles est la présence de différents types de télescopes. Cela influe sur le système de déclenchement. Chaque caméra possède son propre système de déclenchement dans le cas où un signal est détecté. Cette information est ensuite envoyée à un système central qui prendra la décision finale en fonction du nombre et du type de télescope qui ont déclenché. Il y a trois types de déclenchements qui sont conservés :

- CT5 seul déclenche. Ce mode est appelé HESS II Mono.

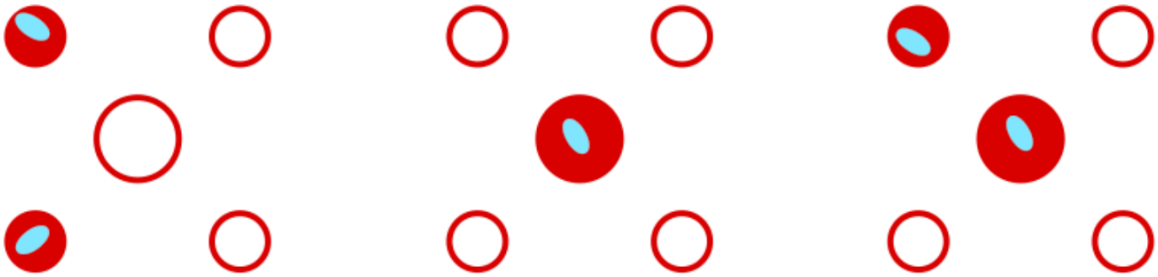

Figure 9.5: Les trois configurations de déclenchement différentes pour H.E.S.S. Chaque télescope est représenté par un cercle, le cercle central le plus grand représentant CT5. Un cercle rempli représente un télescope dont le déclenchement est dû à la détection de la lumière Cherenkov. Le cas de gauche représente le déclenchement H.E.S.S.-I Stereo où au moins deux télescopes CT 1-4 détectent la gerbe. Le cas du milieu est le déclenchement H.E.S.S.-II Mono, où seul le télescope CT 5 déclenche. Le cas de droite est le déclenchement H.E.S.S.-II Stereo, où CT 5 et au moins un des télescopes CT 1-4 se déclenchent. Figure issue de Chevalier (2017)

- Au moins deux télescope CT1-4 déclenchent. Ce mode est appelé HESS I Stereo.
- Au moins deux télescope CT1-5 déclenchent dont CT5. Ce mode est appelé HESS II Stereo.

La figure 9.5 est un schéma des différents modes de déclenchement. Une fois le déclenchement effectué par le système central, l'événement est enregistré.

Une analyse en temps réel est effectuée sur site. Elle est particulièrement utile pour communiquer rapidement à la communauté astronomique des résultats sur des sources transitoires. Les données sont par la suite envoyées en Europe dans différents centres de données, où elles seront calibrées puis analysées. En fonction de ce qui est souhaité, il est possible d'utiliser les données de seulement certains télescopes, ou au contraire de combiner l'ensemble des données acquises.

9.3 Le projet CTA

9.3.1 L'instrument

CTA (Cherenkov Telescope Array) est la prochaine génération d'IACT, dont le but est d'élargir la gamme d'énergie, d'améliorer la sensibilité et la résolution angulaire et en énergie. Pour atteindre ces objectifs, CTA sera composé de trois types de télescopes optimisés pour différentes gammes d'énergie : les Large-Sized Telescopes (LST) de grande taille pour les basses énergies, les Medium-Sized Telescopes (MST et SCT) de taille intermédiaire pour les énergies intermédiaires et les Small-sized Telescopes (SST) de petite taille pour les hautes énergies.

Deux sites accueilleront les deux réseaux de télescopes de CTA : l'un dans l'hémisphère nord à La Palma, Espagne, et l'autre dans l'hémisphère sud à Paranal, Chili (Fig. 9.7). Le site du nord accueillera 4 LST et 9 MST, tandis que le site du sud accueillera 14 MST et 37 SST.

9.3.2 Les capacités scientifiques de CTA

CTA devrait augmenter de manière significative les performances par rapport aux instruments actuels utilisés en astronomie VHE, avec une amélioration de la sensibilité, de la résolution en énergie et de la résolution angulaire. CTA sera capable de couvrir tous les sujets scientifiques standards de l'astronomie gamma à très hautes énergies et aura une sensibilité à courte échelle de temps supérieure de plusieurs ordres de grandeur à celle des instruments actuels, en particulier aux faibles énergies. Cela rendra l'expérience particulièrement performante pour l'étude des phénomènes transitoires, y compris les noyaux actifs de galaxie et les GRBs. La figure 9.8 présente les performances du CTA par rapport à la génération actuelle et à *Fermi*/LAT.

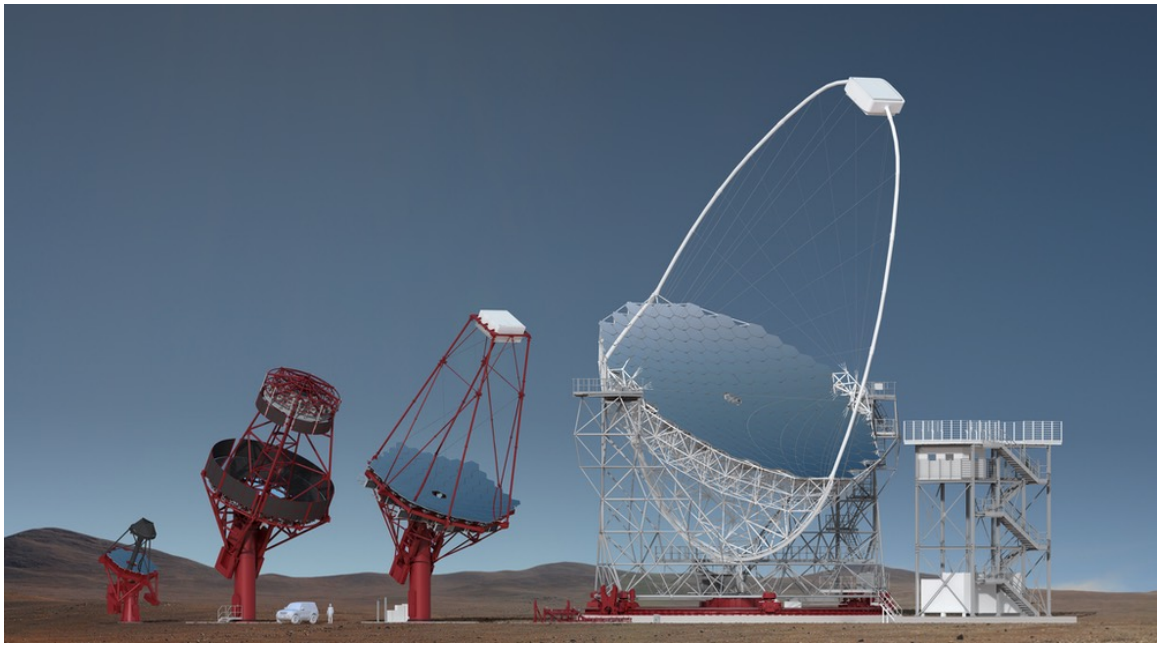

Figure 9.6: Vue artistique de l'ensemble des designs de télescopes pour CTA. De la gauche vers la droite : SST, SCT, MST et LST. Credit : Gabriel Pérez Diaz, IAC

CTA possédera également un champ de vision (FoV) beaucoup plus large que les instruments actuels, ce qui lui permettra de rechercher plus facilement des contreparties aux alertes transitoires mal localisées, telles que les ondes gravitationnelles (GW), les neutrinos ou certains sursauts gamma (GRB). L'élargissement du champ de vision permettra potentiellement à CTA de découvrir de nouveaux phénomènes transitoires.

Outre ses capacités d'étude des phénomènes transitoires, CTA devrait réaliser un relevé galactique d'un ordre de grandeur plus profond que les relevés actuels, ce qui permettra de mieux comprendre les sources galactiques et l'origine des rayons cosmiques. CTA réalisera également le premier relevé extra-galactique, couvrant 25% du ciel, ce qui permettra la première étude non biaisée de population des sources extra-galactiques.

9.4 Large-Sized Telescope

Les Large-Sized Telescope (LST) de l'observatoire CTA sont principalement axés sur les basses énergies et le repositionnement à grande vitesse. Leur taille les classe parmi les plus grands télescopes Cherenkov. Un prototype, nommé LST-1, est en cours de test depuis 2019 à La Palma (Fig. 9.9).

Afin d'assurer ce repositionnement rapide, la structure est constituée de matériaux composites pour un ratio résistance-poids optimal. Le poids total du télescope est ainsi de seulement 103 t. Cependant, cette structure peut se déformer ce qui a des impacts pour le pointé mais aussi le système optique.

Afin de permettre le repositionnement en moins de 30 secondes pour n'importe quelle direction dans le ciel, trois moteurs d'une puissance totale de 360 kW sont nécessaires, deux pour l'axe azimutal et un pour l'axe en élévation. Ces moteurs assurent autant les mouvements rapides que le suivi avec précision des sources lors des observations.

Le système optique est composé d'un réflecteur parabolique unique de 28 m de distance focale et 23 m de diamètre. Ce miroir est composé de 198 facettes qui peuvent chacune être contrôlées indépendamment afin de permettre la meilleure résolution angulaire possible en toutes conditions. Au bout de l'arche, face au miroir, est installé la caméra dite Cherenkov composée de 1855 tubes photo-multiplicateurs (PMT) possédant un champ de vue total de 4.5°.

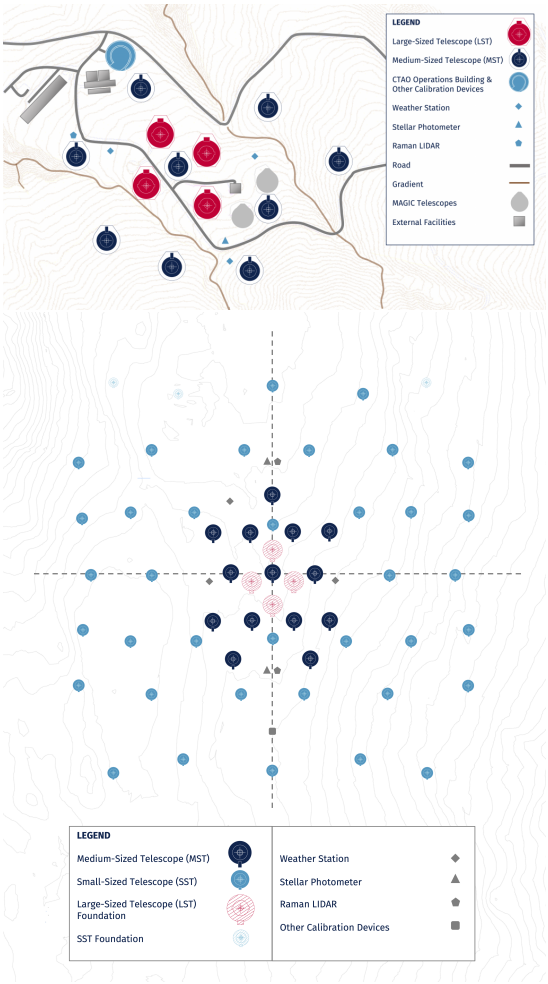

Figure 9.7: Plan des réseaux de télescopes prévus pour le site de l'hémisphère nord (haut) et de l'hémisphère sud (bas).

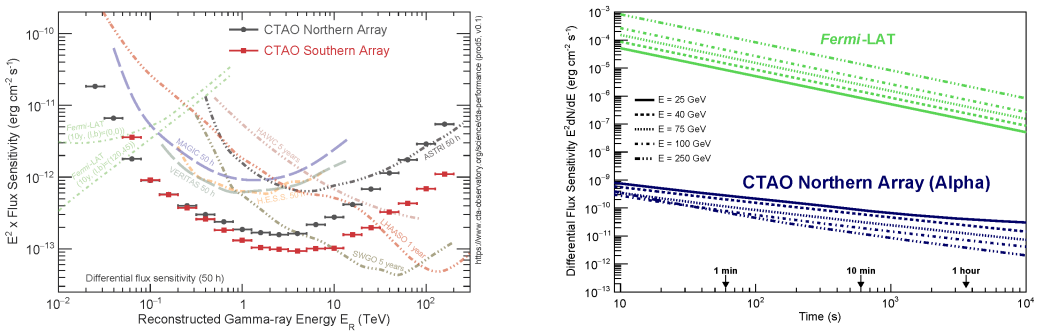

Figure 9.8: Sensibilité de CTA comparée à plusieurs expériences (gauche). Sensibilité sur de courts intervalles de temps à différentes énergies pour le réseau nord de CTA ainsi que *Fermi*/LAT (droite).

Au centre du miroir, une cavité est aménagée pour placer des équipements nécessaires à la prise de données de calibration, à la correction du pointé ou encore à la mesure des performances optiques (Fig. 9.10). Pour la correction du pointé, on y trouve notamment deux caméras, la CDM et le StarGuider ainsi que deux lasers servant de références optiques qui sont imagés sur une cible sous la

Figure 9.9: Image du prototype LST-1

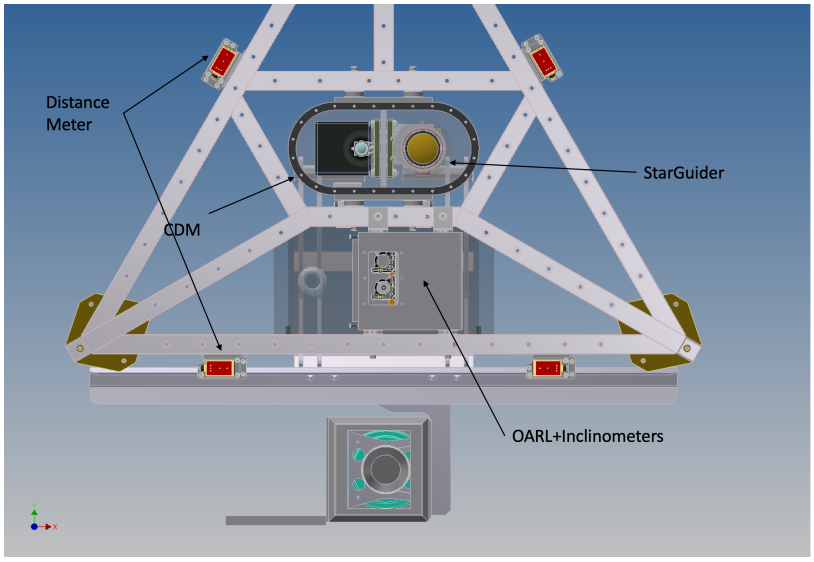

Figure 9.10: Équipement au centre de la structure supportant le miroir LST-1.

caméra. Il existe également sur la caméra des LEDs permettant de déterminer la position de celle-ci. La combinaison de l'ensemble de ces systèmes permet une correction fine du pointé du télescopes.

Part III

Online correction of the pointing of the telescope

Chapter 10

Online correction of the pointing of the telescope

Contents

One of the requirements of the LSTs telescopes is the ability to determine the pointing of the telescope at less than 1 arcminute with online correction and less than 14 arcseconds after offline correction. A precise knowledge of the pointing is important for future stereoscopic observations and also to avoid any bias on the reconstructed source's position in the sky. To achieve this, three different systems help to correct the calibration.

10.1 Pointing correction on LST telescope

Online correction is achieved with what is called *bending model*. The system measures the systematic pointing error of the telescope at regular temporal and spatial intervals to derive a model that will be used by the *drive system* for correction. The system's name originated from the expected primary source of systematic error, which was believed to be the bending of the telescope's structure. This chapter is dedicated to the explanation, development and results of this system.

Two other systems are used for offline pointing corrections. The first one is the StarGuider (SG). This system uses a CCD camera placed at the centre of the dish (called StarGuider), which is pointing slightly offset to the Cherenkov camera. This allows the camera to see half of the Cherenkov camera and a part of the sky on the side. The exact pointing of the StargGuider could be determined using the stars visible in the sky. The position of the Cherenkov camera in the FoV of the StarGuider could be determined using the LEDs (see chapter 8 and Fig 10.1). With the two pieces of information, it is possible to determine the absolute pointing of the Cherenkov camera.

The second one, called Camera Displacement Monitor (CDM), monitors at a high frequency (10 Hz) the position of the Cherenkov camera compared to the optical axis. As the camera is a weight at the extremity of an arch, it could move significantly under the influence of various forces. Among them are the wind on the camera, oscillation induced by drive movement, ... To achieve this,

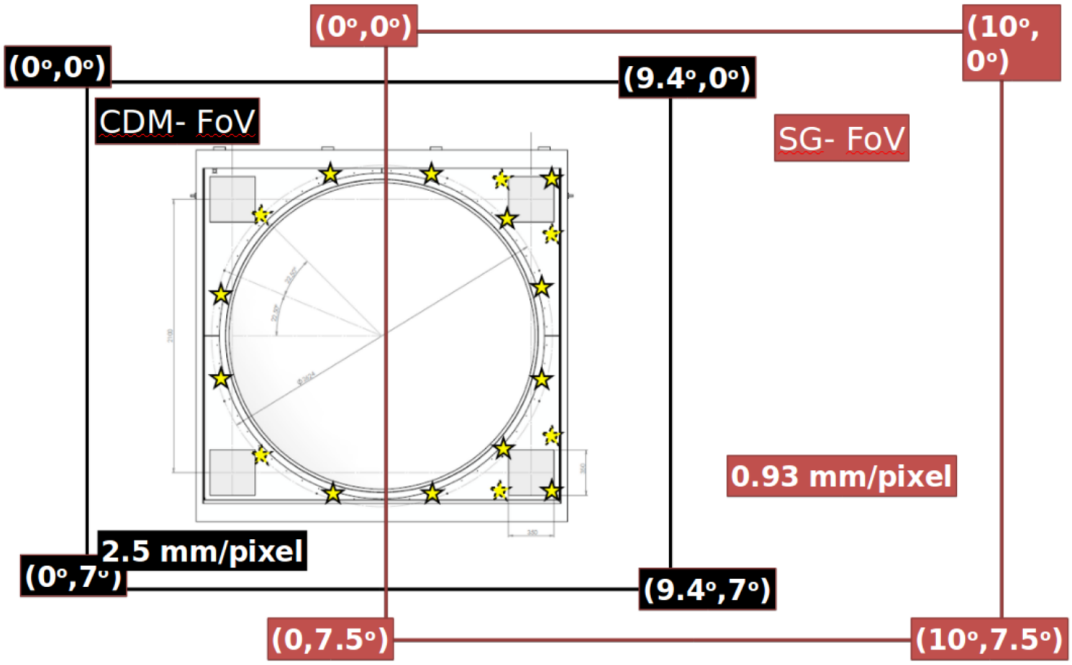

Figure 10.1: Sketch of the field of view of the CDM and the StarGuider. The camera frame and the LEDs are represented

a CMOS camera, also called CDM, is placed at the centre of the dish. Two Optical Axis Reference Laser (OARL) are fired from the centre of the dish up to a target below the camera and used as a reference by the system. The LEDs on the Cherenkov cameras are also used to determine the centre of the Cherenkov camera in the CDM (see Fig 10.1). The images taken by the CDM are analysed in real-time, and the position of the LEDs and OARLs are saved. Then an offline correction could be determined by combining information from the SG and CDM at the analysis level.

10.2 Working principle of the bending model program

The full process, from data acquisition, analysis and correction determination, has been developed in the course of my PhD. The program has been written in python and integrated into the LST framework to interact with the different sub-systems of the telescope.

The *bending model* is based on a set of measurements of the pointing across the sky. These measurements are performed by pointing to a star with the telescope. The Star Imaging Screen (SIS) of the Cherenkov camera is at the centre and at a focal distance of the telescope (see chapter 8). The pointed star will be imaged on the screen, and the difference between the star's position and the centre of the Camera is the misspointing measurement. A sketch of this principle is given in figure 10.2.

For the measurement, the CDM camera is then used to take a picture of the Cherenkov camera. The star position is extracted from this image, and the position of the camera is determined using the LEDs.

The repetition of this procedure on different pointing allows having an overview of the correction to apply in the whole sky. A *mechanical model*, fitted on a set of measurements of the misspointing, is then used by the *drive system* to apply online corrections.

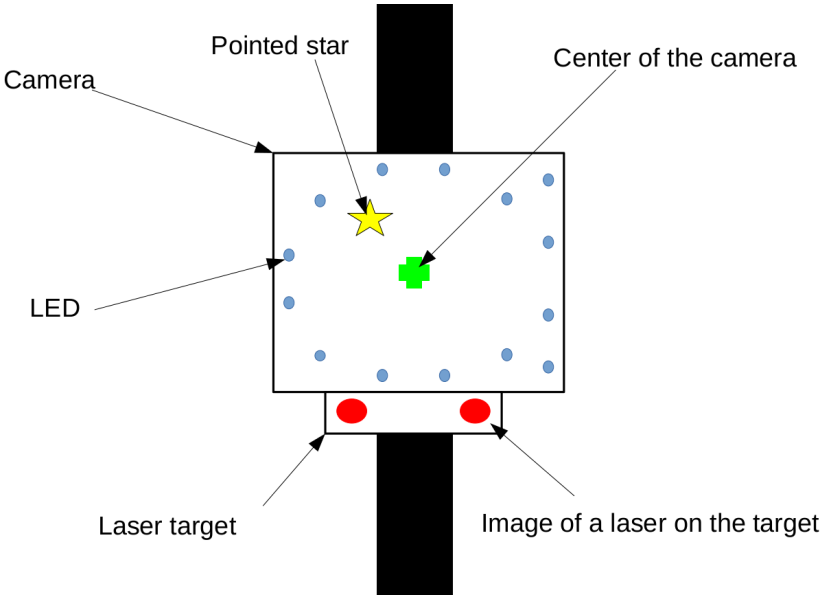

Figure 10.2: Working principle of the *bending model*. The scheme represents the FoV of the CDM camera. It's observing the Cherenkov camera, with its LEDs, the OARLs image of the target below and the star pointed image on the SIS. The star is not at the centre due to the pointing error (exaggerated in this figure).

10.3 Selection of the star to observe

The selection of a star is an important step as it will impact not only the observation time but also the accuracy of the system. Minimizing the observation time is important as the time dedicated to *bending model* data acquisition is limited. A short observation time on stars allows to cover more directions of the sky in the same amount of time, improving the precision of the system.

10.3.1 Constraints on the star selection

The sensitivity of the overall system is quite low, in fact, it's less sensible to stars on the target than stars observed directly on the sky. To assess this, we can compute the amplification factor due to the telescope compared to the direction observation of the sky. The effective mirror area of the telescope is $370\,\mathrm{m}^2$. The CDM is placed at the centre of the dish, so its distance from the target is equivalent to the focal length of the telescope f. If we assume the white target diffuses light uniformly in every direction (so in a half sphere), the light collected by the telescope is redistributed on a surface equivalent at $2\pi f^2$ equal to $4926\,\mathrm{m}^2$ for the LST. If we make the ratio between the area of light collection and redistribution, we obtain ~ 0.075 . So if we had pointed the CDM directly at the sky to observe the star, we could have collected 13 times more light than by the optical system of the telescope and reflection on the SIS, and this without even taking into account the non-perfect reflectivity of the mirror and the SIS. In consequence, bright stars are needed as the sensitivity of the system will be quite low.

Another requirement is the need to know the position of the star accurately at the time of the observation. As we will consider only the brightest stars in the sky, this means that the star will be mainly close to the solar system. As a consequence, their proper motion will have a significant impact on their exact position in the sky as it will move across time. As an example, if we consider the Barnard's Star, the star with the highest apparent proper motion of $\approx 10\mathrm{arcsec.yr}^{-1}$. In thirty years (the estimated lifetime of the telescope), the star will have moved by $\sim 5'$. This error is way above the requirement of the system, and even if most of the stars have a much smaller proper motion (Fig. 10.3), not correcting it could bring significant systematic error.

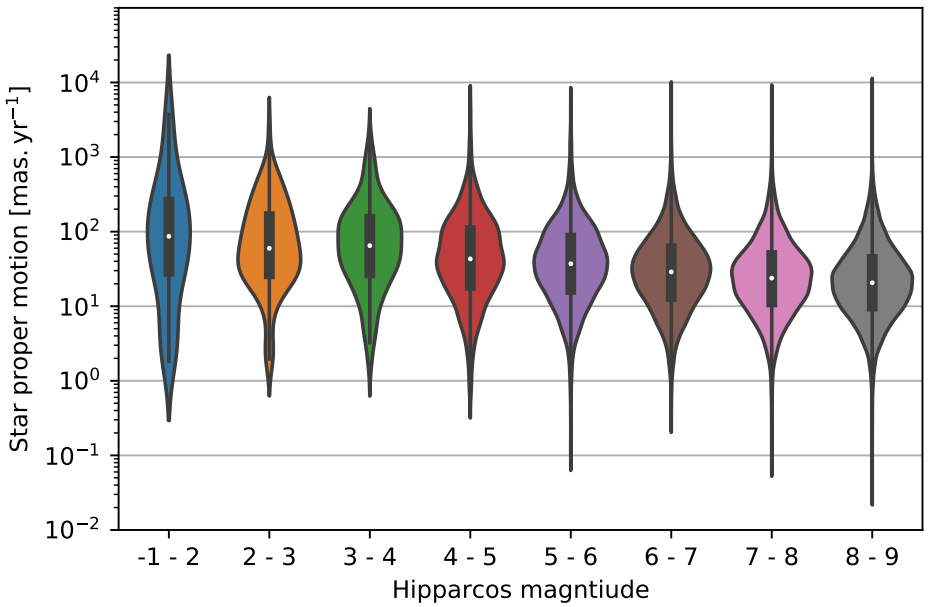

Figure 10.3: Violin plot of the proper motion of stars in the Hipparcos catalogue in function of their magnitude

One last important requirement is the ability to determine the absence of any stars with a similar or higher luminosity close to the observed star. There are three reasons for this. The first one is the optical angular resolution of the telescope, which is of the order of 0.1°. So if two stars are too close, they will become indistinguishable and will bring systematic error. The second one is that the presence of a nearby star would complexify the analysis significantly as it would need an additional step to identify each star and determine their positions precisely, as it would need to take into account the potential contamination of the signal by another star. The third one is the acquisition of dark images during data acquisition. As the CDM does not have any shutter, dark images are performed on a darker part of the sky (See section 10.4.2.2 for more explanation). As a consequence, it is necessary to determine the absence of a bright star in the part of the sky used for dark images to minimise contamination.

10.3.2 Star catalog selection

Based on these constraints we can determine the requirements for the catalogue to use :

- A precise measure of proper motion for stars up to a visual magnitude of ~ 6
- Completeness[1] as close as possible to 100% up to a visual magnitude of ~ 9
- Cover the sky for a declination between $-40°$ and $90°$. A full sky coverage would allow the system to work on potential LSTs in the southern hemisphere.
- Reliable information for the brightest star, i.e. no saturation of the instrument which has been used to make the catalogue.

The requirement of having reliable information on bright stars will discard two famous catalogues for astrometry. The first one, is the catalogue from the Gaia satellite. The instrument suffers from

[1] Estimation of the fraction of the existing stars that are effectively in the catalog

saturation effect at a magnitude of $\sim 6-8$ (Gaia Collaboration et al., 2018). The second one, the USNO-B catalogue, uses a collection of measurements from multiple telescopes and a lot of archival photographic plates that saturate at a magnitude around ~ 12 (Monet et al., 2003).

The selected catalogue is the Hipparcos one. The HIgh Precision PARallax COllecting Satellite (Hipparcos) mission is the older brother of the Gaia mission. The satellite was launched in 1989 by the European Space Agency on board of an Ariane IV rocket. The satellite stopped the observations in 1993.

The Hipparcos catalogue is constituted of 118 218 stars (Perryman et al., 1997) and is complete on the full sky up to a magnitude of 7.3 with a limiting magnitude of 12.4. The precision on the position of the stars is $\sim$0.8 mas and precision on the proper motion around $\sim$0.9 mas yr^{-1}. The figure 10.4 show the density of stars with a magnitude below 6 from the Hipparcos catalogue.

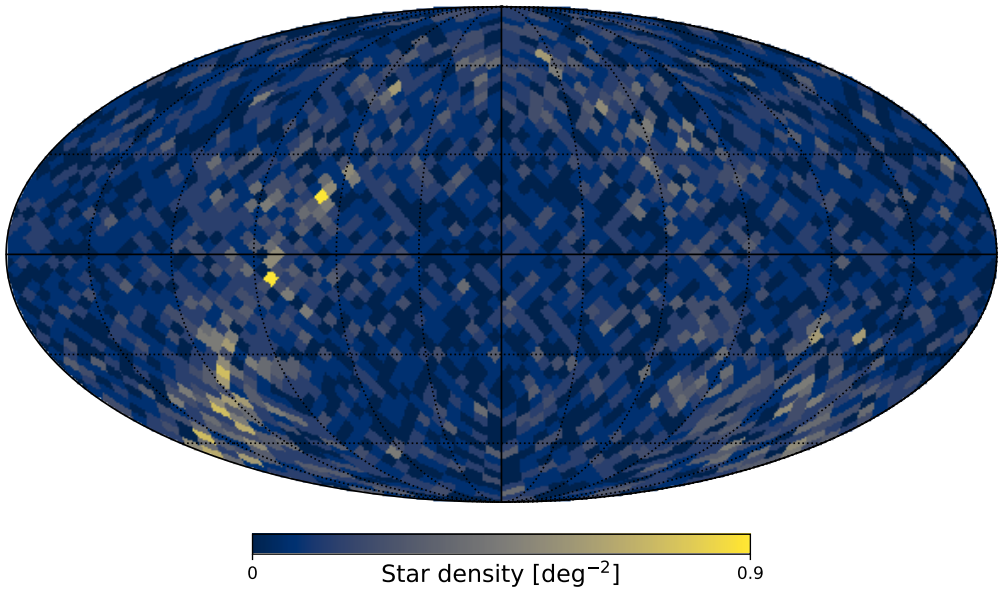

Figure 10.4: The density of stars in the Hipparcos catalogue brighter than a magnitude 6

One of the missing astrometry information in the Hipparcos catalogue is the radial velocity. A calculation performed on the Barnard's Star shows that a computation of the position in 2060 without taking into account the information about the radial velocity would lead to an error of $\sim 3''$. To then complement the Hipparcos catalogue, the Mean Radial Velocities Catalog of Galactic Stars (MRVCGS) is used. This catalogue is a compilation of several catalogues and multiple publications of spectral measurement of the radial velocities of stars. Especially it includes the radial velocity for 20574 stars of the Hipparcos catalogue (Barbier-Brossat and Figon, 2000).

The Hipparocs catalogue also has another nice advantage. The relative spectral sensitivity of CDM has a shape close to the Hipparcos one (Fig. 10.5). One of the main differences is the CDM's IR bump, which will likely be partially suppressed by the low reflectivity of the LST mirrors in this spectral band. Another big difference is the three colour filters of the CDM, but as all the filters will be summed during the analysis (see section 10.5), this will have no impact. These similarities will greatly simplify the process of calibrating the observation time as a function of the magnitude of the star (see section 10.5.8).

10.3.3 Computation of the position of the stars and quality criteria

The Hipparcos catalogue gives the position of the stars for the epoch J1991.251, corresponding to the middle of the observation period of the mission. As we need the position at the time of the

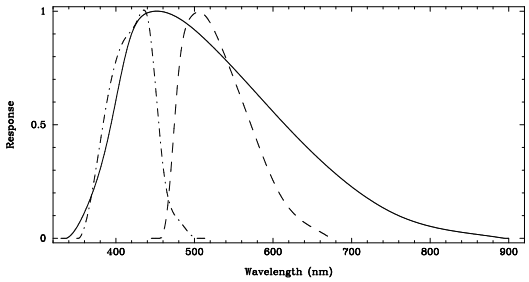

(a) Spectral response of the Hipparcos instrument (plain line). The dashed lines are the spectral response from the Tycho instrument. The figure is extracted from Publication (1997).

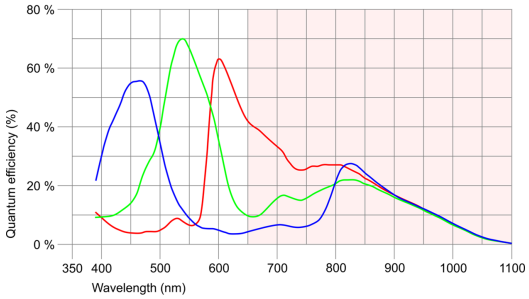

(b) Spectral response of the CDM camera for each pixel colour. Figure extracted from the maker documentation (camera UI-3590CP-C-HQ Rev.2).

Figure 10.5: Spectral response of Hipparcos and the CDM

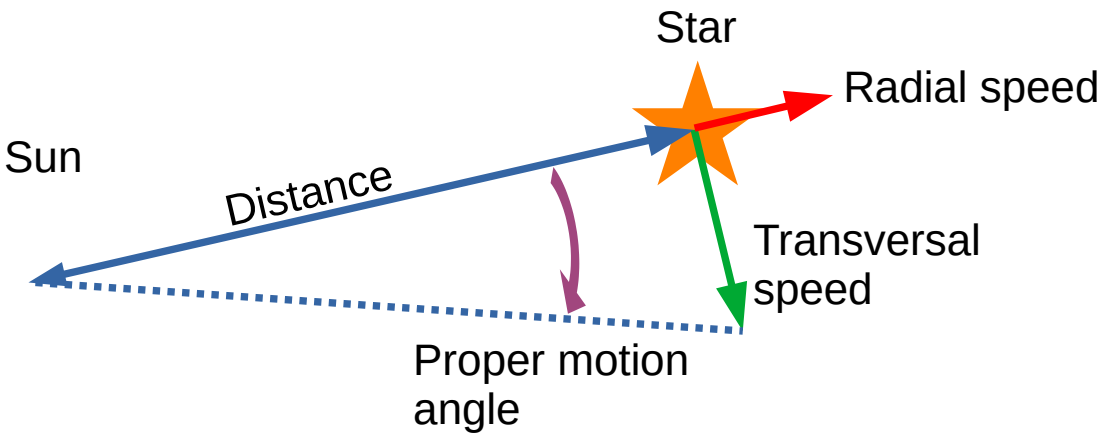

Figure 10.6: Sketch of the movement of a star relative to the sun. The proper motion angle is the most important parameter for correcting the position in the sky of the star as a function of its displacement relative to the sun.

LST observations, the position of the stars needs to be computed to take into account their proper motion. The computation itself is done with the python package `astropy` (Astropy Collaboration et al., 2022) at each time a series of observations is started.

First, the distance of the star is computed using the parallax information from Hipparcos. To this distance results, additional information is added, the position, proper motion, epoch of observations taken from Hipparcos and radial velocity from the MRVCGS to compute the actual position of the star (Fig. 10.6). The *drive system* of the LST expects input coordinates to be given in the International Celestial Reference System (ICRS) reference frame, and as Hipparcos is already providing coordinates in this frame, no conversion is needed.

Finally, a quality flagging step is performed. This step is to ensure that stars picked for observations by the *bending model* program will have an accurate position. As the LST will have an operating life of at least 30 years, it was decided to require an accuracy better than 1″ up to 2060. This is close to be seventy years after the measurement by Hipparcos.

The first criterion rejects all the stars that do not have radial velocity information. The second criterion rejects any stars which are considered as binary in Hipparcos or MRVCGS. The two main reasons for this criteria are to avoid stars that will have a close companion and stars that would have a more complex proper motion due to their companion. The third criterion is then to reject all the stars that are flagged with uncertainty or approximate value on the radial velocity in the MRVCGS. The final criterion is to reject all the stars that have a parallax value smaller than three

times the uncertainty of this value, to assess that a distance estimation is available for that star. These criteria allow keeping 24% of the stars brighter than magnitude 3 and 29% of the stars brighter than magnitude 6.

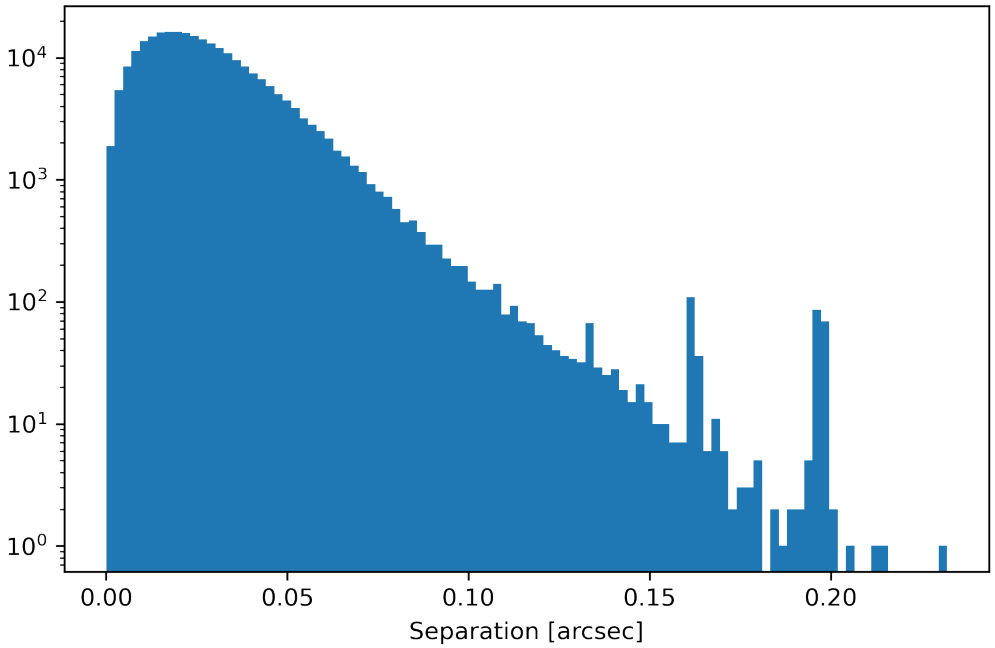

Figure 10.7: Distribution of the uncertainty on the position of the stars selected from the Hipparcos catalogue for the date 2060.

In order to verify that this set of criteria allows respecting the requirement, set a less than 1″ uncertainty in 2060 to minimise systematic uncertainty, a simple MC sampling was performed. First, the position in 2060 was computed for all the selected stars in the catalogue. Then the computation was performed another thousand times with a simulated stars catalogue. For the parameters of each star, the value was taken following a gaussian distribution centred on the measured value and, as standard deviation, the error on the parameters in the catalogue. Then the position of each simulated star in 2060 is compared to the one obtained with the stars in the catalogue in 2060. The results can be seen in figure 10.7. The maximum separation obtained is below 0.25″, which is more than enough to guarantee that the uncertainty coming from the catalogues data would have no impact on the results of the *bending model*.

10.3.4 Star selection

Finally, we need an algorithm to select a star in a given direction in the sky. In input to this algorithm will be given the altitude and azimuth targeted for the misspointing measurement, the maximum distance of the star compared to the targeted region and the expected time of observation.

The first step of the algorithm is to search the stars with a valid quality flag that are within the disk centred on the targeted direction and, as radius, the maximum distance allowed. The position given in an AltAz frame is transformed into the given position in the ICRS frame for the time of observation. The distance of this point to the stars of the catalogue is then computed, and only the stars matching the criteria are then kept.

The rest of the algorithm is then iterative. In this list of selected stars, the brightest one is picked (brighter stars imply shorter observation time). Several observation criteria are then checked. If the star passes all the criteria, the star is selected. Otherwise, the star is removed from the list, and

the next brightest star is picked. In case no stars are found, an Exception is raised by the code to inform the program that called it that no star was found.

The different observation criteria are :

- The altitude is within the observable range of the telescope. The zenith angle needs to be in the range between 0.8° and 70°. The existence of a minimum zenith angle is caused by the altazimuthal mount of the telescope. Due to this mount, the azimuth movement of the telescope to follow the track close to the zenith requires a very high rotation speed and below a given zenith, the telescope is not able to rotate fast enough in order to track the star. The maximum value corresponds to the standard range for observations with LST.

- If the moon is up in the sky, it needs to be in a distance included between 20° and 130°. If the moon is too close to the FoV of the CDM, it will cause a big lens flare making the image very hard to analyse. Otherwise, if the moon is too far, it will directly illuminate the SIS and the faint signal from the star will become very hard to detect.

- It will be checked that no star brighter than magnitude 5 or brighter than 3 magnitudes fainter than the star magnitude ($\sim$ 15 times fainter than the observed star) in a radius of 0.6°. This is to be sure that no other star will be detected on the SIS.

- A dark patch will be searched at a distance of 2° of the star. A dark patch is defined as a part of the sky with no star brighter than magnitude 5 or brighter than 3 magnitudes fainter than the star magnitude in a radius of 1°. This position will afterwards be used as dark images by the analysis.

10.4 Acquisition procedure

10.4.1 Technical limitations and constraints

The overall idea of the *bending model*, as explained above, is rather simple. First, pick a star and track it, take an image with the CDM and find all the elements (LEDs, OARLs, and star) in it. Nevertheless, this rather simple idea was challenged by several issues discovered during the first tests.

10.4.1.1 Brightness and reflection of the LEDs and OARLs

One of the first issues discovered during the first test was the brightness of the LEDs and OARLs which are not compatible with long exposure time. An exposure time of 50 ms was sufficient to saturate the sensors of the CDM at their positions. As any saturation would cause issues for the precise localization of the LEDs and OARLs, in order to localize them, a short exposure time is needed.

Another issue quickly identified is the reflection of the LEDs and OARLs at a position close to the centre of the SIS, where the image of the star should appear (Fig. 10.8). It comes from the reflection of these on the main mirror of the telescope which focuses their images at the center of the camera. The reflections are brighter than most of the stars, and in consequence, it's very complicated to identify any star that would be observed.

The conclusion of these two issues is that OALRs and LEDs should be acquired through a different set of images than the ones used for stars. The exposure of this set of images should be small in order to avoid any reflections.

10.4.1.2 Long exposure time for the stars

Due to the sensitivity of the CDM, high exposure time is needed to detect a star. The maximum exposure time allowed by the CDM is one second, and it is not sufficient to detect faint stars. The figure 10.9 shows 3 different stars observed with a 1-second exposure. Only a star with a magnitude

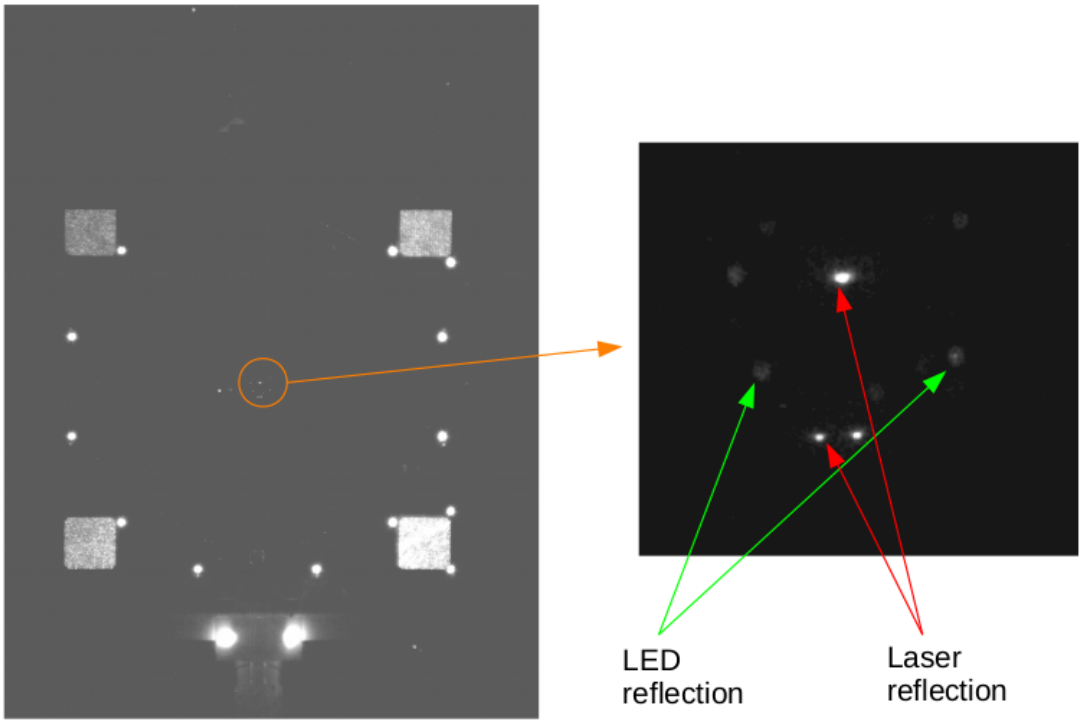

Figure 10.8: Image from the CDM with the LEDs and OARLs on. The panel on the right is a zoom on the target were the reflection of the LEDs and OARLs could be seen.

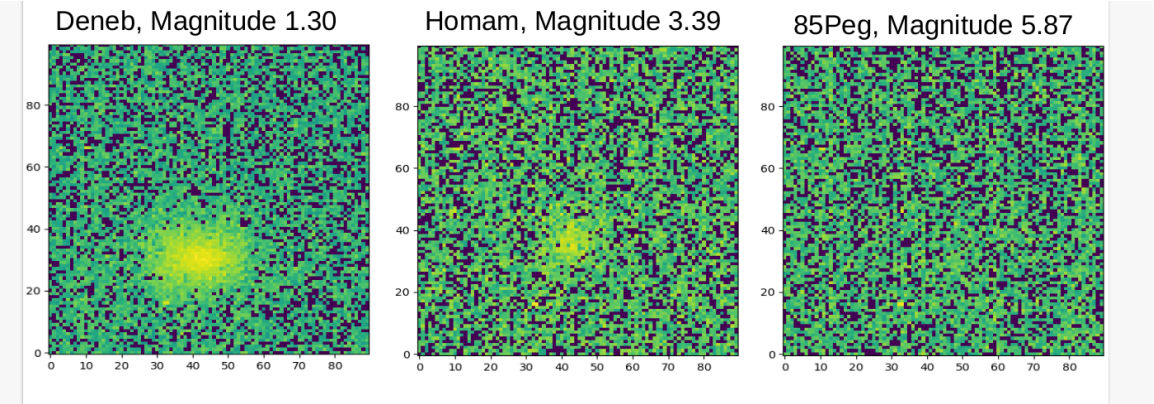

Figure 10.9: The image of multiple stars of various magnitude with a single image of 1s of exposure.

below 3 can be detected with the CDM. As a consequence, multiple exposures will be needed in order to be able to detect the signal.

To further reduce the noise from the CCD sensor of the CDM, images without a star (aka, dark images) are also taken, and 50% of the acquisition time is spent on the star and 50% on the dark patch position. The number of needed images as a function of the star magnitude has been roughly determined on a subset of stars at the beginning of the development. Now, this is recomputed for each observation, increasing the statistics available each time (see section 10.5.8).

10.4.2 Detailed procedure

10.4.2.1 Telescope preparation

The first step is to check the status of all the telescope systems and prepare them for data acquisition. Depending on the nature of the action needed to put the systems, the *bending model* program will either execute the action or raise an error. For example, if the telescope is parked, it is not suitable for the program to manage the unpark procedure as there are a lot of safety checks to perform for executing this action.

At the end of this step, to start the acquisition, the telescope needs to be in a state where:

- The telescope needs to be unparked and not track any source
- The Cherenkov camera state needs to be the one dedicated to *bending model* acquisition
- The camera shutter is open
- The SIS needs to be centred
- The CDM camera is ready to acquire images
- The mirrors need to be focused

10.4.2.2 Data acquisition

When the preparation step is finished, the acquisition loop is started. This loop is run for every acquisition.

1. Get the star from the dynamic scheduler, the scheduler determines the region of observation and star to optimize observation time and sky coverage.
2. The star position is tracked with the telescope. The *bending model* waits for the emission of the precise tracking flag by the *drive system* before going further.
3. The LEDs and OARLs are turned on.
4. A series of ten images of 20 ms of exposure with the OARLs and LEDs light on is taken. These data will be used to determine LEDs and OARLs localisation.
5. The LEDs and OARLs are turned off.
6. A series of images of 1 s of exposure is taken. The exact number will depend on the brightness of the star (see section 10.5.8). These data will be used to determine star localisation.
7. The LEDs and OARLs are turned on.
8. A series of ten images of 20 ms of exposure with the OARLs and LEDs light on is taken.
9. The LEDs and OARLs are turned off.
10. The tracking is stopped and the dark patch position is tracked
11. A series of images of 1 s of exposure is taken. The number of images will be the same as the images taken on the star. These data will be used as dark images.

There are two series of images with LEDs and OARLs to have an average value corresponding to the data taken for the observation of the star.

When the observation time given to the *bending model* is finished, the program will put the telescope in the initial state.

10.4.2.3 Inclinometers scan

Another automatic acquisition procedure was added to the *bending model* program called `inclinometer scan`. During the development of the *bending model*, it has been proven that using the value of the inclinometers taken at different telescope positions could help constrain the model (see section 10.8).

The principle of this acquisition is much simpler as it only needs to use *drive system* to point and read data from the inclinometers. This procedure could even be performed just after sunset as it is insensitive to the light (but the sun needs to be below the horizon to avoid any dangerous reflection with the mirrors).

The scan is performed in two different axes, azimuthal with a zenith angle of 45° and zenithal with an azimuth axis of 0°. For each axis, the telescope will be moved from one extremity to the other. The movement is stopped at regular intervals to acquire inclinometer data at this position. Each stop has a duration of two minutes, and the inclinometers are read every second to catch the oscillation of the structure. Each scan is performed with a rotation of the drive in each direction to search for the hysteresis of the system.

10.4.3 Technical implementation

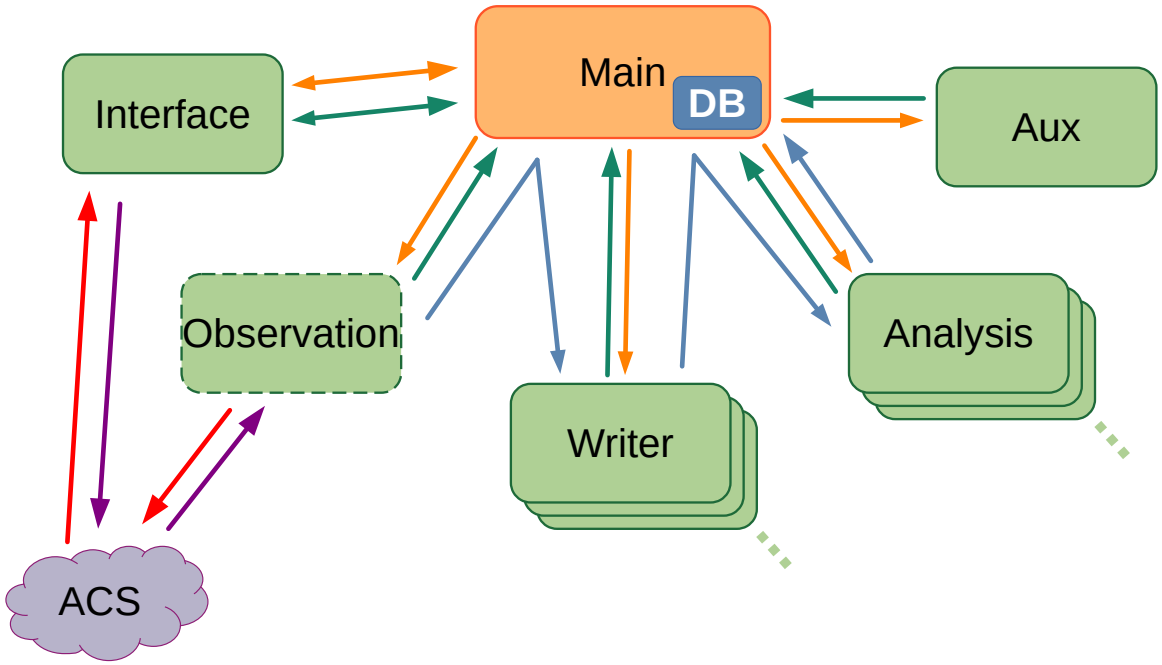

Figure 10.10: Diagram of the process running in the *bending model* program. The orange box represents the main process that orchestrates everything and possesses the database. The green boxes are the processes depending on the main one. The red arrows are the instructions communicated through ACS and the purple ones are the information feedback through ACS. The orange arrows are the flux of the instruction circulating inside the program, the green arrows are the information feedback and the blue arrow is the path of the data in the program.

The *bending model* software is written in python and heavily used libraries like astropy, pandas, numpy, scipy and matplotlib. For the interactions and control of the telescope component, the CTA collaboration has decided to use the `ALMA Common Software (ACS)` framework (Chiozzi et al., 2002). ACS is used in the *bending model* program for all communication purposes.

The *bending model* used an architecture with multiple processes (Fig. 10.10). Some parts of the program have a heavy computing load sustained for several minutes and need to be separated in order to avoid blocking another part of the program.

- The first process called main is always running. It's in charge of the orchestration of the the whole program, transmitting data between the different parts and handling the database. It manages the potential crash of the other processes and will restart them.

- One process is handling the interface of the *bending model*. This is the way to control the execution and action of the *bending model*.

- One process is handling the automatic observation procedures. This process only exists during observations and launches at each new procedure. There are two versions of this process depending on the actual acquisition (stars or inclinometer scan).

- There are several writing processes. The purpose of this process is to read the raw data of the CDM then compress and write them in the data format defined for the *bending model*. This step could take from a few minutes up to a few tens of minutes depending on the amount of data and the compression level chosen. Each process could handle one observation at a given time. The writing load of the multiple observations is automatically distributed between the processes and the number of working processes could be easily defined in the configuration file.

- Several analysis processes are also running. The purpose of this process is to analyse the data acquired. It typically takes a few tens of minutes per observation. Each process could handle one observation at a given time. There is an automatic repartition of the charge between the process and their number is defined in the configuration file.

- Finally, the last process is handling auxiliary tasks. All these tasks are short but compute-intensive tasks. For example, it handles the generations of the webpages for the control of the results of the *bending model*.

10.4.4 Scheduler and time efficiency of the acquisition procedure

The time allocated for *bending model*l acquisition will be limited. Following CTA guidelines, a total of 9 h per moon cycle will be dedicated to the *bending model* with 3 h with a faint moon and 6 h with a bright moon. It is then important to optimise the time spent on data acquisition. Various optimisations have been performed during the development. However, another important part is to optimise drive movement. As it takes a few minutes to make a complete turn at normal speed, we want to minimise them as much as possible.

This task is performed by the scheduler. As planning exactly the exact time spent for each acquisition could be very hard, the scheduler is fully dynamic. Each time the scheduler is called, it will determine the best star to observe at the given time.

To guide its selection, the scheduler relies on a grid of the sky. The objective is to have data as recent as possible for each point of the grid, ensuring that the model will be based on a recent full-sky view. This grid is defined with regular intervals on the azimuth axis and cosinus zenith axis (see Figure 10.11). On the row of the grid at the lowest zenith angle, the number of azimuth points is divided by two. The density of grid points at low zenith angles without this correction would have made it hard to find a star. For each grid point, the sky region associated with this point is the circle centre on the point, and as radius, the half distance to the closest grid point.

In the first step, the scheduler will divide the grid into four categories as a function of the age of the last measurement associated with this grid point :

- The ultra-low priority corresponding to the last acquisitions (less than two days)

- The low-priority category with acquisitions between two days and two week

- The intermediate priority category (between two to four weeks)

- The high-priority category with old data (more than four weeks)

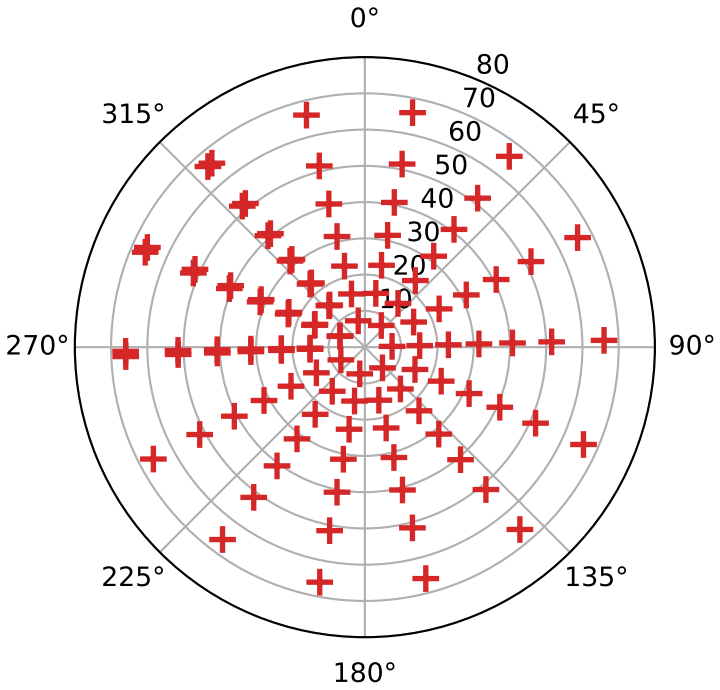

Figure 10.11: Grid of the bending model covering the sky.

The scheduler takes each category by order of priority. For each grid point in the category of interest, it will search for a star using the catalogue. The region of interest used 0.5 deg is smaller than the grid region to avoid a star at the edge that could fall outside of the region during the acquisition. The position of the star is evaluated considering the approximate time needed by the *drive system* to reach the position and the typical time for setting everything before the start of the acquisition.

For each couple (Star and grid point), the scheduler will compute the observation time needed as a function of the star's magnitude. The information about the drive speed, acceleration and deceleration are gathered and used to compute the time needed to reach the star position. Both times, which are the only values dependent on the grid point itself, are then added. The obtained value is used to determine which star to observe with the aim to minimise the total time spent on acquisition.

If there are no stars available for the observation related to the current category, the next lower-priority category will be used.

10.5 Data analysis

The analysis of the data is subdivided into several steps. It starts with the input of the raw data and finishes with the correction to apply.

10.5.1 Data format

The raw data format output by the CDM is a series of files in a FITS format, one for each image. The image is a raw output of the sensors scaled to 16 bits (10 bits reading from the sensor). Each FITS file has several metadata, like the position of the telescope. The size of each file is 35 MB. As several hundreds of images could be taken for one measure, the total size of the data could reach up

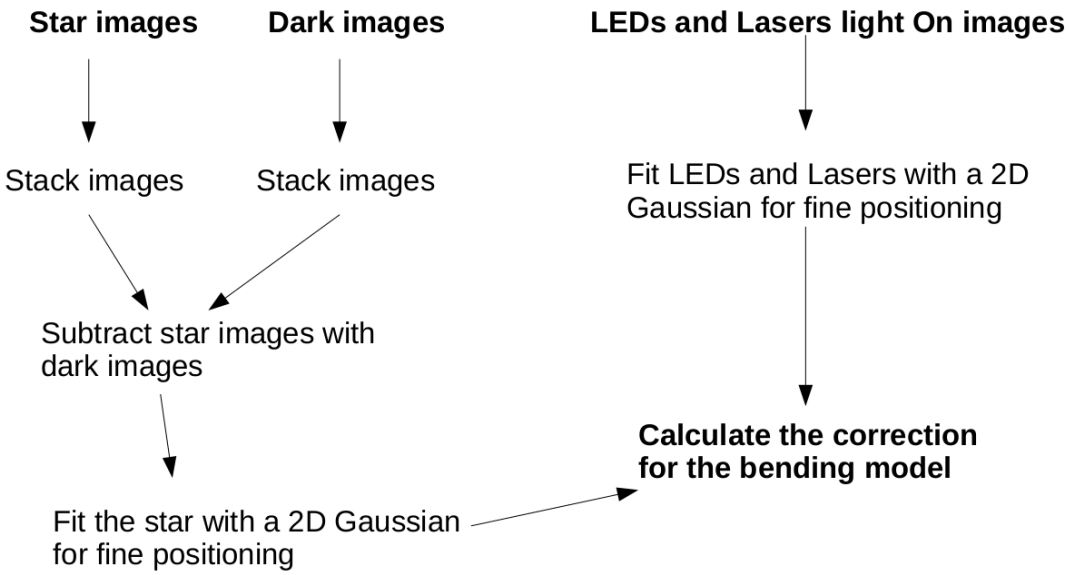

Figure 10.12: Diagram of the different steps of the analysis of the *bending model* data.

to 30 GB, making then impossible to load in RAM at the same time and increase the reading time. Such an output format is not convenient for the *bending model*.

To solve all these issues, the data are written in a new format specific to the *bending model* program, using the library `pytables`, which comes on top of the HDF5 file format. HDF5[2] is a hierarchical file format capable of handling large datasets. One of the benefits of this format is the ability to read only a part of the file without the need to load the full file in RAM. Due to its capabilities, performances and portability, its usage is widespread in HPC[3] applications. The format also supports native compression, which helps to reduce disk footprint and increases read speed.

All the images taken for one grid point are merged into one big HDF5 table, which has one line per image, with the first columns being a 2D table and then one column for each metadata in the original FITS file. There will also be some metadata at the top level of the file to give information about the general condition of observation like the star observed, the weather parameters, etc...

For the compression, the different algorithms available in pytables have been tested and compared (Fig. 10.13). Each algorithm could be set to a different compression level scale between 1 and 9. Both the write speed, read speed and compression factor have been considered for the choice. The final choice is the algorithm `Zstandard` with a compression level of 6 for its very good compression factor and fast read speed while maintaining decent writing speed.

10.5.2 Data filtering

During the first acquisition, one issue spotted in the data quality was the appearance of short intervals of light illumination by cars or other light sources. Depending on the nature, it could either illuminate the whole camera or create a new spot on the image. This could affect the analysis results and decrease the sensitivity of the system.

To determine which images are affected by this light pollution, two factors are used, the average luminosity value of all the pixels and the standard deviation of the luminosity of all the pixels. The first value will help identify the global illumination of the camera frame, and the second will identify smaller size light spots.

[2] https://www.hdfgroup.org/solutions/hdf5/
[3] High Performance Computing

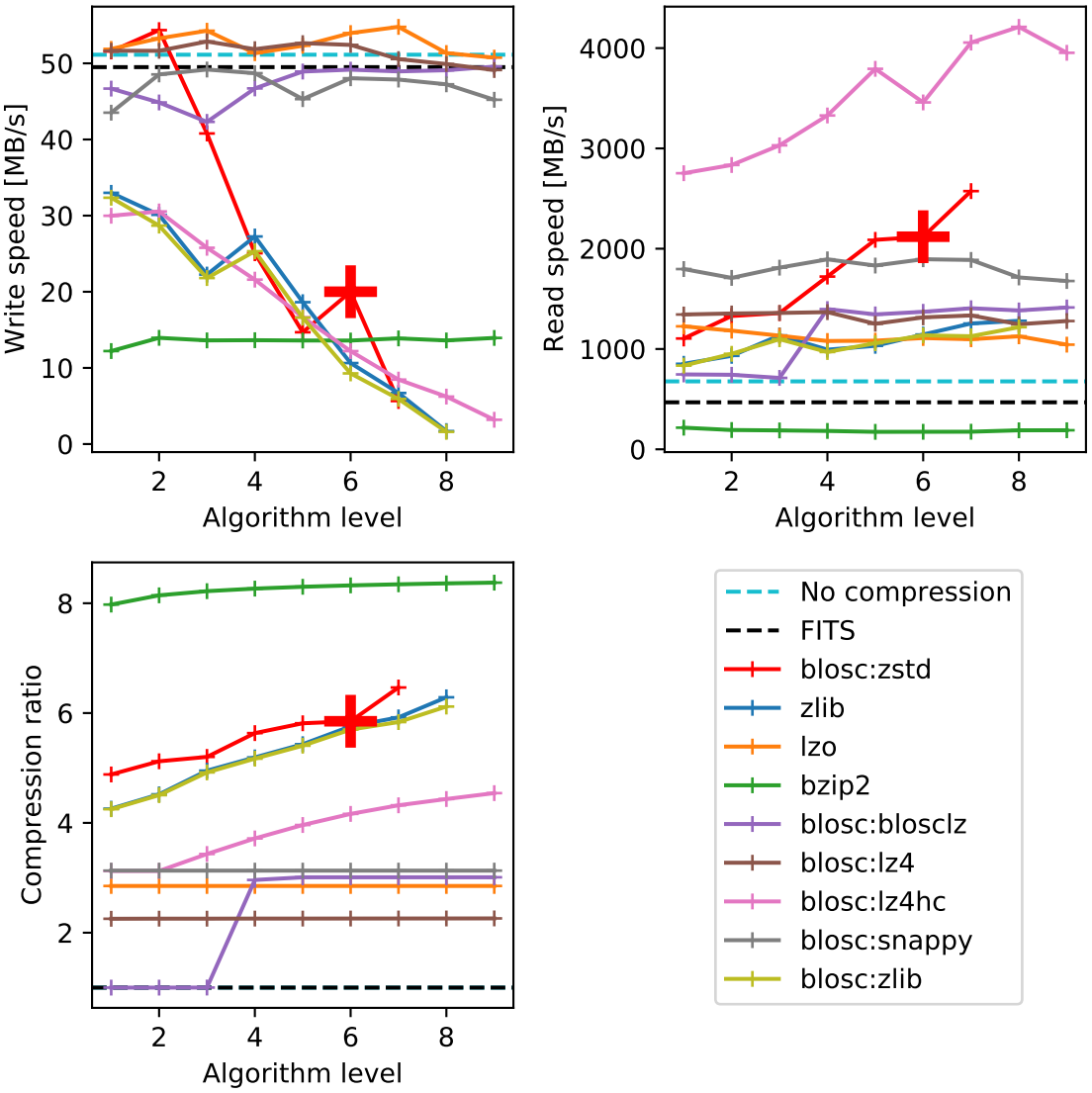

Figure 10.13: Performance of the different compression algorithms tested on *bending model* data and compared to no compression and FITs format. Write speed (top left), Read speed (top right) and Compression ratio (bottom left. The red cross corresponds to the chosen configuration. (blosc:zstd level 6)

To determine which images should be removed, an algorithm that will call double sigma-clip has been used. A standard sigma-clip algorithm is used to remove values outside of the central distribution. In our double sigma-clips, an iterative algorithm, the average value and standard deviation are computed, and then all the data outside of a given interval in number of standard deviations are flagged as invalid.

For the *bending model*, the two sets of values extracted from the images (mean and standard deviation) will be filtered at the same time. At each loop cycle, the algorithm is first applied separately on both datasets to then keep only the images that are the union of the two datasets. In this way, it helps remove bias on one of the sets of values that will be caused by an effect seen on the other. For example, if a car illuminates the full camera frame, the average luminosity will go very high, and the standard deviation will increase but by a much smaller fraction. Coupling the

sigma clips algorithm help improve sensitivity and reduce false positive.

This algorithm runs iteratively up to the convergence point, where the final selection is always the same between the two steps of the loop. Note that the selection performed at each loop cycle is made on all of the original data to avoid removing images that would have been rejected due to extreme outliers.

The algorithm is run separately on the images with LEDs and OARLs on, and on images with LEDs and OARLs off.

10.5.3 Demosaicing and stacking

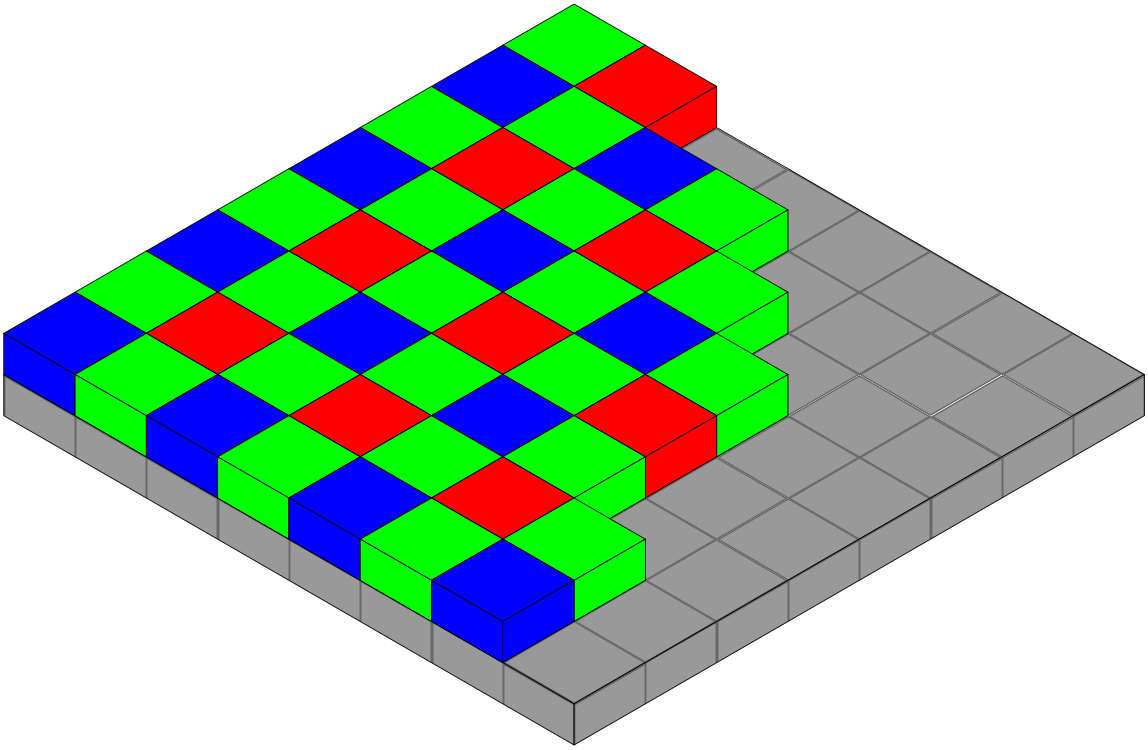

Figure 10.14: Representation of camera sensor with a Bayer filter on top. The individual pixels (grey square) are all covered by a given colour filter (colour square) that forms a repetitive pattern. This specific pattern is the Bayer one. [4]

The sensor of the CDM is a colour sensor with a colour filter put in front of each pixel. The pattern of the filters used in the CDM is the Bayer filter (Fig. 10.14), the most widely used filter pattern for colour cameras. The sensor is divided into a square group of four pixels. In each group, there are two green pixels and one red, one blue. The number of green pixels is double the other to reproduce the better sensitivity of the eye in this spectral range.

For the *bending model* program, the colour information is not needed, so we transform these raw images into greyscale images during the demosaicing process. Images taken of the star and the dark patch are firstly stacked separately. Then the stacked dark image is subtracted from the stacked star image. A correction factor is applied to the dark image to take into account the potential difference in exposure. The stacking and dark subtraction steps allow for signal integration, improving the signal-to-noise ratio and removing hot pixels.

The images taken with OARLs and LEDs are treated individually and only demosaiced as the resulting images from the stacking process. The algorithm used is the simplest one. Each group of

[4] Credit : Colin M.L. Burnett, https://commons.wikimedia.org/wiki/File:Bayer_pattern_on_sensor.svg

four pixels of the pattern will become only one pixel on the demosaiced images. The final value of this large pixel is the sum of the value measured in all the pixels with a factor of 0.5 for the green pixels to take into account that there are twice as many green pixels as other colours.

The main advantages of this demosaicing algorithm are its rapidity and simplicity. Moreover, it minimises the assumption and bias that other methods based on interpolation could bring. The main disadvantage is that the final pixels in the image are twice the size of the original one, lowering the resolution.

10.5.4 Identification of light source in the image

The next step is to identify light sources in the images. The procedure is almost the same for the bright LEDs and OARLs, and the faint star.

First, the background in the image is determined as well as the associated noise. For this, the intensity of each individual pixel is sent to a sigma clip algorithm to remove outliers caused either by the light source we are searching for or other perturbations. Then the value of the background is defined as the median of the remaining pixel and the noise level as the standard deviation. In the case of the analysis of star images, this step is performed only on the part of the image corresponding to the SIS rather than the full image.

The next task is to identify the regions of the image with deviation from this background. For this step, the `opencv` library, specialised in computer vision, is used. This task is subdivided into several steps. The first one is to identify which pixels are above a given threshold corresponding to the signal-to-noise ratio (SNR). The SNR value required for an individual pixel is 25 for the analysis of LEDs and OARLs images and 3 for the analysis of star images. Then the pixels above the threshold will be grouped if they are contiguous. A circle is adjusted on each group to have the smallest possible size but still encompass all the pixels of the group.

The final task is to remove all the hotspots that are very likely not related to what we are looking for. In the case of the star images, all the hotspots that are outside of a circle of $\sim 9'$ are removed. This circle is larger than the worst pointing deviation observed and is quite small. This is important as some reflections of very bright stars have been observed. The root cause of such reflection is still not clear.

All the hotspots that have a circle radius of fewer than 3 pixels and with inside less than 8 pixels above the threshold are removed. This helps to remove hotspots caused by background fluctuations as stars, LEDs, and OARLs present hotspot larger.

Another cleaning step is applied mainly for OARLs. All spots for which their centre is within a circle of another bigger spot are removed. The image of OARLs presents some scattering of the light, and a lot of small hotspots could be present close to the main one.

Most of the faint stars are barely above background noise, but this small deviation from the background could be seen on a scale of 10 pixels wide for the stars. By correlating each pixel with its neighbours, it should not affect too much the signal of the star but would significantly reduce the noise level and, by so, boost the SNR of the star.

To perform this action, the image is convoluted with a kernel. Two types of kernels have been tested (top hat and gaussian) with different sizes. The one that gave the best results was the gaussian one with a standard deviation of one pixel (Fig. 10.15). This has led to more than one order of magnitude of sensitivity improvement. Figure 10.16 shows the observation time needed for reaching a spot SNR of 10 in function of the magnitude of the star observed. The improvement brought by this method is clearly visible. This modified image is only used for hotspot search, and all the other steps of the analysis are performed on the non-blurred image.

Finally, the last cleaning step is to remove all the spots for which the total intensity within the circle is below a given SNR of 30 for the OARLs and LEDs, and 4 for the stars.

At the end of this procedure, a collection of hotspots with their approximate position and size that would need to be identified is returned. Therefore, it is possible to identify and link the hotspots to LEDs, OARLS or star-candidate.

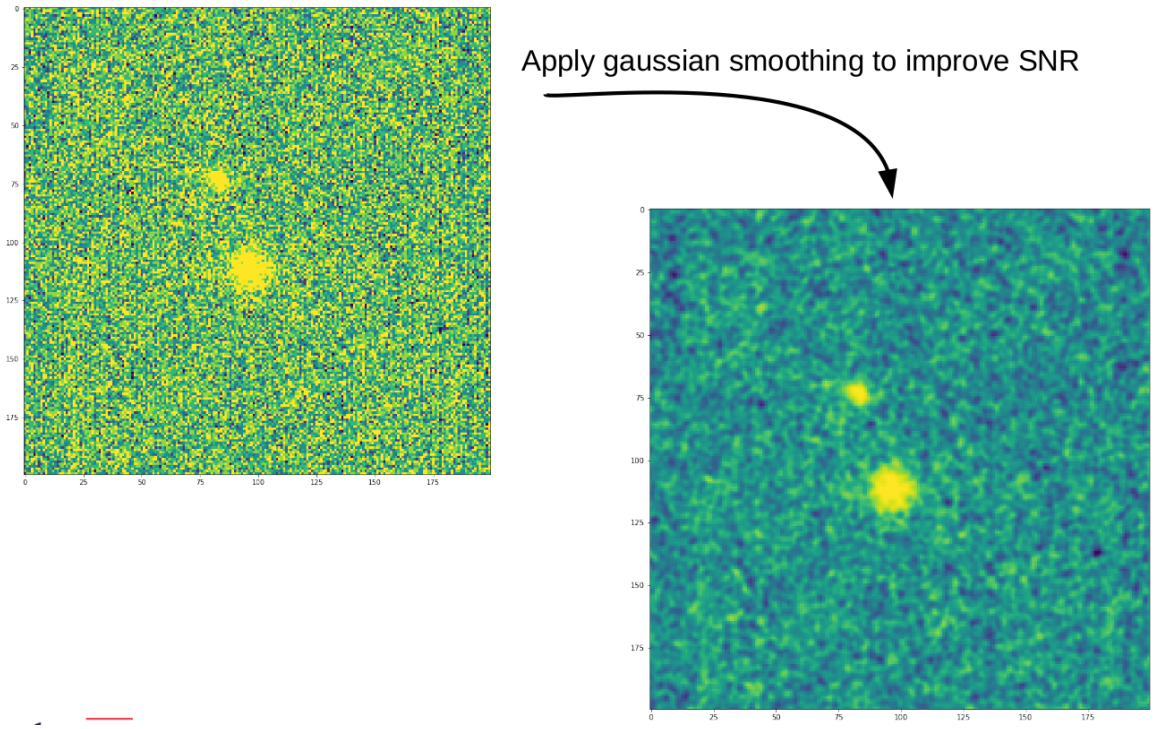

Figure 10.15: The left panel show the image of a star in the data after stacking. The right panel is the image of the same star after the application of the spatial convolution.

10.5.5 Position of the LEDs and OARLs

10.5.5.1 OARLs identification

The OARLs identification is mainly based on their typical position in the image. The algorithm searches for the brightest spot in a forty-pixel range compared to the base position. Fig. 10.17 shows an image with the OARL and LEDs as seen by the CDM. The identification of which one is the first (OARL 0) and which the second (OARL 1) is also based on their position.

10.5.5.2 LEDs identification

The LEDs identification is also performed based on their *usual* position but with a different algorithm since their positions are susceptible to change much more due to the bending of the arch which holds the camera.

The first step is to identify the hotspots that are in a ring centred on the approximate location of the camera and as radius the approximate radius of the camera. To take into account the uncertainties, all the hotspots that are within 10% of the radius are kept. Then a second pass is performed, but this time the ring for the search is the output of the fit of a circle on the kept hotspot. The margin is also lower by 5% of deviation.

Identification of each individual LED can then be performed. In the *bending model* program, the LEDs are enumerated in their order on a trigonometric circle using their angle position. The search allows for a deviation of the position of a maximum of 10°. The LEDs which are not placed in the circle are not used for the analysis, and they are just not considered and identified in the analysis. The results of the LEDs identification step are shown in figure 10.17. At this point, the centre of the Cherenkov camera has not yet been determined.

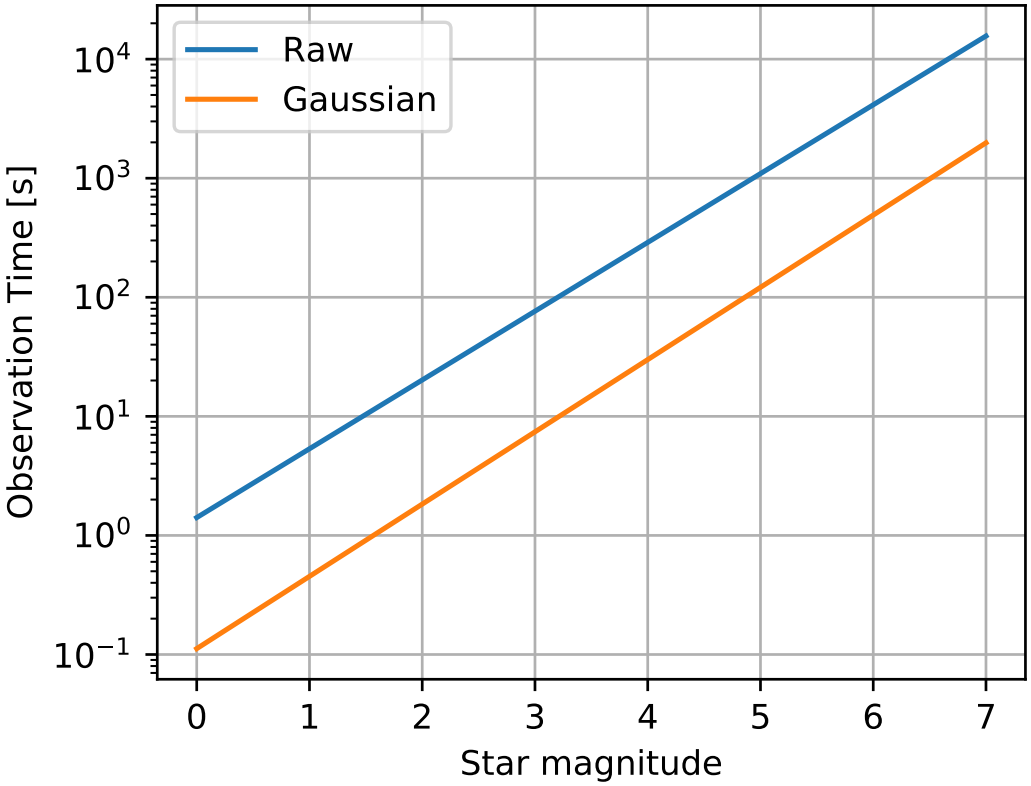

Figure 10.16: Observation is needed to reach an SNR of 10 for an analysis of the raw data vs an analysis of the data with application of the spatial correlation.

10.5.5.3 Determination of the centre of the Cherenkov camera

The previous step allowed for the identification of hotspots and the identification of the OARLs and LEDs, but their localisation is still the approximation issued from the hotspot extraction step. Each individual hotspot will be fitted with a 2D Gaussian using a small piece of the images extracted from the main image. This smaller image is centred on the approximate position obtained previously. This allows running the fit on a fairly simple zone with a more or less constant background. Running the fit on the full image would require a proper modelisation of the elements, including the camera frame and will also be very compute-intensive. The modelisation of and the fit is run with `astropy`, which uses `scipy` fitting procedure in the backend. An example of the fit for the OARLs is shown in figure 10.18 and for the LEDs in figure 10.19.

The centre of the Cherenkov camera is determined with a fit of the circle on the obtained position of the LEDs performed in two steps. The first one is a fit with the `least_square` minimisation of `scipy` to initialise the second fitting step. The second fitting step uses the `iminuit` python package, which is a wrapper around the Minuit minimiser (James and Roos, 1975). The second fit takes into account the uncertainty on the LEDs position and uses Minos to determine the uncertainty on the fitted circle parameters. The reason for this two-step fitting is to combine the advantage of both fitting procedures: Rapidity of `scipy` and robust results of Minuit once well initialised.

Finally, as each image with LEDs and OARLs is analysed separately, the results are combined to determine the average position and uncertainties associated.

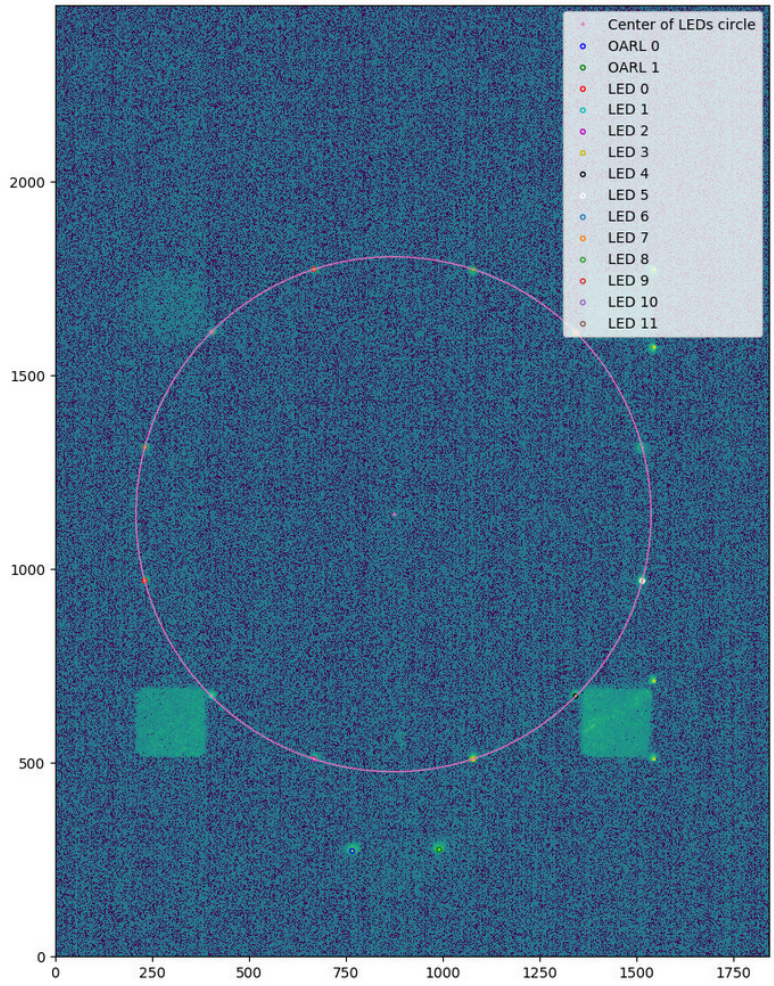

Figure 10.17: An image of the light on and the identification of the LEDs and OARLs by the analysis of the *bending model*. The circle is the fitted circle on the LEDs.

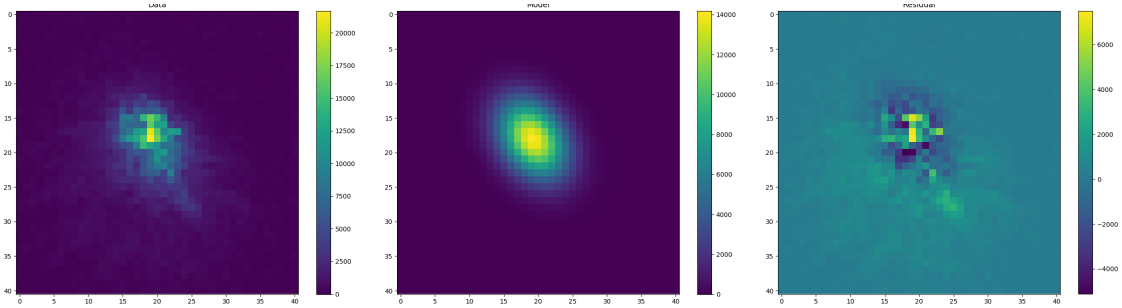

Figure 10.18: Results from the fit of the image of one OARL. The left panel is the data, the middle one is the fitted model and on the right one is the residual.

10.5.6 Position of the star

From the LED circle, the position of the centre of the camera can be obtained. The identification step is relatively simple. If there is more than one spot in the small search region, it is likely caused by a reflection or another star which will make the determination of the "real" star very complex.

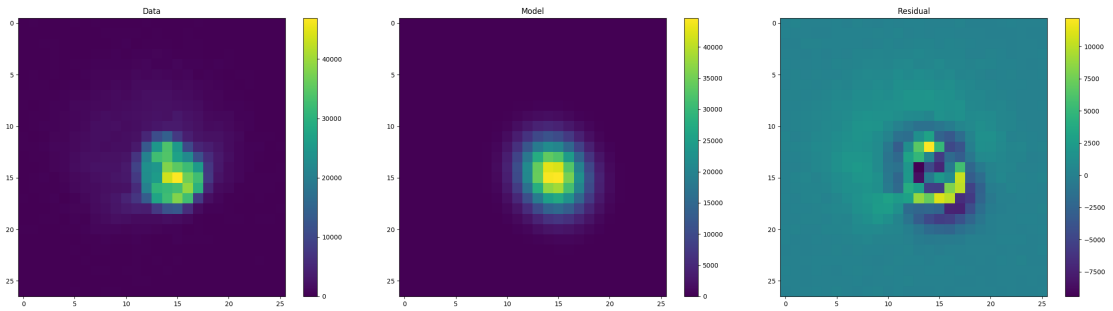

Figure 10.19: Results from the fit of the image of one LED. The left panel is the data, the middle one is the fitted model and on the right one is the residual.

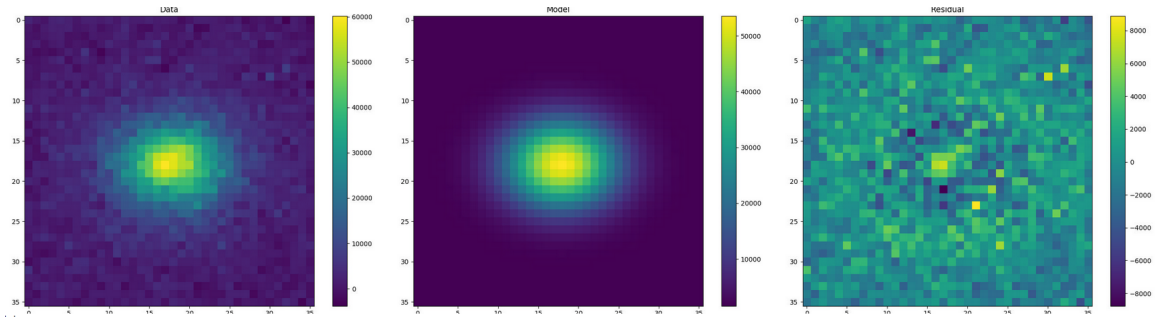

Figure 10.20: Results from the fit of the image of one star. The left panel is the data, the middle one is the fitted model and the right one is the residue.

In this case, an error is raised, and the analysis will not go up to the end. If there is only one spot, it is identified as the star.

Here again, the position of the star is obtained with a fit on a cut part of the image centred on the hotspot position. The main difference is that this time the fit comports multiple steps. The first one is identical with a fit using only a 2D gaussian model. The second step is adding a constant to the fit to model the background. Due to the small signal-to-background ratio of the stars, it is important in this case to take into account the background. Finally, sometimes the star shape is elongated on one axis due to sub-optimal mirror alignment or small drive movements.

Due to the small SNR of the stars, the fit has proven to have an issue to properly converging if the orientation of the elongated shape was not close to the real solution. To avoid this, the fit is rerun 8 times with initialisation of the orientation of the elongated shape rotated of 22.5° each time, allowing it to cover all the orientation. The fit results with the lowest residual is the one kept as the final results. An example can be found in figure 10.20.

10.5.7 Computation of the telescope misspointing

At this stage, the position of the LEDs and OARLs and the precise position of the stars are known. The last part is to map this to sky positions to determine the misspointing (correction) to apply and the associated uncertainty.

This part heavily uses the `astropy` wrapper on the World Coordinate System (WCS) library (Greisen and Calabretta, 2002). This library allows us to compute the transformation from the camera referential to the sky referential by taking into account deformation due to the projection.

The Cherenkov camera defines a plan tangential to the spherical sky on which the sky is projected. Then, for an angle θ, the projected distance on this tangential plan will be different from one point to another. In figure 10.22, a sketch is provided. We assume no projection or distortion from the CDM.

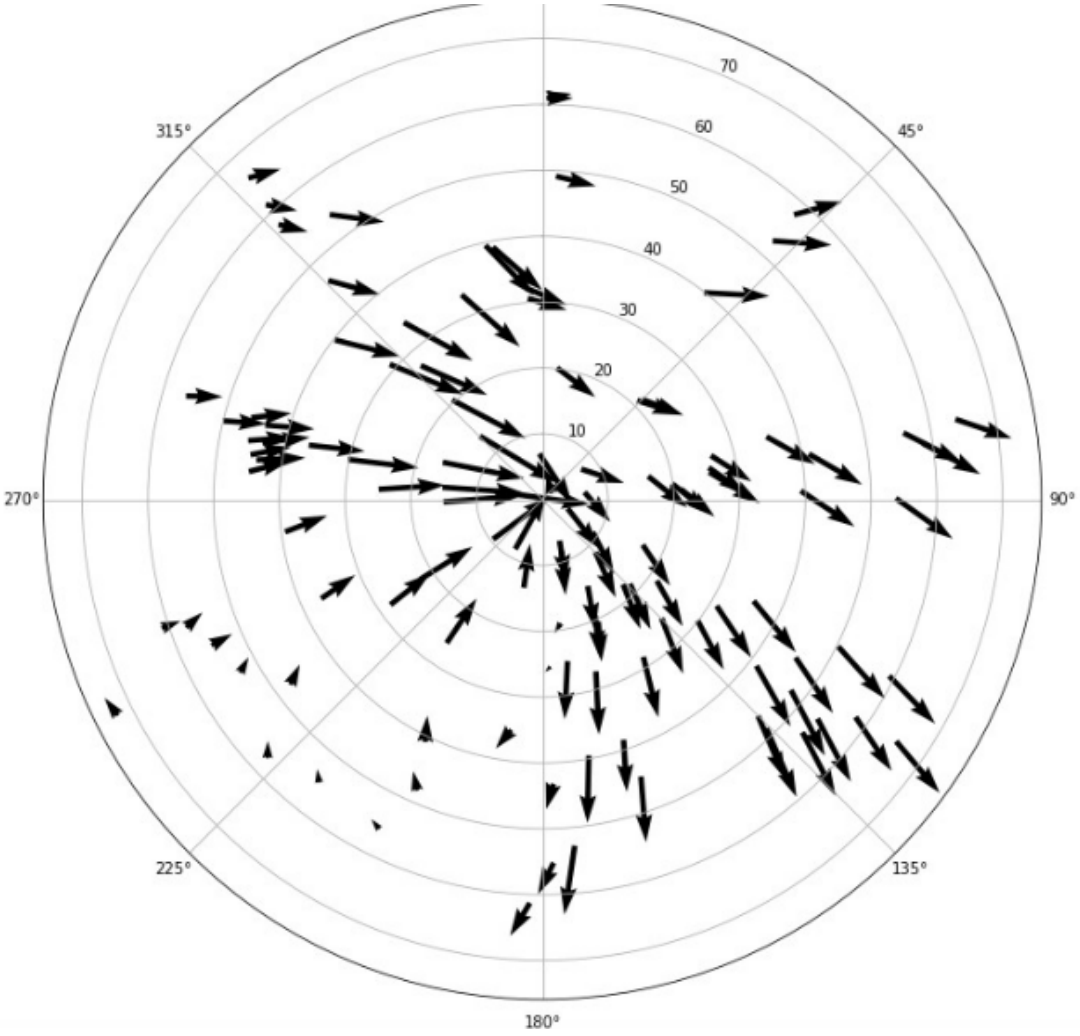

Figure 10.21: Representation of the measured misspointing to apply across the sky.

For setting the function that will perform the transformation `astropy`, expect some information :

- the Center of the Cherenkov Camera is taken as the centre of the projection, in this case, it will be the center of the LEDs circle
- The position of the centre of the projection in the sky frame, in this case the telescope pointing in the AltAzimuthal frame. The information used is the drive pointing without pointing correction as the impact of the small pointing deviation on this computation will have a negligible impact
- The equivalent size of CDM pixel at the centre of the projection α which can be determined using the LED circle and the focal length of the telescope.

Then using the WCS library, we can compute the position of the star in the sky (with the assumption that the projection error due to the misspointing is negligible). The measured misspointing is the difference between this position and the pointing position of the *drive system*. The errors on the star position, centre of the camera, etc ... are propagated using a Monte Carlo sampling assuming a gaussian distribution of each parameter.

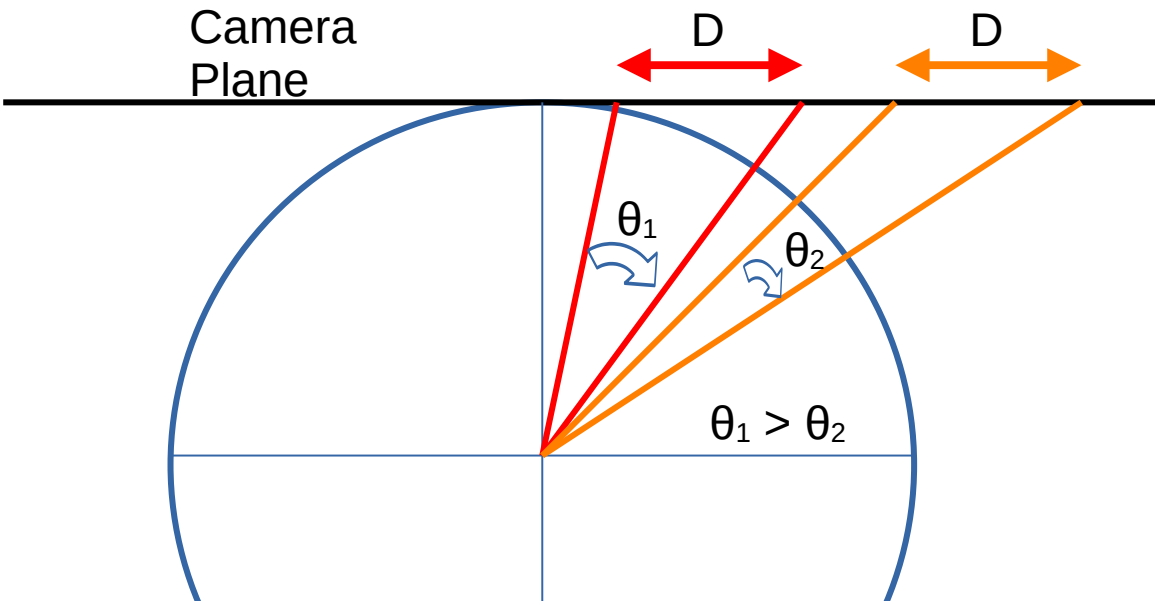

Figure 10.22: Tangential projection of the sky on the camera plane. The two identical distances D placed at a different position compared to the centre of the projection lead to two different angular distances on the sky θ_1 and θ_2.

At the end of this stage, we have the main results we are looking for, measurement across the sky of the LST misspointing. Figure 10.21 shows such measurements for the acquisition campaign of April-May 2022.

10.5.8 Computation of the parameters for calibration of the exposure time

Thanks to the high number of images on each star, it is easy to measure the evolution of the SNR as a function of the time and optimise the number of images taken and hence the time spent. The star position and size issued from the analysis are used to know in which region to measure the signal from the star. The background and noise are estimated the same way as for the detection of the star hotspot. The convolution kernel is also applied to the image.

The SNR as a function of the exposure time (Fig. 10.23) can be well fitted, for all observations, with a simple square root in function, SNR $= a\sqrt{t}$ where a is the scaling factor.

With all the observations at our disposal, the behaviour of the scaling factor a as a function of the star magnitude m can be determined. Making the hypothesis that the scaling factor is proportional to the luminosity $I = I_{ref}10^{-\frac{m}{2.5}}$, we have $a(m) \propto 10^{-\frac{m}{2.5}} \quad s^{-\frac{1}{2}}$. Figure 10.24 shows the value of a as a function of m for different observations taken during dark time and the corresponding fit $a(m)$.

Putting all together, we have an estimation of the needed exposure time T_{obs} to reach a predefined SNR which is used to optimise the data taking:

$$T_{obs} = \left(\frac{\text{SNR}}{a(m)}\right)^2$$

.

10.6 Analysis of the inclinometers scan

The data taken from the inclinometers have been added at a late stage of the development but are helpful to constrain the deformation model (called the mechanical model after) of the telescope.

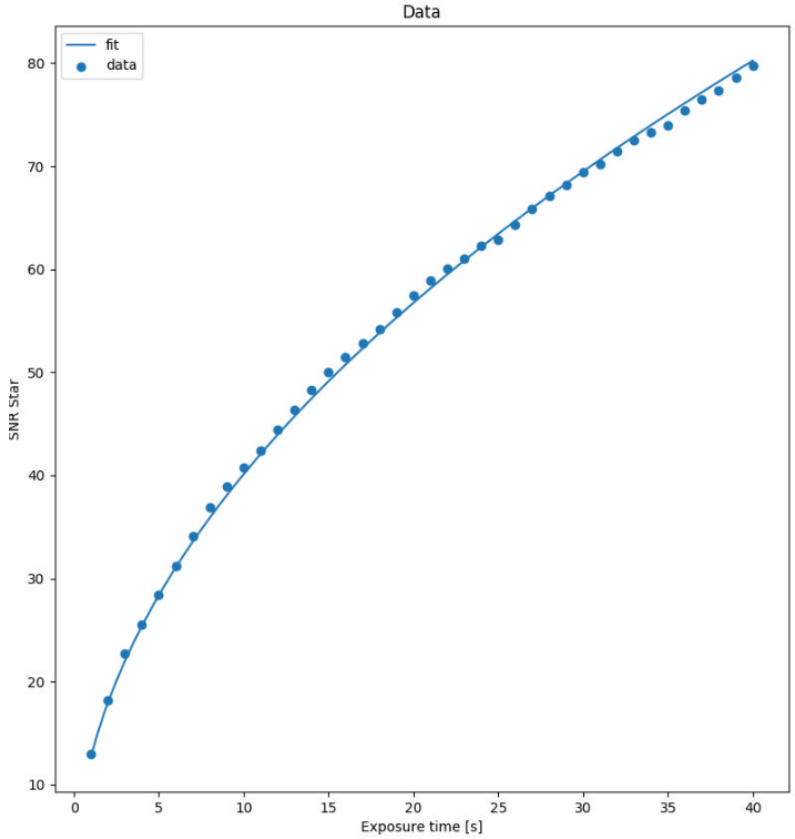

Figure 10.23: Evolution of the SNR as a function of the integration time.

The objective is to extract the baseline from the inclinometers, but oscillations could be seen following the stop of the drive at a given position. A way to avoid these oscillations would be to wait for them to stop, but this would severely increase the time needed to make a scan. The idea is then to model these oscillations to be able to extract the baseline with a fit. There are two inclinometers, one measuring the inclination of the optical axis[5] and one of the elevation axis. The models for the two axes are different as the effect seen on the two axes is different.

For the optical axis, a constant represents the baseline, and on top of this constant is added an exponential for the stabilisation of the system (Fig. 10.25). The elevation axis is a bit more complex. Two sinus functions representing harmonic oscillations are added to the constant baseline. The first one is modelling an attenuated harmonic oscillator (sinus function multiplied by an exponential) and the second one is a standard harmonic oscillator (simple sinus function). The description of the oscillation is not perfect with this model, but the symmetric residual indicates that the baseline should be well constrained (Fig. 10.26). On both axes, these methods allow having fairly small uncertainty on the value of the baseline.

When this method is applied to every position of the scan, we can see the variation of the measure of the inclinometers in function of the position (Fig. 10.27).

10.7 Optimisation of the *bending model*

During the development of the *bending model*, some attention has been put on the optimisation both of the acquisition procedure but also of the analysis. The optimisation of the acquisition procedure

[5]The optical axis is the axis on which is performed the rotation to allow movement on elevation. In a perfect system, it is parallel to the ground.

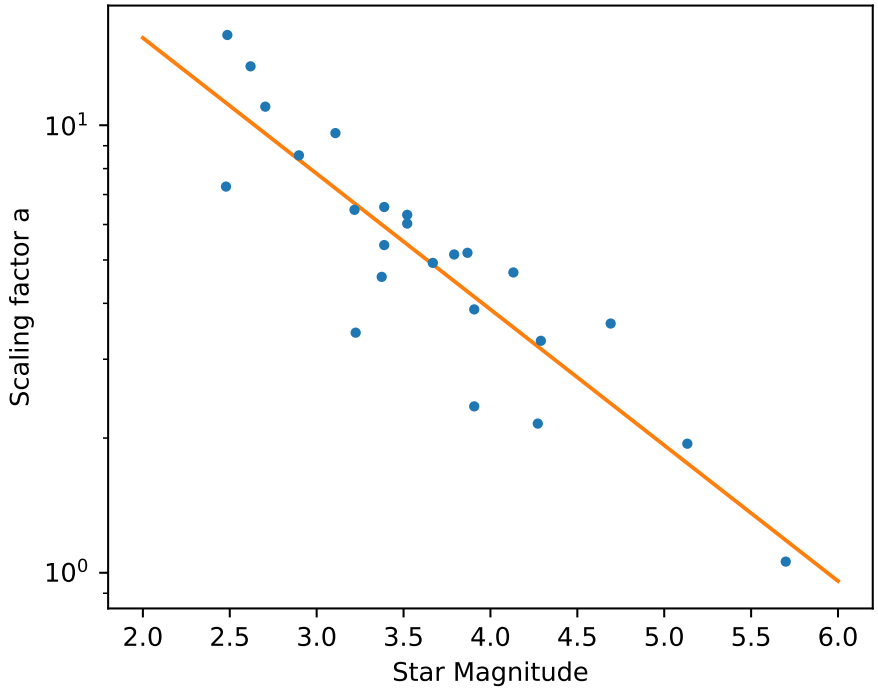

Figure 10.24: Fit of the function (orange curve) to describe the evolution of the scaling factor for computing the SNR in function of the magnitude of the star (blue point).

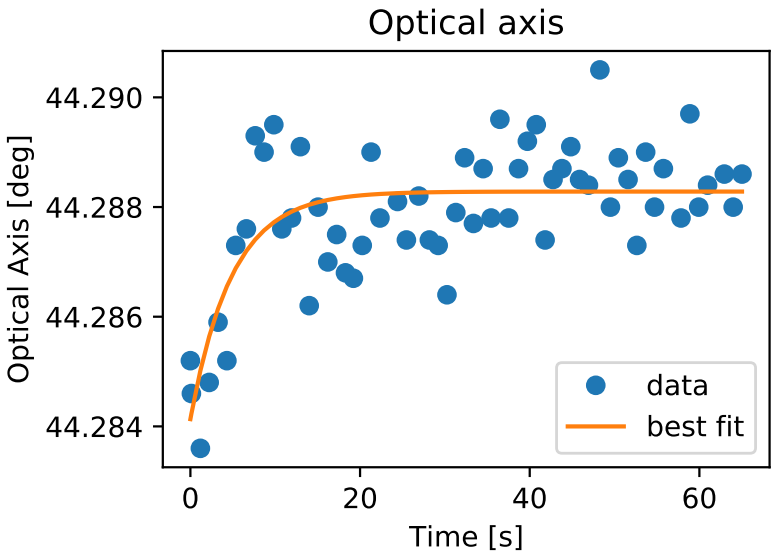

Figure 10.25: Inclinometer data for the optical axis with the fit of the model.

is important to be able to cover the full sky grid during the 9 h dedicated to the *bending model* of each moon cycle. The optimisation of the analysis was important to not have a very high compute requirement to run the *bending model* as the program runs on a machine which is not dedicated to it.

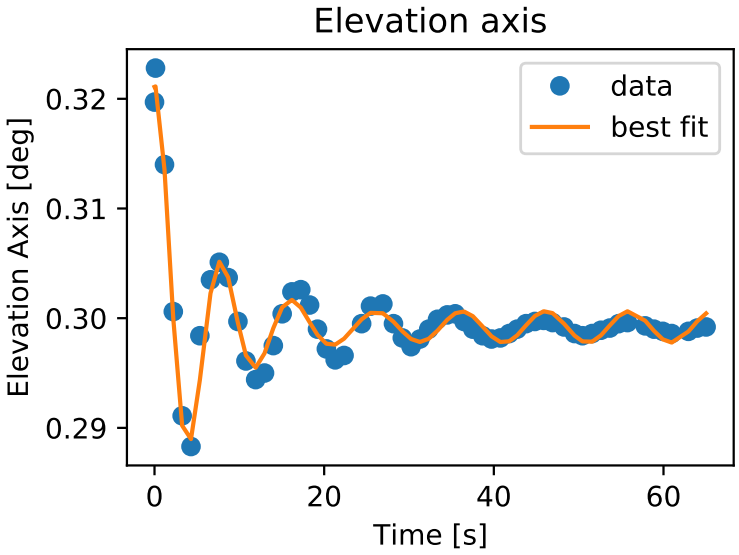

Figure 10.26: Inclinometer data for the elevation axis with the fit of the model.

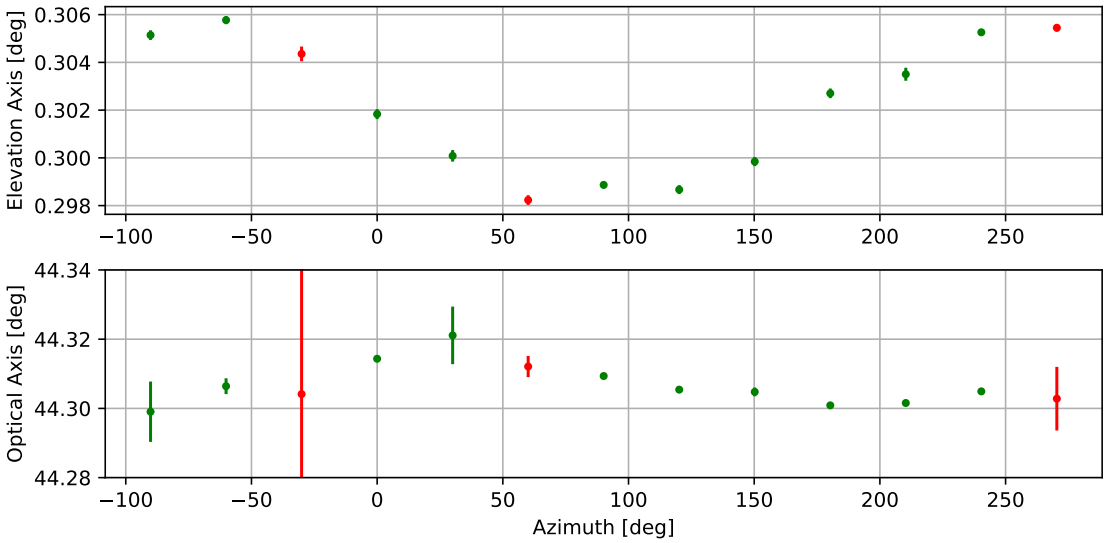

Figure 10.27: Results from an azimuth inclinometer scan.

10.7.1 Optimization of the acquisition procedure

The optimisation of the acquisition procedure is the most important, as all the time spent on *bending model* acquisition is not spent on the acquisition of scientific data. The sky grid of the *bending model* has 110 points. To allow full coverage of it in 9 h a bit less than 5 min should be spent on each point, and this without taking into account the time needed for preparing the telescope at each start of series of observation.

In order to minimise the acquisition time for each point several actions have been taken :

- Work on the analysis to increase sensitivity. An increased sensitivity allows for shorter integration time. The required integration for a given magnitude has been reduced by one order of magnitude.

- Optimisation of the gain of the CDM. Data with different gain settings has been acquired to have the best sensitivity reducing the integration time by a factor three on top of the analysis improvement.
- Optimisation of the telescope movement and integration with the final version of the scheduler
- Optimisation of the compute time for searching a star in the catalogue, needed for being able to run the scheduler quickly
- Improvement of the startup procedure following improvement on subsystem (like the possibility of moving the SIS with the telescope in any position)

All this work allows for a significant reduction of the acquisition time going down from an average duration of 484 s to 345 s (30% reduction). It also removes all the outliers of the very long acquisition that could go above 800 s.

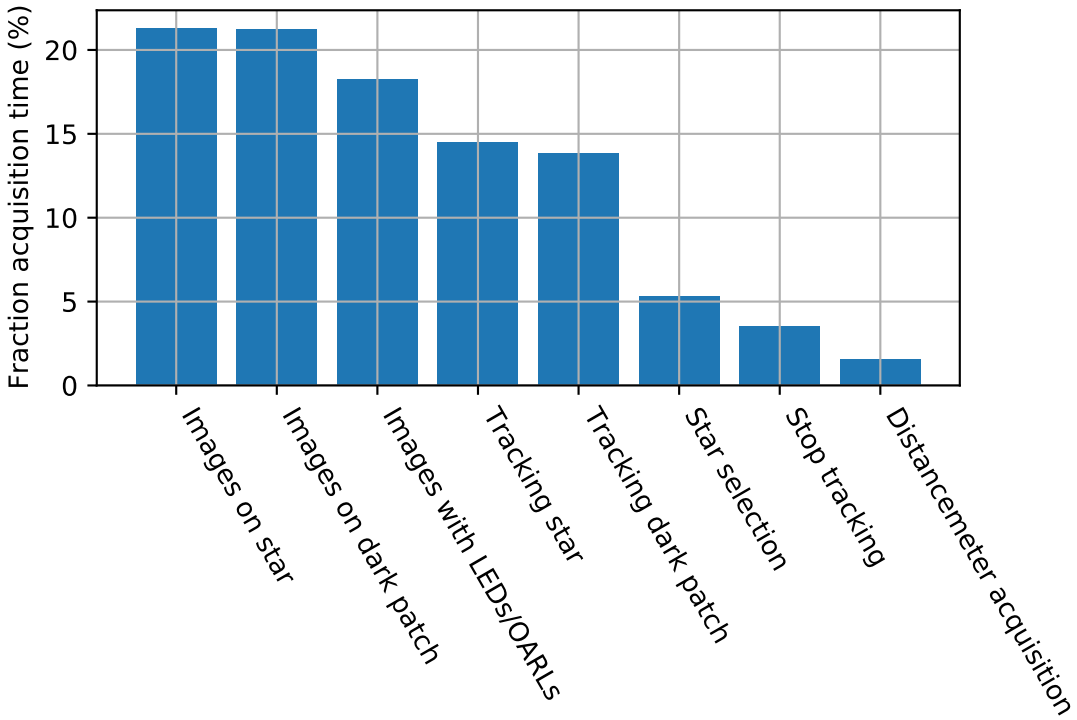

Figure 10.28: Percentage of the acquisition time dedicated to each type of action

However, the acquisition time only allows acquiring ~ 94 grid points in 9 h. To acquire an entire grid within the time requirement of CTA, a 15% improvement in time is still needed. The acquisition time is actually shared among several steps without any dominating (Fig. 10.28).

The acquisition of images on the star and dark represents half of the acquisition time in total. Reducing the acquisition time needed for stars would be complicated as most observations hit the 60 s lower limit. The reason for this limit is linked to the drive. Some oscillations around the position with a period of $\sim$15 s are present, especially in the early time of tracking. After a movement, there is already a waiting time for the drive to stabilise in order to avoid most of these oscillations. However, at the time of the acquisition of the star, it could still represent a few arcseconds. The minimal integration time of the *bending model* allows averaging these oscillations, so a shorter integration would require a longer waiting time before starting acquisition.

A way to reduce the acquisition time would be to reduce the amount of dark for the brighter star. Some checks would be needed to verify that it will not impact the analysis to have a significant

difference in exposure time between the two datasets (star and dark). Nevertheless, the gain would be limited as it will only concern the brightest star and, in consequence, would not provide the required 15% time reduction.

Another issue that slows down the *bending model* is the delay in getting information on a system through ACS. The theoretical latency should be around 1 s as it corresponds to the frequency of update of the value in ACS, but in practice, waiting of a few seconds is often observed. As the *bending model* acquisition procedure is sequential, all this waiting time adds up and could have a significant impact on the acquisition time. As no improvement is foreseen in the near future, a way to minimise the impact would be to make the code of the acquisition procedure asynchronous in order to run in parallel all actions that could be run in parallel. This would imply completely rewriting all the code dedicated to acquisition. The gain will be moderate but would likely help to reach the requirement.

Finally, another solution that could be explored is the impact of having missing points in the grid on the fitted model. To match the CTA requirement, a combination of all these solutions will likely be needed.

10.7.2 Optimisation of the analysis

The optimisation of the analysis was important to allow the *bending model* to run on a shared server.

One of the most important optimisations was the data format described above. The initial version of the analysis was reading directly multiple FITS files multiple times. For each observation of a single star, the time needed to reach the step of the stacked images ready to be analysed was typically around 30 minutes (depending on the exact amount of data). With the actual version, this step typically takes 2 to 3 minutes. Most of the gain is caused by the change of data format, but also, some rearrangements of the filtering procedure were done to allow the need to read the data only two times to reach the state of stacked images instead of three times.

Another part of the optimisation was to improve the speed for filtering away the false spots detected in the images. This step was always fast for images with LEDs and OARLs due to the small number of spots, but on the first version of the *bending model*, it was very slow for the star. To improve the sensitivity of the analysis, the threshold to make a spot is very low, giving a lot of false spots. The order of the filters applied on the spots to remove the false one has been decided in order to run the slowest filters the latest so on the smaller amount of spots possible. Also, some change to the internal data representation and on the way to compute some filters has been made to allow for fast spot detection. The spot detection on the star was originally taking around 15 minutes, and the optimisation allowed it to run in approximately 10 seconds now.

Finally, the last step of the analysis optimised in order to gain significant time is the fitting of the spot for precise localisation. Most of the optimisation here consists of improving the accuracy of the initial guess of the fit and reducing as much as possible the size of the image fitted.

With all these optimisations, running the analysis takes now 20 to 30 minutes per observation of a single star instead of more than an hour initially, while the analysis has been pushed further with a more complex fitting procedure to allow for good uncertainty estimation of the final measure. The analysis time is low enough that with a few processes running analysis in parallel with different observations to analyse each, it is possible to follow the rhythm of acquisition of the observations. Further optimisation is likely possible but was not performed as the analysis speed is good enough for our needs.

10.8 Mechanical model

As a result of the analysis, we have the information of the misspointing on a hundred of given directions. However, the drive-system could follow a track anywhere in the sky, so we need a way to give the correction in any part of the observable sky.

The very first version of the *bending model* used spline fitting to make interpolation and extrapolation of the data. The part where data were interpolated gave acceptable results but with some

issues in specific directions where correction to apply was changing quickly. The part of the sky relying on extrapolation gave very bad results.

To improve the situation, a model was developed to explain the misspointing, and is fitted to the data. This model is then used to determine the misspointing in any position of the sky. The correction to apply is simply the inverse of this misspointing. This is a good approximation as the corrections are small compared to the scale at which the correction changes as a function of the sky position.

10.8.1 Component of the model

Beyond the drive tracking regulation performance, several effects can lead to telescope misspointing. Environmental conditions, such as the wind, could impact the pointing, but these could hardly be corrected online and will be corrected by offline systems.

The model presented here corrects systematic effects due to the structure deformation that could still slowly evolve across time due to the ageing of the telescope. This model is composed of several components that are presented below.

10.8.1.1 Systematic shift

Encoders placed on each rotational axis are used to measure the telescope orientation but may suffer from systematic error. The azimuth encoder has been calibrated using theodolite measurement of the telescope structure in park position with respect to outside landmarks. The elevation has been calibrated by pointing to the zenith and using an electronic level. Even if a precision well below the degree could be achieved using those methods, it is not sufficient for our needs. The remaining systematic errors on both axes are then making a shift that needs to be compensated.

Additionally, a part of the systematic shift could be caused by the mirror not focused at the centre of the camera but slightly away.

Systematic error on the azimuth position :

$$Az = Az_{encoder} + A_1$$

Systematic error on the elevation position :

$$Zd = Zd_{encoder} + A_2$$

10.8.1.2 Azimuth tilt

Defaults in the structure and ground assembly can contribute to a misspointing of the telescope. The first effect is a defect in the verticality of the azimuth axis and is assumed to come from a defect in the horizontality of the telescope foundation as a whole. Non-planarity of the rail surface beyond this overall tilt is not taken into account at this stage.

Non-verticality of the azimuth axis :

1. Spherical coordinates to cartesian ones

$$\begin{cases} X_1 = cos(Zd) * sin(Az) \\ Y_1 = sin(Zd) * sin(Az) \\ Z_1 = cos(Az) \end{cases}$$

2. Rotation of ϕ angle around Z axis (azimuth axis)

$$\begin{cases} X_2 = X_1 * cos(\phi) - Y_1 * sin(\phi) \\ Y_2 = Y_1 * sin(\phi) - Y_1 * cos(\phi) \\ Z_2 = Z_1 \end{cases}$$

3. Rotation of θ angle around Y-axis

$$\begin{cases} X_3 = Z_2 * sin(\theta) - X_2 * cos(\theta) \\ Y_3 = Y_2 \\ Z_3 = Z_2 * cos(\theta) - X_2 * sin(\theta) \end{cases}$$

4. Rotation of $-\phi$ angle around Z axis (azimuth axis)

$$\begin{cases} X_4 = X_3 * cos(-\phi) - Y_3 * sin(-\phi) \\ Y_4 = Y_3 * sin(-\phi) - Y_3 * cos(-\phi) \\ Z_4 = Z_3 \end{cases}$$

5. Cartesian coordinates to spherical ones

$$\begin{cases} \phi = arctan(\frac{Y_4}{X_4}) \\ \theta = arctan(\frac{Z_4}{X_4^2+Y_4^2}) \end{cases}$$

10.8.1.3 Non-orthogonality of the elevation axis

Another effect from the structure is linked to the orthogonality in between the azimuth axis and the elevation axis which can also be imperfect, the elevation bearings not being located exactly at the same height for instance. Non-symmetric deformation of the structure under gravity with respect to this effect and the deviation from verticality is not taken into account at this stage.

Non-orthogonality of the azimuth and elevation axes :

1. Spherical coordinates to cartesian ones

$$\begin{cases} X_1 = cos(Zd) * sin(Az) \\ Y_1 = sin(Zd) * sin(Az) \\ Z_1 = cos(Az) \end{cases}$$

2. Rotation of α_{NO} angle around X-axis (horizontal axis orthogonal to perfect elevation axis)

$$\begin{cases} X_2 = X_1 \\ Y_2 = Y_1 * cos(\alpha_{NO}) - Z_1 * sin(\alpha_{NO}) \\ Z_2 = Y_1 * sin(\alpha_{NO}) + Z_1 * cos(\alpha_{NO}) \end{cases}$$

3. Cartesian coordinates to spherical ones

$$\begin{cases} \phi = arctan(\frac{Y_2}{X_2}) \\ \theta = arctan(\frac{Z_2}{X_2^2+Y_2^2}) \end{cases}$$

10.8.1.4 Bending of the structure

The structure deforms mainly under gravity due to the telescope's lightweight design. This effect is referred below as 'structure bending'. This is the effect that gave the name to the model.

Structure bending :

$$Zd^{'} = Zd - A_{bending} * sin(Zd)$$

10.8.1.5 Transformation to telescope pointing

The misspointing measurement output by the *bending model* is tangential to the coordinate system at the pointed position. All the components of the model are computed as a function of their action on the AltAzimuthal frame. This transformation makes the conversion to the same frame as the output of the analysis.

1. Conversion from spherical coordinates to camera plane coordinates

$$\begin{cases} (\theta_{nom.}, \phi_{nom.}) - Nominalpointing \\ (\theta_{true}, \phi_{true}) - Truepointing \end{cases}$$

2. Rotation angle to apply (from correction above)

$$\begin{cases} \alpha_X = \alpha \\ \alpha_Y = \theta_{true} \\ \alpha_Z = -\phi_{true} \end{cases}$$

3. Spherical coordinates to cartesian ones

$$\begin{cases} X_1 = cos(\phi_{nom.}) * sin(\theta_{nom.}) \\ Y_1 = sin(\phi_{nom.}) * sin(\theta_{nom.}) \\ Z_1 = sin(\pi/2. - \theta_{nom.}) \end{cases}$$

4. Rotation of α_Z angle around Z axis

$$\begin{cases} X_2 = X_1 * cos(\alpha_Z) - Y_1 * sin(\alpha_Z) \\ Y_2 = X_1 * sin(\alpha_Z) + Y_1 * cos(\alpha_Z) \\ Z_2 = Z_1 \end{cases}$$

5. Rotation of α_Y angle around Y axis

$$\begin{cases} X_3 = Z_2 * sin(\alpha_Y) + X_2 * cos(\alpha_Y) \\ Y_3 = Y_2 \\ Z_3 = Z_2 * cos(\alpha_Y) - X_2 * sin(\alpha_Y) \end{cases}$$

6. Rotation of α_X angle around X axis

$$\begin{cases} X_4 = X_3 \\ Y_4 = Y_3 * cos(\alpha_X) - Z_3 * sin(\alpha_X) \\ Z_4 = Y_3 * sin(\alpha_X) + Z_3 * cos(\alpha_X) \end{cases}$$

7. Cartesian coordinates to spherical ones

$$\begin{cases} \phi = arctan(\frac{Y_4}{X_4}) \\ \theta = arctan(\frac{Z_4}{X_4^2 + Y_4^2}) \end{cases}$$

10.8.2 Model fitting

For example, we will use the data of the last model acquired during the April-May 2022 acquisition campaign (Fig. 10.29. Most of the grid was covered, and only a few points did not have valid data.

The model is fitting simultaneously on misspointing measurement and inclinometer scan (Fig. 10.30). The inclinometer scan results are actually only used to constrain the angle on the azimuth tilt component. The prediction of the model is mainly in agreement with the measurements, even if some systematic seems to remain (Fig. 10.31).

10.9 Results and perspectives

At the time where this manuscript was written, three successive models had been acquired. A first one in November 2020, a second one in May 2021 and a final one in April-May 2022. The first one did not use the mechanical model for the final determination of the correction but only fitted with spline functions.

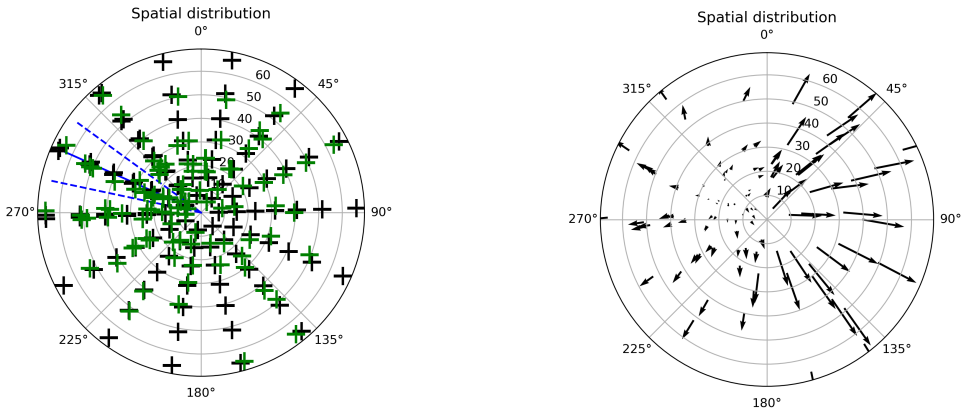

Figure 10.29: The left panel is the sky with a polar view of the altazimuthal frame. The grid is represented with a back cross along with the exact position of the point used for the model as a green cross. The right panel represent the measurement of the correction to apply fr each of these measurement points.

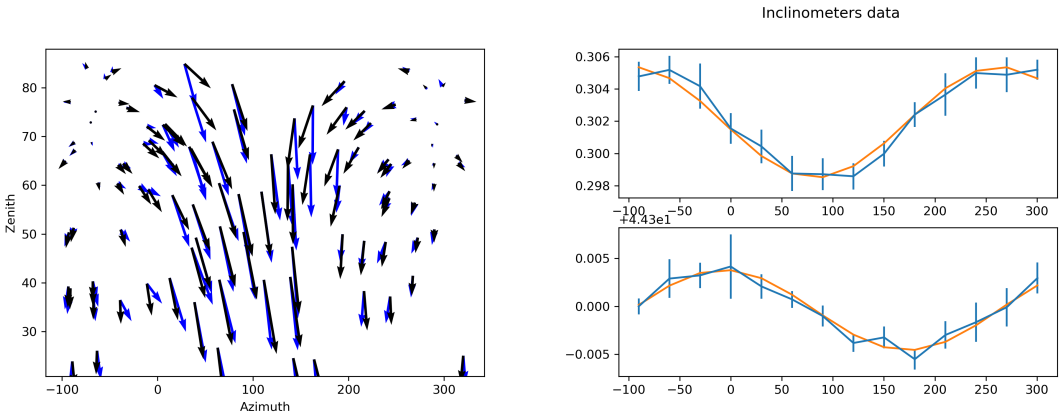

Figure 10.30: The left panel represent across the sky the correction measured (black arrow) with the correction from the fitted model (blue arrow). The right panel represent the measure from the inclinometers (blue data) alongside with the model prediction (orange line).

The second model was the first to use the mechanical model for determining the final correction to apply in any part of the sky. Some verification data were acquired for this model. Such data consists in doing a standard acquisition but with the *bending model* provided to the drive to make the corrections. The model used is the one that is to be tested. If the model were perfect, we should always obtain a correction of zero for these measures. The second model, on verification data, reached an average error of 21.1″ with a maximum correction of 38″ (Fig. 10.32). Most of the distribution within the requirement of 30″ even if some outliers are still present. Sadly, due to a bug in the CDM system, the drive position was not recorded, so we do not know the position of the measurement in the sky, preventing an analysis in order to understand the origin of the outliers. In this model we added to the mechanical model a sinus variation as a function of the azimuth for the azimuth correction. This effect was not understood at the time, but later, an issue was discovered on the time synchronisation of the different elements of the *drive system*, leading to a delay in the position of the telescope along the track of the source, causing this sinusoidal effect.

The issue has been fixed, and the next acquisition will allow assessing that this issue was effectively at the origin of this additional component has disappeared. The sensitivity of the *bending model* to such a small deviation is encouraging for the performance of the system.

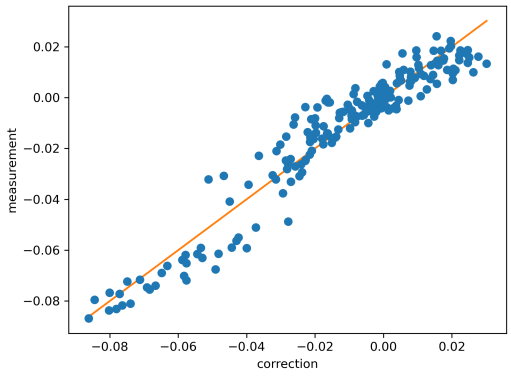

Figure 10.31: The intensity of the correction is measured in function of the one predicted by the model. The orange line is the y=x line. If the model and measures were perfect, all the data should be on this line.

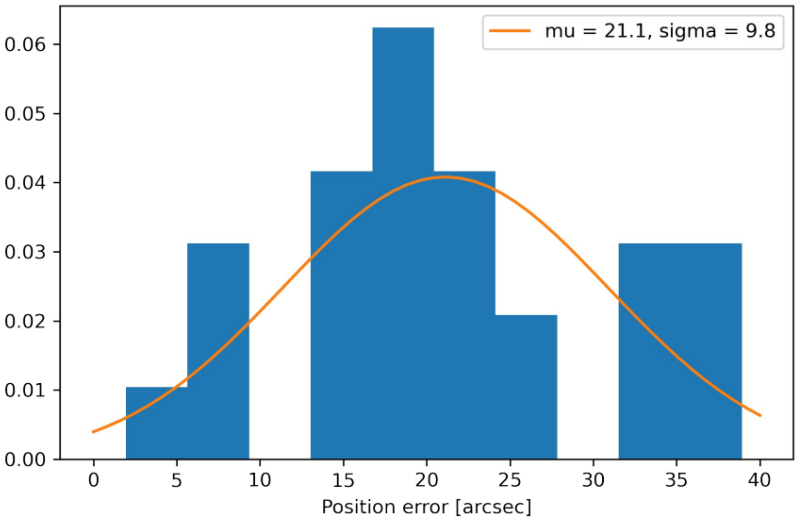

Figure 10.32: Distribution of the error remaining after the application of the bending model fitted with gaussian distribution.

The last model does not have verification data, as the operation of the LST-1 has been suspended for several months after its acquisition. However, due to the evolution in the LUT of the AMC, and the fix of the issue of the drive, a new model is required to describe this new configuration of the telescope. It is currently under acquisition.

The slow pace of *bending model* acquisition is mainly explained by two factors, multiples suspension of the LST-1 operation (ice storm, volcanic eruption, ...) and the actual ping-pong procedure with the AMC system. The AMC use actually only LUT to determine the mirror position as a function of the zenith. Any pointing error will have some impact on the LUT creation procedure. In consequence, any improvement of the *bending model* helps to improve LUT and vice-versa. So each time a system performs an acquisition campaign, it waits for the other system to have finished its following campaign before starting a new one. Also, the actual *bending model* acquisition uses a LUT configuration which is not optimal for all the zenith but should improve the model correction for the specific task of LUT acquisition. In consequence, the outliers above the requirement are maybe explained by the specificity of the actual acquisitions (not possible to verify this hypothesis due to the lack of pointing information in the verification data).

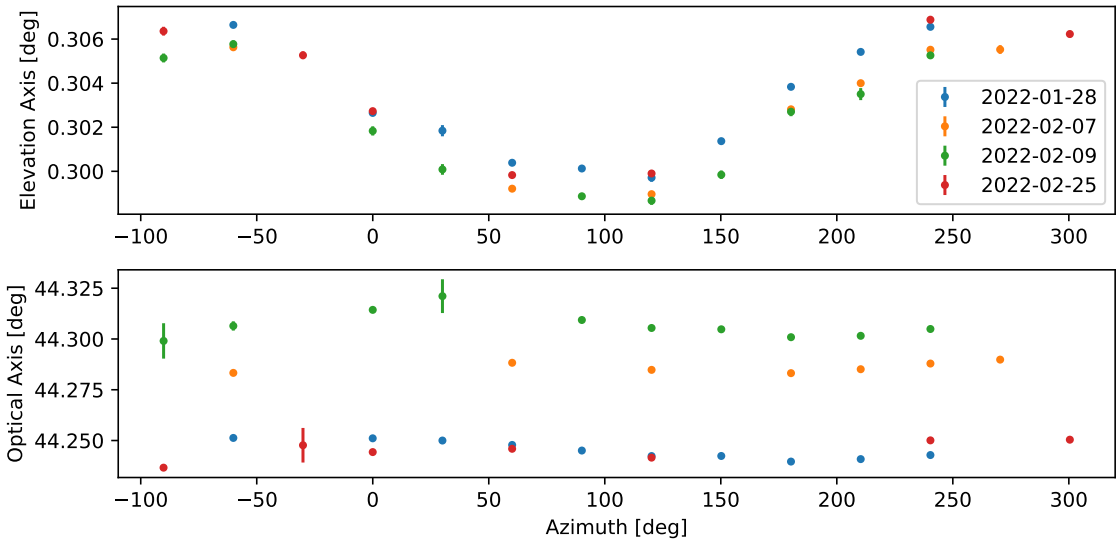

Figure 10.33: Results of multiple azimuth scans on a time span of one month. The temperature during the nights of the 28th of January and 25th of February was around 0 °C and for the nights of the 7th and 9th of February around 9 °C.

The next step will be to verify the new model and check its compliance with the requirements. Following this, integration of the *bending model* program to the telescope control unit program should allow a more easy and frequent acquisition. This is likely important as data on inclinometers have shown significant differences as a function of the day 10.33 of acquisition. As there was a large temperature difference, it could explain at least a part of this difference between the scans. Having regular data acquisition should allow us to study the impact of weather and also aging of the structure and confirm the observed difference.

To achieve the requirement to acquire a full model in 9 h, it's likely that some improvement in data-taking efficiency would still be needed. But at the time it's hard to be certain as acquisition efficiency data are biased by the frequent stops of the acquisition due to issues encountered either with a telescope system or the communication with them.

One big hypothesis of the actual analysis is that the CDM and the main camera are perfectly vertical. It is likely that a small deviation exists which would impact the measure. The relative angle between the two could be measured using LEDs, but they do not allow any absolute measurement of the camera compared to the sky. One idea to have a reference is to use stars from the sky directly observed by the CDM, but the number of these is limited and quite a lot of development is needed to be able to use them to make such measurements.

Finally, to better estimate the systematical error of both systems, it is planned in the future to make simultaneous acquisitions with the StarGuider system to compare the results.

Chapter 11

Résumé de la partie 3

Contents

L'une des exigences pour les télescopes LST est la capacité à pointer le télescope avec une erreur de moins d'une minute d'arc et de déterminer la position du télescope avec une précision meilleure que 14 secondes d'arc après une correction hors ligne. Une connaissance précise du pointé est importante pour les futures observations stéréoscopiques et également pour éviter tout biais sur la position de la source reconstruite dans le ciel.

11.1 Correction du pointé sur le télescope LST

Trois systèmes différents permettent de corriger le pointé au sein du LST.

La correction en ligne est réalisée à l'aide de ce que l'on appelle le *bending model*. Le système mesure l'erreur systématique de pointé du télescope à intervalles temporels et spatiaux réguliers afin de dériver un modèle qui sera utilisé par le *drive system* pendant les observations. Le nom du système provient de la source principale attendue de l'erreur systématique : la déformation de la structure du télescope. Ce chapitre résume l'explication, le développement et les résultats de ce système.

Deux autres systèmes sont utilisés pour les corrections de pointé hors ligne. Le premier est le StarGuider (SG). Ce système utilise une caméra CCD placée au centre de la parabole (appelée StarGuider), dont le pointé est légèrement décalé par rapport à la caméra Cherenkov. Cela permet à la caméra de voir la moitié de la caméra Cherenkov et une partie du ciel sur le côté. Le pointé exact du StarGuider peut être déterminé à l'aide des étoiles visibles dans le ciel. La position de la caméra Cherenkov dans le champ de vision du StarGuider peut être déterminée à l'aide des LEDs. Avec ces deux informations, il est possible de déterminer le pointé absolu de la caméra Cherenkov.

La seconde, appelé Camera Displacement Monitor (CDM), surveille à haute fréquence (10 Hz) la position de la caméra Cherenkov par rapport à l'axe optique. La caméra étant une masse située à l'extrémité d'une arche, elle peut se déplacer de manière significative sous l'influence de diverses forces. Parmi celles-ci, on peut citer le vent sur la caméra, l'oscillation induite par le mouvement de la structure, etc. Pour ce faire, une caméra CMOS, également appelée CDM, est placée au centre de la parabole. Deux lasers de référence à axe optique (OARL) sont tirés depuis le centre de la parabole sur une cible située sous la caméra et utilisée comme référence par le système. Les LEDs de la caméra Cherenkov sont également utilisées pour déterminer le centre de la caméra Cherenkov dans l'image de la CDM (voir Fig 11.1). Les images prises par la CDM sont analysées en temps réel et la position des LEDs et des OARLs est enregistrée. Une correction hors ligne peut alors être déterminée en combinant les informations du SG et du CDM.

11.2 Principe de fonctionnement du programme du *bending model*

Le processus complet, de l'acquisition des données à l'analyse et à la détermination des corrections, a été développé au cours de mon doctorat. Le programme a été écrit en Python et intégré dans le cadre du LST pour interagir avec les différents sous-systèmes du télescope.

Le *bending model* est basé sur un ensemble de mesures du pointé dans le ciel. Ces mesures sont effectuées en pointant une étoile avec le télescope. Un écran peut être positionné au centre de la caméra Cherenkov à la distance focale du télescope. Cet écran s'appelle Star Imaging Screen (SIS) (voir chapitre 8). L'étoile pointée sera imagée sur l'écran, et la différence entre la position de l'étoile

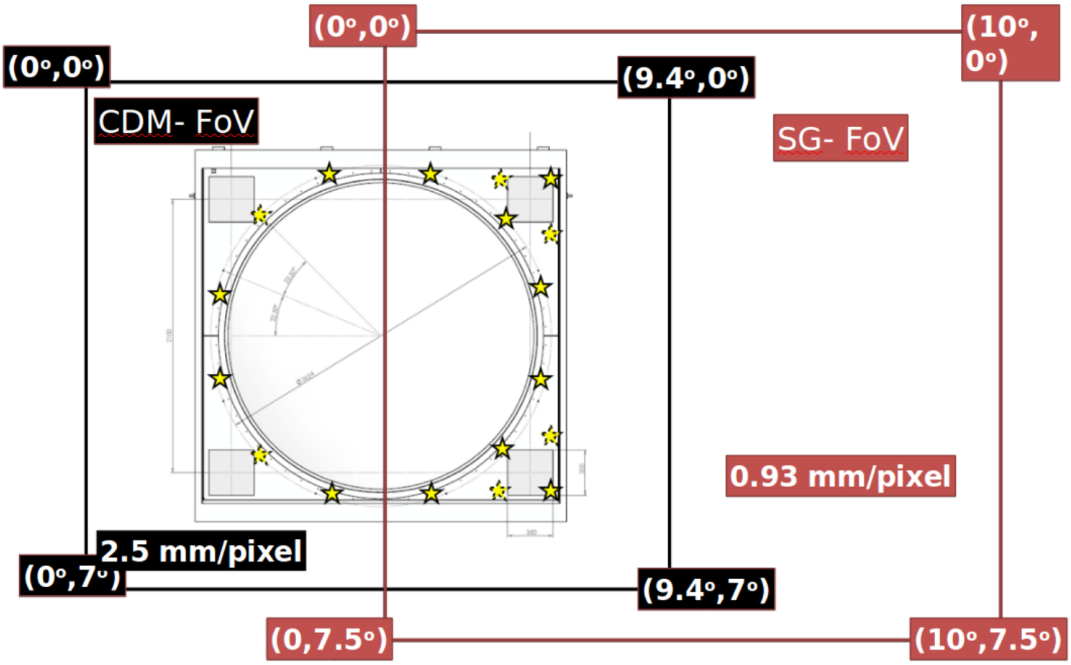

Figure 11.1: Schéma du champ de vision de la CDM et du StarGuider. Le cadre de la caméra et les LEDs sont représentés.

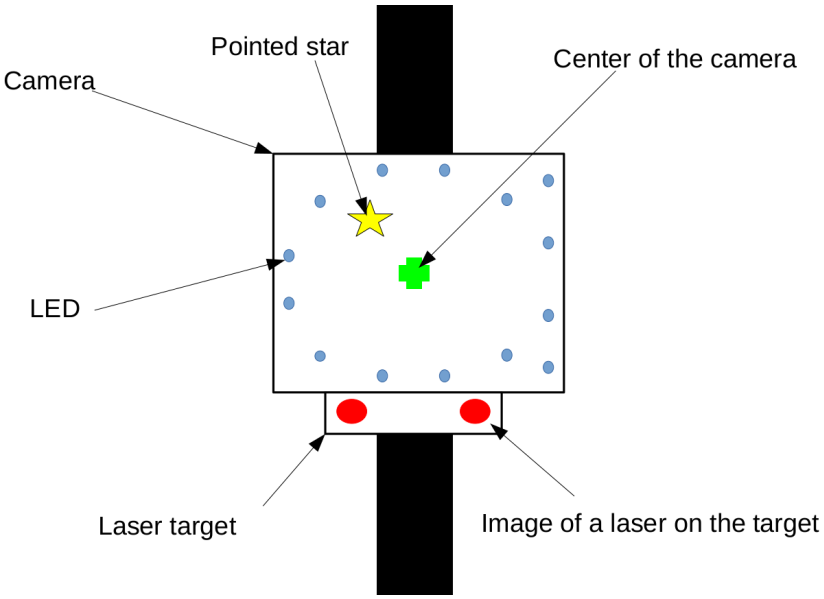

Figure 11.2: Principe de fonctionnement du *bending model*. Le schéma représente le champ visuel de la caméra CDM. Elle observe la caméra Cherenkov, avec ses LED, l'image des OARL de la cible en-dessous et l'image de l'étoile pointée sur le SIS. L'étoile n'est pas au centre en raison de l'erreur de pointé (exagérée sur cette figure).

et le centre de la caméra est la mesure de l'erreur de pointé. La figure 11.2 donne un aperçu de ce principe.

Pour la mesure, la caméra CDM est ensuite utilisée pour prendre une image de la caméra Cherenkov. La position de l'étoile est extraite de cette image, et la position de la caméra est déterminée à l'aide des LED.

La répétition de cette procédure sur différents pointages permet d'obtenir une vue d'ensemble de la correction à appliquer sur l'ensemble du ciel. Un *mechanical model*, ajusté sur un ensemble de mesures d'erreur de pointé, est alors utilisé par le *drive system* pour appliquer des corrections en ligne.

11.3 Sélection des étoiles observées

La sélection de l'étoile à observer est une étape importante car elle aura un impact sur le temps d'observation mais aussi sur la précision du système. Il est important de minimiser le temps d'observation car le temps consacré à l'acquisition des données du *bending model* est limité. Un temps d'observation court sur l'étoile permet de couvrir plus de directions du ciel dans le même laps de temps, ce qui améliore la précision du système.

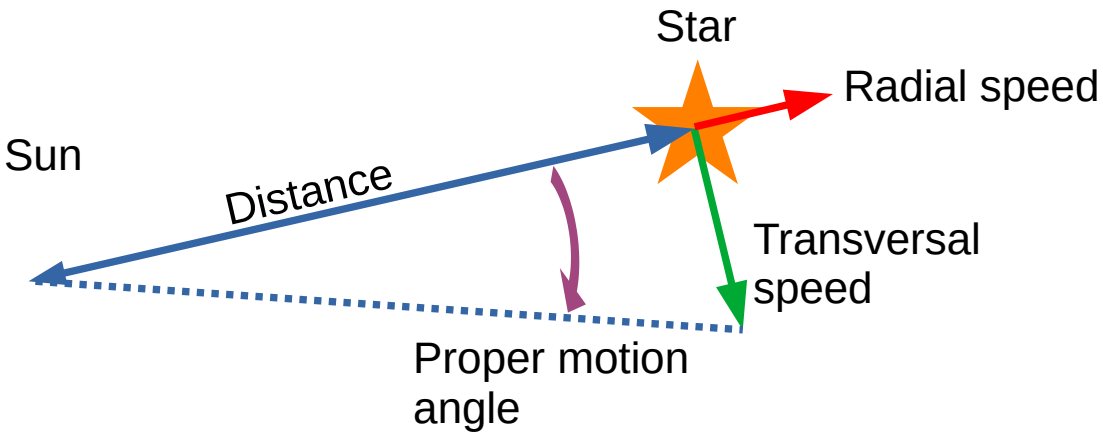

Figure 11.3: Croquis du mouvement d'une étoile par rapport au Soleil. L'angle de mouvement propre est le paramètre le plus important pour corriger la position dans le ciel de l'étoile en fonction de son déplacement par rapport au Soleil.

Un premier paramètre pour la sélection est par conséquent la magnitude de l'étoile. Le système est relativement peu sensible malgré le large miroir du LST. En effet, la lumière de l'étoile arrivant sur la cible est réfléchie dans toutes les directions. Ainsi, par simple effet géométrique, la CDM capte 13 fois moins de lumière provenant de l'étoile que si elle était simplement pointée vers le ciel, et ce, sans tenir compte de la réflectivité non parfaite des différentes surfaces. Il est aussi nécessaire de connaître précisément la position de l'étoile, et donc le mouvement propre de celle-ci (Fig. 11.3). Toute incertitude sur celle-ci augmentera les incertitudes systématiques du système. Finalement, comme la CDM ne possède pas d'obturateur, il sera nécessaire de trouver une zone proche sans étoile brillante pour acquérir des images noires.

Le catalogue d'étoile utilisé est le catalogue Hipparcos. Il est complet sur l'ensemble du ciel jusqu'à une magnitude de 7.3. Ainsi, combiné au catalogue de vitesse radiale, le Catalogue général de vitesses radiales moyennes pour les étoiles galactiques, il est possible de déterminer précisément le mouvement propre des étoiles, permettant ainsi de calculer avec précision leur position pour les observations. Il a été montré qu'avec les critères de sélection actuels, la précision sur la position des étoiles en 2060 (fin de vie estimé des LST) sera supérieure à 0.2 arcseconde.

11.4 Procédure d'acquisition

La procédure d'acquisition a nécessité quelques raffinements par rapport au principe de fonctionnement décrit précédemment. Cela pour deux principales raisons :

- L'exposition maximale permise par la CDM est de seulement 1 s, ce qui ne permet que de détecter des étoiles extrêmement brillantes.
- Les LED et OARL sont particulièrement lumineux. Une exposition d'une 50 ms suffit pour les saturer. De plus, des réflections créeent des spots lumineux dans la zone dans laquelle on s'attend à observer l'étoile. Ils sont particulièrement brillants par rapport aux étoiles, pouvant masquer celles-ci et rendant compliquée toute identification.

Du fait des contraintes mentionnés ci-dessus, l'acquisition des images est divisée en trois phases principales :

1. Une série d'image avec une courte exposition (20 ms avec les LED et OARL allumés. Ces images servent à déterminer la position de ces dernières.
2. Une série d'image avec une exposition de 1 s avec les LED et OARL éteints. Ces images permettent d'acquérir le signal venant de l'étoile. Le nombre dépendra du temps d'intégration requis pour la détection de celle-ci.
3. Une série d'image avec une exposition de 1 s avec les LED et OARL éteints, comme la précédent série, mais en pointant le télescope dans une direction proche mais sans étoile brillante. Ces images serviront d'image noire afin d'améliorer le ratio signal sur bruit de l'étoile dans l'analyse finale.

11.4.1 Planification dynamique des observations

Le ciel a été découpé selon une grille en azimuth et zénith afin de guider la sélection des observations (Fig. 11.4). L'objectif est ainsi d'avoir chaque point de la grille associé à une observation la plus récente possible.

Les zones de recherche d'étoile pour chaque point de la grille étant petites, le choix a été fait d'avoir un système de planification des observations dynamiques. Ne pas le faire aurait nécessité de déterminer avec une grande précision la durée nécessaire à chaque étape de l'acquisition, au risque sinon de ne pas observer les régions du ciel souhaitées.

Ainsi, après chaque phase d'acquisition sur une étoile, la nouvelle étoile à observer pour couvrir un point de grille donné est déterminée. Un point de grille est dit observable si une étoile validant les critères mentionnés précédemment se trouve dans cette région du ciel. Le système considère ainsi l'ensemble des point observables, et en prenant en compte l'âge des dernières observations, et du temps nécessaire à effectuer la mesure[1] déterminera l'étoile à observer.

11.5 Analyse des données

11.5.1 Préparation des images pour l'analyse

Les données sont en premier lieu filtrées afin d'éliminer les images affectées par des lumières parasites (phares de voiture, lampe de poche, etc.). Les images doivent ensuite être dématricée. La caméra étant une caméra couleur, chaque pixel est couvert d'un filtre pour être sensible uniquement à celle-ci. L'étape de dématriçage transforme cette image brute en une image où chaque pixel possède l'information sur les trois couleurs.

Les images avec les LEDs et OARL allumés peuvent être directement analysées, tandis que celles avec l'étoile subissent un traitement supplémentaire afin d'améliorer le rapport signal sur bruit. Les

[1] Le temps pour effectuer la mesure est composé du temps nécessaire au mouvement du télescope ainsi qu'au temps d'intégration

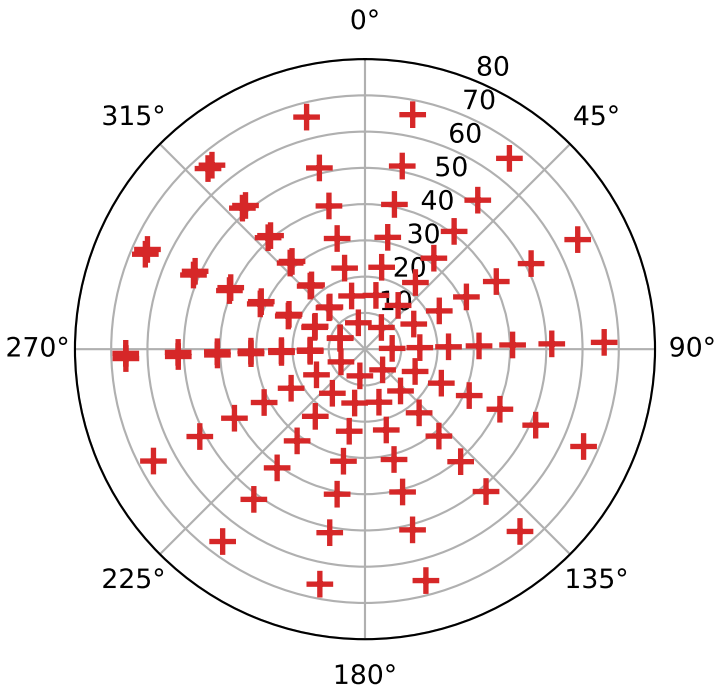

Figure 11.4: Grille à travers le ciel du *bending model*

images sont assemblées en additionnant les images prises sur l'étoile et soustrayant les images noires. L'image résultante est celle pouvant être analysée.

11.5.2 Extraction de la position de la caméra

Les LEDs et OARL sont facilement identifiables dans l'image du fait de leur brillance et de leur position déjà connue. La position de chacun des spots lumineux des LED et OARL est ensuite ajustée indépendamment pour garantir la précision de la mesure. Puis un cercle est ajusté sur les LED, permettant ainsi de déterminer la position du centre de la caméra. Toutes les images avec les LED et OARL allumés sont analysées indépendamment, puis les résultats sont combinés afin d'obtenir le résultat final, en tenant compte des potentielles variations au cours du temps et incertitudes de mesures.

11.5.3 Extraction de la position de l'étoile

Malgré la préparation initiale, le signal de l'étoile peut rester relativement faible. L'image est convoluée avec une gaussienne dont la taille est plus petite que l'étoile, augmentant ainsi le rapport signal sur bruit. Cela a ainsi permis d'améliorer le temps nécessaire à la détection d'une étoile d'un ordre de grandeur. L'étoile est ensuite identifiée puis la position est ajustée afin de déterminer avec précision sa position.

11.5.4 Détermination de l'erreur de pointé

Ensuite, en combinant les précédentes informations et les effets de projections, la direction ainsi que la norme de l'erreur de pointé peut être déterminée. L'assemblage de l'ensemble des mesures permet ainsi d'avoir une vue de l'évolution en fonction de la direction (Fig. 11.5).

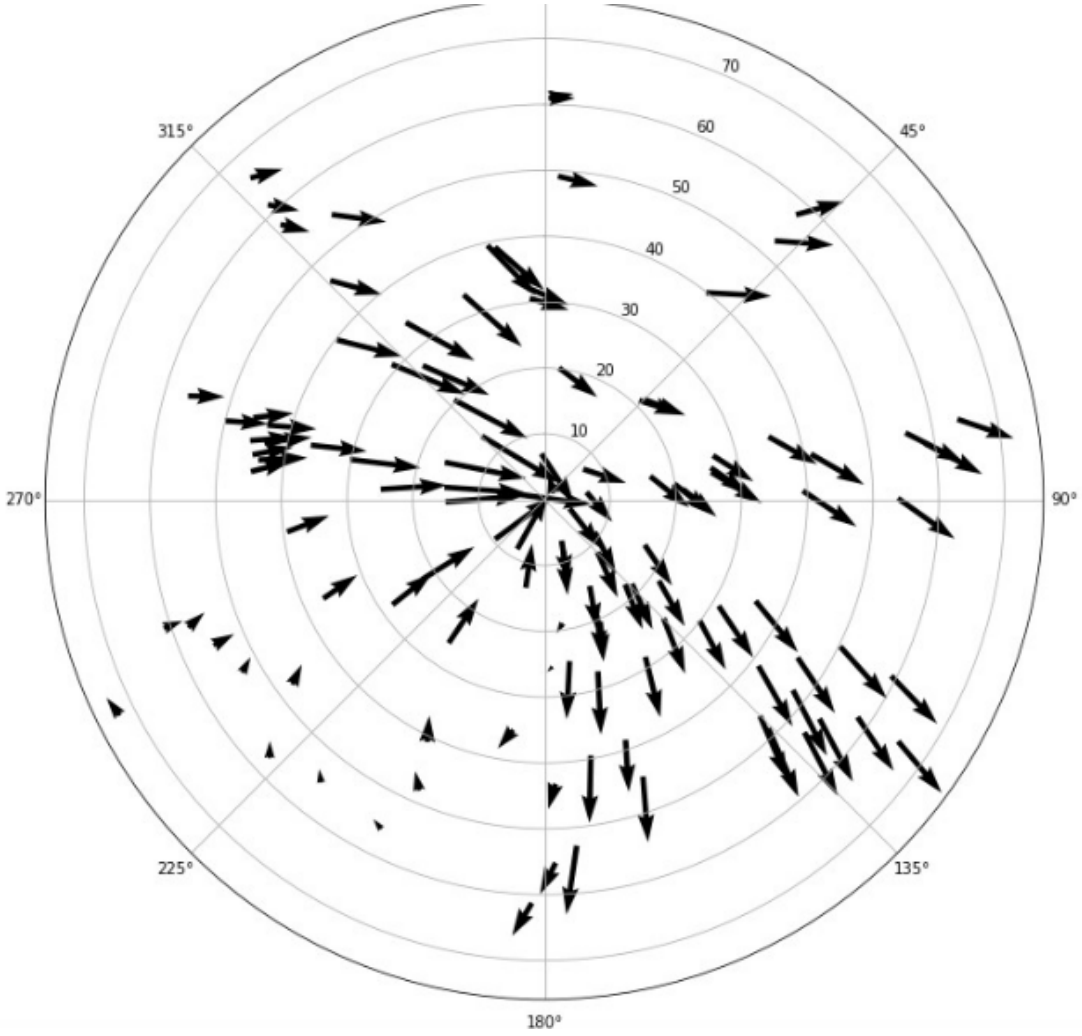

Figure 11.5: Représentation de la mesure d'erreur de pointé sur l'ensemble du ciel.

11.5.5 Ajustement du modèle mécanique

Afin de déterminer la correction du pointé dans n'importe quelle direction, un modèle dit mécanique a été déterminé. Celui-ci contient une description mathématique de chacun des effets attendus sur le pointé (déformation, non planéité, non orthogonalité, etc.). Les paramètres du modèle sont ensuite ajustés sur les données d'erreur de pointé. Ceux-ci sont ensuite communiqués au *drive system* afin qu'il puisse effectuer une correction pour n'importe quel pointé.

11.6 Utilisation des inclinomètres

Le LST possède des inclinomètres au centre de la structure, mesurant l'orientation du télescope sur plusieurs axes. Il a été montré qu'ils étaient capables d'améliorer l'ajustement du modèle final. Une procédure d'acquisition spécifique a été mise en place. Le télescope effectue deux balayage de pointés fixes, un à élévation fixe et azimuth variable, l'autre à azimuth fixe et élévation variable. Après filtrage et ajustement de chaque point de mesure indépendamment, les résultats des balayages sont intégrés à l'ajustement du modèle mécanique.

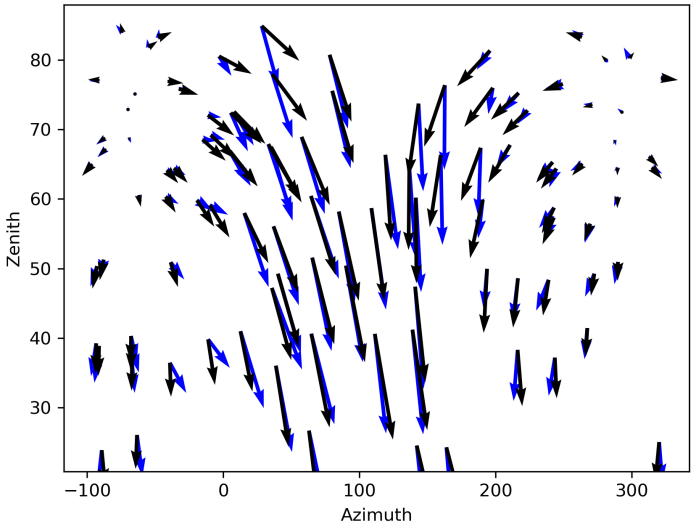

Figure 11.6: Représentation pour chaque point de mesure du ciel de la mesure effectuée (flèches noires) et de la prédiction du modèle après ajustement (flèches bleues).

11.7 Résultats et perspectives futures

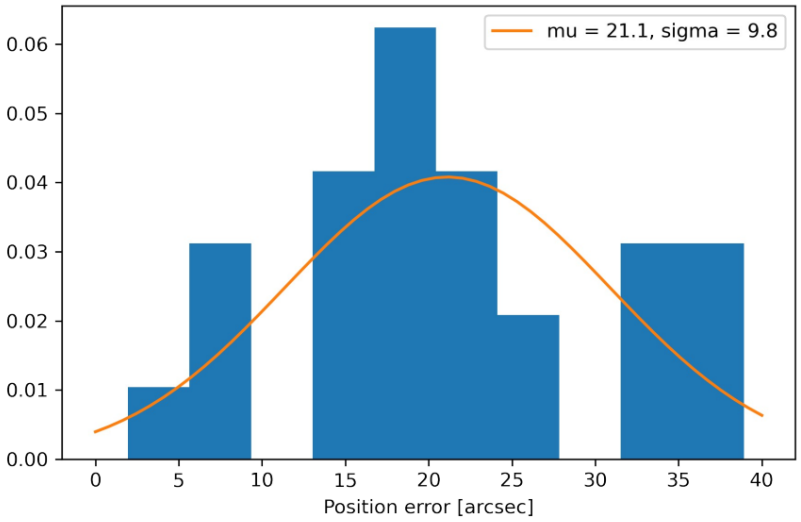

Figure 11.7: Distribution de l'erreur de pointé après application de la correction provenant du *bending model*.

Au moment de la rédaction de ce manuscrit, trois modèles successifs ont été acquis, respectivement en novembre 2020, en mai 2021 et entre avril et mai 2022. Le second modèle a utilisé pour la première fois le modèle mécanique pour la correction finale. Des données de vérification ont été acquises pour ce modèle, atteignant une erreur moyenne de pointé après correction de 21.1″ avec une erreur maximale de 38″ (Fig. 11.7). Les performances obtenues sont ainsi meilleures que les exigences du cahier des charges.

La grande précision du système a permis de découvrir un problème sur la synchronisation temporelle des différents éléments du *drive system*, entraînant un décalage de la position du télescope

le long de la trace de la source observée. Ce problème a été corrigé, et la prochaine acquisition permettra de confirmer l'absence de cet effet parasite.

Le dernier modèle ne dispose pas de données de vérification, les opérations du LST-1 ayant été suspendues plusieurs mois juste après son acquisition. Du fait de l'évolution de la configuration optique du télescope, un nouveau modèle est nécessaire et actuellement en cours d'acquisition.

La prochaine étape sera de vérifier le nouveau modèle et de contrôler sa conformité avec les exigences du cahier des charges. Suite à cela, une intégration du programme *bending model* au programme de l'unité de contrôle du télescope devrait permettre une acquisition plus facile et plus fréquente.

Finalement, pour atteindre l'objectif d'acquérir un modèle complet en 9 heures, il est probable que des améliorations de l'efficacité de la prise de données soient encore nécessaires.

Part IV

Analysis of data from IACTs

Chapter 12

Reconstruction and analysis principle

Contents

In this chapter will be presented the general principle of the Cherenkov data analysis. The example of LST-1 will mainly be used for this chapter. The data analysis could usually be separated into two parts. First, the reconstruction part, during which the raw data from the telescope are transformed into a collection of photons candidate with their direction and energy. During the second part, called the high-level analysis, the list of photons is used to detect sources and, in the case of detection, determine spectra, light curves or spatial shapes.

12.1 Event reconstruction

The event reconstruction of LST-1 is separated into several steps. Figure 12.1 presents the workflow used. As can be seen on the diagram, Monte Carlo simulations and observational data follow a similar path. As it is not possible to generate a calibrated beam of photons at VHE energy from space, Monte Carlo simulations of the atmospheric showers and the telescopes are performed to compute the instrument response.

The event reconstruction of CTA will mainly be the same as for LST-1 with as main difference being the stereoscopic reconstruction that includes data from multiple telescopes. The data level starts with R files (for raw files) that are telescope-specific and will not be stored in the future. The files with a name starting with DL (for Data Level) are standardised and will be archived.

All the reconstruction in LST-1 is performed with the software lstchain (Lopez-Coto et al., 2022) that heavily relies on the `ctapipe` library written for the reconstruction of CTA (Nöthe et al., 2021a).

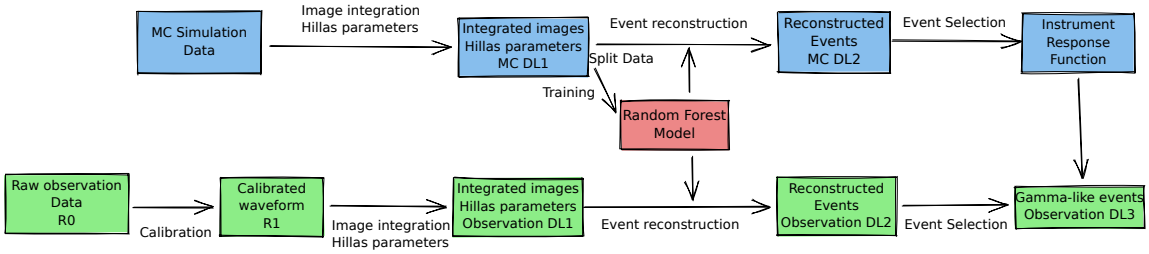

Figure 12.1: Event reconstruction workflow for the LST-1 experiment

12.1.1 Calibration

The raw data R0 output by the telescope is a collection of raw waveforms. There is one waveform per camera trigger with 38 samples of ∼1 ns in each waveform. The value is given in terms of ADC count (Analog Digital Conversion count) coming from the digitalisation of the signal in the camera. The objective of this calibration step is to transform these ADC counts in terms of photo-electron counts (number of photons detected by the photo-multiplier) and also to correct for the potential time deviation from the 1 ns duration of the sample. A more detailed presentation of the LST-1 calibration can be found in (Kobayashi et al., 2021).

Some parts of the calibration step is only concerning the observational data as for the Monte Carlo output, the parameters are already known so they only need to be applied to the data.

12.1.1.1 DRS4 Calibration

The readout frequency of the photo-multipliers is 1 GHz and the information needs to be stored in a buffer in case of a trigger. Each pixel has two gains (Low and High) with each a DRS4 (Digital Ring Sampler) ring. Each DRS4 chip has 2 channels of 1024 capacitors. In the case of a trigger, 40 samples are collected from 40 capacitors at the time corresponding to the trigger. The response of each capacitor could vary and this effect must be corrected using a dedicated calibration run taken at the start of the night, each night with the camera shutter closed.

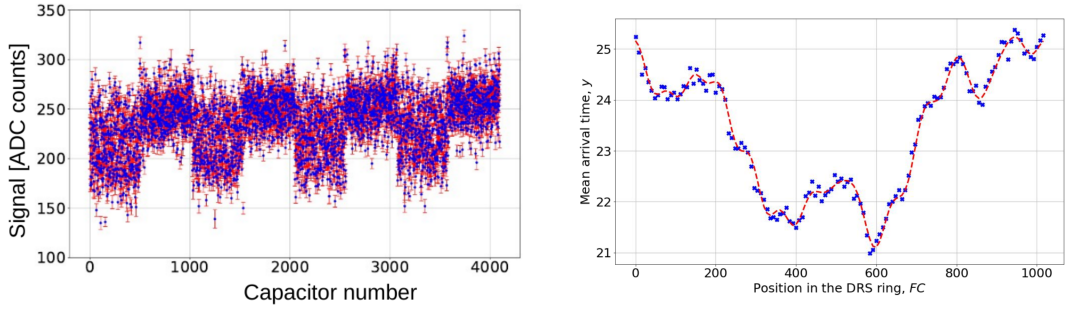

Figure 12.2: (Left) Pedestal values of the individual capacitor of a chip. (Right) mean arrival time of one pixel as a function of the position in the chip. Taken from P. et al. (2020)

The calibration phase is correct for the pedestal difference of each capacitor. This difference can be seen in figure 12.2 (left). A correction of the difference in arrival time of the pulse as a function of the position of the capacitors used in the ring (Fig. 12.2, right).

These corrections only concerned observational data.

12.1.1.2 Pedestal and gain

Then, the next step is to transform the signal in ADC (Analog-to-Digital Converter) count into a number of photo-electrons detected by the photo-multiplier. To help perform this action, two types

of calibration data are acquired through a dedicated run at the start of the night but also during the acquisition of Cherenkov data:

- Pedestal determination, data are taken with a random trigger, so without any signal to allow the determination of the pedestal of the PM.
- Flat-Field calibration, taken thanks to a flash of light from the UV laser of CalibBox placed at the centre of the dish. The CalibBox is designed to provide a determined amount of light to all the pixels of the camera.

The final gain g is computed with this formula :

$$g = \frac{1}{F^2} \frac{\sigma_Q^2 - \sigma_{ped}^2}{\bar{Q} - \bar{ped}} \tag{12.1}$$

with $\bar{Q}$ and σ_Q the average and standard deviation of the charge measured for flat field events, $\bar{ped}$ and σ_ped the average and standard deviation of the pedestal measured on pedestal events and squared excess noise factor $F^2 = 1 + \sigma_{spe}^2$. σ_{spe} is the width of the charge distribution produced by a single photoelectron.

12.1.2 Signal integration

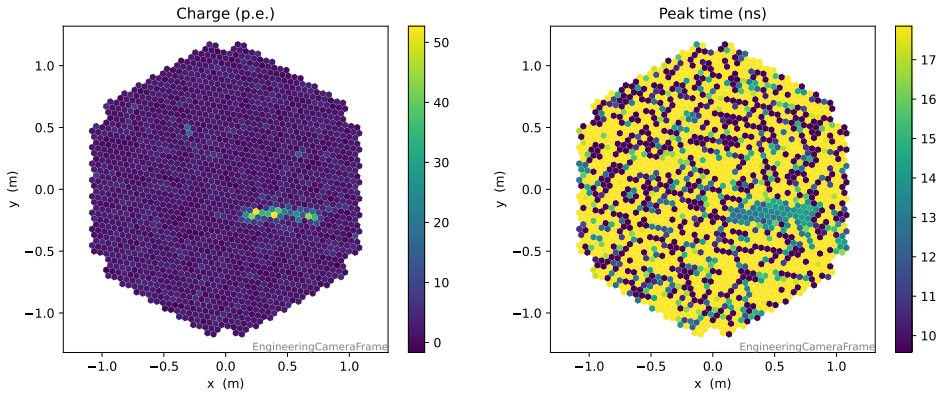

Figure 12.3: The integrated charge and peak time images for one simulated gamma

Starting from the calibrated waveform or R1 data, the signal is integrated in time. Along with the integrated signal is generated a time map representing the time for which the maximum number of photons was registered.

The actual algorithm used to perform this task is called `LocalPeakIntegrator`. For each pixel individually, the algorithm will search for the time with the maximum signal and will integrate into a 12 ns window around that peak. The window is not centred on the maximum but offset by 5 ns after the peak to take into account the response time of the PM.

An example of a simulated event in the LST camera is shown in figure 12.3, left the results of the signal integration, right, the peak time.

12.1.3 Reconstruction of the physical parameters of the particles

The objective now is to reconstruct the parameters of the incoming particles that have created the electromagnetic showers. The Hillas reconstruction method is used in LST-1. This method was first developed in 1985 for the analysis of the data of the Whipple telescope (Hillas, 1985). It has been used since in nearly all IACT experiments with some variations and improvement over time.

12.1.3.1 Image cleaning

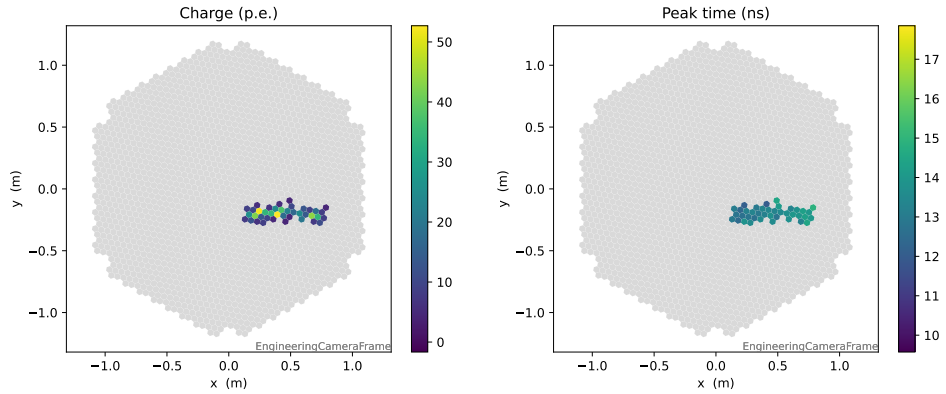

Figure 12.4: The integrated charge and peak time images for one simulated gamma after cleaning

The shower will take only a small portion of the images. It is then needed to extract the part of the images with the signal. The cleaning stage will remove pixels with only a noise signal. There are three rules to perform the cleaning of the image :

- There are at least 8 photo-electrons in the pixel
- There are at least 2 neighbouring pixels with 4 photo-electrons in each one
- There is at least one pixel with an arrival time closer than a 2 ns difference

In the figure 12.4 are presented the results of the cleaning of the previous shower. Most of the pixels were turned off and only the part of the image where the shower is, has been kept.

12.1.3.2 Hillas parameter

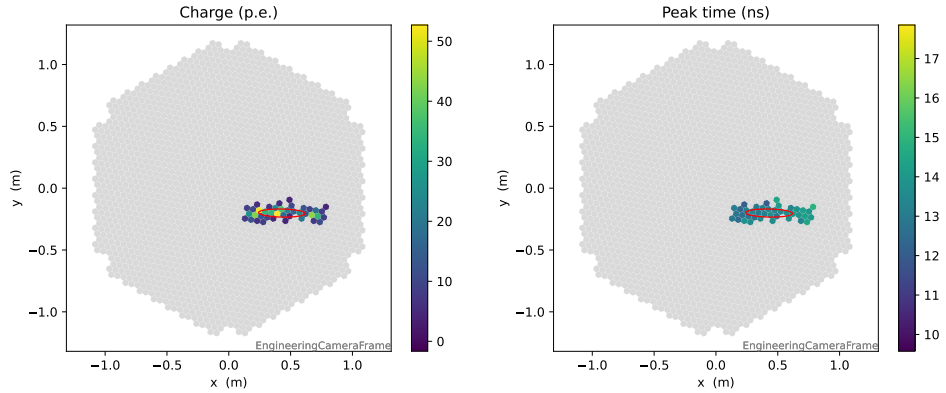

Figure 12.5: The integrated charge and peak time images for one simulated gamma after cleaning and with the ellipse from Hillas parametrisation

The Hillas parametrisation is based on the elliptical shape of the gamma-ray induced showers to compute the moments of the image. The ellipse is determined from the distribution of the signal in the images of the shower (Fig. 12.5). Among the parameters, there will be :

- the length of the ellipse
- the width of the ellipse
- the orientation of the ellipse
- position of the centre of gravity of the image in the camera
- number of photo-electrons after cleaning
- number of islands, an island representing connected pixels after cleaning
- time gradient of the arrival time along the ellipse
- ....

The parameters of each image alongside with the integrated images before cleaning are written in DL1 files (see Fig. 12.1).

12.1.3.3 Reconstruction of the parameter of the particle inducing the shower

The Hillas parameters will now be used to determine the properties of the particles that have created the showers. This is performed using the random forest machine learning algorithm. To train the algorithms, a subset of the Monte Carlo simulation dataset will be used. The other part will serve later to estimate the performance of the instrument.

There is one random forest for each parameter reconstruction: energy, direction and type of particles. The random forest for energy and direction are only trained using simulation of gamma-ray as we are only interested in reconstructing this type of particle correctly. The random forest concerning the types of particles is trained using gamma-rays and proton simulations so that the algorithm can learn the difference between the two types of particles. There is no simulation of heavier ions, that have a huge computing cost, as they will produce showers that will be even more different from gamma-rays and will also be likely rejected by the algorithm based on his training using protons.

The reconstructed parameters are then written in DL2 files (see Figure 12.1).

12.1.4 Event selection

All the events have been reconstructed, but only gamma-events should be kept but represent a very small proportion of the detected events. So the event needs to be selected with the objectives to keep most of the gammas and remove most of the cosmic-rays. Another objective of this selection is also to remove badly reconstructed events.

After event selection, events from Monte-Carlo are then used to estimate the performance of the telescope by computing the Instrument Response Functions (IRFs). Such functions are the effective area, the energy response with both the resolution and the bias, and finally, the angular resolution. All these functions are given as a function of the energy.

These IRFs, alongside the list of selected gamma-like events, are then forming the DL3 data format (Nigro et al., 2021) that could be used for the analysis of the data. This format has the objectives to be common to IACT experiments and is currently being also used by H.E.S.S. and MAGIC experiments for some of their analysis.

More details on this part could be found in the chapter 13.

12.1.5 Template fitting reconstruction

Within H.E.S.S. experiment, another method is often used for event reconstruction. The basic idea is to generate template images for different directions, energies, impact distances, ... and then use the image library to find the one that best fits the observed shower using likelihood fitting. The first implementation of such a method was performed by the CAT experiment in 1998 (Le Bohec et al., 1998).

H.E.S.S. used two different analysis chains, ParisAnalysis and HAP, each has its own algorithms to perform such kind of reconstruction. ParisAnalysis use Model++, which relies on a semi-analytical template (de Naurois and Rolland, 2009), while HAP relies on ImPACT, which uses models only generated from Monte Carlo simulation (Parsons and Hinton, 2014).

These methods allow significant improvements in performance, especially at low energy but at the expense of a much higher computing time.

Some developments are ongoing within CTA and LST to use such methods, but they are not ready to be used yet.

12.2 High-level analysis

The objective of the high-level analysis is to transform the data contained in the DL3 into information that could be used for the modelisation of the sources, like spectra, upper limits or light curves.

In the LST-1 experiment, the `gammapy` library (Deil et al., 2021) is mainly used for performing these actions. It is also the main library intended for CTA and also sometimes used for some H.E.S.S. publications.

12.2.1 Background estimation

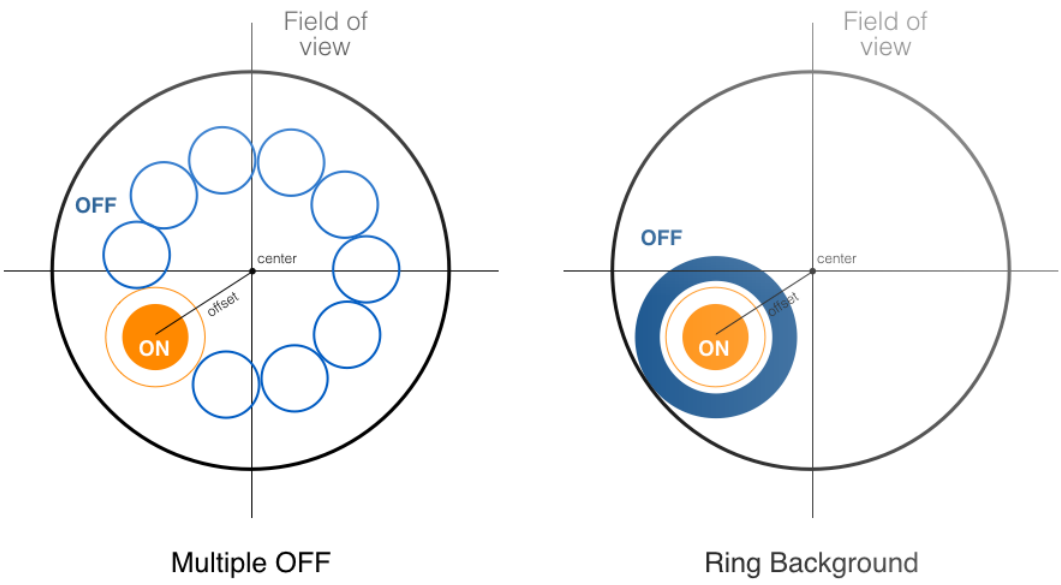

Figure 12.6: Two different methods to estimate background. The left scheme represents a multiple OFF method where several off regions are placed at the same offset distance from the centre of the FoV as the ON region. On the right scheme, the ring background method, the OFF region is a ring placed around the ON region. Figure from Chevalier (2017).

Even if most of the showers induced by cosmic-rays have been removed previously, there is still a significant portion of the data at the DL3 level that is background caused by these showers. Such contamination needs to be estimated. This step is very important because, with the exception of the brightest sources, in most cases, the background would dominate over the signal of the source.

There are several ways to estimate the background. The first one is to perform ON-OFF observations by observing part of the time on the source and part of the time on a similar dark patch. This has mainly been used historically due to its simplicity. However, it is highly sensitive to systematic effects due to the difference in the observation condition between the ON and the OFF observations.

It also requires spending a significant amount of observation time observing only background, and it is now mainly used only for the study of very extended sources.

For the method actually used, the observation needs to be taken in so-called wobble mode. Instead of pointing directly at the target, the telescope is pointed with an offset, and four symmetric positions around the target are used in order to minimise any systematic effect. This allows computing the background on the region of interest, called the ON region, by defining several OFF regions where there are only background events. The excess count N_{excess} is defined by :

$$N_{excess} = N_{ON} - N_{OFF} \cdot \alpha$$

where N_{ON} the number of event in the ON region, N_{OFF} the OFF count and α the correction factor for the difference of acceptance.

In the reflected (also called multiple-off) background methods, OFF regions are placed on a circle at a fixed distance of the pointed direction (implying an assumption that the background is symmetric). Such a method is illustrated in figure 12.6. The background estimation only needs to be corrected from the number of regions in the field of view i.e. the α is just the number of OFF regions.

The multiple-off method is very convenient but could not be used to make a map as it would not be possible to apply it everywhere in the field of view, as it would not be possible to apply such method too close to the centre of the field of view. In this case, the ring background method could be used (Fig. 12.6). The off region is a ring placed around the ON region. However, the background is highly inhomogeneous across the field of view, introducing a difference in acceptance between the ring and the ON region. The computation of this correction factor is based on a background model that could be, in this case, called the acceptance model, and is given by:

$$\alpha = \frac{\int_{ON} Acc_{Bkg}\left(\Phi_x, \Phi_y, E, t\right)\, d\Phi_x d\Phi_y dE dt}{\int_{OFF} Acc_{Bkg}\left(\Phi_x, \Phi_y, E, t\right)\, d\Phi_x d\Phi_y dE dt}$$

with Acc_{Bkg} the acceptance model of the background depends on the angular coordinates $d\Phi_x$ and $d\Phi_y$, the energy E and the time t.

This method could then be applied across the whole field of view in order to create maps. One of the advantages of this method compared to using the background model directly is that the ring could compensate for some of the imperfections of the model but is not well adapted to study diffuse emission or extended sources.

Finally, a method that starts to be used is the use of a background model directly as an estimation of the background (or with a fit of a few parameters). This method allows easier study of complex fields of view or very extended sources but at the expense of being very sensitive to any systematic of the model that is quite common due to the high sensitiveness of the background to the observation conditions, especially at low energies.

More information on the creation of the acceptance model can be found in chapter IV.

12.2.2 Source detection

The standard estimator used for assessing the detection of a source from the measure excess count is Li&Ma (Li and Ma, 1983). The significance of the detection N_σ could be computed with :

$$N_\sigma = \sqrt{-2 \ln \lambda}$$

$$\text{where} \lambda = \left[\frac{\alpha}{1+\alpha}\frac{N_{ON}+N_{OFF}}{N_{ON}}\right]^{N_{ON}} \times \left[\frac{1}{1+\alpha}\frac{N_{ON}+N_{OFF}}{N_{OFF}}\right]^{N_{OFF}}$$

If the factor α is close to 1, the significance can be approximated by :

$$N_\sigma = \frac{N_{ON} - \alpha N_{OFF}}{\sqrt{\alpha\left(N_{ON}+N_{OFF}\right)}}$$

To claim a detection, an excess corresponding to a significance above 5σ is needed. This is equivalent to a probability $p < 5.94 \times 10^{-7}$ that a background fluctuation could cause such an excess. If the excess corresponds to a significance above 3σ ($p < 2.704 \times 10^{-3}$) it could be considered as a hint of signal.

Also, a series of measures without any signal (so only subject to the Poisson noise of the background) should give a significance distribution that will be a normal distribution centred on 0 and with a standard deviation of 1. This property could be useful to check the quality of the background estimation, especially on a sky map where the number of measures (i.e. the number of pixels of the map) will be relatively high.

12.2.3 Spectral information

Getting spectral information is really important for a lot of physics analysis. One of the most used methods for this is the forward folding method first used by the CAT experiment (Piron et al., 2001). This method needs an assumption of the spectral shape. The most common is to start with a simple power law ($F(E) = F_{ref} \left(\frac{E}{E_{ref}}\right)^{-\alpha}$. This is justified by that most emission mechanisms predict a shape close to a power law on a restricted energy range. Then the excess count in each bin is compared to model prediction (taking into account the instrument response) by computing the likelihood. The model's parameters could be fitted on the data by maximising this likelihood. It is then possible to fit different spectral models and, using their likelihood, determine the ones that best describe the data. The discrimination is then based on Wilk's theorem for nested models.

With this method, spectral points could be computed by refitting only the amplitude parameter of the model for each energy bin where you want to compute a spectral point. To be noted that the results could be biased by the spectral model used.

In the case of a lack of detection, it is useful to compute upper limits to constrain the emission model for the studied source. The method used in `gammapy` and in the H.E.S.S. analysis software was first proposed by Feldman, and Cousins (Feldman and Cousins, 1998).

12.2.4 Light curve estimation

As we are also looking at variable sources extracting a light curve could give information on the behaviour of the source. A light curve is a time series for the source flux. To compute the flux in a given time bin, a method similar to spectral point is used. The amplitude parameter of the model is refitted on this specific time bin assuming a given spectral shape.

Chapter 13

Optimisation of the event selection of LST-1

Contents

The event selection, which has been described in chapter 12, is a crucial step for the instrument's performance. In an ideal world, this stage would reject all the cosmic rays and keep all the gammas. In practice, trade-offs need to be made, and depending on the source, different cuts could provide better performance than others. For example, a source with a hard spectral index (hard source) will have a strong signal at high energy. Adopting strict cuts that would suppress a larger part of the background at the expense of effective area at low energy could be interesting. On the contrary, for soft sources (sources with soft spectral index), it is likely preferable to use looser cuts to preserve effective area at low energy, where the signal is, at the expense of background rejection. The current generation, such as H.E.S.S., uses four different selection cuts (Aharonian et al., 2006).

Selection criteria could also be optimised not to give the best sensitivity but the best angular or energy resolution. This aspect will not be covered here.

13.1 Initial context

All this work has been performed using `lstchain` version 0.7, a version that was outdated at the time this manuscript was written. The cuts often used within LST-1 at the start of this work were :

- The intensity of the image needs to be above 100 photoelectrons.
- The ratio width vs length of the ellipse of the Hillas reconstruction is above 0.1. This removes events that were likely not produced by a shower.
- The leakage intensity width 2 is below 0.2. This parameter represents the fraction of the signal contained in the two pixels row closest to the edge of the camera. It removes showers that are likely cut significantly by the edge of the camera and so not fully imaged, introducing a bias in the reconstruction.
- The gammaness is above 0.6. This parameter represents the confidence the random forest classifier has for this event being a gamma compared to a proton. A gammaness of 0 is for a shower very likely to be hadron-induced, and a gammaness of 1 is for a shower very likely to be gamma-induced.
- A theta cut of 0.2°. When performing an analysis of a point-like source, it represents the radius of the circle of the ON region centred on the source.

These cuts will be called `Base` cuts for this chapter.

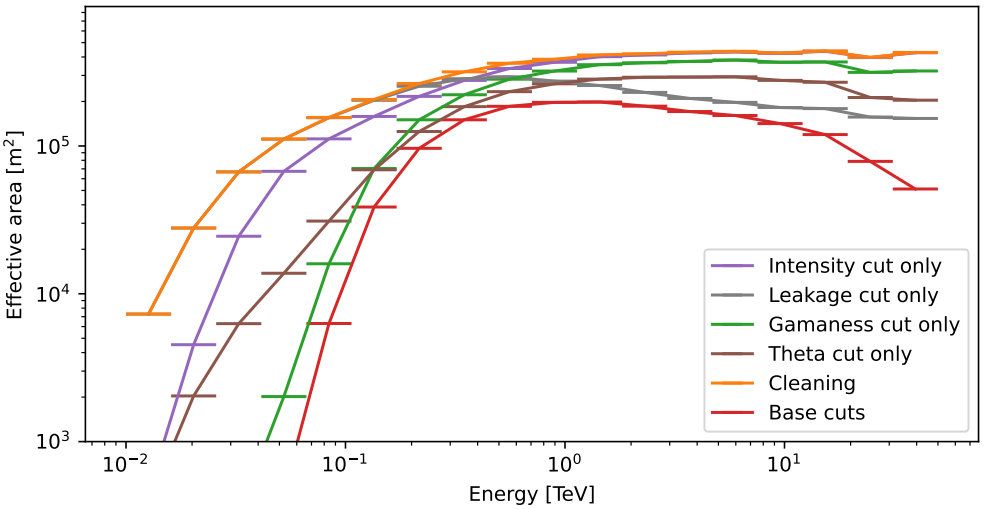

Figure 13.1: Effective area in function of the energy for different cuts applied

With these cuts, most of the low-energy events are removed, making impossible any detection at these energies, and limiting the sensitivity of the instrument for soft sources. For most of the sources of interest of the LST-1 (GRBs, AGN, pulsars, ...), lowering the energy threshold is important. Figure 13.1 shows the effective area after cleaning for these "basic" cuts. The effective area after cleaning is the one that would be reached without any selection cut. However, all the backgrounds would also pass, making it impossible to achieve any detection as it will mask any sources. The figure also illustrates the effective area for each individual cut composing this "basic" set of cuts.

Optimising the performance will require playing on several parameters and finding the best compromise, which will likely depend on the energy range or the source spectra.

13.2 Optimisation algorithm

Cuts optimisation is often performed by maximising the significance of one or a set of simulated sources in a given energy range. A different approach has been used here. As the main objective of

these cuts is to improve sensitivity, optimisation will be made by searching the parameters that allow the detection of the faintest possible source for a given spectral shape. This method allows to take into account other information than the significance to reach the best sensitivity, like a minimum number of photons or a minimum signal-to-background ratio.

13.2.1 Definition of the cut's grid

The optimisation has been performed using a grid search. It is a brute force method, but it is simple and easily covers the whole phase space. Among the already used parameters in LST (see section 13.1), four of them are considered in the optimisation process. The ratio width vs length has been kept constant with respect to the LST `Base` cuts since it mainly removes spurious events and barely suppresses any events on the Monte Carlo.

Another parameter of importance for searching sources is the energy threshold of the analysis. For hard sources, not starting the analysis at the lowest energy threshold could make sense for detection purposes since most of the background is contained at low energy. This is not true for hard sources. In our calculation, we have defined the energy threshold as a parameter.

The grid has five dimensions:

- Minimum intensity from 30 to 5000 with 30 logarithmic bin
- Minimum gammaness from 0.4 to 0.95 by step of 0.05
- Maximum leakage from 0 to 0.7 by step of 0.05
- Maximum theta from 0.05° to 0.25° by step of 0.025°
- Energy threshold of the analysis from 20 GeV to 5 TeV with 11 logarithmic bin

This leads to a total number of combinations to test of 534 600.

13.2.2 How the energy range is computed

The energy range must be handled in a different way than the other parameters. There are different effects that modify it for a given set of cuts.

Events are filtered by applying the cuts, and we need to ensure that the energy range used will allow for the correct computation of the IRFs. By using ≈ 5 bins per decade for IRFs computation, some cuts might remove most of the events of one energy bin, so statistical fluctuation could significantly affect the IRFs computed for this bin. A minimum of 20 events per bin was then required. For the effective area (the essential part of the IRFs in our case), it represents a statistical fluctuation of $\sim 20\%$. This is not small, but as the final result is the integral sensitivity across a high number of bins, the effect will not be too important. This correction will penalise the cuts that remove most of the events as the current Monte Carlo production would be unable to describe them correctly and so allow to make any physical analysis. If the results indicate that highly selective cuts would be favoured, running much more extensive Monte Carlo simulations with an increased statistic would be necessary.

The energy range is then corrected again to limit the contamination of the OFF region by the source. Indeed, at low energy, with the large PSF and the wobble offset of 0.4 degrees, the OFF regions might be contaminated by the source situated in the ON region. To correct that, we have defined as the criterion that the closest point of the OFF region is outside the 80% containment radius. Its main impact will be to increase the energy threshold as it will remove the low energy part where the PSF is large.

Up to now, the energy range has been expressed as a function of the true energy of the events. However, for estimating the background, it is the reconstructed energy that is important. The difference, especially at low energy, could be significant due to the important bias of the reconstruction in energy. To obtain the effective energy range in terms of reconstructed energy instead of true energy, each edge of the energy range is shifted as a function of the bias at the given energy.

13.2.3 Computation of the integral sensitivity

As the aim is to optimise the integral sensitivity, this first building block computes it for any set of cuts configuration. The first inputs are the DL2 Monte Carlo files for electrons, protons, and gamma simulations. The electrons and protons are diffuse (cover the whole field of view) and will be used for background estimation. The gammas are point-like simulations and will be used to compute the IRFs. Alongside to these Monte Carlo simulations, are also provided the cut sets to test, the spectral shape, the energy range, and the observation time. For the spectral shape, as the current implementation supports only power law, the spectral index is provided.

To compute background from the Monte Carlo events, one needs to compensate for the difference in spectra between simulated events and real spectra of cosmic rays by weighting each event. The spectra used for cosmic rays are the same as the `prod3b` of CTA (Observatory and Consortium, 2016). A background model is then computed from the Monte Carlo simulation. This model allows us to compute the number of background events expected for the given observation time.

It is now possible to determine the minimum number of photons to reach a detection. This number will be the maximum of three different criteria :

- Number of photons to reach a 5σ excess.
- Number of photons to have a signal-to-background ratio above 5%
- At least 10 photons were detected

which are quite usual to claim a detection. This minimum number of photons will be called $Nb_{photons}$.

The Monte Carlo simulations of gammas are then used to compute the effective area. From the effective area A_{eff}, it is possible to determine the differential flux equivalent f_ref for the given power law to this number of photons :

$$Nb_{photons} = \int_{E_{min}}^{E_{max}} \int_{0}^{t_{obs}} f_{ref} \left(\frac{E}{E_{ref}}\right)^{-\alpha} A_{eff}\left(E,t\right) dEdt$$

$$f_{ref} = \frac{Nb_{photons}}{t_{obs} \int_{E_{min}}^{E_{max}} \left(\frac{E}{E_{ref}}\right)^{-\alpha} A_{eff}\left(E\right) dE}$$

where E_{max} and E_{min} are the maximum and minimum energy range in true energy, t_{obs} is the observation time, α is the index of the power law and E_{ref} is the reference energy for the differential flux f_{ref}. The choice of this reference energy is not really important, it could even be outside of the energy range, but it must always be the same to perform comparisons. This differential flux f_{ref} will be considered as our sensitivity. The lower this number, the better the cuts.

The implementation uses the libraries `lstchain` (Lopez-Coto et al., 2022), `pyirf` (Nöthe et al., 2021b) and `gammapy` (Deil et al., 2021). The computing optimisation of this part was crucial as it will be called many times during the process, and then some functions of the libraries used have been rewritten specifically for this use case in order to gain performance. The overall runtime of this sensitivity estimation is down to one second, depending on the cuts and the size of the Monte Carlo simulation used.

13.2.4 Determining a few sets of cuts

The integral sensitivity is computed for different simulated "sources". These sources will have simple power-law spectra and are determined by two parameters: the power-law index and the observation time (the flux for the power law is the optimised parameter).

To estimate the best cuts for different classes of sources, a grid is created with two dimensions: the power-law index, ranging from 1.5 to 5.0 by step of 0.25, and the observation time, from 20 min to 50 h with 14 logarithmic bin. The best cuts will be determined for each of these "sources". The code to compute the integral sensitivity is able to compute the sensitivity for the whole grid of sources in an amount of time close to the one for a single source. Adding these two dimensions will

Name of the cuts	`Loose`	`Standard`	`Hard`
Gammaness	>0.65	>0.75	>0.6
Intensity	>120	>350	>2000
Leakage	<0.1	<0.35	<0.35
Theta	<0.125°	<0.125°	<0.125°
Width length ratio	>0.1	>0.1	>0.1
Energy range	85 GeV - 10 TeV	100 GeV - 10 TeV	1.6 TeV - 10 TeV

Table 13.1: The three different selection cuts were selected in our work.

have a small impact on the computing time. The best cuts for each source are easily determined with the grid search.

The grid allows coverage of most of the cases, but defining one set of cuts for each source is not reasonable. Instead, we can have a few sets of cuts that cover a specific part of the phase space (index and observation time). The objective would be that these more generic cuts degrade the sensitivity as low as possible compared to the cuts specific to each source. The selection will be made on several indicators:

- The mean of the relative sensitivity
- The median of the relative sensitivity
- The 25th percentile of the relative sensitivity
- The 10th percentile of the relative sensitivity

The final cuts are then determined by hand. For example, the cut set that gives the best average sensitivity could provide poor sensibility in a few cases. Some other cuts could lower the relative sensitivity by 1% for most of the sources but increase a lot the sensitivity for these few corner cases. On the other hand, like for hard sources, it could be worthwhile to sacrifice the sensitivity for short timescales to improve the sensitivity on longer timescales significantly.

13.3 Results

13.3.1 Selected set of cuts

The figure 13.2 shows the minimal flux needed at 400 GeV to achieve detection as a function of the index and observation time using the best cuts configuration for each source. As we are looking at the integral sensitivity, it does not mean that detection would be achieved at 400 GeV, only that a source with this given flux would be detected by LST-1.

The best cuts to achieve good sensitivity mainly depend on the source's index in our case. Consequently, three different cuts will be determined for three different source indexes:

- `Loose cuts` for sources with an index between 4 and 5
- `Standard cuts` for sources with an index between 2.5 and 3.5
- `Hard cuts` for sources with an index between 1.5 and 2

The cuts selected are detailed in the table 13.1. If we compare to the cuts used before, in the case of the `Loose` cuts, the intensity threshold is slightly increased alongside the gammaness requirement. The leakage cut is significantly more selective as is the theta cut. This much smaller leakage cuts lower significantly the effective area at low energies but allows to remove events that are not greatly reconstructed. The energy range is quite similar to what could be achieved before.

The objective to reach a lower energy threshold is not achieved likely due to the limitation of the contamination of the OFF region by the source. With almost all cuts tested, the minimum

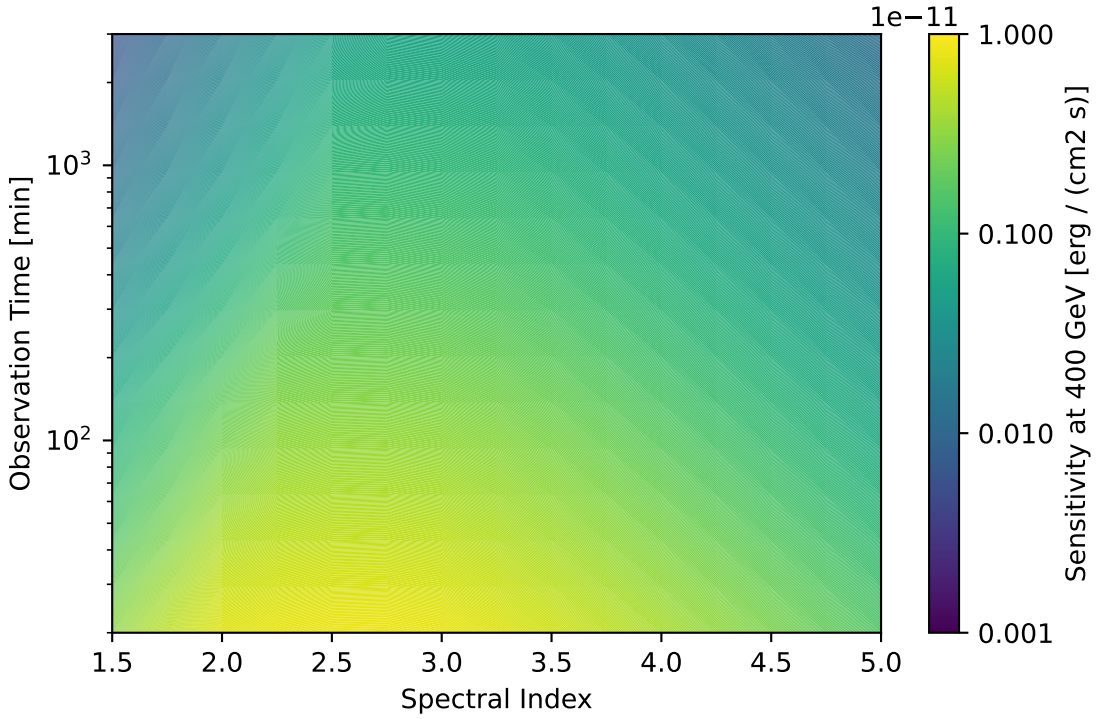

Figure 13.2: The flux at 400 GeV of the faintest detectable source for different observation time and spectral index. The cuts used are chosen per source to give the best sensitivity possible. The apparent lower sensitivity of index around 2.5 is mainly due to the difference of index of power law and the extension of the power law. For hard sources, the detection occurs at higher energies, while for soft sources at lower energies and simply the extension of the power law at 400 GeV that predict a low flux. It doesn't mean that for these sources it will be possible to detect it at 400 GeV.

energy threshold was not lower than with `Loose` cuts. The approach to the contamination was quite conservative, and to improve performance at low energy, this needs to be rethought or suppressed. The rather strict theta cuts for `Loose` cuts could be due to the algorithm trying through this method to lower a bit the energy threshold. The OFF region has the same size as the ON region, and by diminishing its size, it allows a worst PSF by diminishing the constraint on contamination of OFF region. Also, as lower energies are not reachable with the current configuration, it allows us to lower the background a bit and improve sensitivity.

`Standard` cuts lead to much more strict gammaness cuts compared to the `Base` cuts, reducing background, but with more significant leakage cuts to improve effective area at high energies. For the `Hard` cuts, the gammaness requirement goes down again which has for effect of increasing effective area but with a very high threshold on intensity and energy, rejecting all the background from low energies giving an overall much lower background rate.

All these results, especially for `Standard` cuts, need to be taken with a bit of carefulness as the agreement between data and Monte Carlo simulations were not great for this version of `lstchain` for the events with a high gammaness.

In the figure 13.3 is represented for all the sources, the relative sensitivity each selected set of cuts (hard, standard and loose) provides compared to the best cuts, i.e. chosen per source. We could easily identify the spectral index region defined for each cut. The figure 13.4 shows for each selected set of cuts where they performed better than the other two (red regions) and worse in blue regions. This figure allows us to highlight the trade-off made in this work. For example, for short observations and hard sources, `Standard` cuts tend to give more sensitivity compared to the `Hard`

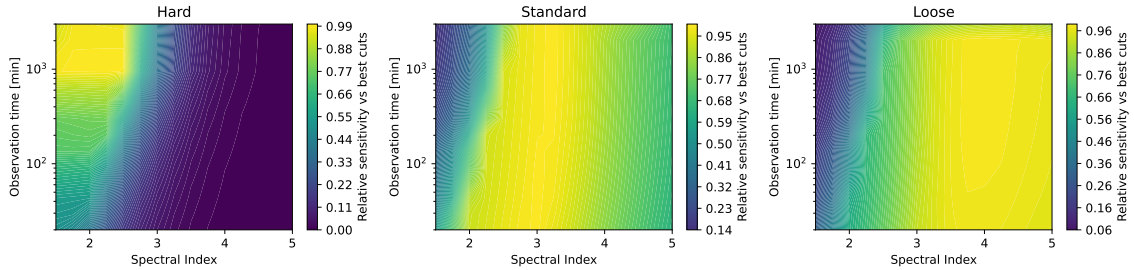

Figure 13.3: Relative sensitivity for each final set of cuts compared to the one tailor-made for each source. The larger the value the better it is. The left panel is the hard cuts, the centre panel is the standard cuts, and the right panel is the loose cuts.

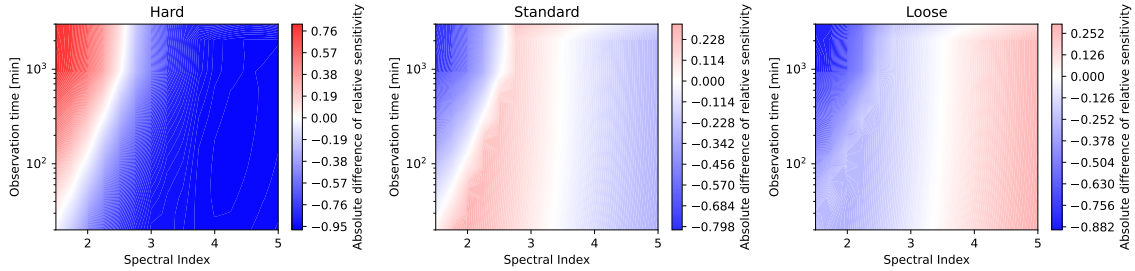

Figure 13.4: Absolute difference of relative sensitivity compared to the one tailor-made for each source for each cut compared to the other ones. If the region is red the cuts performed better than the other two, if blue the cuts are worst than the other two cuts. The left panel is the hard cuts, the centre panel is the standard cuts, and the right panel is the loose cuts.

cuts, design for this region (Power-law index < 2.5).

Finally, if we take the relative sensitivity of the best of the three cuts for each source, we obtain figure 13.5. With these three cuts, for most of the sources, the sensitivity is better than 90% and even often better than 95% compared to tailored-made cuts per source.

13.4 Utility of a full grid of sources

Contrary to the method usually used, we did not use a prototype source to optimise the cuts but rather a set of sources in the grid. To help understand the advantages of this method, a few examples are shown in figure 13.6. The figure represents the difference in relative sensitivity between the cuts optimised for a specific source and our three sets designed to cover all as best as possible all the sources.

The first three panels are for relatively hard sources. The observation time between the first and second case increased by $\sim 50\%$ (one bin in the source grid), but the source-specific cuts obtained changed a lot, and so did their performance.

The second panel presents cuts close to the `Hard` cuts and only gives 1% better performance than for the specific source. At the same time, the shorter observation time gives completely different cuts that perform up to 7% better for hard sources for moderate observation time but more than 12% worse for longer observation time. For the third case, the source is only slightly softer, but the cuts dedicated are way different and much closer to `Standard` cuts.

The three next cases focus on softer sources. The source-specific cuts of the first case give 3% better performance for this case but degrade by up to 11% for the other soft sources. In the second case, with longer observation time, the same cuts increased the performance up to 10% for long observations. However, they cause a loss of around 5% for the shortest observation on soft sources. Finally, if the sources are slightly softer, the cuts do not perform well for all long observation times

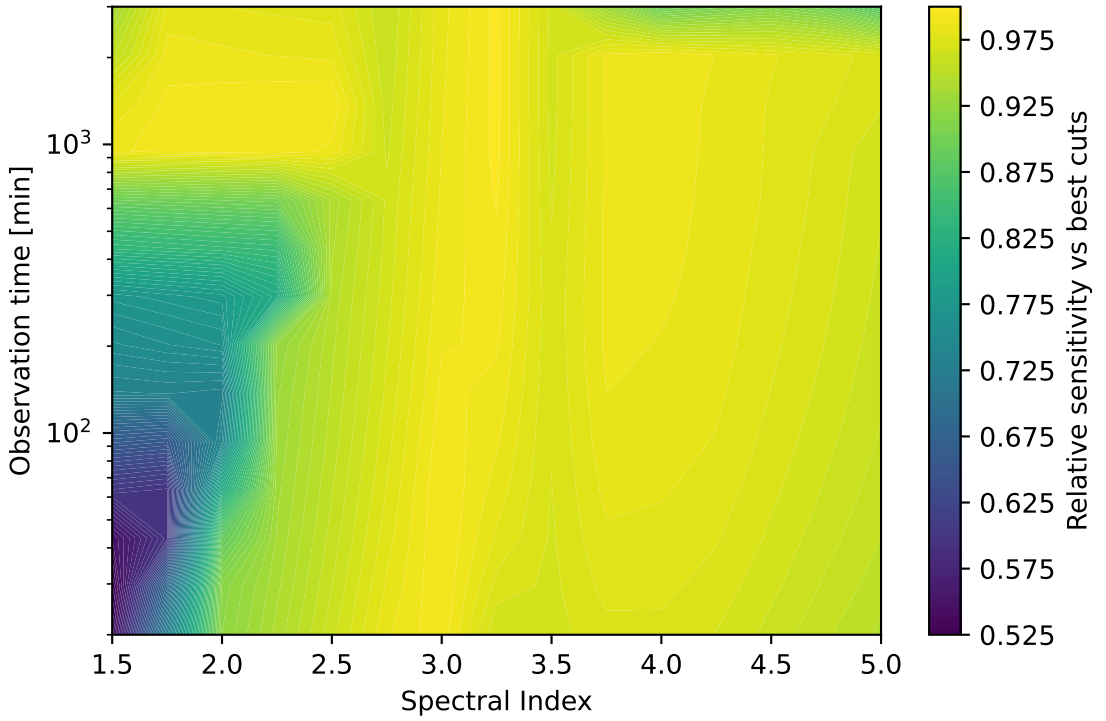

Figure 13.5: Relative sensitivity for the best of all the final cuts compared to the one tailor-made for each source.

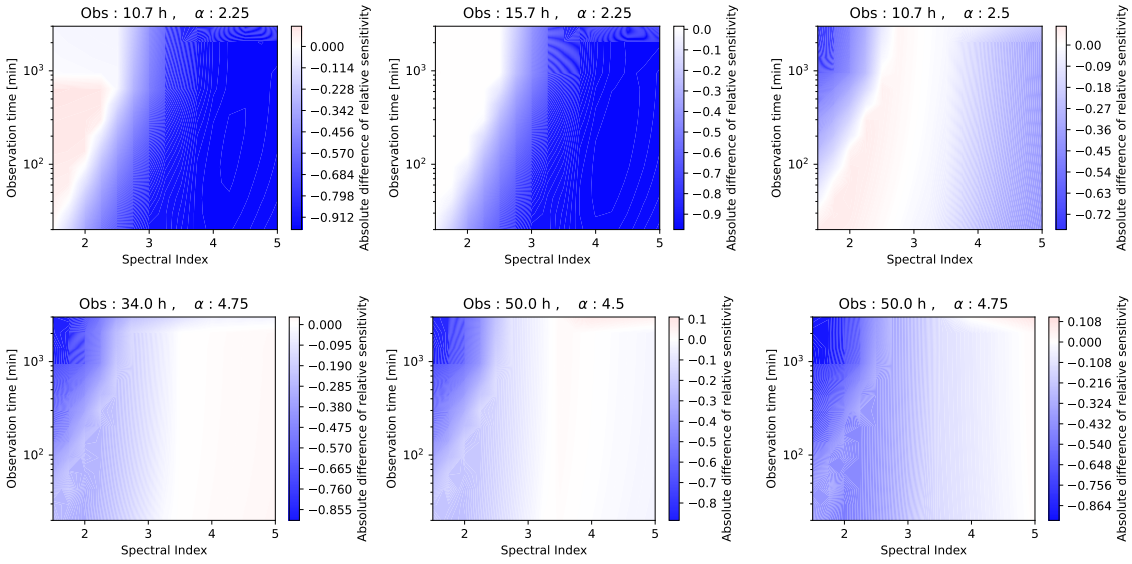

Figure 13.6: The difference of relative sensitivity compared to best cuts for the cuts optimised for global performance and the one for one specific source. The source used is indicated on top of each panel. The red color means better performance than the global cuts and blue worse performance.

and degrade performance for most soft sources with any observation time.

To conclude, testing cuts on only one source for each cut configuration will likely provide not

as optimal performance for all categories of sources with the method used here. Especially as seen above, some minor differences in the source parameters could lead to vastly different cuts and performances.

13.4.1 Instrumental response functions

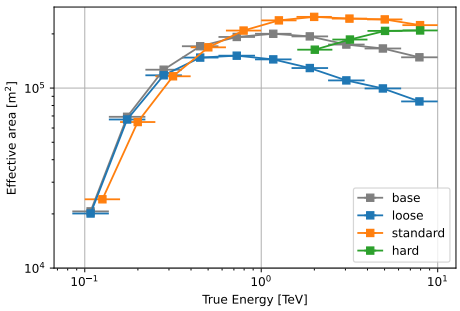

(a) Effective area

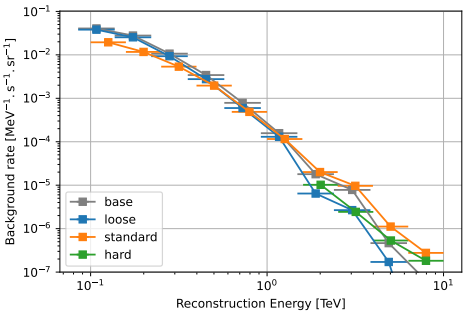

(b) Background

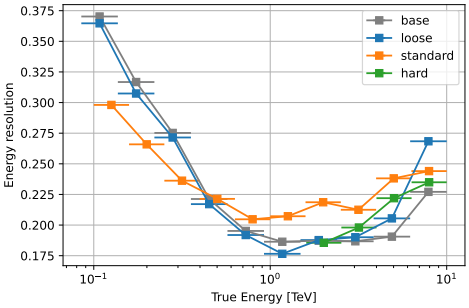

(c) Energy resolution (68% containment)

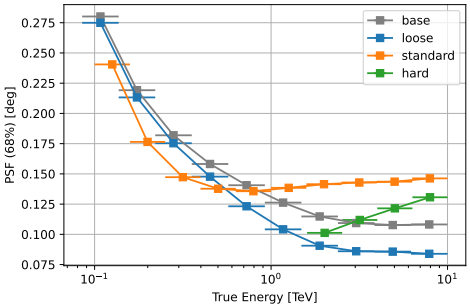

(d) Angular resolution (68% containment)

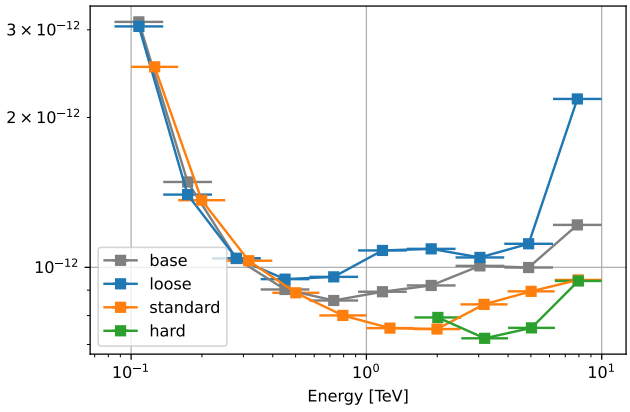

(e) Differential sensitivity for 20 h of observation

Figure 13.7: Instrument response functions as a function of the energy for the three different cuts.

In figure 13.7 is represented by the IRFs obtained for each cut configuration: Effective area, Background rate, Energy and Angular resolution and Differential sensitivity.

The effective area of `Loose` cuts is much better at low energy due to the lower gammaness and intensity cuts, while the effective area at high energy of `Standard` and `Hard` cuts is significantly

better due to the higher upper limit on the leakage. As expected, the background rate is significantly higher for `Loose` cuts at low energies. At high energies, `Loose` cuts will be anyway penalised by the low effective area explaining that the background rate could be a bit lower. The `Hard` cuts allow for lowering even a bit more the high energy background compared to `Standard` cuts. The energy resolution and angular resolution follow a similar pattern. The `Loose` cuts are worse at low energy but due to the more strict cut on the leakage perform better at high energy. Finally, as expected, the differential sensitivity of the `Loose` cuts is only better at low energy, while `Standard` cuts are better at intermediate energy and `Hard` cuts are the best at high energy. Since the optimisation is run on the integral sensitivity and not the differential one, this is likely not an issue. The `Base` cuts are quite close to `Loose` cuts and tend to perform slightly worse at low energy due to a higher background rate and a bit better at high energy.

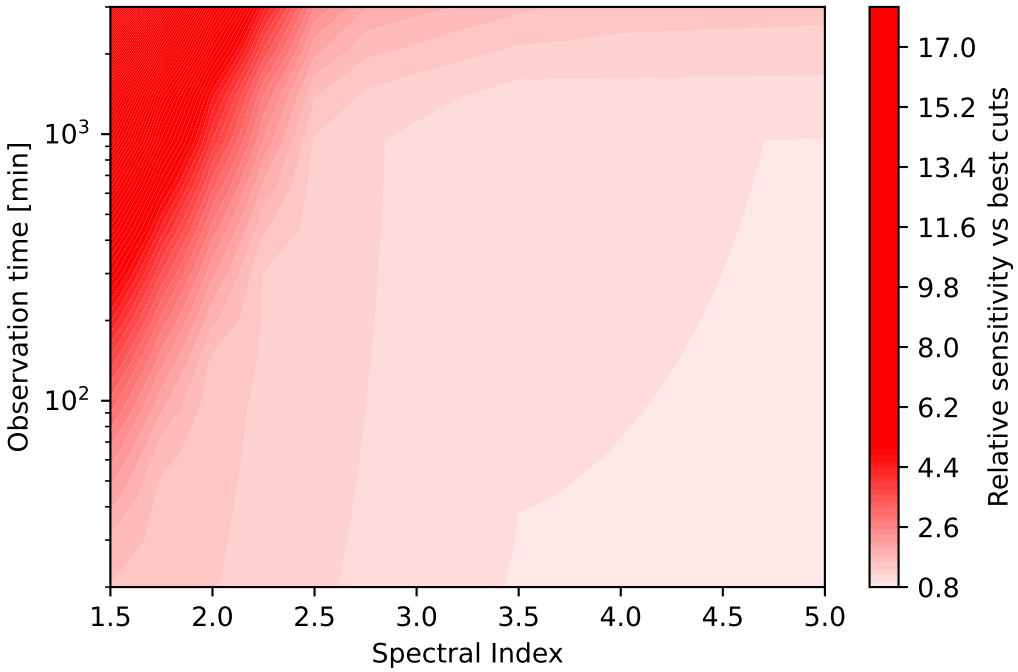

Figure 13.8: Relative difference of sensitivity of the `Base` cuts versus the best of three new cuts for each source

If we compare the performance for each source of the best of three cuts to the base cuts, we obtain figure 13.8. In a few cases, the base cut could be better by a few percent for the shortest observation times. However, for all the other cases, these new cuts are better, with more than 10% better sensitivity for all non-soft sources and up to 17 times better performance for the hard sources with long observation time.

13.4.2 Application to LST-1 observations

To check performance on observational data, two datasets were selected. The first one on the Crab was the reference dataset at the time with 3.4 h of observation time with a zenith angle between 6 deg and 30 deg. The second dataset consist of 1.4 h of data on Markarian 421 with a zenith range between 25 deg and 45 deg. The Monte Carlo used to train the random forest and to perform the optimisation were generated for a zenith angle of 20 deg and are from the standard production of LST.

Cuts	`Base`	`Loose`	`Standard`	`Hard`
Excess	4382.3	2488.3	2481.6	93.8
Background	4992.7	1734.7	932.4	2.2
Significance	47.2 σ	45.6 σ	55.5 σ	17.3 σ

Table 13.2: Results of the different cuts on the Crab

Cuts	`Base`	`Loose`	`Standard`	`Hard`
Excess	984.1	566.7	559.2	13.2
Background	2374.9	821.3	471.8	4.8
Significance	16.5 σ	16.4 σ	20.1 σ	4.5 σ

Table 13.3: Results of the different cuts on Mrk 421

The Crab is the reference source in Cherenkov astronomy with relatively hard and curved spectra (Aharonian et al., 2006). Markarian 421, is an BL Lac object which underwent several flaring episodes and presents spectral variability with an index from 1.9 to 2.7 (Acciari et al., 2014). With these observation times and the spectra of these sources, we could expect the `Standard` cuts to be the best performer.

The results are shown in tables 13.2 and 13.3 which give the number of excess photons, the background rate and the total significance. For both sources, the results are pretty similar. The `Standard` cuts are effectively the best performers, with $\sim 40\%$ better performance than `Base` or `Loose` cuts. These last two cuts provide similar performance but with a much higher background and excess for the `Base` cuts, lowering the signal-to-background ratio. It is interesting to see that `Standard` and `Loose` cuts provide a similar excess but with a very different background for these sources. The `Hard` cuts performed quite poorly, but as the exposure time is relatively low, this is expected. They should provide better results on observation time of at least 10 h for fainter sources. The signal-to-background ratio of these cuts is really high with a nearly pure gamma-ray sample for the Crab.

13.5 Possible improvement

13.5.1 The need to increase the dimension explored

Since the start of this study, gammaness cuts dependent on the energy have started to be used in LST-1. This idea is quite interesting as the ability to separate gamma from cosmic rays depends on the energy (Fig. 13.9). If we compare it as a function of intensity, it seems to be even more related. Currently, the gammaness cut dependent on the energy is defined by requesting a fixed portion of gammas to pass the cuts for each energy bin. This method tends to bring a lot of background at low energy.

It would be worth exploring the same idea for other cuts and defining energy-dependent or intensity-dependent cuts. Also, other parameters could be a valuable addition such as the distance of the centre of gravity of the shower to the camera centre.

However, to explore all these directions, increasing the number of dimensions of the phase space would be necessary. The grid search previously performed has already been computationally demanding, and adding dimensions would make the grid too wide to both compute and store the results. A more efficient method for optimising the cuts would then be needed. The shape of the function minimised (the integral sensitivity as a function of the cuts) is quite complex and noisy due to the statistical fluctuation as it is computed from a limited number of simulated events. Consequently, the method needed for a larger number of dimensions must explore the phase space and be robust to local minimums.

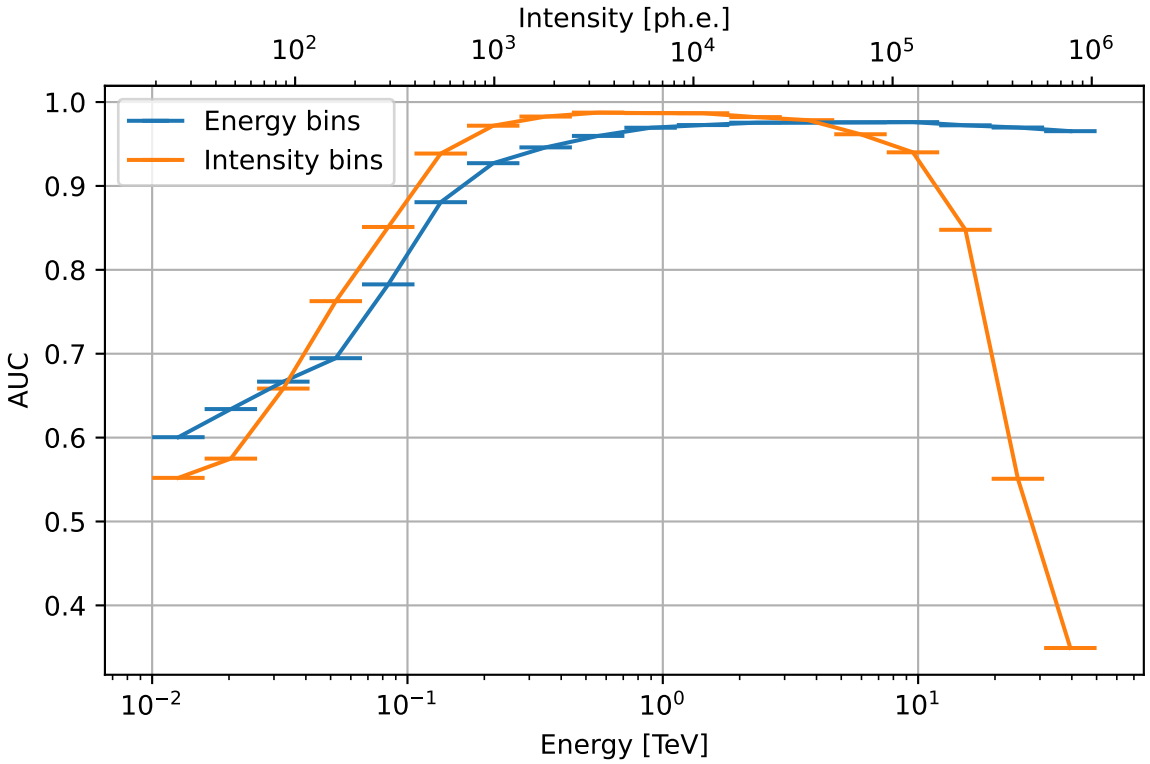

Figure 13.9: AUC for the classification gamma vs protons as a function either of the intensity (orange curve) or the energy (blue curve). The equivalence intensity - energy has been set in order to follow the heart of the distribution in the gamma Monte Carlo but is not a strict equivalence as the relation between the two is much more complex.

13.5.2 Selection of cuts using a minimiser

This section describes the search for a method to retrieve the same results as the one above. The first attempts based on Monte Carlo Markov Chains were quite unsuccessful. Some attempts using the MINUIT (James and Roos, 1975) algorithms using the `iminuit` python implementation (Dembinski and et al., 2020) showed some hint of convergence but with often different results at each run. Running algorithms multiple times with random starting points allowed to have a more stable convergence.

However, we need to estimate how many random starts are needed to achieve a good convergence. For all the results in this section, the convergence will be expressed as a function of how close the sensitivity of the best cuts found is compared to the absolute best sensitivity. This absolute best sensitivity will be computed using the best results from a very high number of starting points.

To perform some preliminary tests, we will only use three different sources and not a grid as before. Observation time will be one hour and spectral indexes will be 1.5, 3 and 5.

The main indicator we will use will be called relative convergence. This is the relative difference between the sensitivity obtained versus the best one achievable with this source and observation time. This value of the best achievable will be estimated using a very large number of starting points.

The tests can be done using random starting points but other methods such as low-discrepancy sequences or quasi-random sequences like the Sobol sequence (Sobol', 1967) can be used. This kind of sequence guarantees a better isodensity of the drawn points compared to a purely random distribution. Figure 13.11 is an example of a random sequence and a Sobol sequence which better explores the phase space.

The results of the convergence tests are shown in figure 13.11. As a function of the number of

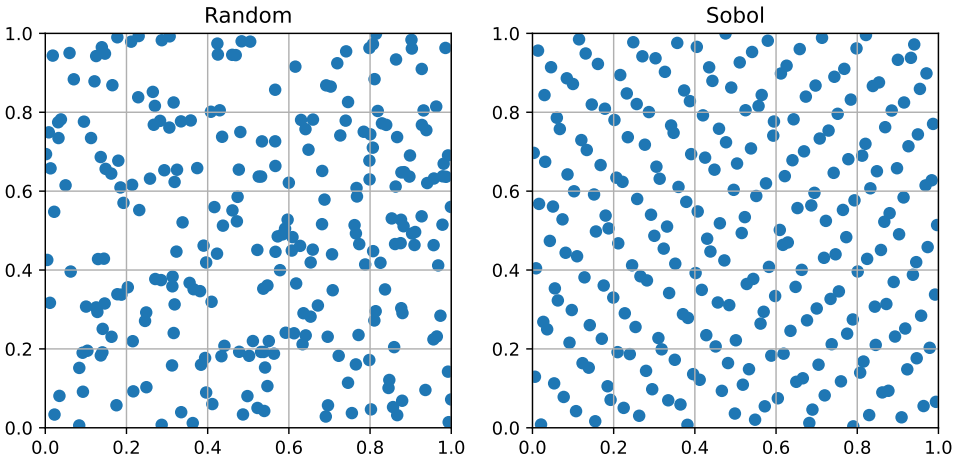

Figure 13.10: Representation of a 2D space with 256 points drawn, on the left using a standard pseudo-random algorithm and on the right Sobol sequence. Each axis of the 2D space is limited to values between 0 and 1.

starting points, the relative convergence is given. As expected, by increasing the number of starting points, a better convergence is obtained. This behaviour gives the general trend of the figure. We consider that we have a good convergence for a value of 1%, obtained for ~ 500 starting points in this case.

The convergence time to reach cuts that will give a sensitivity close to 1% to the absolute results in the case of the spectral index of 5 would still be around a few years of CPU time. If we apply it to the whole source grid, the computing time will start to be way too high to be able to study different cuts configurations.

The `scipy` (Virtanen et al., 2020) library proposes a collection of different minimiser algorithms. The ones that are suitable for a problem with constraint were all tested. The length of the Sobol sequence for the starting point was dependent on each algorithm as a function of their running time. For each algorithm, 6 Sobol sequences were used to estimate the dispersion. Figure 13.12, which is similar as figure 13.11, presents the results with the convergence as a function of the computing time required. The more an algorithm is on the lower left of the graph, the better it is. The dashed line is a linear fit of the data of the same colour. The Nelder-Mead method (Nelder and Mead, 1965) seems to be the one best suited.

For this Nelder-Mead method relaunching the algorithm from the final point could significantly improve the results. This was added and is the grey line on the figure. With this method, it is finally possible to reach a convergence to cuts that give a sensitivity of around 1% of the best possible in a manageable amount of time.

13.6 Future of this work

Now that a method to extend the work is identified, the next step would be to explore the different possibilities of gammaness cuts dependent on either the intensity or the energy. It could also be interesting to explore cuts theta cuts dependent on the energy as the PSF changes a lot in function of the energy.

The background model used is actually based on the Monte Carlo simulations. The accuracy of this background model has not been validated. A first implementation was able to use real data to make this model, but as it was very slow compared to the ones from Monte Carlo, it was put aside. When a cut configuration is identified, comparing results from optimisation on observation data and Monte Carlo will be necessary to assess the absence of systematic error.

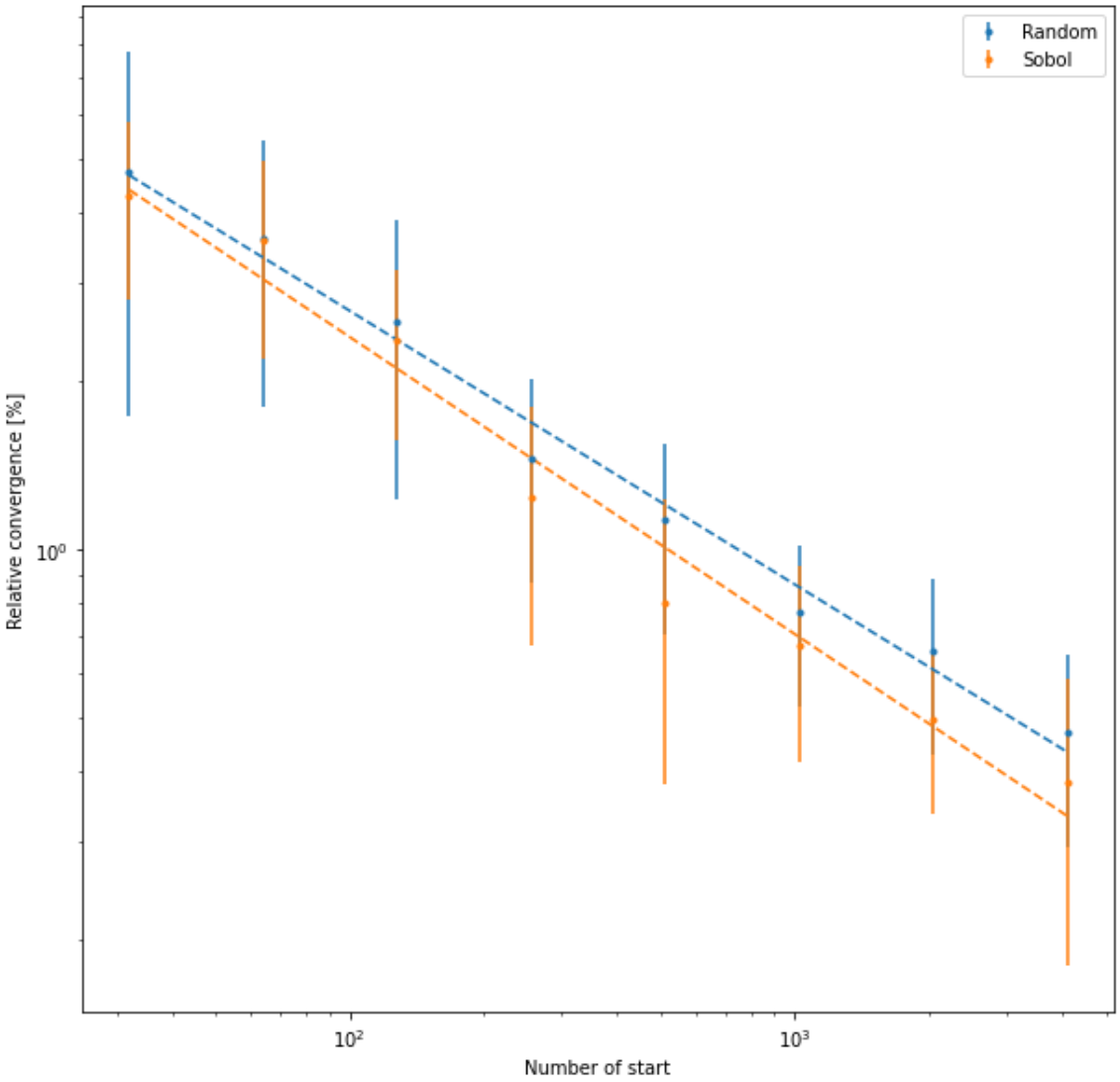

Figure 13.11: Convergence to the best cuts for the iminuit minimiser using a random starting point or Sobol sequence as starting point.

The scheme of the Monte Carlo simulation used in LST-1 has also changed a bit. This work was performed using Monte Carlo simulation at a zenith angle of 20° and an azimuth angle of 180°. The Monte Carlo used to generate IRFs is now across the whole sky but with only gammas simulation. The random forests are trained per declination band. Some reflection would be needed to optimise cuts for this new, more complex situation.

Finally, the cuts will need to be tested on a larger observation dataset to confirm the performances. The code is able to take any DL2 format, so it will be possible to run the optimisation for other reconstructions like deep learning, template-based or Real-Time Analysis.

If needed in the future, the method could also be extended to optimise not the sensitivity, but the angular or energy resolution with a constraint on the loose of sensitivity compared to the cuts focused on sensitivity.

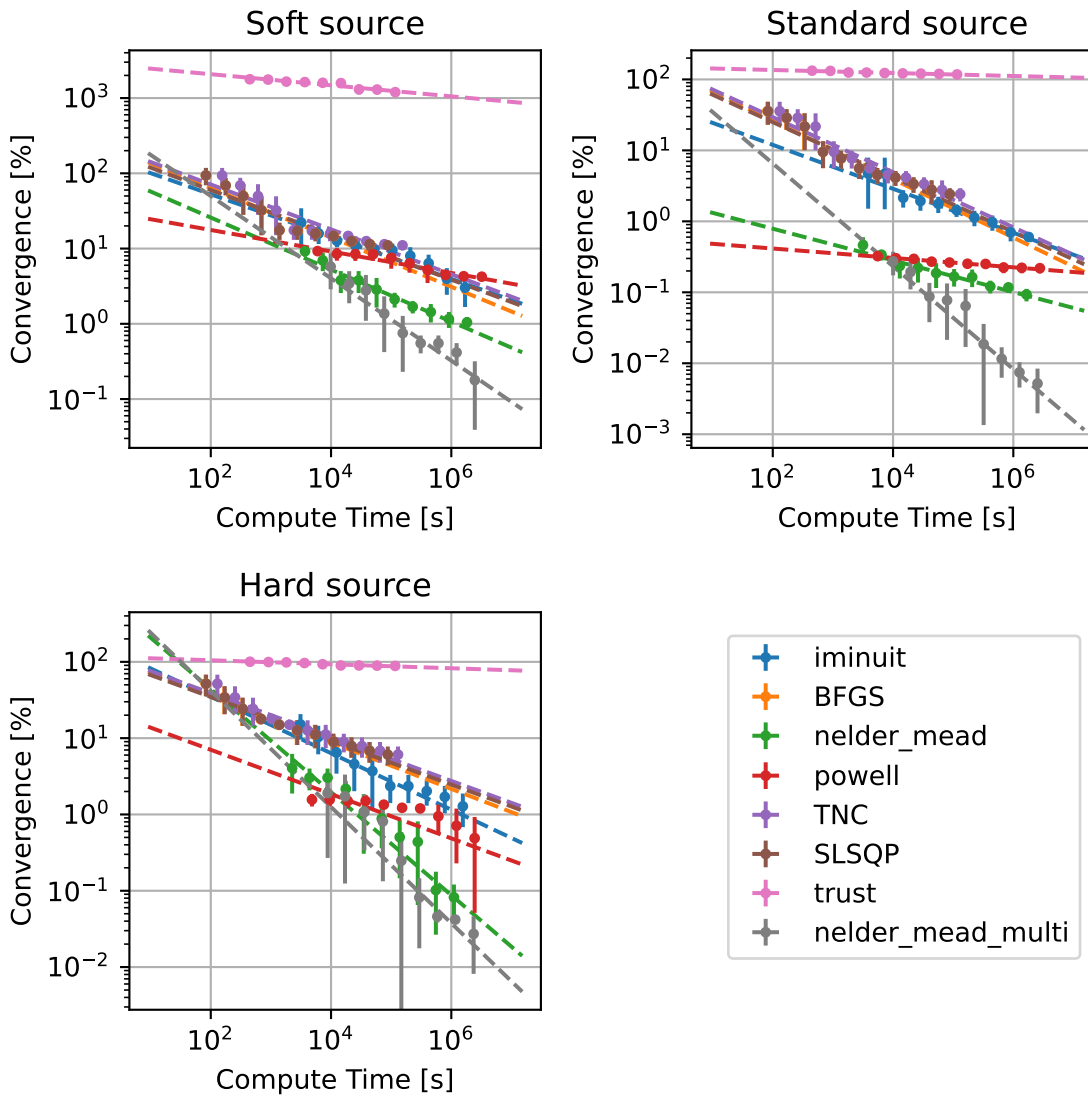

Figure 13.12: Convergence to the best cuts for the several different minimisers using Sobol sequence as starting points. The top left panel is for the case of a soft source, the top right for a standard source, and the bottom left for a hard source.

Chapter 14

Creation of an acceptance model for LST-1

Contents

As mentioned in the chapter 12, the determination of the acceptance is a key element to evaluate the background and producing sky maps to search for sources.

At the start of this work, no acceptance model for LST-1 existed. The first observations of LST-1 were on the Crab Nebulae, AGNs or GRBs with a well-known position, so using only the multiple OFF methods was fine.

In May 2021, LST-1 performed a follow-up observation of GRB 210515B. With the alerts coming from *Fermi*/GBM, the localisation of these GRBs was highly uncertain. Consequently, the GRB could be anywhere in the field of view of the instrument (or even outside). It was then necessary to make an acceptance model that could be used to make a skymap in order to search for a TeV counterpart from this GRB.

14.1 Algorithm for computing acceptance map

14.1.1 A 2D acceptance model

The basis of the algorithm is strongly inspired by the radial acceptance use in H.E.S.S. (de Naurois, 2012) but with a few differences, mainly to manage more easily any shape and number of exclusion regions. An exclusion region is a part of the sky on the FoV that is excluded from the acceptance

calculation mainly because a known source is present. Typically, an exclusion region is placed at the position of a possible source.

The algorithm produced is a 2D model with one dimension for the offset in the field of view compared to the camera centre, one dimension for the energy. As a consequence, the model assumes that the acceptance has a circular symmetry.

All the figures illustrating the algorithm working principles have been generated using data from the public H.E.S.S. DL3 DR1 data release (Collaboration, 2018). From this dataset, the four runs on the Crab have been used. One advantage of this dataset is that two runs have been taken with an offset of 0.5 deg and two with an offset of 1.5 deg. This difference allows a more straightforward checking that the algorithm works with any source position. An exclusion region of 0.5 deg around the Crab has been used.

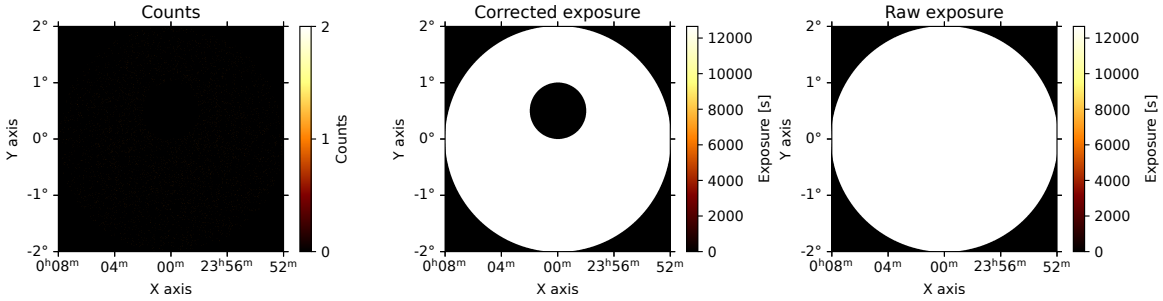

Figure 14.1: The count maps (left panel), the corrected exposure map (centre panel), and the raw exposure map(right panel) for only one run. The hole in the count map and corrected exposure map is due to the exclusion region.

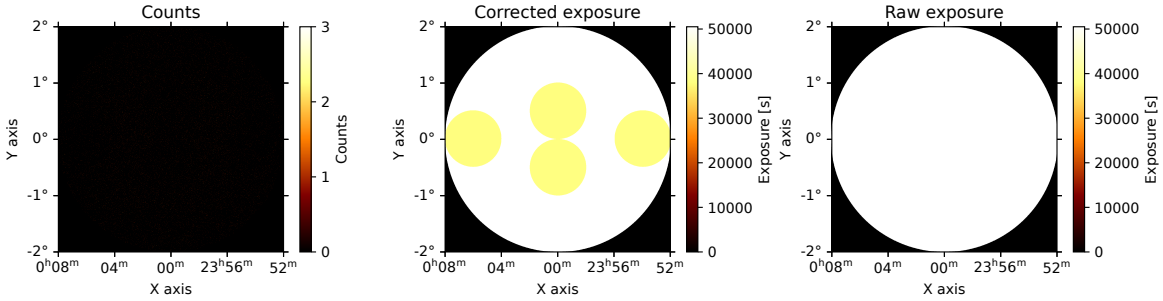

Figure 14.2: The count maps (left panel), the corrected exposure map (centre panel), and the raw exposure map(right panel) for all the runs. The holes in the count map and corrected exposure map are due to each run's exclusion region.

Details of the algorithm used for the computation of the acceptance model:

1. The model is computed in several energy bins, so 3 finely binned (in space and energy) maps of the FoV are used : a count map, a map with the raw time exposure, and the last is the same but corrected for any exclusion region. This map is called a corrected time exposure map. The bin size needs to be small compared to the model's final bin size and the exclusion region but not too small to minimize memory footprint and computing time.

2. For an observation run, The count map is filled with the events and the value of both the exposure time maps are set to the livetime of this run.

3. Pixels in the count map and the corrected time exposure map, that are within an exclusion region, are set to zero. The figure 14.1 presents an example.

4. The process is repeated for all the observation runs to have a map per run.

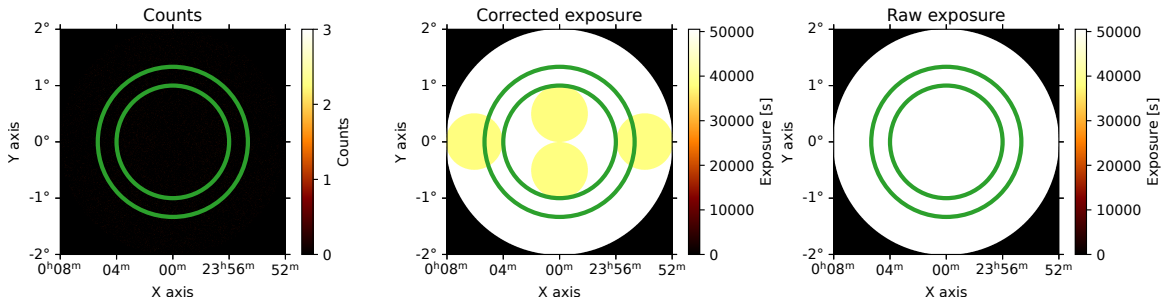

Figure 14.3: The count maps (left panel), the corrected exposure map (centre panel), and the raw exposure map(right panel) for only one run. The annulus represents the region that will be integrated into the current offset bin.

5. All the run-by-run maps are stacked together, and the Fig. 14.2 is obtained. The count maps contain a raw number of event N_{raw} per bin.

6. An annulus at an offset o is defined to fill the offset bin o. The sum of the pixels falling in this annulus is computed for each map (Fig. 14.3). This is where the radial symmetry assumption is used.

7. N_{raw} is corrected by the ratio between the time exposure Exp_{raw} and the corrected time exposure Exp_{corr} :

$$N_{\text{corr}} = N_{\text{raw}} \frac{Exp_{\text{raw}}}{Exp_{\text{corr}}}$$

8. `Gammapy` expects a model that gives in each bin the background count rate per solid angle bin and per energy bin. So, then the solid angle Ω of the annulus of a given offset bin could be computed with :

$$\Omega = 2\pi \left(\theta_{max} - \theta_{min}\right) \frac{\theta_{max} + \theta_{min}}{2}$$

With θ_{max} and θ_{min}, the maximum and minimum offset of the current bin. Finally, the background in the bin $BkgRate$ could be estimated with the following formula :

$$BkgRate = \frac{N_{corr}}{\Omega T_{Obs} \left(E_{max} - E_{min}\right)}$$

with T_{Obs} the total observation time and E_{max} and E_{min} the maximum and minimum energy of the current energy bin.

Finally, we obtain a 2D model of which an example is given in figure 14.4). It could then be used for an analysis to perform the acceptance correction in the ring background estimation method (this is entered in the computation of α; see chapter 12 or as a direct estimation of the background. Figure 14.5 shows the results with the Crab data present in the H.E.S.S. DL3 DR1 when used in combination with a ring background estimation. The background is well normalized with a mean of zero and a variance of 1. Therefore, the algorithm is capable of correctly describing the background of the observations.

14.1.2 Improvement to the model

The algorithm above gives one model that results from stacking all the observation runs, and this model is then used for all the observations. It guarantees the minimisation of statistical fluctuation of the model but could bring huge bias if the observation conditions change dramatically during the data taking.

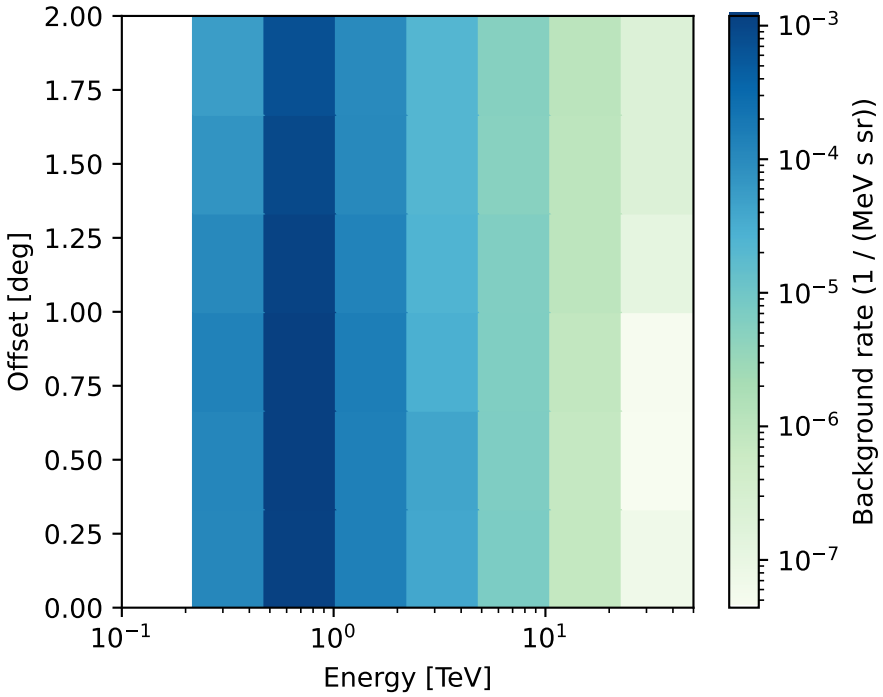

Figure 14.4: The resulting model as a function of the offset and the energy.

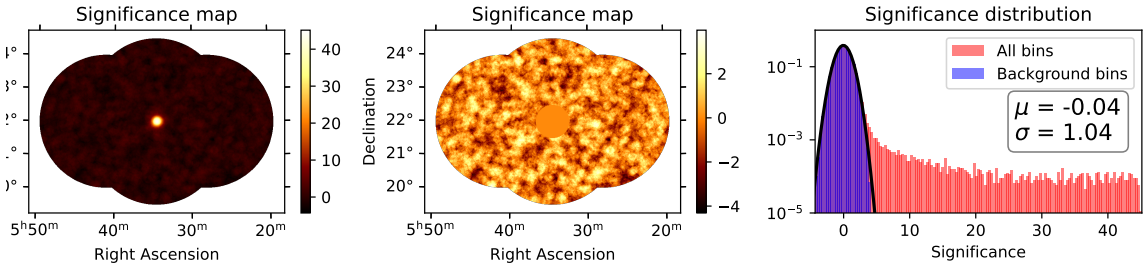

Figure 14.5: The significance map (left panel), significance map without the exclusion region (centre panel) and significance distribution (right panel) for a ring background analysis after applying the algorithm described above. The Crab region has been masked in the second panel to better visualize the background.

One of the most critical parameters is the zenith angle of observations. A different zenith angle means a different airmass and, in consequence, a massive impact on the performance and behaviour of the instrument. The variation of performance is more closely proportional to the cosinus of the zenith angle than the zenith angle itself, as the airmass is inversely proportional to the cosinus of the zenith angle.

The observations runs are therefore binned as a function of the cosinus zenith angle. For each bin, a model is computed using the algorithm described above, and an interpolation between the different bins is done. In the case of a small number of runs with a small zenith dispersion, it is better not to use this correction.

The final step is to normalise the model to the observations. This is performed even if the zenith binning step is deactivated and then performed for all the observations.

14.1.3 Implementation

All the implementations have been performed in Python. The code has been designed to be easily integrated into a gammapy analysis workflow by using as input and output gammapy objects that could be directly used for the analysis. The code has mainly been tested on LST-1 data, but, in principle, it should work with any IACT data. It is accessible to everyone on GitHub[1].

14.2 Results

14.2.1 Test of the background model with a ring background analysis

To test the model, several datasets from LST-1 were used. The data were taken during dark time and reconstructed using the standard reconstruction pipeline. In each case, an excess and a significance skymap are generated using a correlation radius of 0.2°. The analysis has been performed using either a very large energy bin (0.05 TeV-10 TeV) or four smaller energy bins to allows to check the model's performance as a function of the energy.

The analysis is performed with `Gammapy`, using as background estimation method a ring background (presented in chapter 12). So, the model will only be used as an acceptance model for correcting the difference in acceptance between the different parts of the field of view.

The dataset contains two fields of view with known, bright and extragalactic sources, Markarian 421 and Markarian 501, and seven other observations (dark patches or GRB follow-up) used as dark FoV. The dataset also included four runs taken on Crab at a very high offset and at a high zenith range. The aim is to test a vast field of view like the ones expected from future tilling follow-up observations of gravitational waves alert or poorly localized GRB.

In order to assess the quality of the background model, for each analysis, a gaussian fit of the distribution of the significance of the map was performed (with the exception of the exclusion region for the sources). A background that is purely caused by Poisson noise should give a gaussian distribution with the centre of the distribution μ equal to zero and the width σ equal to one. Results are reported in table 14.1, where the mean μ and the variance σ are given for each case.

The standard Crab observations were not included as they were significant spillover of the source compared to the exclusion regions. Similar effects could be seen on the Markarians like in the figure 14.6 with, as seen on the significance map, some signal remaining outside of the exclusion region. This effect for the Markarians was small enough not to have a major impact on the results, while the model was hugely biased for the Crab. Due to the small offset of the observations, increasing the size of the exclusion region was not possible.

[1] https://github.com/mdebony/acceptance_modelisation

Name dataset	Livetime	Zenith range	Results by energy range									
			50 GeV-10 TeV		50 GeV-190 GeV		190 GeV-710 GeV		710 GeV-2.7 TeV		2.7 TeV-10 TeV	
			μ	σ	μ	σ	μ	σ	μ	σ	μ	σ
Markarian 421	6.0 h	9.0°-28.0°	-0.05	1.30	-0.03	1.13	0.25	1.19	-0.02	1.20	-0.10	1.01
Markarian 501	9.0 h	11.0°-28.5°	0.03	1.45	0.01	1.33	0.40	1.36	0.05	1.21	-0.01	1.00
Dark Patch 5	1.0 h	9.9°-15.1°	-0.04	1.11	-0.03	1.08	0.12	1.04	0.00	0.96	-0.12	1.02
Dark Patch 8	4.0 h	10.2°-44.6°	-0.08	2.06	-0.12	2.06	0.62	1.65	0.04	1.04	-0.08	0.99
Dark Patch 29	4.7 h	9.3°-64.9°	-0.18	1.74	-0.02	1.76	-0.05	1.36	0.03	1.11	-0.04	1.06
GRB 210704A	0.9 h	53.0°-59.7°	-0.04	1.06	-0.08	1.06	0.11	1.04	-0.01	1.08	-0.08	1.03
GRB 210731A	1.0 h	56.4°-60.2°	-0.06	1.06	-0.12	1.10	0.09	1.00	0.00	0.98	-0.03	1.10
GRB 210807A	0.4 h	55.1°-56.7°	-0.0	1.15	-0.08	1.01	0.09	1.13	0.00	0.99	-0.06	0.99
Crab Very High Offset	1.0 h	56.6°-70.1°	-0.04	1.05	-0.03	1.02	-0.00	1.01	-0.05	1.03	-0.14	1.03

Table 14.1: Details of the dataset used for testing the acceptance model and the performance associated with a ring background analysis

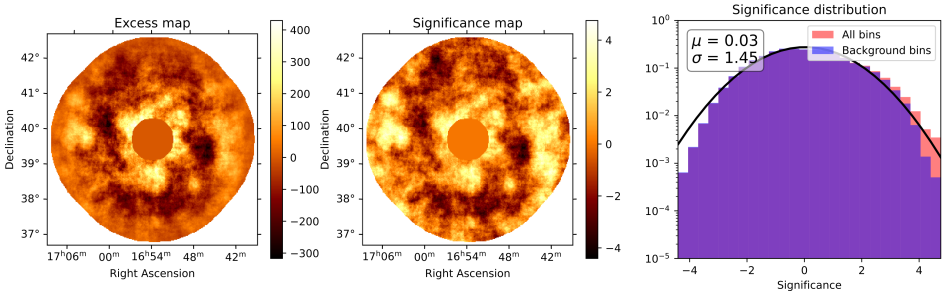

Figure 14.6: Observations on Markarian 501, the excess map (left panel), significance map (centre panel), and significance distribution (right panel) with a ring background analysis between 50 GeV and 10 TeV. The source region has been masked to visualize the background better, and some spillover from the source could be seen close to the exclusion region.

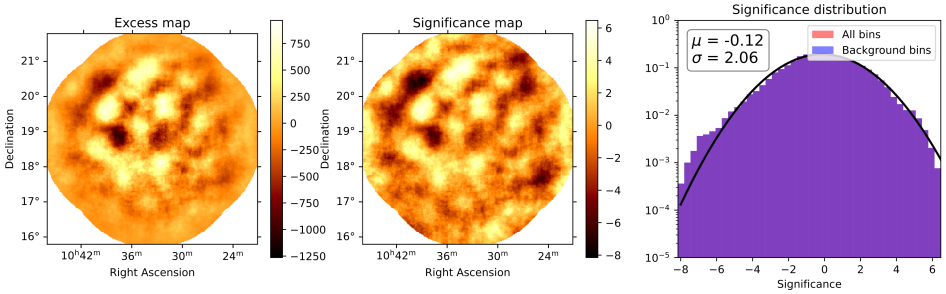

Figure 14.7: Observations on Dark Patch 8, the excess map (left panel), significance map (centre panel), and significance distribution (right panel) with a ring background analysis between 50 GeV and 190 GeV. For this dark patch, the background is poorly described, and some deviation from the gaussian distribution could be seen.

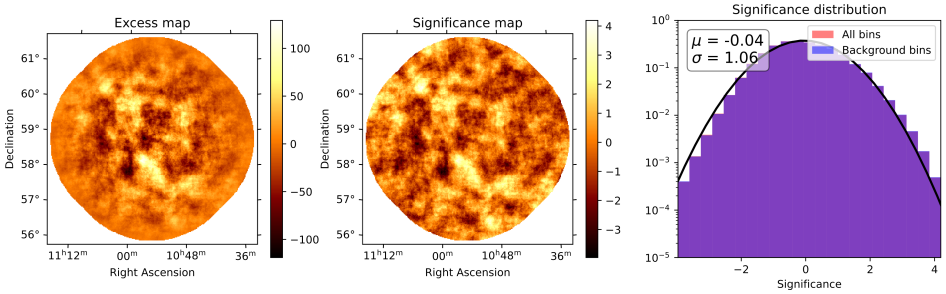

Figure 14.8: Observations on GRB 210704A, The excess map (left panel), significance map (centre panel), and significance distribution (right panel) with a ring background analysis between 50 GeV and 10 TeV. The background is well described for this GRB observation and follows a gaussian distribution.

In most cases, the centre of the distribution is close to zero. It is also possible to notice that the distribution is good enough for a short exposure time to perform source research in the field of view (Fig. 14.8). In the case of the Markarians, the distribution width indicates that some hotspots could reach the traditional significance threshold but are not real and purely background fluctuation. In the case of a hotspot close to the detection threshold, some dedicated verification would be strongly needed. Finally, for Dark Patch 8 and 29 at low energy, the distribution differs significantly from a gaussian one (Fig. 14.7). At higher energies, the situation improves and a good background description is obtained at the highest energies. Due to the very wide zenith range, this indicates that some improvements are still needed in order to achieve a good background description at low

energies.

14.2.2 Use of the model as a direct background estimation

The model obtained can be directly used as an estimation of the background and is then call FoV Background. The results with FoV background are all significantly worse, and most of the time, it was possible to identify some issues like gradient across the field of view (Fig. 14.9). This is not unexpected as the model has only one spatial dimension and is unable to describe such effects.

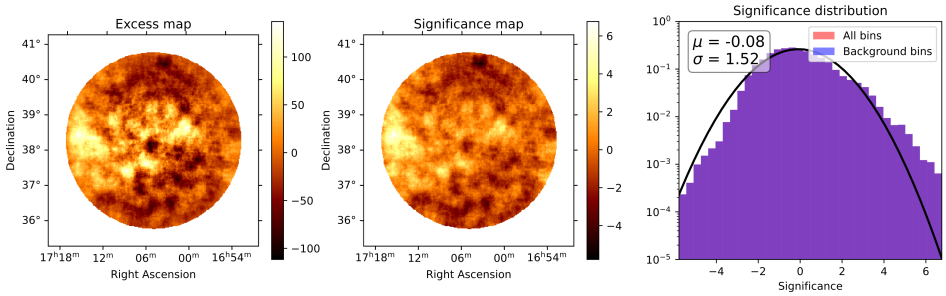

Figure 14.9: Observations on Dark Patch 5, the excess map (left panel), significance map (centre panel), and significance distribution (right panel) with a FoV background analysis between 50 GeV and 10 TeV. For this dark patch observation, the background is poorly described with a FoV background analysis with an important deviation from the gaussian distribution. Some significant gradients in the excess and significance map could be observed.

14.2.3 Results on GRB 210511B

As exposed above, the objective was to search for a counterpart to GRB 210511B. As the dataset is relatively short with a live time of 1.2 hours, the background model algorithm is good enough to search for a counterpart when combined with a ring background analysis. Such analysis was performed, and in the lowest energy bin (50 GeV-190 GeV), a small excess of 5.2σ appeared (Fig. 14.10). There was also an excess of 2.3σ at this position in the energy bin just above (190 GeV-710 GeV). An analysis using multiple off background estimations confirmed an excess of 5.5σ for events below 300 GeV. As there were many trials due to the map generation and multiple energy bins, the total significance post-trial is 4.4σ. This hotspot is not the GRBs searched as the localization is not compatible with the best localization of the event (which is outside of the field of view). It is still not clear if the signal is a real one. The excess is only present at low energies where some external factor like stars could the most easily create a fake signal. Some detailed quality checks were performed, but no instrumental explanation could be found. In the hypothesis that this is an astrophysical signal, there is no obvious counterpart found in several catalogues (4FGL-DR2, TeVCat, ANTF, ROSAT, AGN in NED or Simbad). The lack of detection by *Fermi* of such a soft source (photon index : 4.3 ± 0.5) would indicate that if it is an actual signal, it is a transient one caught by luck during the observations.

14.3 Future of acceptance model in LST-1

Combined with a ring background analysis, this first acceptance model can give reasonable background estimations on short observations. This acceptance model is already usable to search for a counterpart to poorly localised transient events where the observation time is usually short. The hotspot detection confirms this in the observations of GRB 210511B. Even if the astrophysical origin of this hotspot is still questionable, it was not created due to the issue of the background model, as it was confirmed with a multiple-off analysis. On longer observation time, the analysis would need to focus mainly on the high energies to have an acceptable background description.

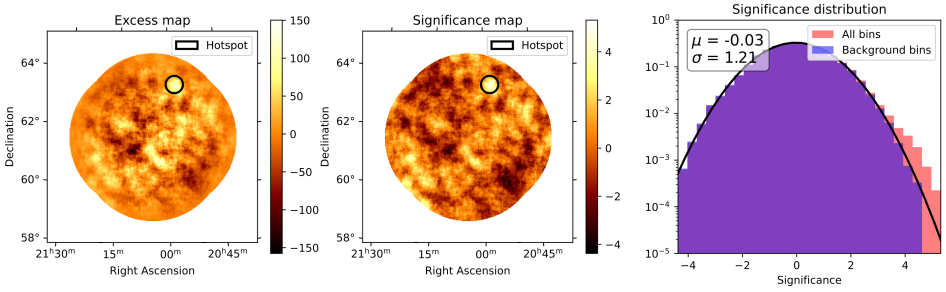

Figure 14.10: The excess map (left panel), significance map (centre panel), and significance distribution (right panel) with a ring background analysis for observations of GRB 210511B. The detected hotspot is indicated in the figures. The best localisation of the GRB is outside of the field of view

A first way to improve results would be to solve the issues observed on the observation of Dark Patch 8 and 29, likely caused by the effect due to the description of the behaviour of the background in the function of the zenith angle. This could be due to the model or ring background analysis itself. Currently, the ring background is performed on the stack of all the runs, as performing it run-wise causes an error in `gammapy`. This needs to be investigated further.

The analysis performed using FoV background estimation showed some systematic effects with often gradients across the field of view and sometimes some features at a smaller scale. This does not affect ring background analysis as the technique is only local, so large-scale effects have a minimum effect on the results. Generating a 3D model with two spatial dimensions could solve the issues seen on FoV background and even improve some results obtained on large offset.

Also, in the context of this work, two contributions have been made to the `gammapy` to help improve analysis based on the ring background method.

Finally, since the start of this work, other projects on LST-1 have started and tried different algorithms to provide a background model. I have written a benchmarking tool that could run analysis automatically on a large number of datasets. Any algorithm could be connected to the tool, allowing them to be compared. Most of the presented results have been obtained using this tool, but no comparison between algorithms has been performed yet.

Chapter 15

Comparison of deep learning reconstruction to Hillas reconstruction

Contents

The Hillas reconstruction is a robust and efficient way to reconstruct events from IACT. However, due to the simple parametrisation of the shower, a lot of information contained in the image is lost during the reconstruction process. Template-based reconstruction, which is used within the H.E.S.S. collaboration Model++ (de Naurois and Rolland, 2009) and ImPACT (Parsons and Hinton, 2014), allows to use more information in the image, improving sensitivity, angular and energy resolution. Nevertheless, these techniques come with a high computing cost that could be difficult to sustain for experiments like CTA.

With the rapid development of deep learning in the last ten years, helped by the development of GPU computing, this technique has started to raise interest among the community to be used for event reconstructions. Training has a considerable computing cost, but the inference on data is much less demanding than template-based reconstruction. The first attempts have been performed in the H.E.S.S. collaboration with a network that is only performing background rejection providing decent performance (Parsons and Ohm, 2020). There are several projects within CTA to reconstruct all the parameters using deep learning. This chapter presents the test of the application on observational data performed with one of the developed deep learning algorithms within CTA named Gammalearn.

15.1 The Gammalearn project

Gammalearn[1] is a project developed by a LAPP team that aims to perform event reconstruction using deep learning first for LST-1 and in the future for CTA. A brief overview of the working

[1] purl.org/gammalearn

principle will be presented here. For more details, it is possible to read the PhD thesis of Mikaël Jacquemont (Jacquemont, 2020).

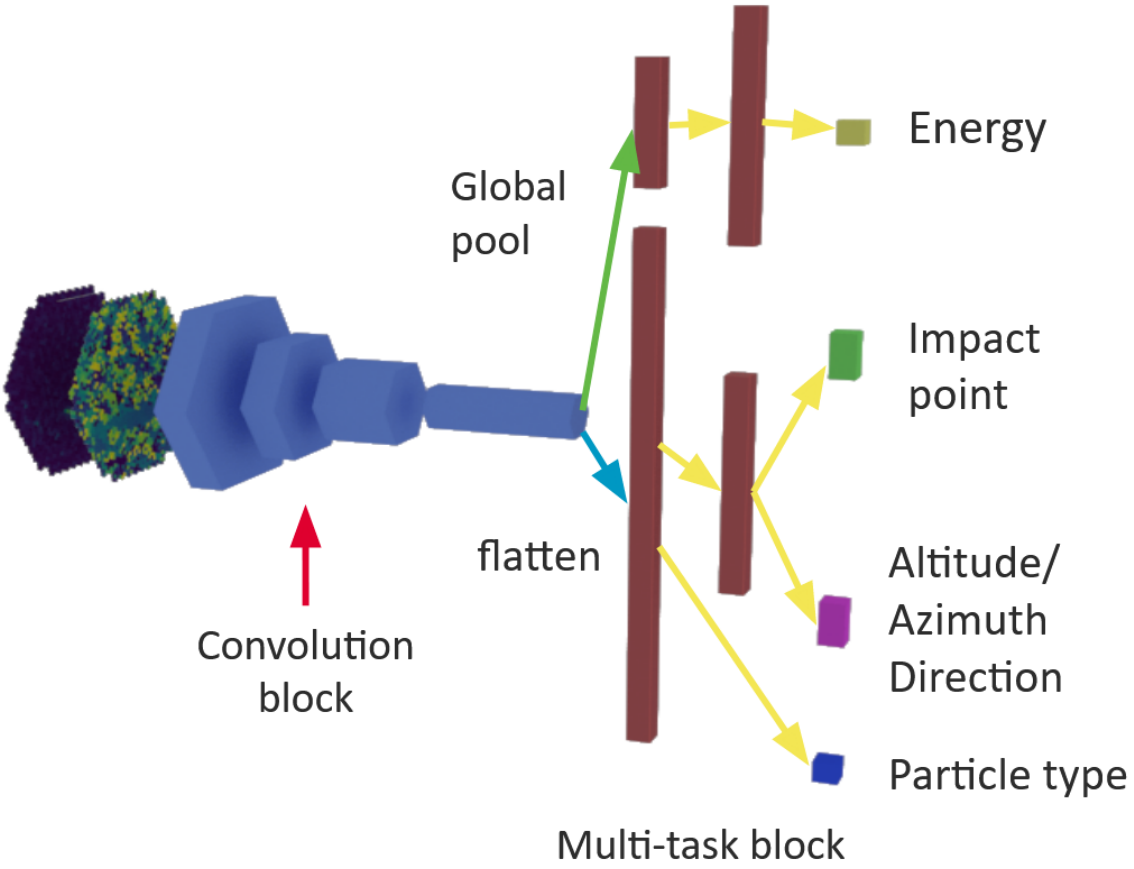

Figure 15.1: The γ – PhysNet convolutional network. It takes as input the integrated charge and the arrival time and outputs all the reconstructed parameters. Figure from Jacquemont et al. (2021a)

The reconstruction uses a convolutional neural network called γ – PhysNet (Fig. 15.1). As input, the network takes for each pixel the integrated charge and the arrival time information. The network is inspired by the network ResNet 56 (He et al., 2016) and is composed of several layers. The first ones are convolutional layers, and they extract learned features from the images. The second part is composed of fully connected layers. Compared to other works, one of the particularities of this network is that it is a multiple-task network, so instead of training one network for each task (i.e. classification, energy and direction determination), it can perform all these tasks on its own. This allows faster training but also as the tasks are linked, better performance of the network.

Compared to Hillas, the parametrisation step is entirely skipped. This way, the network uses all the information contained in the images.

On Monte Carlo simulation, the network shows a significative improvement compared to the standard analysis using Hillas parametrisation and random forest, as can be seen in Fig. 15.2. The gammmaness cuts have been optimised per energy bins to get the best significance for the Crab spectra. The improvement could be seen for all parameters (energy, direction reconstruction, and background rejection), and γ – PhysNet is even more performant at low energies. This leads to sensitivity improvement across the whole energy range and up to one order of magnitude improvement at low energy. Such improvement could be explained by the combination of better background rejection and a better angular resolution to integrate less background for the same quantity of integrated signal.

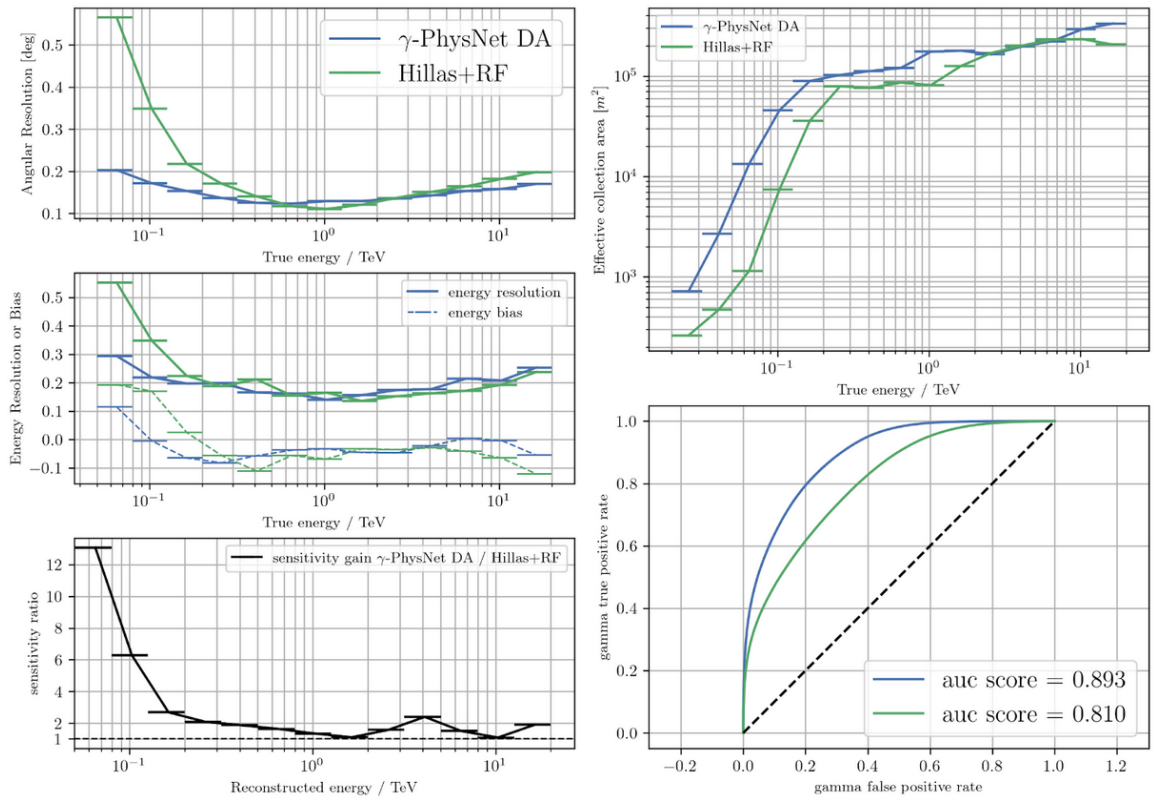

Figure 15.2: Instrument response functions for reconstruction with $\gamma -$ PhysNet and Hillas+RF with cuts optimised per bin to get the best sensitivity in each bin. Figure from CTA-LST Project et al. (2022a)

15.2 Comparison procedure on observations

The process to perform event reconstructions and produce DL3 is nearly the same as for the standard Hillas analysis used in lstchain (described in chapter 12). The only difference is the replacement of the step DL1 to DL2.

The dataset used is composed of 11 runs on the Crab during the night of the 11th November 2021 for a total duration of 3.4 h and a zenith angle between 6.5° and 30°, and 4 runs on Markarian 501 taken on the night of 20th March 2021 for a total observation time of 1 h and a zenith angle between 12.5° and 20°.

One specificity of the dataset on the Crab is the higher NSB than usual data taken on extra-galactic fields. This is due to the much higher star density on the galactic plane. As deep learning tends to be quite sensitive to the difference between training data and observational data, specific training of the network has been performed with some Poisson noise added to the Monte Carlo images in order to match the NSB of the field of view. The effect on simulations can be seen in figure 15.3, which shows the pixel charge for our data set and our simulations. The same operation was performed for the training of the Random Forest associated with the Hillas parametrisation. In each case, the comparison will be made with algorithms trained on Monte Carlo simulations with and without added noise.

To compare both pipelines, the chosen procedure is to determine gammaness cuts per energy bin in order to match the background rate. While this allows a direct comparison of the results, this will penalise the neural network, which tends to have a better background rejection.

Following the reconstruction, a classic analysis will be performed using gammapy. A multiple-off background estimation is used alongside a significance computation using Li&Ma (Li and Ma, 1983).

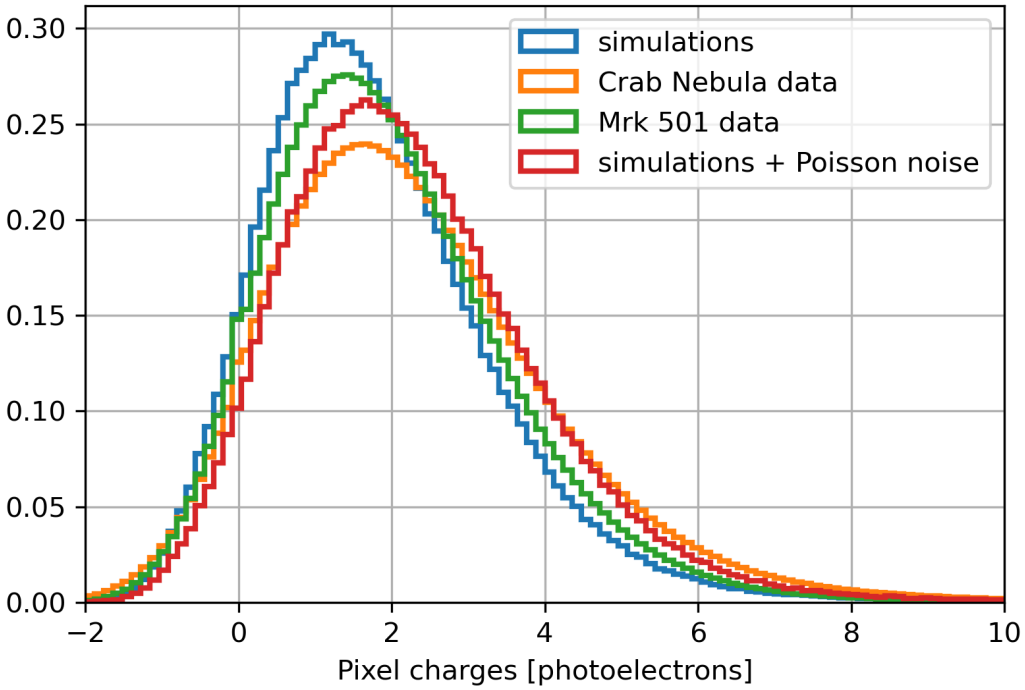

Figure 15.3: Distribution of the charge in the images obtained for the simulations and the two different field of views studied

15.2.1 Markarian 501

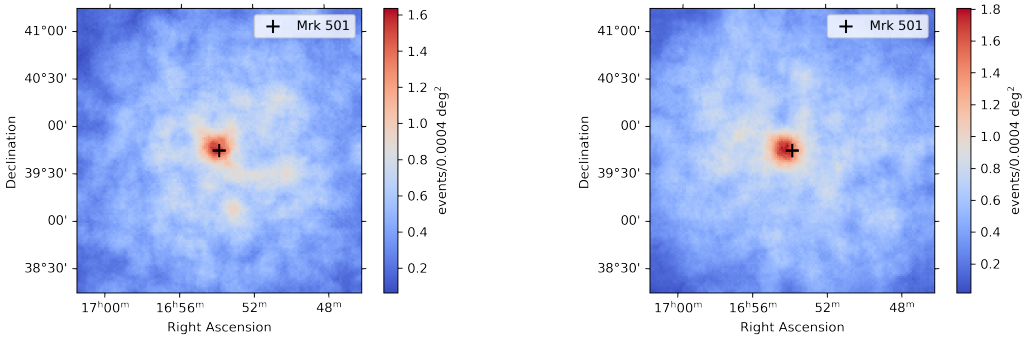

Figure 15.4: Counts map of the observations on Markarian 501 for the two different reconstruction algorithms. Left is the standard LST1 analysis (Hillas+ RF) and right is our neural network (γ-PhysNet).

The count maps are given in Figure 15.4. The hotspot, corresponding to the source, is not centred on the source position (obtained in other wavelengths) with the deep learning reconstruction, which is not the case for the Hillas reconstruction.

By looking at the count map of the two runs edge of the zenith range (Fig. 15.5), an explanation of this phenomenon could be found. For the case with a zenith angle of 20°, the count map is relatively circular, whereas, in the case of a zenith angle of 12°, the count map presents some severe deformations. γ − PhysNet is trained on Monte Carlo simulations at 20° of zenith angle. This could be a sign of an issue with the reconstruction direction at a zenith angle too different from the one

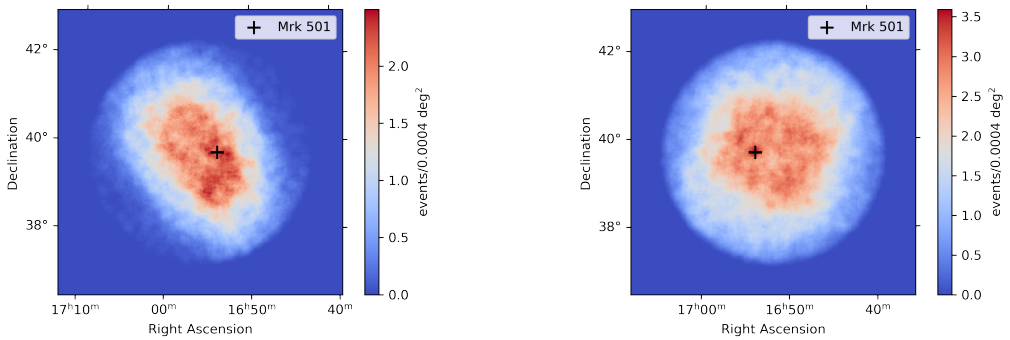

Figure 15.5: Counts map of two different run on Markarian 501 at two different zenith angles (left 12° and right 20°) obtained with the reconstruction using γ − PhysNet

used for training. As Markarian 501 was not bright enough at the time of the data taking to be easily seen on only one run, it is not possible to confirm or infirm that this effect is the cause of the offset.

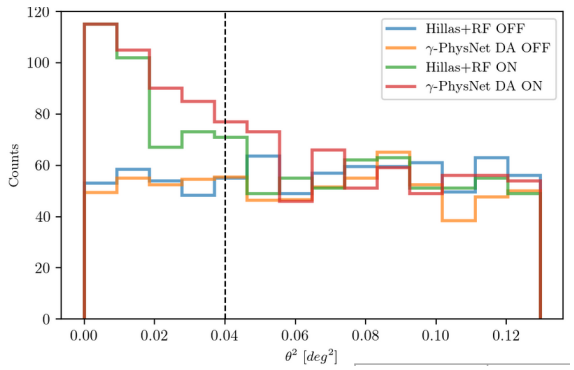

Figure 15.6: Theta square plot for both reconstruction algorithms on the observations of Mrk 501

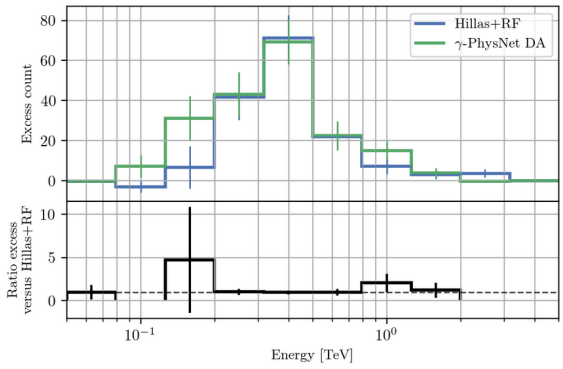

Figure 15.7: Excess in function of the energy for both reconstruction algorithms on the observations of Mrk 501

As a theta cut of 0.2° is being used for the analysis, this small offset on the position is not a big issue. Figure 15.6 gives the theta square for both reconstructions and table 15.1 summarises the results. The measured excess is 30% (±23%) more intense with γ − PhysNet than for the Hillas + RF reconstruction, leading to a greater significance of 9.8σ than the 7.6σ of the Hillas + RF reconstruction. The excess is mainly localised at low energies (close to 100 GeV), as expected from the simulations. This is visible in figure 15.7. The excess does not go well below 100 GeV. It is due to the cuts made to have the same background per energy bin, and the Hillas + RF configurations used here do not go below these energies.

Reconstruction	Excess	Significance	Background counts
Hillas+RF	148.7 γ	7.6 σ	238.3
γ − PhysNet	192.7 γ	9.8 σ	226.3

Table 15.1: Excess and significance results for Markarian 501

The excess is smaller than what could be expected from simulations. Among the causes is the issue spotted on the direction reconstruction that is likely also affecting other parameters. Another explanation can be found in the cuts made to match the background of the Hillas + RF as they might

limit the γ – PhysNet performances compared to the MC analysis where cuts have been generalised for best sensitivity. Indeed, as the background rejection is better with γ – PhysNet, cuts with less background would be more in favour of this new reconstruction method, and these cuts are not the best situation for the algorithm to shine.

15.2.2 Crab Nebulae

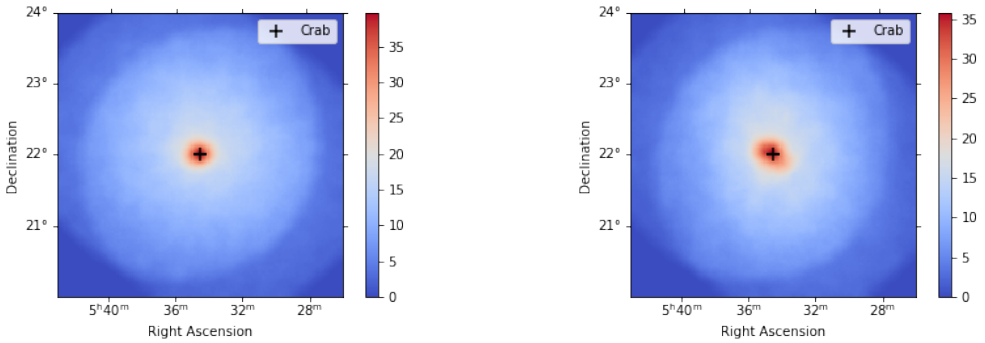

Figure 15.8: Counts map of the observations on the Crab Nebulae for the two different reconstruction algorithms. Left is the standard LST1 analysis (Hillas+ RF) and right is our neural network (γ – PhysNet).

The Crab dataset is a bit larger than the one on Markarian 501, with a brighter source, a more complex field and a higher NSB. When making the first comparison of the significance between the two chains, we obtained a significance of 44.0σ for Hillas + RF, while the reconstruction with γ – PhysNet is only at 39.5σ. This result is not aligned with the one obtained on Markarian 501 above. A quick look at the count map (Fig. 15.8) shows some important deformation of the hotspot of the Crab for γ – PhysNet. If we look at the one obtained at a low zenith angle (Fig. 15.9), pretty big aberrations could be seen as also some dependency on the azimuth angle. The observation conditions are clearly too far from the training condition (zenith : 20°, azimuth : 180°) and causing issues.

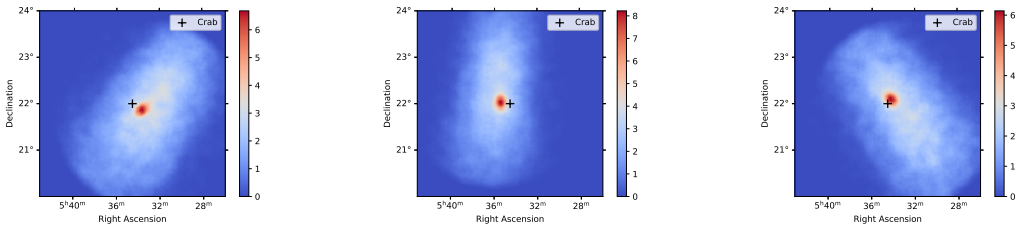

Figure 15.9: Count map of the Crab nebulae with γ – PhysNet for several zenith and azimuth angles. From left to right : Zenith 8.5° and Azimuth 146°; Zenith 6.7° and Azimuth 175°; and finally Zenith 8.6° and Azimuth 215°.

We could focus on the three runs that are between 15° and 25° zenith angle. The count maps (Fig. 15.10) are then similar to the one obtained for Markarian 501 with a very small offset for the position of the Crab with the reconstruction using γ – PhysNet.

Again, Figure 15.11 gives the theta square plot, and table 15.2 summarises the results. A higher excess could be seen with γ – PhysNet than for Hillas+RF. Adding the Poisson noise added in the Monte Carlo leads to slightly better performance for Hillas + RF and has no impact for γ – PhysNet. These results are quite different from the one obtained in a previous study on the Crab

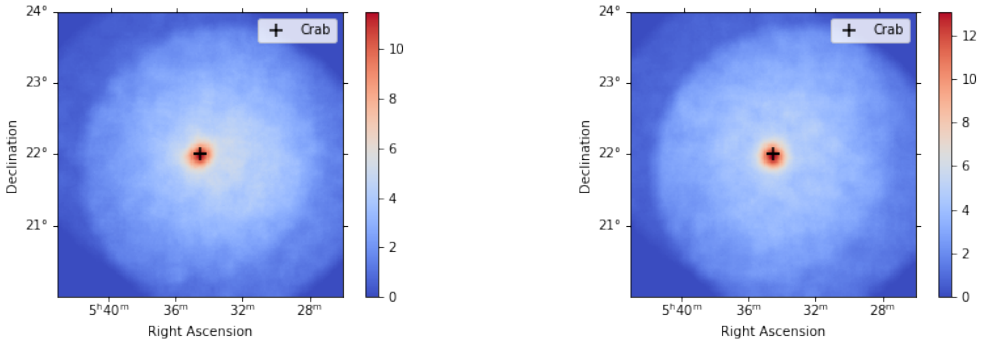

Figure 15.10: Counts map of the observations on the Crab Nebulae for the two different reconstruction algorithms and using only runs close to 20° of zenith angle. Left is Hillas + RF and right is γ – PhysNet

Reconstruction	Excess	Significance	Background counts
Hillas+RF	1230.9 γ	24.8 σ	1463.1
Hillas+RF (Poisson Noise)	1310.4 γ	26.1 σ	1478.6
γ – PhysNet	1612.3 γ	31.4 σ	1461.7
γ – PhysNet (Poisson Noise)	1605.9 γ	31.3 σ	1466.1

Table 15.2: Excess and significance results for the Crab

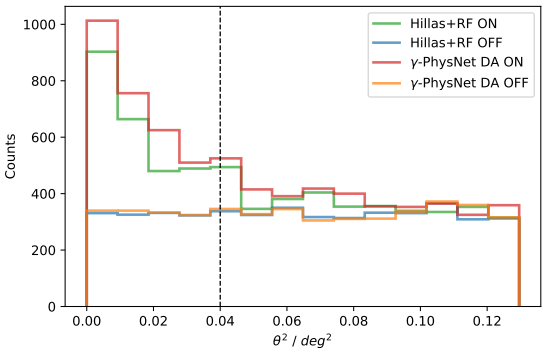

Figure 15.11: Theta square plot for both reconstruction algorithms on the observations of the Crab

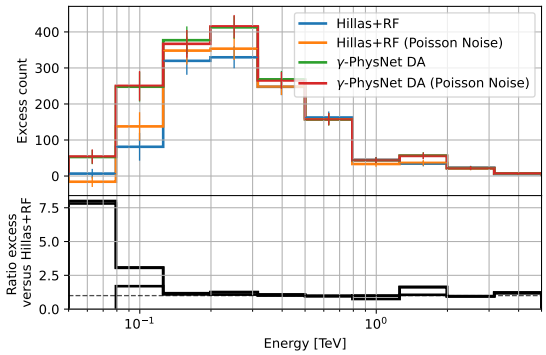

Figure 15.12: Excess in function of the energy for both reconstruction algorithms on the observations of the Crab

with γ – PhysNet (Jacquemont et al., 2021b). In this study, the excess and significance obtained with γ – PhysNet without Poisson noise added to the Monte Carlo simulations were quite similar to the one for Hillas+RF, while it was only with the simulations with Poisson noise as a training sample that the results were significantly better. There was not enough statistic to see the small effect seen on the Hillas+RF here.

The dataset was not the same as in this previous study and was one of the first data acquired on the Crab, and since then, the parameters of the camera of the telescope have changed alongside with the optical transmission of the system. There were also evolutions in the calibration of the data that might have had an impact.

15.3 Conclusion and perspectives

This study, among the first applications of deep learning algorithm to observational data, has shown a successful detection of Markarian 501 and the Crab with a better excess and significance compared to Hillas + RF reconstruction. However the results also show that the challenges to reach a fully working reconstruction are still numerous as some issues on the reconstructed parameters could be seen, especially when using observations at a different zenith angle than the training one.

As deep learning tends to be sensitive to the difference between the data used for training and inference, this is likely the main cause of these issues. It is known there is a difference between the real optical PSF and the one of the simulation. A previous study with $\gamma -$ PhysNet has shown better performance by training the algorithm using simulation data with the same NSB than for the observations. This effect was not observed during this study, a few possible explanations for this have been mentioned, but the effective reason for this difference in results is not known at the time. One big difference that has been seen during this study was the difference between the pointing of the telescope and the single one used for the simulation used for training.

Also, new Monte Carlo simulations are available, covering the whole sky and with a better agreement with observational data, which should allow getting better results from $\gamma -$ PhysNet but also cause new challenges for the training as the amount of data has raised significantly.

To conclude, the perspective for this kind of reconstruction seems great in the future with significant improvement to the performance of the instrument, but the challenges to have a reliable and trustworthy reconstruction are still numerous. The Gammalearn team is working hard to overcome them, and this is the subject of the thesis of Michael Dell'Aiera at the LAPP.

Chapter 16

Résumé de la partie 4

Contents

16.1 Principe de fonctionnement de la reconstruction et l'analyse des données

Cette section présente le principe général de l'analyse des données Cherenkov. L'exemple du LST-1 sera principalement utilisé pour cette section. L'analyse des données peut généralement être divisée en deux parties. Tout d'abord, la partie reconstruction, au cours de laquelle les données brutes du télescope sont transformées en une collection de photons candidats avec leur direction et leur énergie. Au cours de la deuxième partie, appelée analyse de haut niveau, la liste des photons est utilisée pour détecter les sources et, en cas de détection, déterminer les spectres, les courbes de lumière ou les formes spatiales.

16.1.1 Reconstruction des évènements

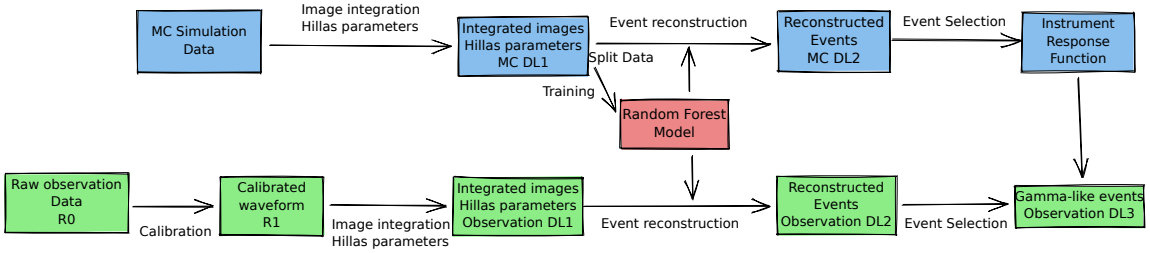

Figure 16.1: Processus de reconstruction des évènements pour LST-A

Le processus de reconstruction des évènements pour LST-1 est présenté dans la figure 16.1. Le traitement des données des simulations Monte-Carlo (servant notamment à déterminer les performances de l'instrument) et des données d'observations sont proches, mais des différences subsistes.

La première étape, spécifiques aux observations, est la calibration. L'objectif est de transformer les images brutes du capteur en images avec une estimation du nombre de photons arrivés dans chaque pixel. Pour cela, les gains et piédestaux de chaque pixel sont estimés, et les corrections de différence de réponse temporelle sont effectuées.

Ensuite, pour l'ensemble des données, elles sont intégrées et la zone avec du signal provenant de la gerbe sera extraite à l'aide d'une étape dite de nettoyage. Ensuite, les paramètres dits de Hillas sont calculés. Ces paramètres contiennent les moments ainsi que des informations simples sur la géométrie de l'image à l'aide d'une ellipse déterminée à partir de la distribution du signal.

Une partie des données issues des simulations Monte-Carlo sert à entraîner des algorithmes de machine learning appelés random forest. Ceux-ci déterminent à partir des paramètres de Hillas les paramètres de la particule ayant crée la gerbe, sa direction, son énergie et si la particule est un gamma. Les données de simulations utilisées pour l'entraînement ne sont pas utilisées par la suite.

Les random forests sont utilisés pour déterminer les paramètres des particules ayant créées les gerbes. Puis une sélection des données est effectuée afin d'éliminer au maximum les gerbes due au rayonnement cosmique, mais aussi sélectionner les gerbes les mieux reconstruites, améliorant ainsi la résolution angulaire et en énergie.

Les données de simulations sont ensuite utilisées pour calculer les fonctions de réponse instrumentale, décrivant les performances de l'instrument. Celles-ci sont adjointes aux données observationnelles formant la sortie finale de cette première étape. Ce résultat permet par la suite de faire l'analyse physique de la source.

16.1.2 L'analyse de haut niveau

L'objectif de l'analyse de haut niveau est de transformer les données issues de l'étape précédente en informations qui pourraient être utilisées pour la modélisation des sources, comme des spectres, des limites supérieures ou des courbes de lumière.

Dans l'expérience LST-1, nous utilisons principalement la librairie python `gammapy` pour effectuer ces analyses.

Une des premières étapes est d'estimer le fond. En effet, celui-ci reste important malgré la sélection de données effectuée précédemment et, par conséquent, ne pas le prendre correctement en compte pourrait mener à des erreurs importantes. Pour les sources ponctuelles comme les sursauts gamma, deux méthodes sont souvent utilisées (Fig. 16.2). La première fait l'hypothèse d'une symétrie circulaire du fond à travers le champs de vue, tandis que la deuxième est une estimation plus locale mais qui nécessite un modèle pour décrire la forme à large échelle du fond.

Ensuite, il sera possible à l'aide de la méthode de Li&Ma d'estimer si une potentielle source émet un signal qui se détache significativement du fond et ne peut lui être attribué. Il sera possible ensuite de déterminer un spectre en ajustant une fonction sur les données. Le modèle utilisé est souvent une loi de puissance, car de nombreux mécanismes de production de photons à très haute énergie prédisent des spectres proches de la loi de puissance. Il est aussi possible en quantifiant les données par intervalles temporelles d'obtenir une courbe de lumière.

16.2 Optimisation des critères de sélection des évènements

16.2.1 Contexte initial

La sélection des événements qui a été décrite ci-dessus est une étape cruciale pour les performances de l'instrument. Dans un monde idéal, cette étape permettrait de rejeter tous les rayons cosmiques et de conserver tous les photons. En pratique, il faut faire des compromis et, selon la source, certaines coupures peuvent être plus performantes que d'autres. Par exemple, une source ayant un indice spectral dur (source dure) aura un signal fort à haute énergie. Il pourrait être intéressant d'adopter des coupures strictes qui supprimeraient une plus grande partie du bruit de fond au détriment de la surface effective à basse énergie. Au contraire, pour les sources à indice spectral mou (sources molles), il est probablement préférable d'utiliser des coupures moins restrictives pour préserver la surface effective à basse énergie, où se trouve le signal, au détriment du rejet de l'arrière-plan. La

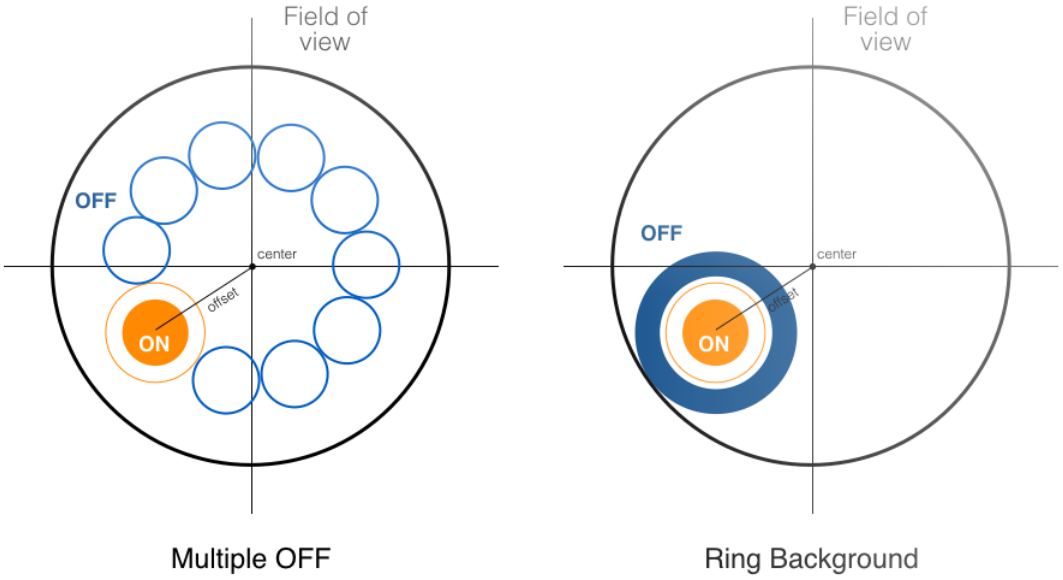

Figure 16.2: Deux méthodes différentes pour estimer le fond. Le schéma de gauche représente la méthode multiple OFF, dans laquelle plusieurs régions OFF sont placées à la même distance du centre du champ de vue que la région ON. Sur le schéma de droite, la méthode d'estimation de fond en anneau, la région OFF est un anneau placé autour de la région ON. Figure issue de Chevalier (2017).

génération actuelle, comme H.E.S.S., utilise des critères de sélection différents en fonction de l'étude menée.

Les critères de sélection pourraient également être optimisés non pas pour obtenir la meilleure sensibilité, mais la meilleure résolution angulaire ou énergétique. Cet aspect ne sera pas abordé ici.

Au début de cet étude, un jeu de coupure était souvent utilisé. Il sera dénommé coupure `Base`. Il opère une sélection sur plusieurs paramètres :

- L'intensité de l'image de la gerbe
- Le ration largeur sur longueur de l'ellipse des paramètres Hillas
- La fraction du signal sur les bords de la caméra. Plus cette fraction est élevée, plus une large fraction de la gerbe n'a pas été imagés.
- La distance angulaire à la source : seuls les évènements reconstruits proches de la source sont utilisés.
- La gammanness : un paramètre généré par les randoms forest représentant la confiance de l'algorithme dans le fait que l'évènement soit ou non un photon

16.2.2 Optimisation des coupures

L'objectif étant d'optimiser les coupures pour différents types de sources et temps d'observations, une grille de possibilité sera définie avec comme premier axe, le temps d'observation et comme second, l'indice spectral de la source. Une première optimisation des coupures est effectuée individuellement pour chaque source. Puis pour extraire seulement quelque jeux de coupure, qui permettent de couvrir chacun individuellement le plus de cas possible.

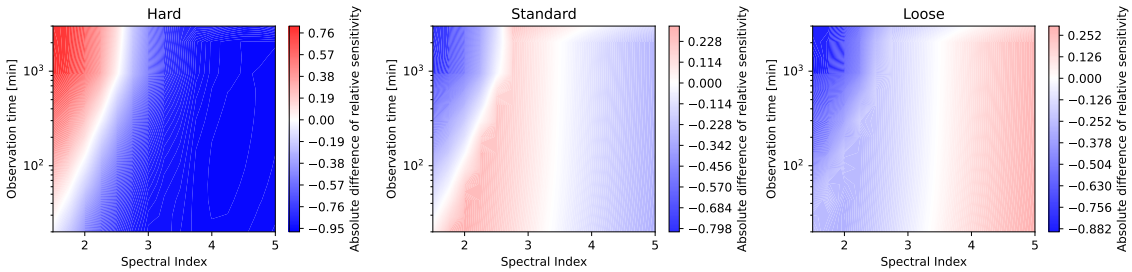

Figure 16.3: Différence absolue de la sensibilité proportionnelle obtenue par rapport à la sensibilité sur mesure pour chaque source, pour chaque coupure par rapport aux autres. Si la région est rouge, les coupures sont plus performantes que les deux autres, si elle est bleue, les coupures sont moins performantes que les deux autres. Le panneau de gauche représente les coupures `Hard`, le panneau central les coupures `Standard` et le panneau de droite les coupures `Loose`.

Nom des coupures	`Loose`	`Standard`	`Hard`
Gammaness	>0.65	>0.75	>0.6
Intensity	>120	>350	>2000
Leakage	<0.1	<0.35	<0.35
Theta	<0.125°	<0.125°	<0.125°
Width length ratio	>0.1	>0.1	>0.1
Gamme en énergie	85 GeV - 10 TeV	100 GeV - 10 TeV	1.6 TeV - 10 TeV

Table 16.1: Les trois différents jeux de coupures obtenus

L'optimisation a été effectué à l'aide d'une recherche en grille (différente de la grille de source). Pour chaque paramètre, sur une gamme définie, un échantillonage est effectué. Ensuite, la combinaison optimale des paramètres est recherchée à travers l'entièreté de la grille pour chaque source testée.

L'optimisation cherche à maximiser la sensibilité intégrée. Ainsi, pour un indice spectral donné, l'algorithme recherche la combinaison permettant de détecter le flux le plus petit possible. Ensuite, trois jeux de coupure ont pu être identifiés : ils sont listés dans le tableau 16.1.

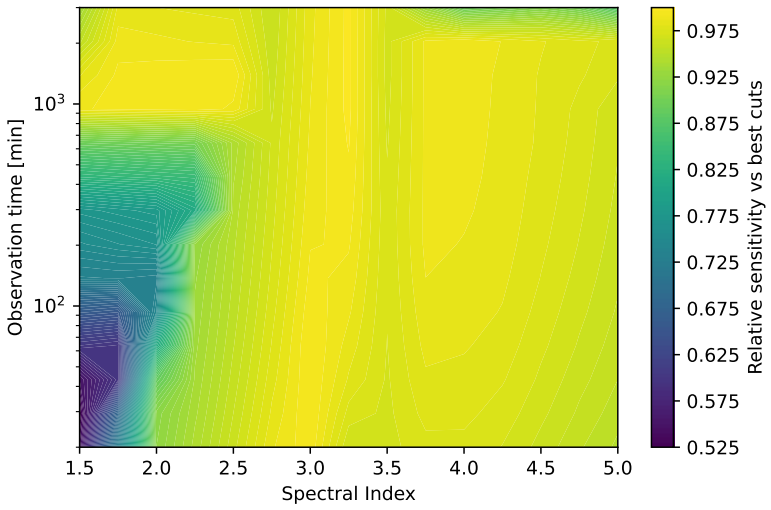

Figure 16.4: Proportion de la sensibilité de la meilleure des coupures finales par rapport à celle faite sur mesure pour chaque source.

Coupure	`Base`	`Loose`	`Standard`	`Hard`
Excès	4382.3	2488.3	2481.6	93.8
Fond	4992.7	1734.7	932.4	2.2
Signifiance	47.2 σ	45.6 σ	55.5 σ	17.3 σ

Table 16.2: Résultat des différent jeux de coupures sur des observations de la nébuleuse du Crabe

Les différents jeux de coupures présentent des différences qui leur permettent d'être plus efficace sur une partie données des sources (Fig. 16.3). Si pour chaque source, on choisi le plus optimal des trois jeux de coupures, on peut voir que la sensibilité est proche du cas ou les coupures sont généré par source (Fig. 16.4). Ainsi l'objectif d'obtenir une sensibilité optimal avec un nombre restreint de jeux de coupure est atteint. Dans le cadre de test sur des données observationelles, une amélioration des performances par rapport au jeu de coupure `Base` à pu être observé (Fig. 16.2).

16.2.3 Augmentation du nombres de dimensions

La recherche en grille a permis, du fait de sa simplicité, le développement de la méthode et l'obtention des premiers résultats. Cependant, cela limite l'ajout de paramètres supplémentaires pour les coupures. La possibilité d'ajouter des dimensions à la recherche permettrait par exemple de rendre les critères de sélection dépendant de l'énergie, ce qui pourrait amener des gains de sensibilités.

Plusieurs méthodes alternatives on été étudiées. La méthode retenue la plus prometteuse est l'utilisation d'un minimiseur pour explorer l'espace des paramètres et trouver la solution optimale, avec de multiples points de départs afin de s'approcher de la solution la plus optimale possible. Les résultats de la comparaison de différents minimiseurs sont présentés dans la figure 16.5. La solution la plus optimale est l'utilisation de l'algorithme de minimisation Nelder-Mead. Cette méthode pourra être utilisée dans le futur afin d'améliorer les résultat obtenus en augmentant le nombre de dimension.

16.3 Comparaison entre la reconstruction par apprentissage profond et la reconstruction de Hillas

16.3.1 Le projet Gammalearn

La reconstruction de Hillas est une méthode robuste et efficace pour reconstruire les événements des IACTs. Cependant, en raison de la paramétrisation simple de la gerbe, de nombreuses informations contenues dans l'image sont perdues au cours du processus de reconstruction. La reconstruction basée sur des modèles, utilisée dans le cadre de la collaboration H.E.S.S., Model++ et ImPACT, permet d'utiliser une plus grande quantité d'information contenue dans l'image, améliorant ainsi la sensibilité et la résolution angulaire et énergétique. Néanmoins, ces techniques s'accompagnent d'un coût informatique élevé qui pourrait être difficile à supporter pour des expériences telles que le CTA.

Avec le développement rapide de l'apprentissage profond au cours des dix dernières années, aidé par le développement des processeurs graphiques, cette technique a commencé à susciter l'intérêt de la communauté pour être utilisée dans les reconstructions d'événements. L'entraînement a un coût de calcul considérable, mais l'inférence sur les données est beaucoup moins exigeante que la reconstruction basée sur les modèles. Les premières tentatives ont été réalisées dans le cadre de la collaboration H.E.S.S. avec un modèle qui n'effectue que la phase de réjection du fond de cosmique. Il existe plusieurs projets au sein du CTA pour reconstruire tous les paramètres à l'aide de l'apprentissage profond. Cette section présente le test de l'application sur les données d'observation réalisé avec l'un des algorithmes d'apprentissage profond développés au sein du CTA, appelé Gammalearn.

Le modèle développé, appelé $\gamma - \text{PhysNet}$, est un algorithme de deep-learning utilisant la convolution et ayant comme propriété d'avoir plusieurs sorties, lui permettant de reconstruire simultanément tous les paramètres, le type de particule, l'énergie et la direction. Ce réseau a su montrer lors d'études sur des simulations Monte-Carlo des gains par rapport à la reconstruction classique

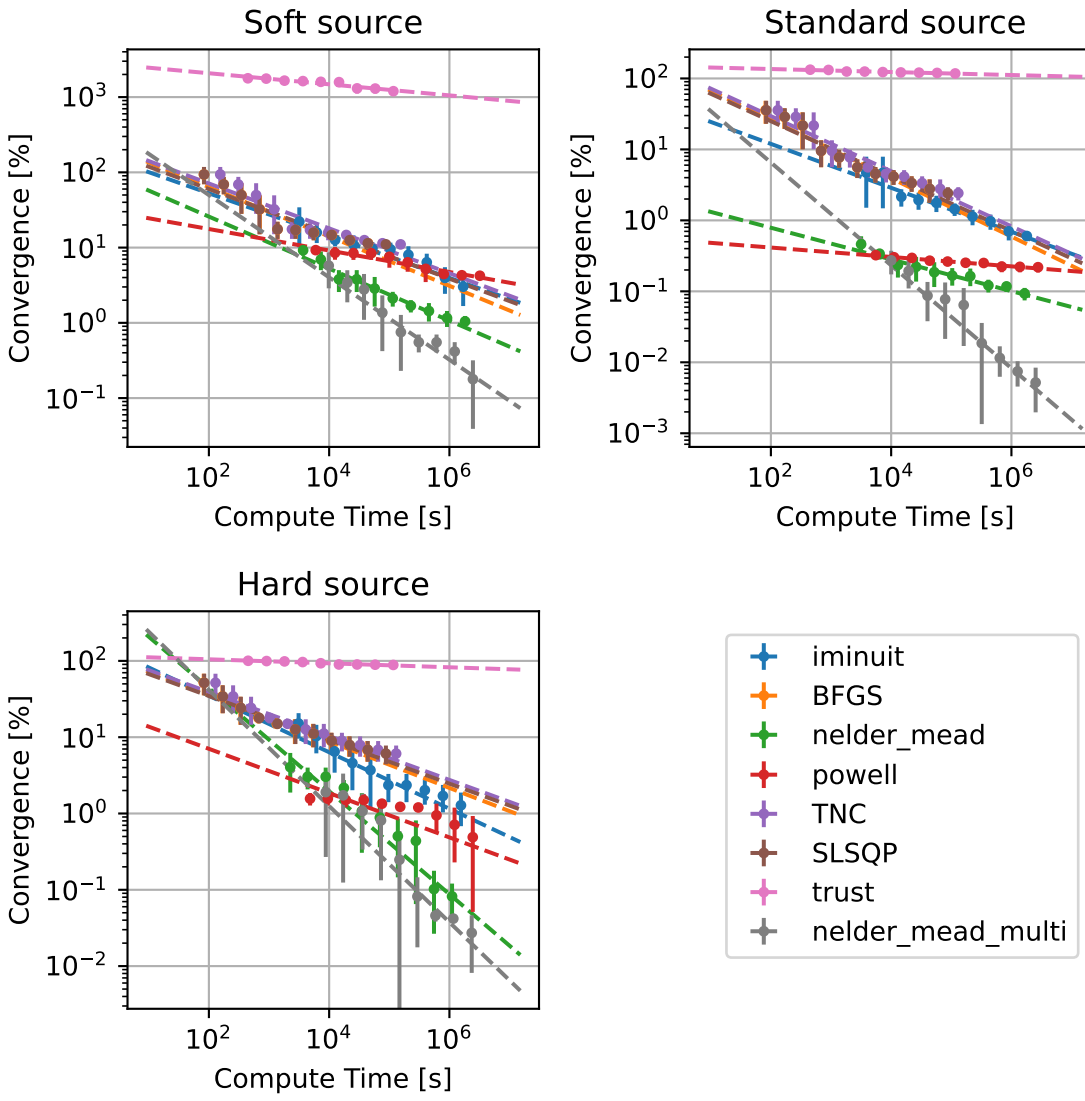

Figure 16.5: Convergence vers les meilleures critères de sélection pour les différents minimiseurs utilisant la séquence de Sobol comme point de départ. Le panneau supérieur gauche correspond au cas d'une source molle, le panneau supérieur droit à celui d'une source standard et le panneau inférieur gauche à celui d'une source dure.

utilisant Hillas (Fig. 16.6), que ce soit sur la sensibilité, ou la résolution angulaire ou en énergie CTA-LST Project et al. (2022a). Ces gains sont particulièrement important aux plus basses énergies où le gain en sensibilité peut atteindre jusqu'à un ordre de grandeur.

16.3.2 Applications sur des données d'observation

Lors de leur application, les modèles de deep-learning tel que γ – PhysNet peuvent facilement rencontrer des problèmes lors de l'application sur les données réelles du fait des différences entre données simulées et données observationelles. Afin de tester l'algorithme, des données sur deux sources ont été utilisées : la nébuleuse du Crabe et Markarian 501. Pour réaliser cette analyse, les coupures utilisées pour γ – PhysNet ont été adaptées afin d'avoir le même niveau de fond que la méthode Hillas+RF.

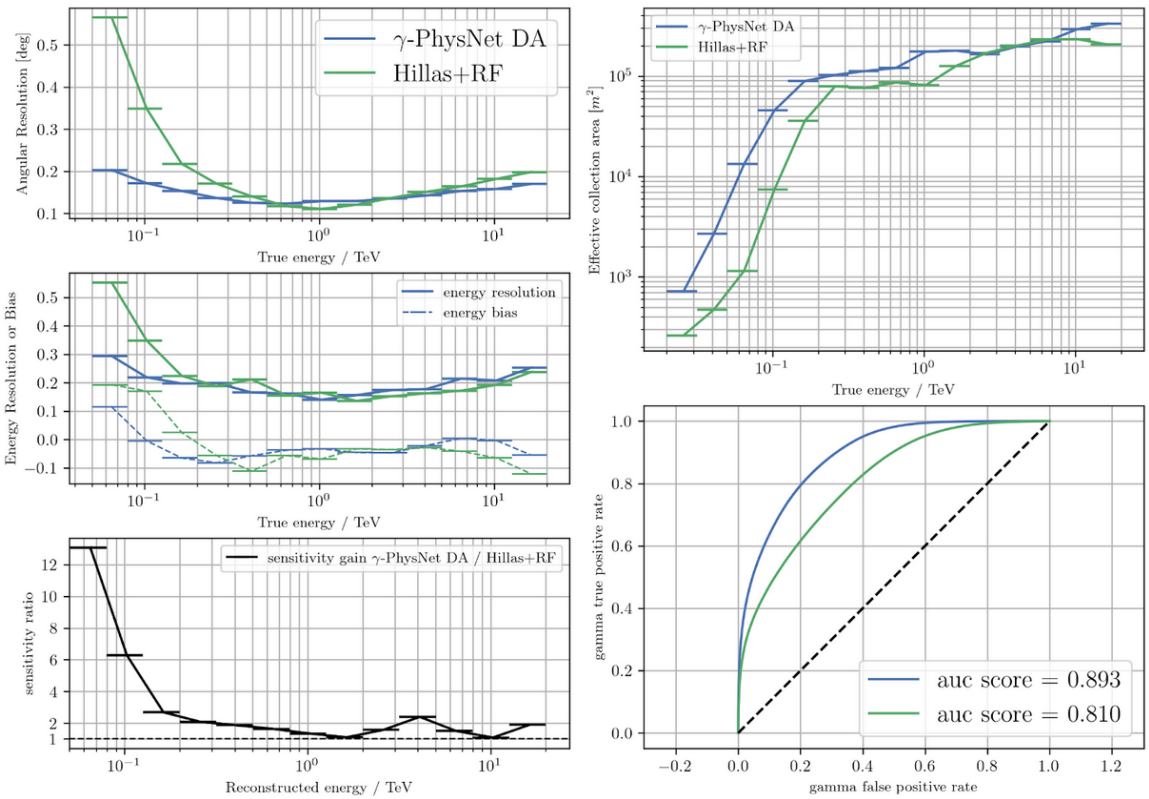

Figure 16.6: Fonction de réponse instrumentale en utilisant respectivement pour la reconstruction le réseau $\gamma -$ PhysNet et la méthode Hillas+RF avec des coupures optimisées par bin pour obtenir la meilleure sensibilité dans chaque bin. Figure issue de CTA-LST Project et al. (2022a)

En dehors de ce point là, et de l'utilisation de deux méthodes de reconstructions différente, l'analyse est faite de manière standard.

Reconstruction	Excès	Significance	Nombre d'évènements de fond
Hillas+RF	148.7 γ	7.6 σ	238.3
$\gamma -$ PhysNet	192.7 γ	9.8 σ	226.3

Table 16.3: Excès et significance pour Markarian 501

Markarian 501 est un noyau actif de galaxie. Il est dans un champs observationel simple, car extragalactique (pas de NSB, pas d'autre source d'émission, ...). Les résultats de ce test sont présentés dans le tableau 16.3. L'excès supplémentaire mesuré avec $\gamma -$ PhysNet par rapport à Hillas + RF est de 30% ($\pm$23%). Cela mène à une plus grande significicance 9.8σ à la place de 7.6σ. L'excès supplémentaire est principalement présent à basse énergie comme attendu des simulations. Cependant, cet excès est plus faible qu'espéré, mais cela peut être dû à plusieurs facteurs. En premier lieu, les coupures sont différentes de l'analyse sur les simulations, mais un biais sur la direction en reconstruction effectué par $\gamma -$ PhysNet a également été observé, menant à un excès qui n'est pas centré sur la position de Markarian 501, réduisant potentiellement l'excès total.

La nébuleuse du Crabe, étant dans le plan galactique, forme un champs observationel plus complexe, notamment du fait de lumière parasite due aux étoiles qui affectent les images des gerbes. Pour cette raison, chaque algorithme de reconstruction a été également entraîné avec des images de simulation Monte-Carlo modifiées en injectant du bruit poissonnien dans les images issues des simulations pour se rapprocher du niveau de bruit réel. L'ensemble des résultats sont visibles dans le tableau 16.4. L'ajout de bruit poissonien aux simulations Monte-Carlo a eu un effet marginal sur

Reconstruction	Excès	Excès	Nombre d'évènements de fond
Hillas+RF	1230.9 γ	24.8 σ	1463.1
Hillas+RF (Bruit de poisson)	1310.4 γ	26.1 σ	1478.6
γ – PhysNet	1612.3 γ	31.4 σ	1461.7
γ – PhysNet (Bruit de poisson)	1605.9 γ	31.3 σ	1466.1

Table 16.4: Excès et significance pour la nébuleuse du Crabe

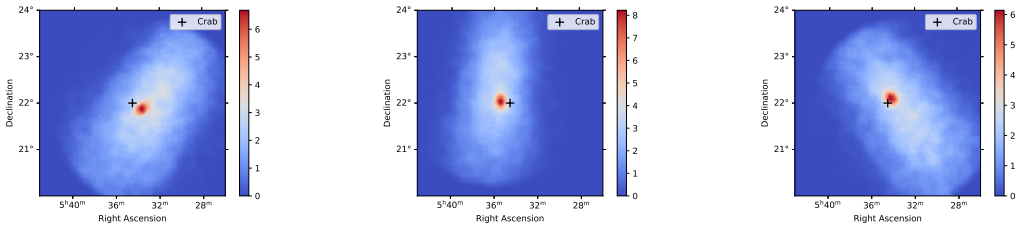

Figure 16.7: Carte de comptage obtenue avec γ – PhysNet pour la nébuleuse du Crabe à différents angles zénithaux and azimutaux. De gauche à droite : Zénith 8.5° et Azimuth 146°; Zénith 6.7° et Azimuth 175°; et finalement Zénith 8.6° and Azimuth 215°.

γ – PhysNet et faible sur Hillas+RF. On peut également constater le gain en excès de γ – PhysNet par rapport à Hillas+RF.

Cependant, un problème qui se démarque encore touche à des biais majeurs dans la reconstruction en direction comme montré sur la figure 16.7. On constate que cela dépend à la fois de l'angle zénithal et azimutal, qui dans tous ces exemples sont significativement différents de la direction pointé fixé dans les simulations utilisés pour l'entraînement, montrant ainsi la sensibilité du réseau au condition d'entraînement.

16.3.3 Perspective

Cette étude a permis une détection avec succès de la nébuleuse du Crabe et de Markarian 501 à l'aide d'une reconstruction effectuée par le réseau γ – PhysNet. Cependant, nous avons pu mettre en avant une sensibilité aux conditions d'entraînement dans la reconstruction en direction, et une sensibilité moins bonne qu'espérée des simulations bien que meilleures que la méthode standard. Cela donne un bon espoir pour l'utilisation de ces méthodes de reconstructions dans le futur avec, à la clef, des améliorations de performance, mais de nombreux défis restent à surmonter avant d'avoir une reconstruction fiable.

16.4 Création d'un modèle d'acceptance pour LST-1

Un modèle d'acceptance est un élément important pour évaluer le fond sur l'ensemble du champ de vue et ainsi produire des cartes du ciel. Au début de ce travail, il n'y avait pas de modèle d'acceptance développé pour LST-1, parce que toutes les sources observées étaient ponctuelles avec une position bien définie.

En mai 2021, LST-1 a observé GRB 210515B. L'alerte provenant de Fermi/GBM, la précision sur sa localisation est faible. Par conséquent, le GRB pouvait se trouver n'importe où dans le champ de vue de l'instrument (voire même à en dehors de celui-ci). Il était alors nécessaire de créer un modèle d'acceptance qui pourrait être utilisé pour générer une carte du ciel afin de rechercher une contrepartie à ce GRB.

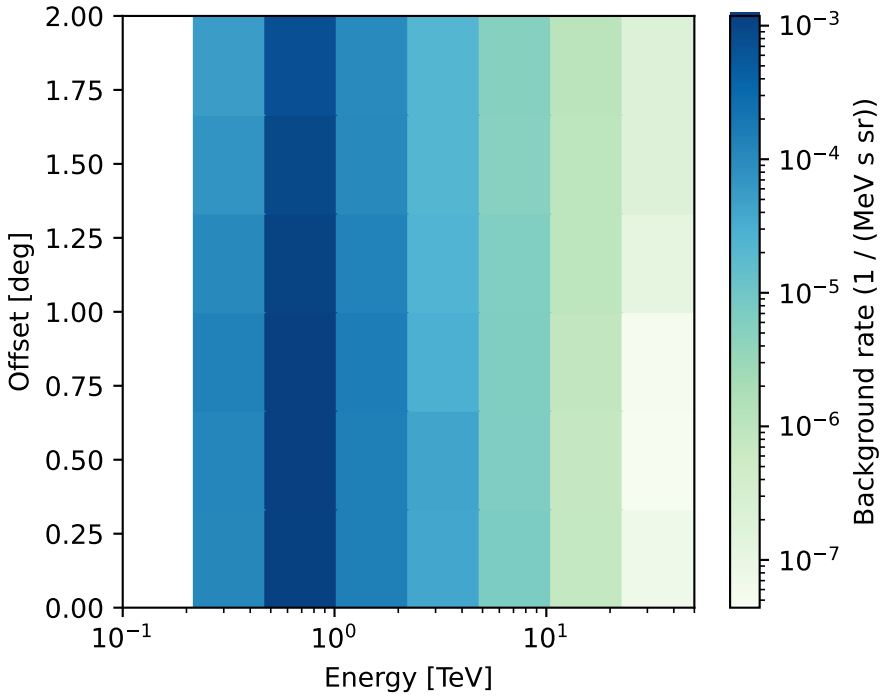

Figure 16.8: Exemple de modèle de fond obtenu avec l'algorithme implémenté.

16.4.1 Création du modèle

Le modèle créé repose sur l'hypothèse d'une symétrie circulaire du fond dans le référentiel de la caméra, et prend en compte les régions d'exclusions dû à ce potentiel source. Le modèle est dépendant de énergie. La figure 16.8 montre un exemple de modèle obtenu en sortie d'algorithme. L'angle zénithal ayant un impact très important sur le fond, afin d'améliorer le modèle obtenu, celui-ci peut être calculé par bin d'angle zénithal, voire interpolé en fonction de l'angle zénithal.

L'implémentation a été faite en Python et a été conçue pour s'intégrer facilement dans un programme d'analyse basé sur `Gammapy`. L'outil est librement accessible sur GitHub[1]

16.4.2 Test du modèle

Le modèle a été en premier lieu appliqué sur le champ de la nébuleuse du Crabe en utilisant les données publiques de HESS. Cela a permis une bonne description du fond dans le champ de vue, la distribution de significance suivant une loi normale (Fig. 16.8). L'application sur des données de LST-1 a donné également de bons résultats dans certains cas comme l'observation de GRB 210704 (Fig. 16.10), mais parfois des résultats de mauvaise qualité comme l'observation du Dark Patch 8 où des déviations importantes de la distribution par rapport à la loi normale peuvent être observées (Fig. 16.11). Cela montre que le background n'est pas encore parfaitement compris et qu'il est nécessaire d'investiguer l'utilisation de modèles de fond plus complexes pour LST-1, mais le travail présenté ici permet déjà d'analyser un certain nombre de champs de vue de manière satisfaisante.

[1] https://github.com/mdebony/acceptance_modelisation

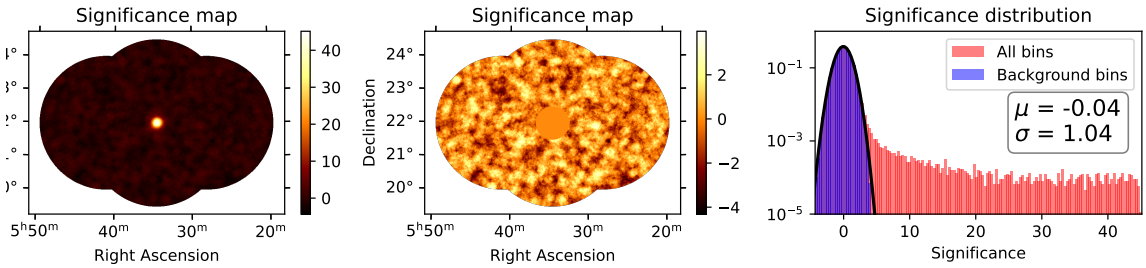

Figure 16.9: Carte de significance (figure de gauche), carte de significance sans la région d'exclusion (figure centrale) et distribution de significance (figure de droite) pour une analyse ring background utilisant le modèle d'acceptance développé dans ce travail.

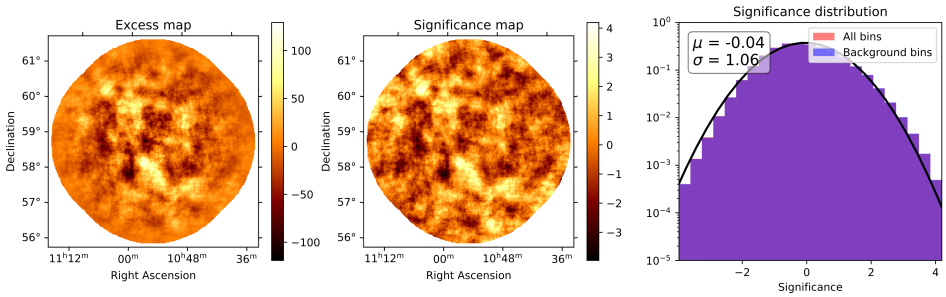

Figure 16.10: Observation de GRB 210704A avec LST-1, avec la carte d'excès (figure de gauche), la carte de significance (figure centrale), et la distribution de significance (figure de droite).

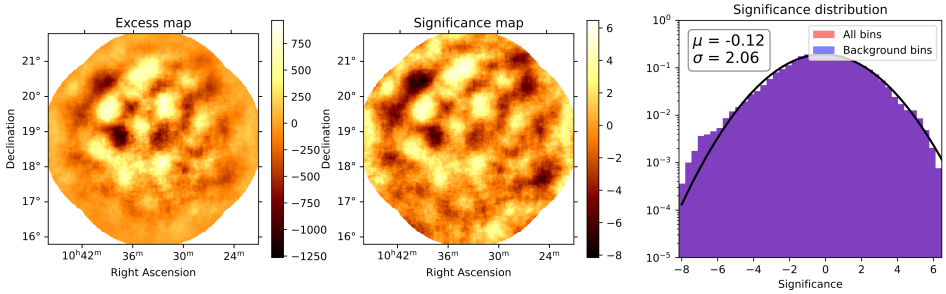

Figure 16.11: Observation de Dark Patch 8 avec LST-1, avec la carte d'excès (figure de gauche), la carte de significance (figure centrale), et la distribution de significance (figure de droite).

Part V

Gamma-Ray Bursts at Very High Energies

Chapter 17

First follow-ups of Gamma-Ray Bursts with LST-1

Contents

LST-1 is still under commissioning but has already started to take scientific data and observation programs on transient sources like GRBs. The first follow-up of GRBs was performed on GRB 201216C on the night of the 17th of December 2020. Since then, the number of GRB follow-ups has continuously increased.

17.1 The follow-up strategy

I directly participated in establishing the current strategy for GRB follow-up. The current observation criteria are weak to follow as many GRBs as possible. This is possible due to the low observation time pressure of the instrument in the current commissioning phase. With the LST-1 soon entering normal science operations, this strategy might be revisited and especially for GBM alert (see chapter 18).

All the alerts from the various instruments are received on-site by the transient handler (CTA-LST Project et al., 2022b). This system will then, based on the strategy described below, identify the GRB to follow. When a GRB passes the criteria, an email is sent and a warning is displayed to the shifters. Automatic follow-up of the alert is currently under testing. When this is fully functional, it will help to reduce the delay of observations.

When received, the alert is separated into two classes, the well-localised ones (*Swift*/BAT, INTEGRAL, *Fermi*/LAT) on one side and the one coming from *Fermi*/GBM on the other. The common part of both cases is that the maximum zenith angle of the observations is 70°, and the typical follow-up time is 2 h.

For well-localised alerts, the GRBs are followed if :

- The delay of the observations is below 1 h and the duration of the observation window is above 10 min
- The delay of the observations is below 24 h and the duration of the observation window is above 40 min
- The delay of the observations is below 48 h, the duration of the observation window is above 80 min and a redshift measurement below 0.2 is available.

This strategy allows maximising the number of short delay follow-ups performed, where the likelihood of detection is higher. For longer delays, the minimum length of the observation windows ensures a good enough sensitivity. Finally, when a close redshift is confirmed, we open the possibility of performing a longer delay follow-up, as the light emitted by the source should not be dramatically absorbed by the interaction with the EBL.

The alert coming from *Fermi*/GBM suffer from considerable uncertainty on the position, justifying their specific treatment. First, an alert should pass the selection criteria for *Fermi*/GBM to ensure that the GRBs have a reasonable chance of being close to the position given by GBM (position uncertainty $< 2^\circ$ and significance $> 20\sigma$). Despite this selection, the chance of having the GRBs within the field of view is below 30%. To counter this, it is possible to use a probability map given by *Fermi*/GBM to make multiple pointing in order to maximise the chance of having the GRBs in the field of view. This method comes from the follow-up of gravitational waves and is called tilling (Ashkar et al., 2021).

The probability map is not available in the early time as it could take tens of minutes to a few hours for this map to be generated. Therefore, the strategy is to start observations without this map by observing directly the position given by *Fermi*/GBM, and then, when the map is available, start the tilling procedure. Finally, a GRBs is followed if :

- The delay of the observations is below 1 h, and the duration of the observation window is above 10 min.
- The delay of the observations is below 4 h, and the duration of the observation window is above 60 min.

The maximum delay of observation is way shorter than for localised GRBs. This is due to the sensitivity of the observations being expected to be much lower for two reasons. First, the GRB could be on the edge of the field of view where the performances of the instrument are significantly degraded. Secondly, the tilling procedure allows maximising the chance to observe the real position of the GRB but lowers the integration time, therefore lowering the sensitivity.

Since this follow-up strategy has been decided, I have worked on improving it for the follow-up of the *Fermi*/GBM ones. For more details, see chapter 18. This new proposed strategy is currently under discussion for implementation within the GRB group of LST-1.

One of the instruments able to detect and localise GRBs that are currently not considered is GECAM (Li et al., 2020). The system is composed of two satellites developed by the Chinese Academy of Sciences and launched in 2018 by a Long March 11 rocket. It is only since September 2022 that the instrument started to send public alerts, explaining the lack of a follow-up strategy. The instrument has comparable performance to *Fermi*/GBM so a similar strategy would be needed.

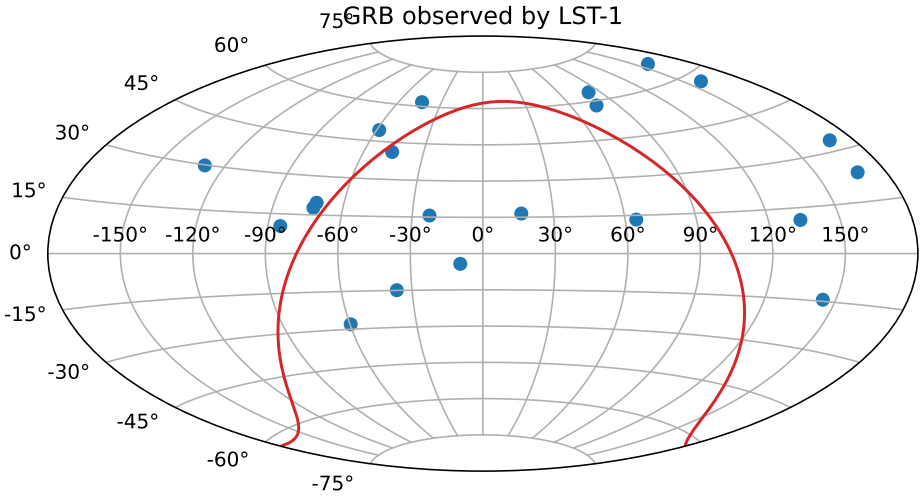

Figure 17.1: Position across the sky of the GRBs observed by LST-1

17.2 GRBs observations with LST-1

Up to now, 22 GRBs have been observed by LST-1 and the list is given in table 17.1 and their position on the sky are shown in figure 17.1. The number is not as high as could be expected from the strategy. This is due to two factors. First, the telescope stopped operation for nearly six months due to the volcanic eruption on the island of La Palma at the end of the year 2021. Secondly, as the telescope is still under commissioning, if some tests are run at the time of the observations, they are not guaranteed. As the commissioning approaches the end and with the implementation of the automatic re-pointing currently being tested, the number of GRBs observed should continue to increase. This will also help to reduce the delay of observations as it difficult to go below 30 min currently due to the manual procedure.

	T_0	T_{90} [s]	Redshift	Observation start time	Delay [min]	Zenith [deg]	Trigger Instrument
GRB 201216C	2020-12-16 23:07:31	16	1.1	2020-12-17 20:57:03	1310	40	*Swift*/BAT
GRB 210511B	2021-05-11 11:26:39	6	-	2021-05-12 03:37:54	971	42	*Fermi*/GBM
GRB 210704A	2021-07-04 21:14:53	1.06	-	2021-07-04 23:32:43	138	60	*Fermi*/GBM
GRB 210731A	2021-07-31 22:21:08	22.51	1.25	2021-07-31 23:02:22	41	60	*Swift*/BAT
GRB 210802A	2021-08-02 11:46:46	11	-	2021-08-03 22:13:30	2067	34	*Fermi*/GBM
GRB 210807A	2021-08-07 10:20:06	156.30	-	2021-08-08 03:55:14	1055	60	*Swift*/BAT
GRB 220302A	2022-03-02 07:40:19	20.0	-	2022-03-03 05:23:06	1302	55	*Swift*/BAT
GRB 220310A	2022-03-10 00:27:57	33.1	-	2022-03-10 01:24:58	56	20	Maxi
GRB 220311A	2022-03-11 16:33:10	10	-	2022-03-12 02:20:54	587	45	INTEGRAL
GRB 220501A	2022-05-01 19:51:51	202	-	2022-05-01 20:51:30	60	65	*Swift*/BAT
GRB 220521A	2022-05-21 23:20:21	13.5	5.6	2022-05-21 23:55:00	35	45	*Swift*/BAT
GRB 220527A	2022-05-27 09:17:15	10.5	0.857	2022-05-28 04:15:00	1138	55	*Fermi*/LAT
GRB 220603A	2022-06-03 23:48:50	10.5	-	2022-06-04 00:22:00	33	40	*Fermi*/GBM
GRB 210930A	2022-09-30 11:11:52	180.5	-	2022-10-01 01:16:45	845	30	*Swift*/BAT
GRB 221009A	2022-10-09 13:16:59	327	0.151	2022-10-10 20:21:00	1865	50	*Swift*/BAT
GRB 221016A	2022-10-16 23:39:22	21.86	-	2022-10-16 23:54:00	15	65	*Swift*/BAT
GRB 221024A	2022-10-24 13:00:27	120	-	2022-10-25 05:02:00	1082	60	*Swift*/BAT
GRB 221025A	2022-10-25 00:58:18	0.4	-	2022-10-26 03:37:00	159	45	*Fermi*/LAT
GRB 221028A	2022-10-28 13:16:27	57.1	-	2022-10-28 22:02:00	346	40	*Swift*/BAT
GRB 221119A	2022-11-19 15:02:53	66	-	2022-11-19 04:04:00	781	50	*Fermi*/GBM
GRB 221218A	2022-12-18 08:14:10	-	-	2022-12-18 19:38:00	684	40	INTEGRAL
GRB 221221A	2022-12-21 22:39:30	5	-	2022-12-21 23:04:00	25	33	*Fermi*/GBM

Table 17.1: List of all the Gamma-Ray Bursts observed by LST-1 up to the end of 2022

Run Number	Significance	Offset	Zenith angle
4718	3.9σ	1.6°	45°
4719	0.6σ	2.4°	43°
4720	2.4σ	2.2°	41°
4721	3.3σ	1.9°	39°

Table 17.2: Results of the analysis of the hotspot run per run for observation data on GRB 210511B.

17.3 Analysis of a few bursts

This section presents the analysis of two bursts I have worked on and that present a particular interest. All the results presented here have been generated with the 0.9 version of `lstchain` and using the `Base` cuts described in the chapter 13.

17.3.1 GRB 210511B

GRB 210511B was one of the first observed GRBs by LST-1 and was the first one originating from *Fermi*/GBM. Detected during the day of the 11th of May 2021 (Bissaldi et al., 2021), it was followed with a 16 hours delay for a total of 70 min of observations. Due to the large uncertainty on the localisation, it has motivated the development of a background model to be able to search for a signal anywhere in the field of view. More details on the background modelling performed are available in chapter IV.

17.3.1.1 Analysis and results of the LST-1 observations

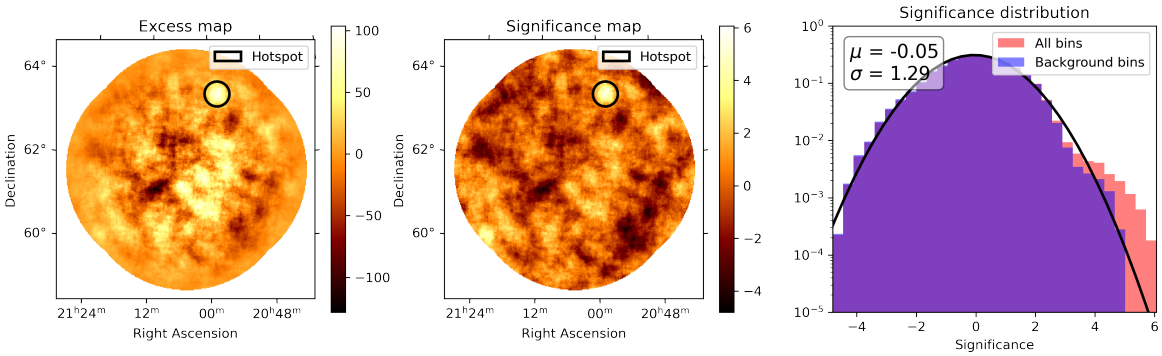

Figure 17.2: Excess map (left panel), significance map (centre panel), and distribution of the significance (right panel) for the observations of GRB 210511B for an energy between 50 GeV and 190 GeV, the circled in black is the hotspot identified.

Using the background model, a hotspot was identified in the lowest energy bin, 50 GeV to 190 GeV (Fig. 17.2) with a significance of 5.2σ. The bin just above in energy shows an excess significance of 2.3σ. Moreover, the total significance with all the data stacked is 4.6σ. By taking into account all the analysis and maps performed on the FoV, this leads to a 4.4σ post-trial significance.

A soft hotspot at a large observation offset could be easily caused by an issue with the camera, the calibration or the reconstruction. The first step was to perform quality verification of the data, and no issue was found at any of the available quality checks.

The position measured for the hotspot is RA $= (314.471 \pm 0.017_{stat})°$ and Dec $= (63.250 \pm 0.010_{stat})°$. To confirm that the existence of the hotspot was not due to an issue with the background model, an analysis with a multiple OFF background estimation was performed. Due to the apparent softness of the spectra, only events below 300 GeV were used. This led to successful detection of the hotspot with an excess significance of 5.5σ (Fig. 17.3).

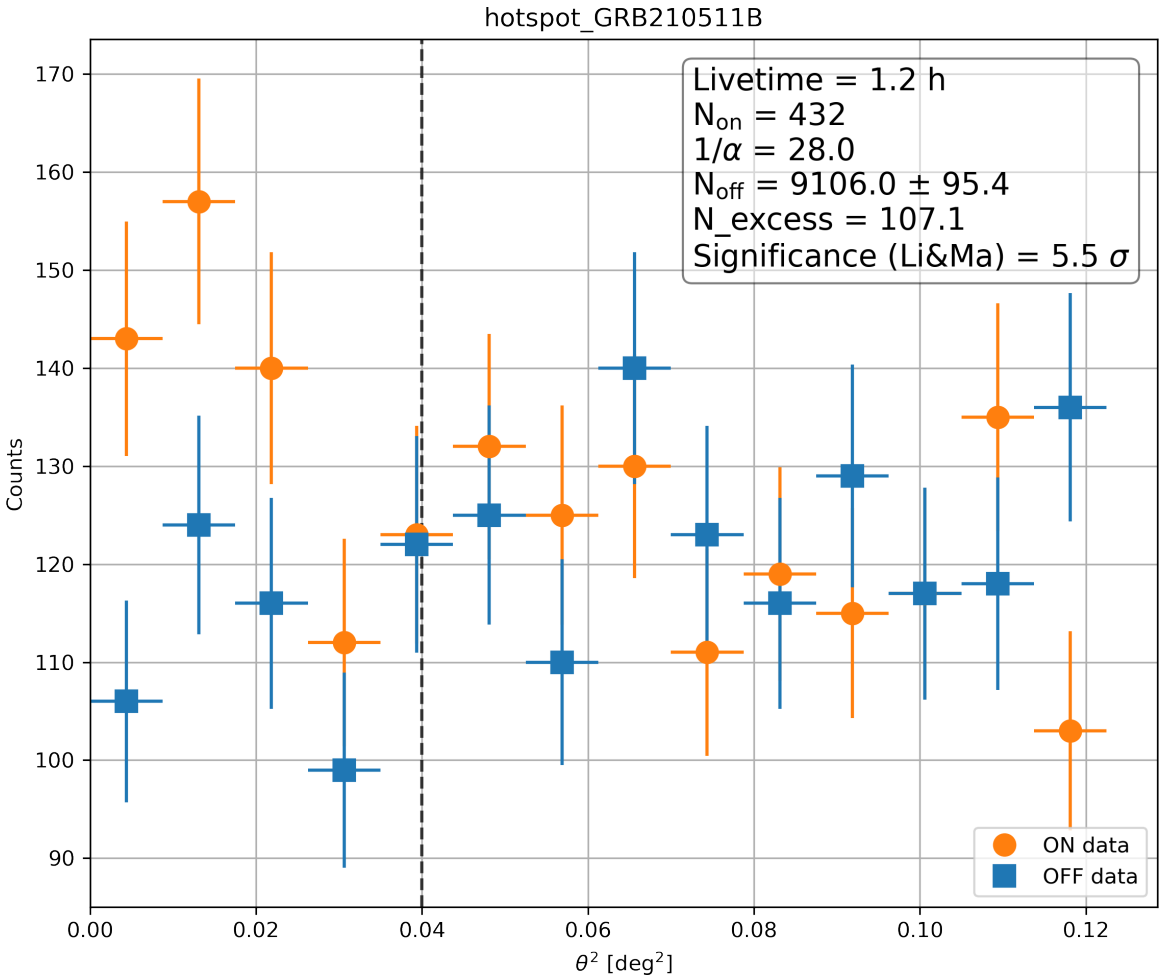

Figure 17.3: Theta square plot for the hotspot position on the observation of GRB 210511B for energy below 300 GeV

The table 17.2 shows the results of the analysis of each run. It is possible to see the hint of a signal in three of them. The one without any signal corresponds to the one with the highest offset, so the least sensitive run.

A spectral analysis was performed, and the data were best fitted by a power law of index $4.3 \pm 0.5_{stat}$ with an amplitude of $(1.3 \pm 0.7_{stat})^{-11}\mathrm{cm}^{-2}.\mathrm{s}^{-1}.\mathrm{TeV}^{-1}$ for a reference energy of 447 GeV. As the analysis of LST-1 has not been validated on high offset observations, these results need to be taken carefully. The soft index is in agreement with what we have expected from the first results above.

17.3.1.2 Identification of the hotspot

The day after the observations, the IPN network gave a better localisation of the burst (Hurley et al., 2021), which was completely outside of the observed field of view as can be seen on figure 17.5). The LST hotspot could not be caused by the GRB.

A search based on the localisation for the counterpart in other wavelengths was performed. No credible counterpart was identified in TeVCat (Wakely and Horan, 2008), the *Fermi*/LAT catalogue 4FGL-DR2 (Abdollahi et al., 2020), the pulsar database ANTF[1], the NED database or the Simbad one.

[1] https://www.atnf.csiro.au/research/pulsar/psrcat/

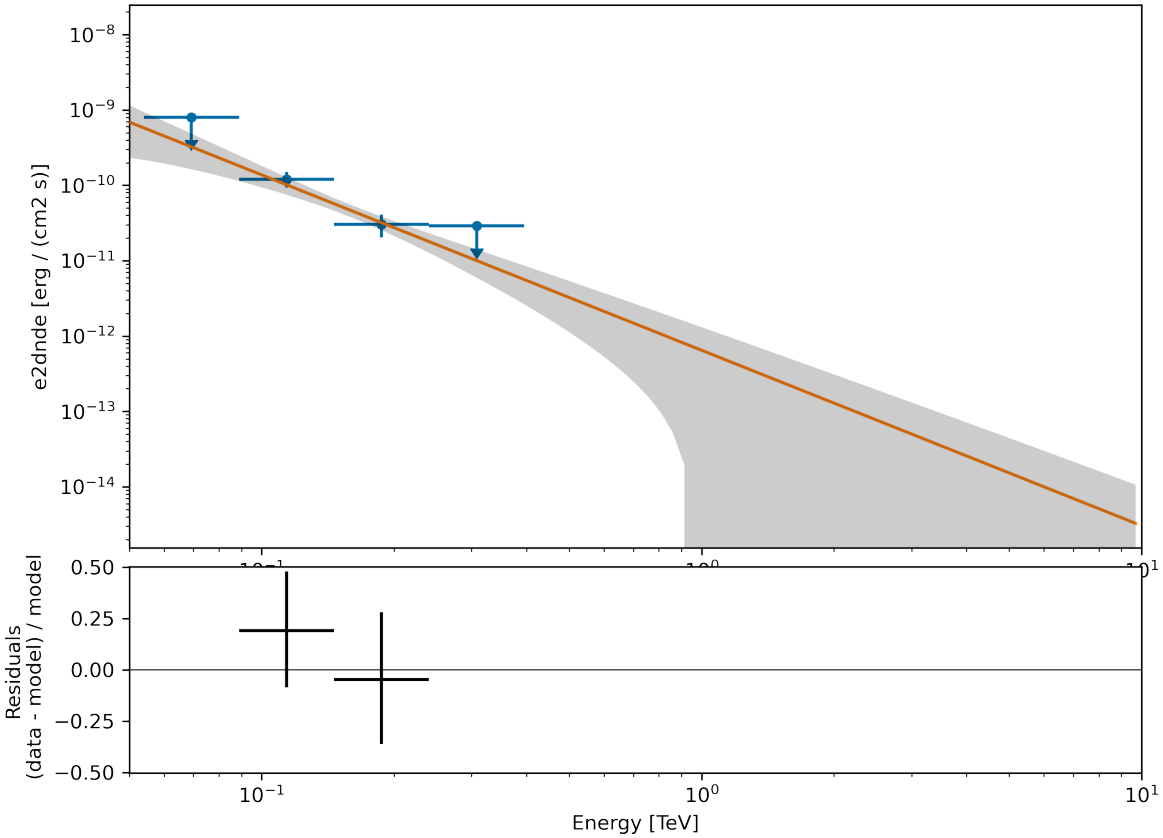

Figure 17.4: Measured spectra of the hotspot

A *Fermi*/LAT analysis on the position using data on the three days before to three days after the burst did not reveal any detection. This result is compatible with the LST-1 observations.

To conclude, the hotspot is detected in an energy range covered by *Fermi*/LAT. The lack of presence of a counterpart in the 4FGL-DR2 would tend to reject the possibility of having a new steady source, and so if the signal is real, it is likely due to a transient source. Even if no issue was found in the data quality, the question could be asked if it is a real signal or an issue with either the hardware, the calibration or the reconstruction. It is at this stage impossible to determine with high confidence if it is a real signal. As the number of trials on the data is already quite high due to being used for testing background models, any further steps need to be thought carefully. Rerunning an analysis with fully optimised event selection cuts will be likely interesting to get a better perspective on this hotspot.

17.3.2 GRB 210704A

GRB 210704A was first detected by *Fermi*/GBM on the night of the 4th of July 2021 (Malacaria et al., 2021). This is a long GRB with a relatively short T_90 of 4.7 s. It was a bright GRB with the peak flux in the top 2% and the fluence in the top 6% of the GRBs detected by the instrument. The observations started 2 h after the burst for 55 min at a high zenith angle. the *Fermi*/LAT collaboration communicated the detection of this burst the next day (Berretta et al., 2021). This was followed by the detection of the afterglow by *Swift*/XRT (D'Ai et al., 2021).

17.3.2.1 Next Day Analysis

The real-time analysis of the LST is not yet fully functional. For this reason, performing next-day analysis on GRBs is important as it is the only way to know if there is a signal in the data to

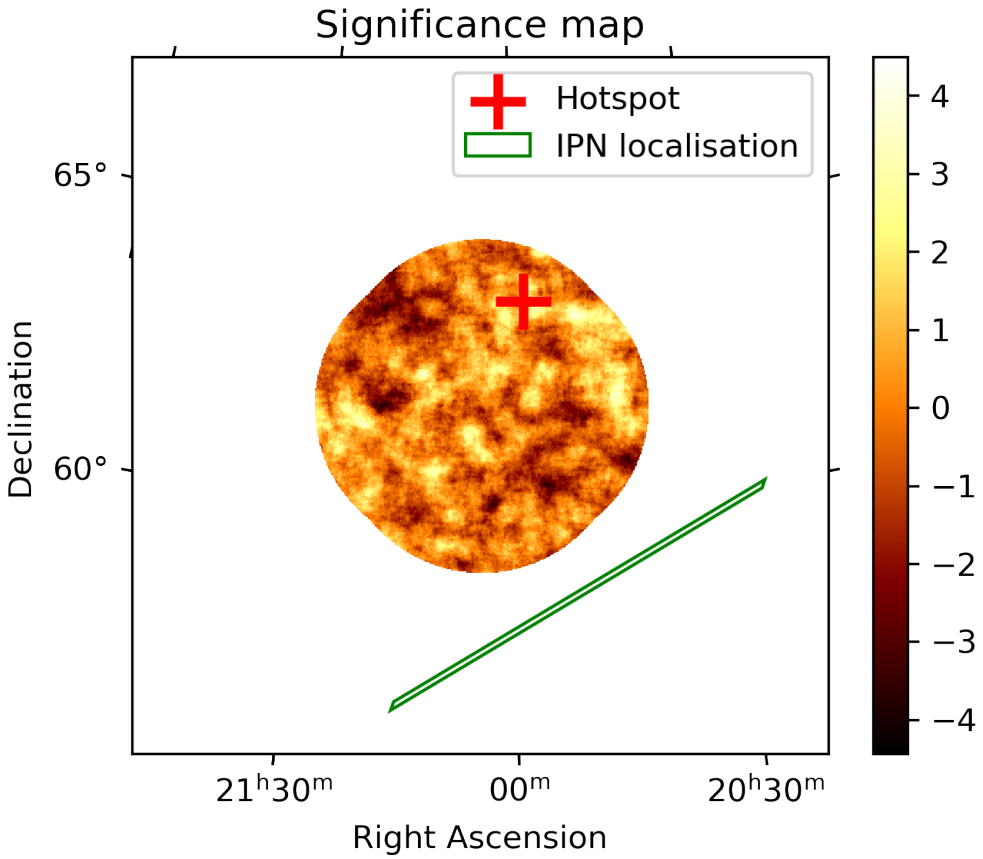

Figure 17.5: Significance map of the observation on GRB 210511B with in green the localisation by IPN.

continue observations the next night. The data are automatically processed up to the DL2 level by the LST-OSA[2] pipeline. The results are typically available in the afternoon. Then it is possible to process up to DL3 using scripts from `lstchain`, but doing it by hand is a bit time-consuming as you need to localise each file to give to the scripts, and the scripts need to be called for each run, each time with a processing time. Then, the analysis from the DL3 needs to be performed using `gammapy`.

To perform a quick analysis, I have made a tool that automatically determines all the parameters for `lstchain` scripts. Then all needed scripts are submitted as jobs on the computing farms with dependency between them when the action is needed to be executed in a specific order. This allows the processing of the data in parallel in one command. Then some jupyter notebooks were prepared to have only a few parameters to change in order to analyse the data. This allows us to get the analysis results in 30 to 60 minutes after LST-OSA finishes the processing so before the night. The tools and notebooks have continued to evolve and are used at LAPP for a lot of different analyses.

With these tools, GRB 210704A was the first source to be analysed the next day in the LST collaboration. It is now quite common for GRBs to have analysis results the next day.

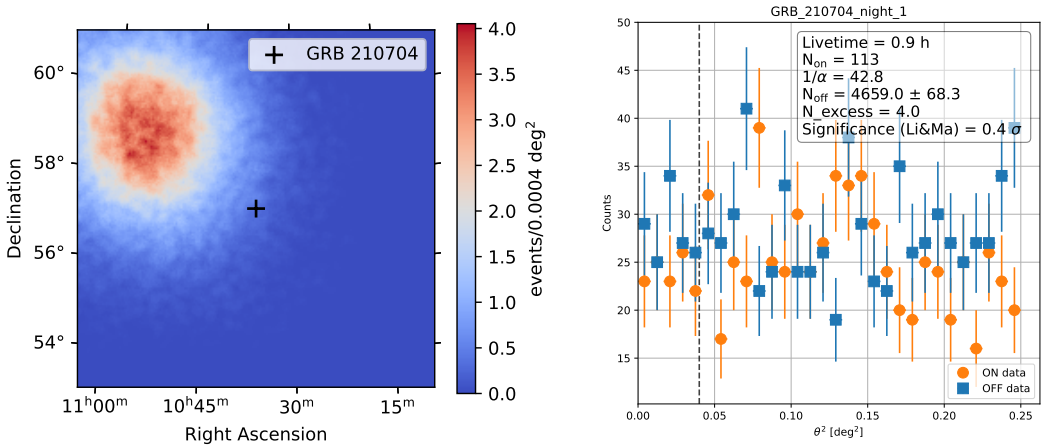

Figure 17.6: Analysis results from the GRB 210407A observations on the first night with on the left panel the count maps and on the right panel the theta square plot representing the excess in function of the square angular distance to the source position.

17.3.2.2 Analysis results

The *Swift*/XRT position was on the very edge of the field of view with an offset varying between 2.6° and 3.3°. The counts' map is given in figure 17.6, confirming the limit of the field of view with likely events quite badly reconstructed. The analysis with a Multiple-OFF background estimation leads to no signal at all with an excess significance of 0.4σ (Fig. 17.6).

The very challenging observation condition (high offset and high zenith) of the first night might have hidden a possible TeV counterpart. Moreover, the detection of the GRBs by *Fermi*/LAT was an argument in favour of observation during the following night on the XRT position. Due to technical issues, only 20 min of observations were acquired. No signal was found with a significance of 0.8σ (Fig. 17.6).

17.3.2.3 Test with the Crab

The analysis of LST-1 has yet to be tested for such high offset observations. Some optimisation is likely possible, but to get an idea of what performance we could expect, Crab observations in similar conditions were requested. 80 min of Crab observation at 2.5° of offset and with a zenith angle between 50° and 65° were acquired. The offset is a bit smaller than for the observation of the burst but already led to no detection with an excess significance of 1.2σ (Fig. 17.8), so it was decided not to plan any further observation on the Crab.

We could conclude that the very challenging observation conditions have likely contributed to the lack of any signal measured on this GRB.

[2] https://github.com/cta-observatory/lstosa

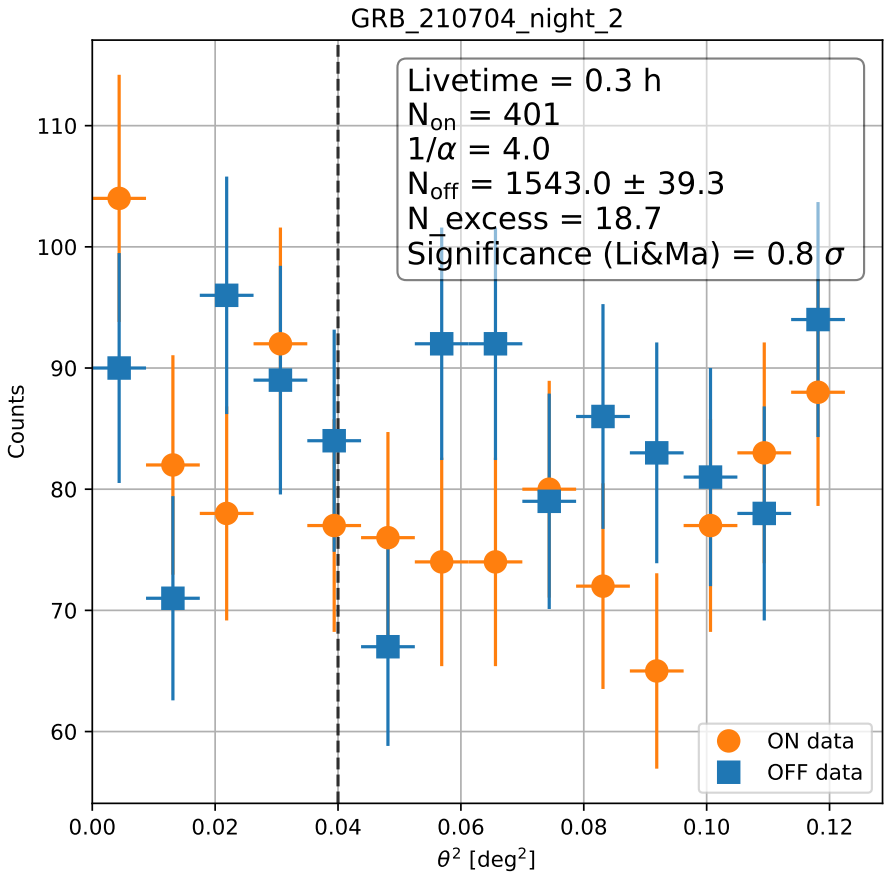

Figure 17.7: Theta square plot representing the excess in function of the square angular distance to the source position for the second night of observation on GRB 210407A

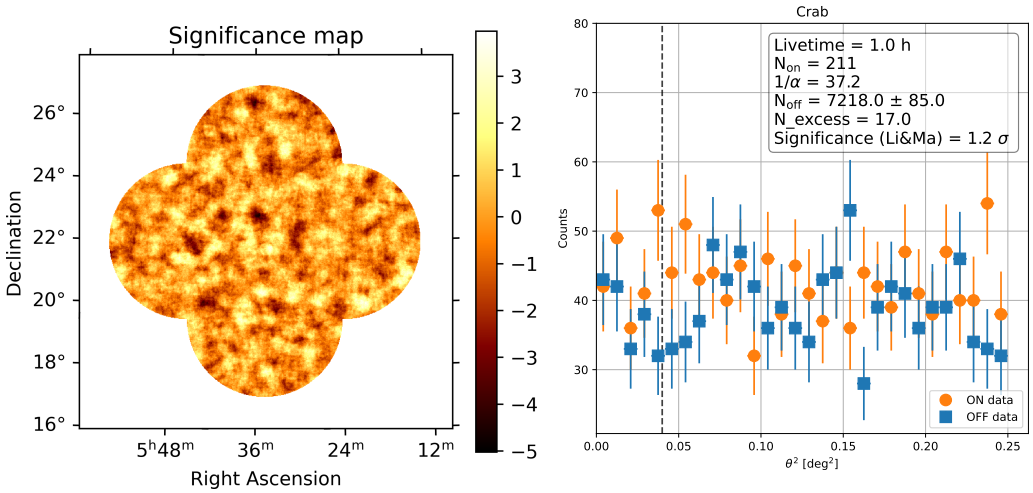

Figure 17.8: Significance map (left panel) and theta square (right panel) plot for high offset and high zenith observation on the Crab.

Chapter 18

Improving selection criteria for GBM follow-up

Contents

The Gamma-ray Burst Monitor (GBM) onboard *Fermi* detected a high number of GRBs and is more sensitive to short GRBs than *Swift*/BAT. So following alerts from this instrument allows us to follow more GRBs with a small delay and also increases the chance of following short GRBs that have yet to be detected at VHE. However, the follow-up of the alerts sent by *Fermi*/GBM is complex due to the large uncertainty on the position, much larger than the field of view of Cherenkov instruments. The uncertainty on the position of the GRBs could vary quite a lot as a function of the alert.

Currently, the Cherenkov instruments follow the GBM alerts but select them only based on the significance of the GRB and the position uncertainty provided by the GBM. For example, LST-1 only observe events with a position uncertainty of 2° and a minimum significance of 20. Finding and optimising selection criteria for the alert to follow could help to improve the efficiency of the observations by selecting GRB which has a higher chance of being within the FoV.

18.1 The *Fermi*/GBM instrument

The GBM instrument is composed of a total of 14 detectors, 12 NaI crystals scintillators that provide the low energy data (8 keV-1 MeV), and 2 BGO crystals scintillators that provide the high energy data (400 keV-40 MeV) (Meegan et al., 2009). The orientation of the low energy detectors (Fig. 18.1) ensure that several of them can cover any localisation in the sky. The high energy detectors are placed on each side of the spacecraft to ensure that any part of the sky is at least visible by one of them.

These multiple crystals scintillator detectors provide a very large energy range, and a good temporal resolution but do not have any direct imaging capabilities. The direction of the burst

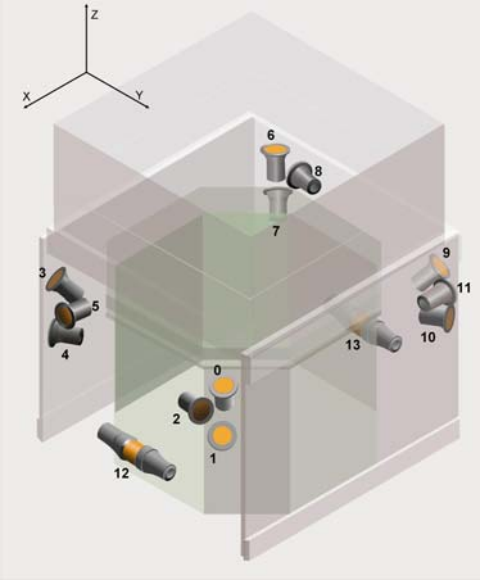

Figure 18.1: Position and orientation of the detectors of GBM in the *Fermi* spacecraft. Figure from Meegan et al. (2009).

is then determined through the relative count rates in the different detectors, explaining the poor angular resolution of the instrument.

More details about the *Fermi*/GBM instrument can be found in Meegan et al. (2009).

18.2 Alert from *Fermi*/GBM

The GBM instrument triggers on a burst when the rate of at least two of the NaI detectors exceeds a given number of standard deviations above the background. Following this trigger, the instrument will send alerts emitted by the spacecraft directly and also data to ground facilities that will provide new alerts and information, with better precision but a higher delay.

The alerts are then sent to the GCN system[1] and will be redirected to other instruments through automated notices. There are four types of notices for GBM [2] :

- GBM_Alert, these notices are sent just after the trigger of GBM and do not contain any spatial information. The main aim is to inform that GBM has detected a burst and will send more information
- GBM_Flight_Position, these notices contained the estimation of a first position estimated from onboard treatment. There could be sometimes multiples of these notices emitted as the amount of data collected increases. These notices also contained information about the classification of the burst (GRB, SGR, TGF, ...).
- GBM_Ground_Position, these notices contain localisation information obtained from treatment performed on the ground. They tend to be more accurate. There also could be multiples of them as more data are transmitted by the spacecraft.
- GBM_Final, these notices contain the final estimation of the position using all the data and the best available algorithms. There is also a human implicated in reviewing the analysis.

There is also a fifth type of notice dedicated to sub-threshold detection, which is rarely used and with a high delay. We will not consider them here. The different types of information that could be

[1] https://gcn.nasa.gov/
[2] https://gcn.gsfc.nasa.gov/fermi.html

Type of Notice	GBM_Alert	GBM_Flight_Position	GBM_Ground_Position	GBM_Final
Trigger time	×	×	×	×
Position		×	×	×
Position uncertainty		×	×	×
Significance of the burst	×	×	×	
Integration time	×	×	×	
Classification		×		
Hard Ratio		×		
List detector triggered	×	×	×	
Intensity		×		
Probability map			×	×

Table 18.1: Information contained in each type of notices sent by *Fermi*/GBM

found in each type of notice are listed in table 18.1. For our analysis, if the information is missing from one type of notice, we will use the information given in the previous ones. For example, for classification, it will be the one of the last `Flight` notices used for both `Ground` and `Final` notices, and for the integration time, it will be the one from the last `Ground` notices used for `Final` notices.

It is worth noticing that the position uncertainty given in `Ground` and `Final` notices only includes statistical uncertainty, while the probability maps, produced by `Ground` and `Final` notices, also include systematic uncertainty.

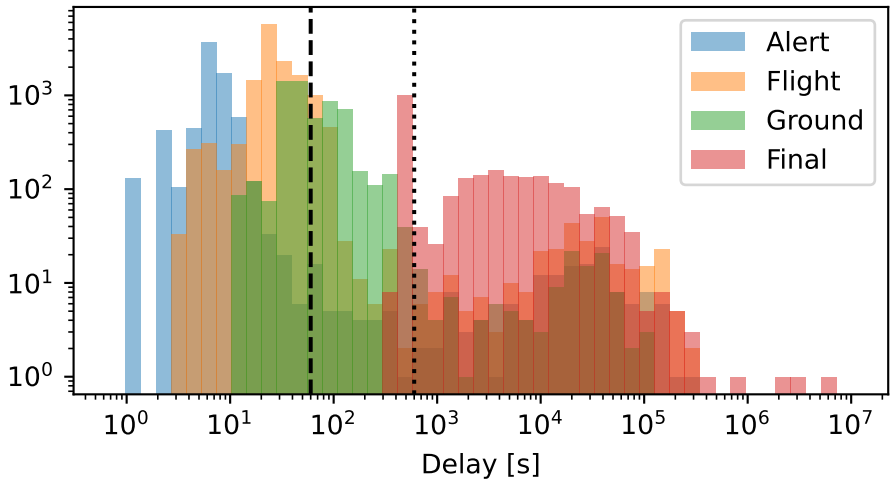

Figure 18.2: Distribution of the delay for each type of notice sent by the GBM instrument. The dashed line represents the minute of delay, while the dotted line corresponds to ten minutes of delay. This figure was made using ~ 30000 notices sent by *Fermi*/GBM over 13.5 yr for a total of 7874 events.

The delay of the notices after the trigger depends quite a lot on their type. The distribution of these delays can be seen in figure 18.2. The first notices with position, the `Flight` ones, arrive typically with less than a minute of delay with a peak of the distribution around 20 s. The `Ground` notices distribution peak around one minute of delay, but a longer delay is not unusual. The `Final` notices typically arrive just shy of ten minutes of delay but have a long tail of the distribution, with non-rare cases of notices arriving with a few hours of delay.

Consequently, it is not possible to only use `Final` notices with the best localisation as we will always have a significant delay.

18.3 Matching data with *Swift*/BAT

18.3.1 Why using the *Swift*/BAT catalogue

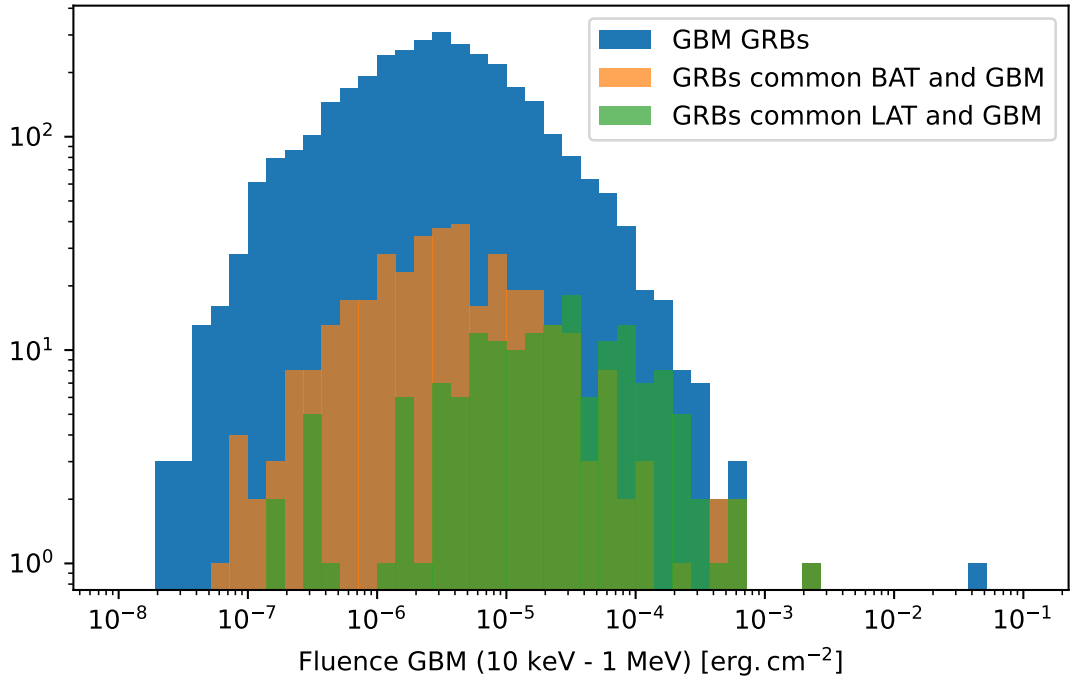

Figure 18.3: Distribution of the fluence in *Fermi*/GBM for all GBM GRBs (blue), GRBs common with *Swift*/BAT (orange), and GRBs common with *Fermi*/LAT (green)

The aim is to select GRB for which the localisation is well reconstructed by GBM. To build and improve our burst selection criteria, the exact position of the burst needs to be known. Onboard the same satellite, the *Fermi*/LAT instrument could detect GRBs and is an option for a cross-match, but it will not be used for several reasons :

- The localisation accuracy of *Fermi*/LAT is typically around ∼0.4° and could go up to a degree sometime. This will add some uncertainty to the results of the study.
- Due to the low sensitivity, the LAT tends to select only bright GRBs adding bias to the study (Fig. 18.3)
- The number of GRBs detected by both *Swift*/BAT and *Fermi*/GBM is larger (360) than the ones by both *Fermi*/LAT and *Fermi*/GBM (219)

The *Swift*/BAT experiment has detected numerous GRBs with a precise localisation (a few arcminutes). The number of common GRBs is relatively large (360), and its performances should allow to avoid significant bias in the study due to possible differences in properties between GRBs detected only by GBM and GRBs detected by both instruments.

18.3.2 Matching procedure

All GCN notices emitted by *Fermi*/GBM[3] before April the 5th 2022 were downloaded and parsed to build a database. This database is composed of 29963 notices for 7874 different GBM triggers.

[3] https://gcn.gsfc.nasa.gov/fermi_grbs.html

All the triggers, likely not GRBs, were removed, reducing the number of notices to 16364 for 3667 events.

For *Swift*/BAT, the GRBs were gathered from the *Swift* GRB table[4]. As it only contains events already classified as GRBs, no further selection was applied.

The match was performed by searching for events for which the trigger time of *Swift*/BAT and *Fermi*/GBM was within a one-minute time window. The few events with a very high difference in position were checked manually, based on the circular available on GCN, and four events were removed. This led to a total of 360 common events for a total of 1687 GBM notices. If most of the events contained at least one `Flight` notice and one `Ground` notice, half of the events lacked a `Final` notice.

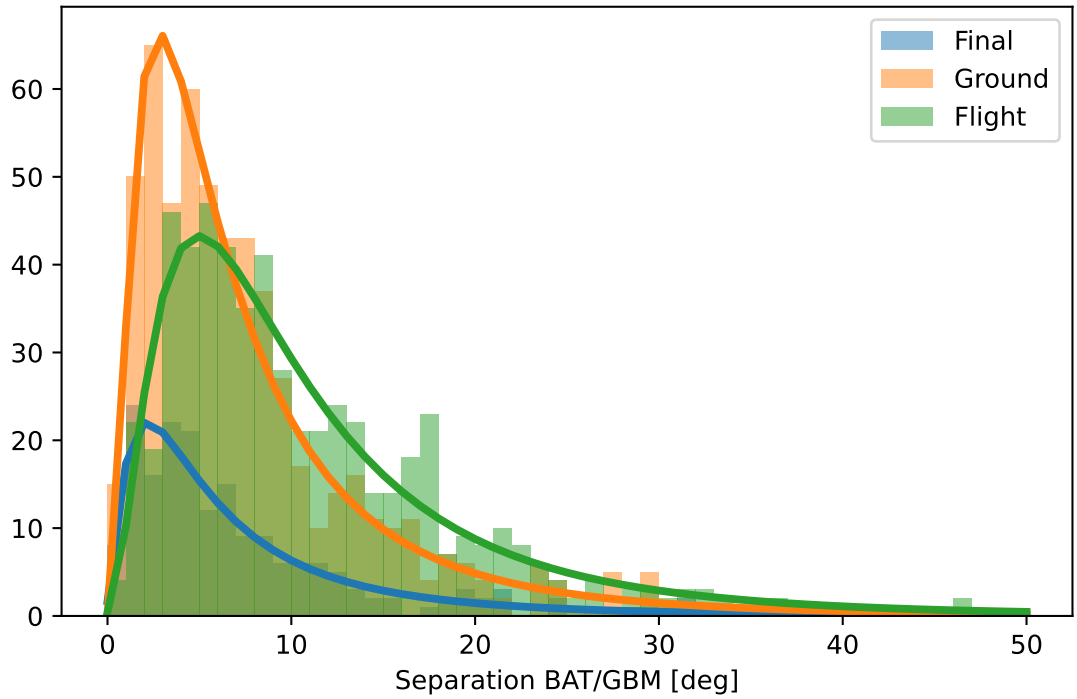

Figure 18.4: Distribution of the difference of position between *Swift*/BAT and *Fermi*/GBM for each notice sorted by type

The figure 18.4 shows the distribution of the separation between the position given by GBM and by BAT for each notice. If we apply no filter, the peak of the distribution for `Final` notice is at $\sim$2.2°, but with the long tail, the 68% and 90% containment are respectively at $\sim$8° and $\sim$17.5°. With a typical field of view of Cherenkov instruments of 2° of radius, this shows the huge challenge of following these alerts. If all alerts are followed without any selection, this will lead to only 17% of the alerts with the GRB within the field of view.

18.3.3 Checking for potential bias in the subset of notices

As we have selected a sub-sample of all the notices, it is important to check the impact of the selection to ensure that no bias has been introduced. All the parameters included in the notices have been checked, and the distribution of a few of them is shown in figure 18.5. One parameter, named `number of photons` and computed from others, was added. This parameter is a rough estimation of the number of photons detected based on the multiplication of the duration of the integration window and the intensity count rate of photons.

[4] https://swift.gsfc.nasa.gov/archive/grb_table/

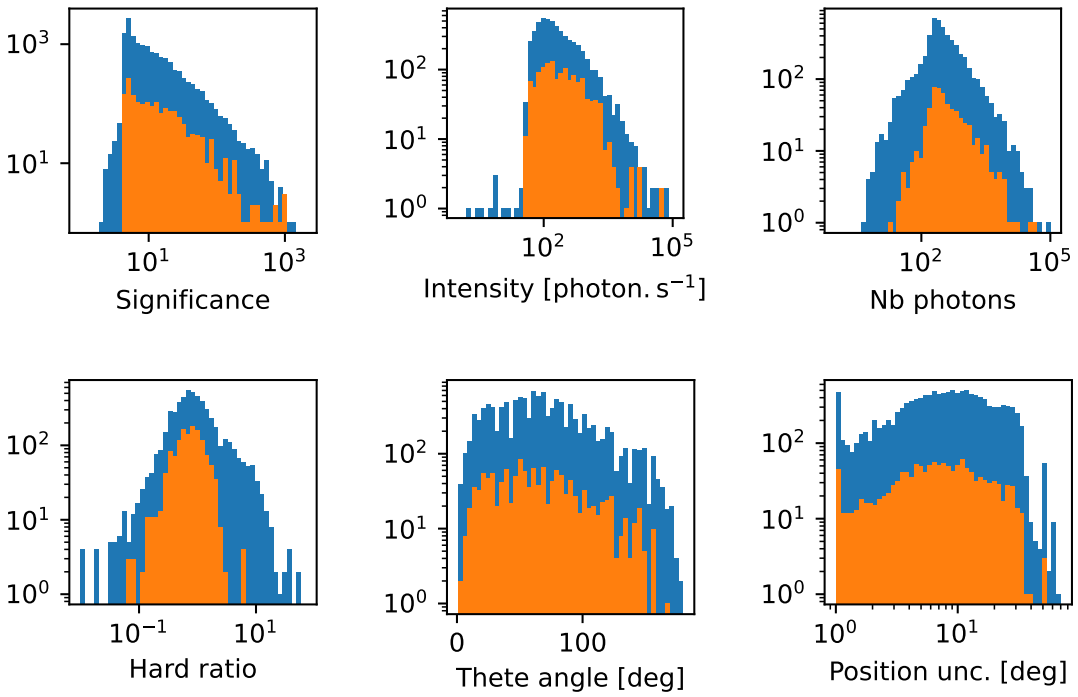

Figure 18.5: Distributions of various parameters for all GRB notices (blue) and for the ones corresponding to GRB also detected by *Swift*/BAT (orange).

No major bias could be seen on most of the parameters. The main difference is on the hard ratio, which is the ratio of the number of high-energy photons versus the number of low-energy photons. This difference is not a complete surprise, as *Swift*/BAT (15 keV-300 keV) focus a lot more on low energies compared to the much wider energy range of *Fermi*/GBM (10 keV-30 MeV). This parameter could have an impact on the reconstruction of the localisation as this is the low energy detector of GBM that provides it, but there is no easy way to compensate for it.

18.4 Selecting and optimising the selection criteria

18.4.1 What are the pertinent selection criteria ?

At this stage, quite a lot of parameters are available from various notices. Some of them will have a small to no impact on the accuracy of the position detected by GBM. The first step is to search for a correlation between parameters and the maximum separation between the GBM and the BAT position, which is a proxy for the GBM measurement error (Fig. 18.6).

There are four parameters which can be used for the selection that stick out :

- Position uncertainty
- Significance
- Intensity
- Number of photons

The degree of correlation between three of the four parameters (significance, intensity, number of photons) is quite high. This is then inefficient to optimise the cuts on all three parameters, but we will try to find which of these three parameters, coupled with the position uncertainty, will give the best results and optimise the cuts.

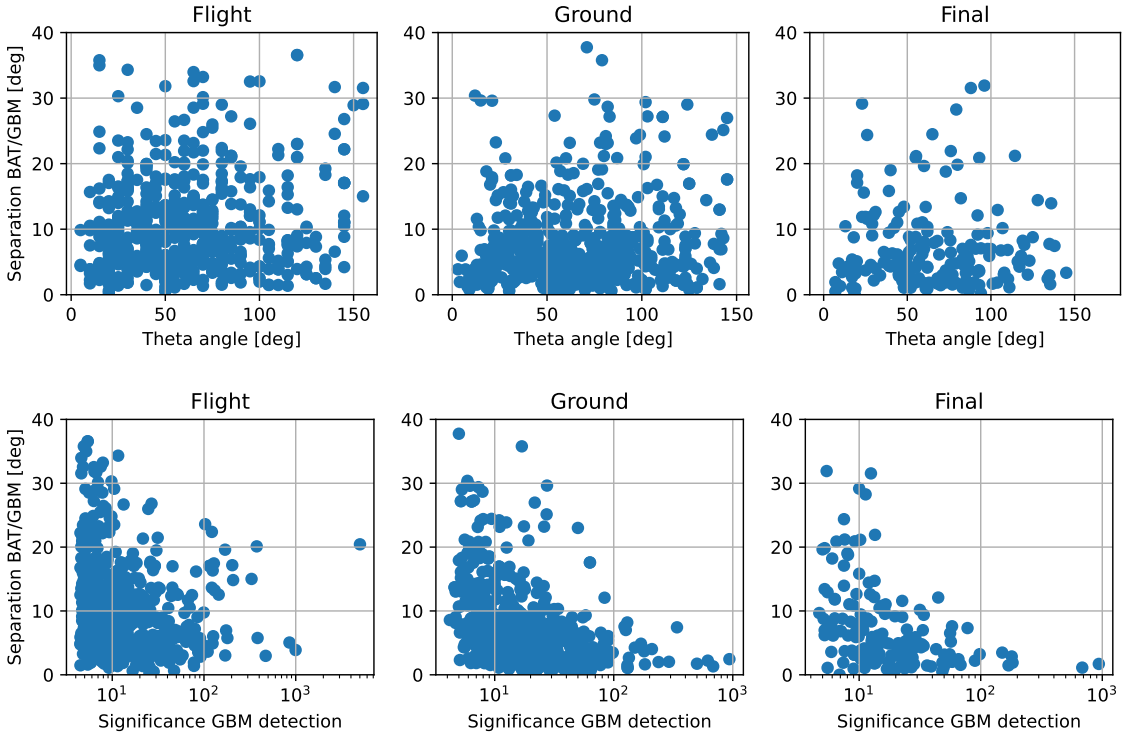

Figure 18.6: Scatter plot of the separation between the GBM and BAT position as function of the theta angle (top row) and the significance of the detection (bottom row). The left panel is for `Flight` notices, the middle one for `Ground` notices and the right one for `Final` notices.

18.4.2 Test performance of selection criteria

To test these criteria' capacity to identify the well-localised GRBs, we will look at a few indicators as a function of the values used for selection. As the aim is to maximise the efficiency of the observations, i.e. following more GRBs with a higher chance of having them on the FoV, one indicator is the fraction of GRBs kept after applying the selection. Other indicators must be linked to the accuracy of the localisation.

At the time, the observations were conducted in pointed mode. The telescope is pointed in the direction given by GBM and only on this one for the full observation time. To match this procedure, we will use a radius of 2° to compute the fraction of GRBs after selection for which the GBM position is within a 2° radius with respect to the BAT position. We call it $F_{2\mathrm{deg}}$.

In the future, as the localisation of GBM is much worse than our field of view, observations will be conducted using the tilling method. This method is currently under implementation for LST-1 based on the method used by H.E.S.S. for follow-up of gravitational waves (Ashkar et al., 2021). The overall idea is to use the probability map given by GBM to determine a series of pointing to cover a larger proportion of the uncertainty region. For this case, we will use two different indicators, the radius R, for which 50% (and 90%) of the GRBs have a GBM measurement error below R. We call them R_{50} and R_{90}.

This difference is motivated by the objectives which are not to maximise the chance of having the GRBs within one single field of view but to minimise the number of pointing to make in order to achieve a large coverage of the uncertainty region. To estimate the parameters linked to localisation, a fit of a log-normal distribution on the separation between the position of GBM and BAT is used, as tests on various cases have shown it is able to describe quite well the shape of the distribution.

These indicators could give quite different behaviour due to the shape of the systematic uncertainties. Authors from the GBM collaboration have modelled them as composed of two gaussian

distributions, one forming the core with a width of 3.7(3)° and a tail with a width of 14(2)° (Connaughton et al., 2015) for `Ground` and `Final` notices (with a difference in the relative normalisation of the distribution for the two types of notices). Due to this very long tail, the behaviour will not always be the same between our indicators.

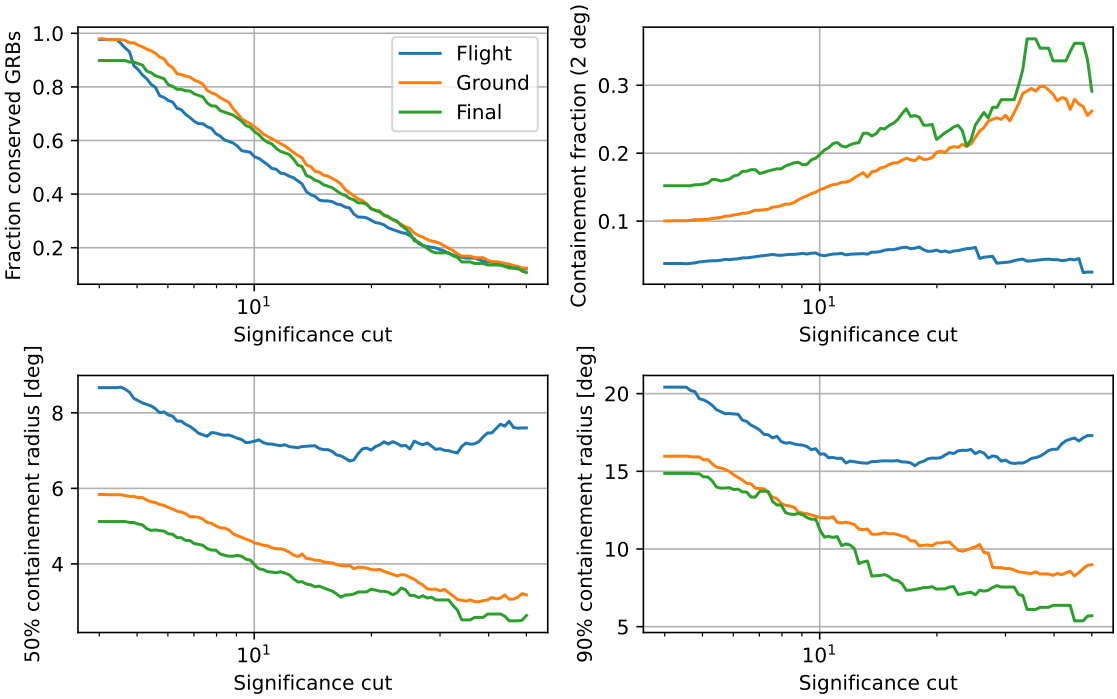

Figure 18.7: Evolution of the fraction of conserved GRBs (top left panel), $F_{2\text{deg}}$ (top right panel), R_{50} (bottom left panel), R_{90} (bottom right panel) as function of the significance cut used, for the `Flight` notices (blue), `Ground` notices (orange), `Final` notices (green).

The figure 18.7 shows the indicators as function of the significance cut. With a higher cut on the significance, more GRBs are lost (top left panel), but the GBM localisation improves.

When only using one parameter for the selection, each indicator linked to localisation ($F_{2\text{deg}}$, R_{50} and R_{90}) could be expressed as a function of the fraction of conserved GRBs. The results for each indicator are shown in figure 18.8. For $F_{2\text{deg}}$, the better selection will be the more on the top right corner, while for R_{50} and R_{90}, the best will be at the lower right corner.

From these results, we could see that the intensity cuts will be either on par or have worse performance than other cuts. We will remove it for the next part of the analysis. It is also possible to see that the selection criteria have little impact on the `Flight` notices, while it is possible to improve by a factor of two the localisation with strict cuts compared to no cuts for other types of notices. The localisation is also very poor compared to the others notices. The `Flight` notices are still important but deserve special treatment, which is explained in section 18.4.4.

18.4.3 Combining two selection criteria

We are now left with two parameters (significance and the number of photons) to be combined with the GBM position uncertainty. Figure 18.9, top left, shows the fraction of selected GRB for each cut value of the significance and the GBM position uncertainty. Since we want to improve the observation efficiency, we can use a predefined fraction i.e. 0.3. This gives us an ensemble of couples {position uncertainty, significance} as seen in the figure. For each other indicator ($F_{2\text{deg}}$, R_{50} and R_{90}), we can find the best couple of this ensemble which maximises each indicator. The example is

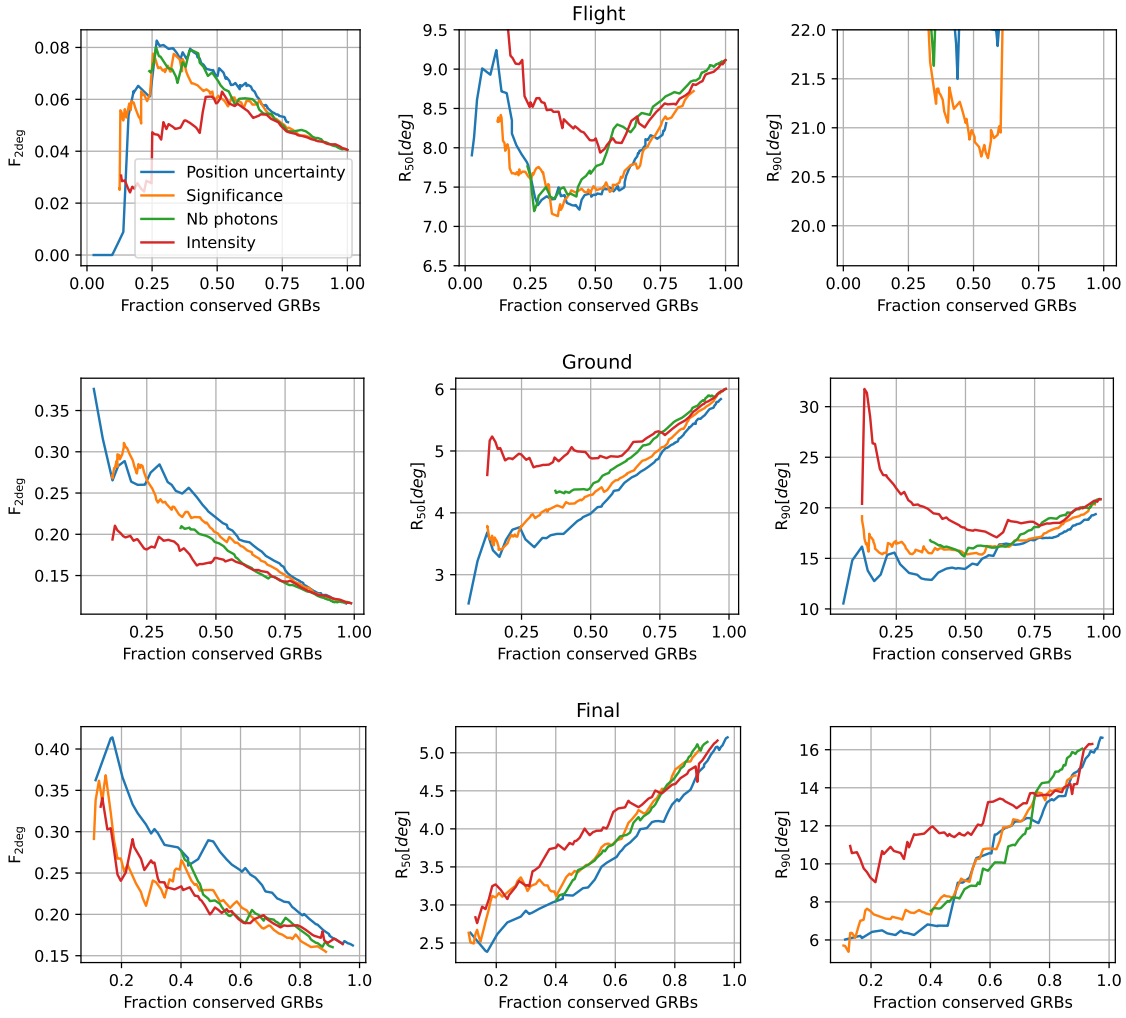

Figure 18.8: Evolution of $F_{2\text{deg}}$ (left columns), R_{50} (middle columns), R_{90} (right columns) as function of the fraction of conserved GRBs when applying cuts on the position uncertainty (blue), significance (orange), number of photons (green), and intensity (red). The `Flight` notices are the first row, the `Ground` notice the second row, and the third row the `Final` notices.

also shown as a cross on the three other panels of figure 18.9 for the `Ground` notices and the couple {position uncertainty, significance}.

This can then be done for different values of the fraction of selected GRB and for both couples {position uncertainty, significance} and {position uncertainty, number of photons}. The final results, obtained for different values of the faction of selected GRB, are shown in figures 18.10 and 18.11.

18.4.3.1 Pointed observations

The figure 18.10 shows the best values of $F_{2\text{deg}}$ we can have as a function of the GRB we want to follow for `Ground` and `Final` notices. The crosses are the current LST cuts, the instrument following then 18% of the alerts. This is clearly not optimal in terms of efficiency since the same fraction of GRBs can be followed but with a higher chance of being within the FoV. While for `Ground` notices, both parameters (significance and the number of photons) give similar results, the cut on the number of photons performs better for `Final` notices.

As in the current state of LST-1, the objectives are to follow a large number of GRBs. For a

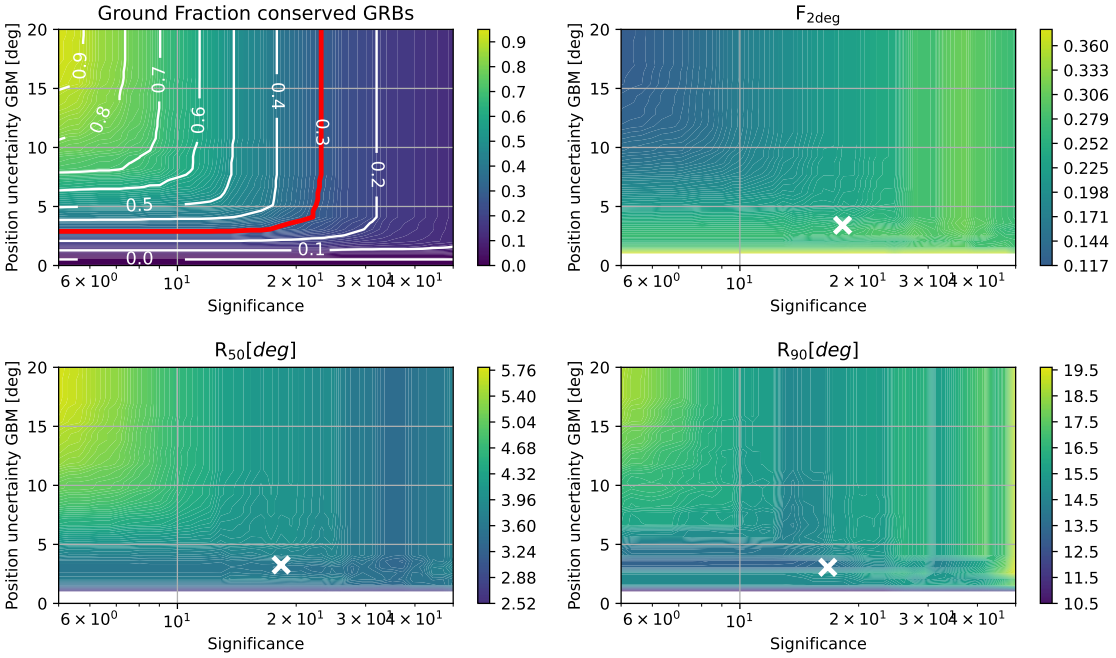

Figure 18.9: Fraction of conserved GRBs (top left panel), $F_{2\text{deg}}$ (top right panel), R_{50} (bottom left panel), and R_{90} (bottom right panel) as function of the significance and the position uncertainty for `Ground` notices. The white crosses represent for the three indicators the optimal value on the 30% contours (red line).

$F_{2\text{deg}}$ of 27.5% (black dotted line), which is a bit better than the current selection for `Ground` and worse for `Final`, up to 50% of the GRBs can be followed.

As some GRBs could miss `Ground` or `Flight` notices, it is not always possible to compute the estimation of the number of photons. For this reason, three cuts will be determined. The one for `Ground` alert using position uncertainty and significance, and two for `Final` alert, using position uncertainty and for one case significance and for the other case the number of photons. The one using significance will be used as a fallback when it is not possible to compute the one based on the number of photons.

The new proposed cuts for pointed observations alongside to the old ones are summarised in table 18.2. With these cuts, 52% of the observations will start with a `Ground` notice, allowing for low delay observations, while only 2% of the observations will lead to GRBs that do not pass the selection applied on `Final` notices which will lead to aborted observations.

	Current `Ground`	New `Ground`	Current `Final`	New `Final`	Alternative `Final`
Position uncertainty	$<2^\circ$	$<3.1^\circ$	$<2^\circ$	$<4.5^\circ$	$<3.4^\circ$
Significance	$> 20\sigma$	$> 18.5\sigma$	$> 20\sigma$		$> 5\sigma$
Number of photons				> 185	
Fraction GRBs conserved	18%	29%	18%	49%	37%
$F_{2\text{deg}}$	26%	27.5%	32%	27.5%	27.5%
R_{50}	3.7°	3.5°	2.7°	3.3°	3.0°
R_{90}	15.1°	13.8°	6.4°	7.4°	6.8°

Table 18.2: Selection criteria for `Ground` and `Final` notices in the case of pointed observations with their performance.

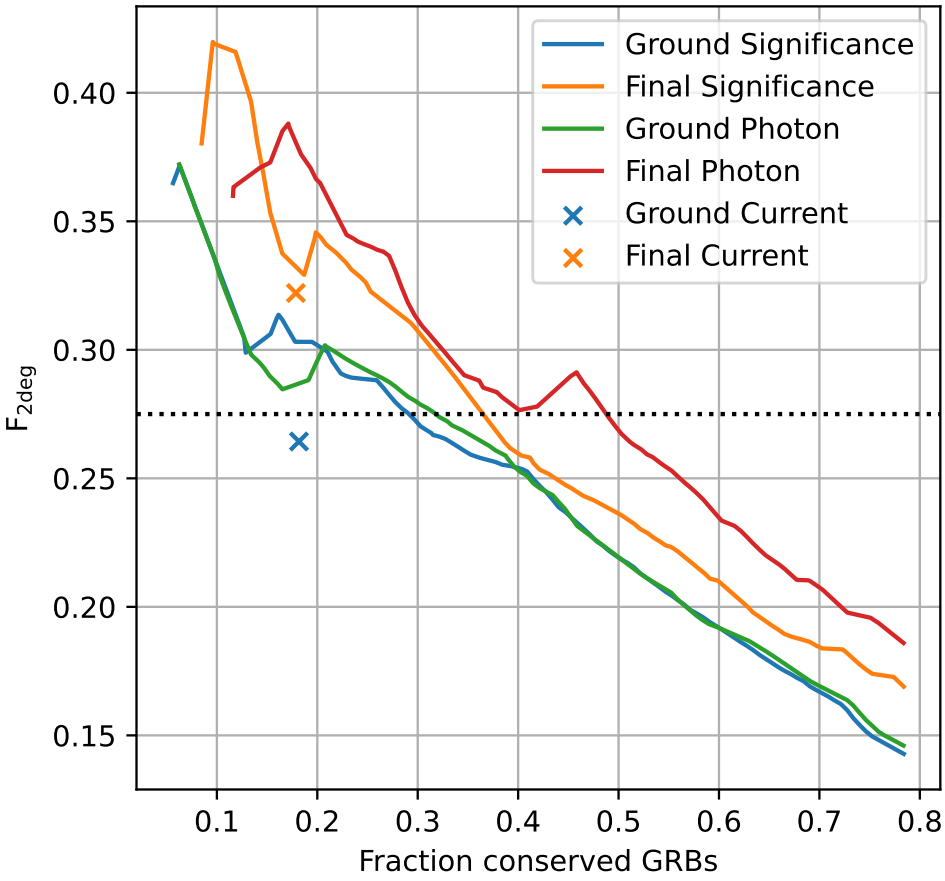

Figure 18.10: Containment fraction at 2° in function of the fraction of GRBs passing selection criteria for `Ground` and `Final` notices. For each type, the cross represent the actual selection criteria, the significance curve the optimise criteria using as parameters significance and position uncertainty, and the photons curve the optimise criteria using as parameters number of photons and position uncertainty. The dotted lines represent the target chosen for the containment fraction.

18.4.3.2 Tilling observations

For the case of tilling observations, we look at indicators giving containment radius (Fig. 18.11). The smaller these numbers, the less different pointings will be required to cover a significant portion of the containment radius. For `Ground` notices, the two types of selection criteria performed similarly again, and have a small impact on R_{90}. For `Final` notices, the selection cuts using the number of photons again perform better than the ones using the significance. The effect on R_{90} is more important but R_{50} seems to be a better indicator since the effect is stronger. The crosses in figure 18.11 give again the current cuts which are suboptimal.

In the same way as for pointed observations, we will determine only one cut using significance and position uncertainty for `Ground` notices while using two different cuts, using the number of photons and position uncertainty for the `Final` notices. This will allow us to fall back on the second if there are no `Flight` or `Ground` notices, needed to compute the estimated number of photons.

The resulting selection criteria and their performances are given in the table 18.3. The selection

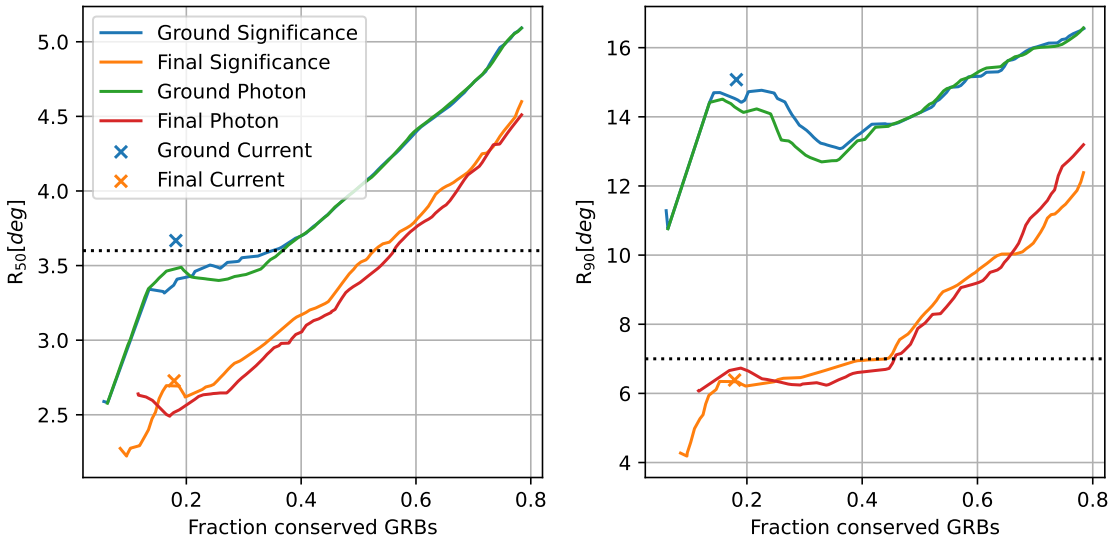

Figure 18.11: 50% and 90% containment radius as a function of the fraction of GRBs passing selection criteria for `Ground` and `Final` notices. For each type, the cross represents the actual selection criteria, the significance curve the optimise criteria using as parameters significance and position uncertainty, and the photons curve the optimise criteria using as parameters number of photons and position uncertainty. The dotted lines represent the target chosen for `Ground` notices (on the left panel) and on the `Final` notices (on the right panel).

	Current `Ground`	New `Ground`	Current `Final`	New `Final`	Alternative `Final`
Position uncertainty	$<2^\circ$	$<3.4^\circ$	$<2^\circ$	$<5.6^\circ$	$<4.0^\circ$
Significance	$> 20\sigma$	$> 12.8\sigma$	$> 20\sigma$		$> 5.3\sigma$
Number of photons				> 500	
Fraction GRBs conserved	18%	34%	18%	47%	44%
$F_{2\text{deg}}$	26%	26%	32%	23%	25%
R_{50}	3.7°	3.6°	2.7°	3.3°	3.3°
R_{90}	15°	13.2°	6.4°	7.1°	7.0°

Table 18.3: Selection criteria for `Ground` and `Final` notices in the case of tilled observations with their performance.

on the `Ground` notice allows covering 62% of the GRBs that will pass the selection on `Final` notices. Only 2.5% of the alerts followed based on `Ground` notices will not pass the criteria for `Final` notices.

18.4.4 The case of the `Flight` notices

In the previous sections, we discussed about `Ground` and `Final` notices but not `Flight` notices. As seen previously, choosing them to optimise localisation accuracy is quite complex and will always lead to poor performance. However, following `Flight` notices could still be interesting as they have a delay that could go below ten seconds after the trigger, allowing a very fast response to hope for observations of a very early afterglow phase and maybe even a prompt phase.

The figure 18.12 allows us to visualise the expected fraction of GRBs that could be followed right from the `Flight` notices, and that will pass `Final` notices selection criterion versus the number followed from a `Flight` notices but that will not pass `Final` notices selection criterion. It is possible to identify from `Flight` notices, a significant portion of the GRBs that will have passed the selection criteria of `Final` notices while having only a small fraction of GRBs that will not have `Final` notices with good localisation.

In both cases, using selection criteria based on significance and position uncertainty than the

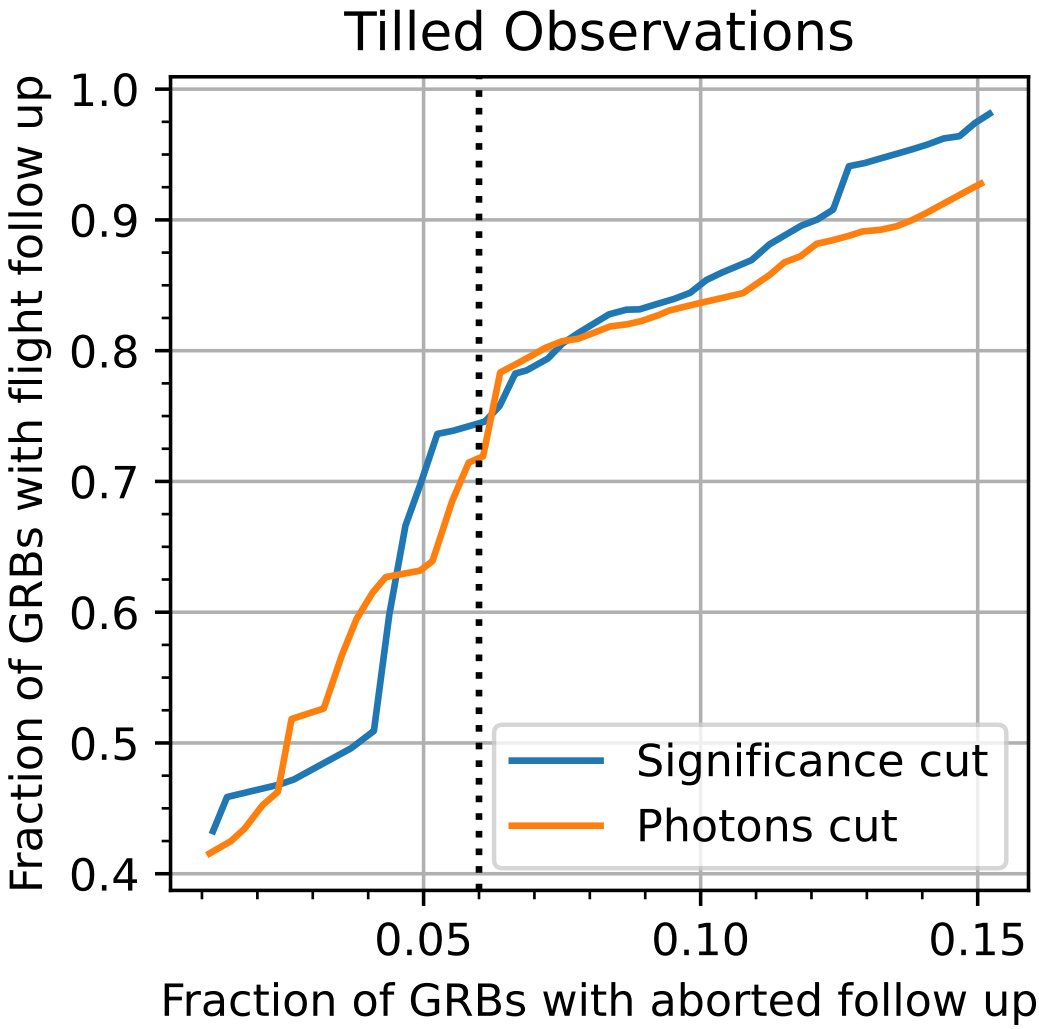

Figure 18.12: Fraction of GRBs that will pass `Final` notice selection that could be followed with selection on `Flight` as a function of the of fraction of GRBs that will pass `Flight` criterion but failed `Final` notice one. The dotted lines represent the chosen target.

number of photons and position uncertainty gives similar results. For pointed observations, it is possible to follow 79% of the GRBs that will pass `Final` selection criterion while having only 6% of the follow-up that will be rejected at the stage of the `Final` notices. The criterion is significance above 13σ and position uncertainty below 13.4°. For tilled observations, it is possible to follow 75% of the GRBs that will pass `Final` selection criterion with only 7% of the follow-up that will lead to not passing follow-up notices. The criterion is significance above 13σ and position uncertainty below 13.4°.

18.5 Proposal of follow-up procedure

Based on the results mentioned before, it is possible to propose this follow-up procedure :

1. At a reception of alert notices, nothing to perform

2. At the reception of a `Flight` notice, if passing the selection criterion, start observations on the coordinates indicated, on new `Flight` notices, do not update pointing

3. At the reception of a `Ground` notice, if observations already started with a `Flight` notice, stop the current run and change pointing for the new coordinates, otherwise, test the selection criterion and only start observations if they pass. As long as there are no `Final` notices, update position based on the last `Ground` notices only at the start of a new observation run.

4. At the reception of a `Final` notice, if observations already started with a `Flight` or `Ground` notices, wait for the end of the current run before updating pointing. Otherwise, start observation if the GRBs are passing the selection criteria.

5. If there are no `Ground` or `Final` notices after one observation run based on `Flight` notices, stop the observations.

The choice to not update at every new notice is to avoid spending all the time moving the telescope and so missing the low delay observations. On some GRBs, in a few minutes, it is possible to receive more than ten `Flight` and `Ground` notices. When tilling will be implemented, runs acquired based on `Flight` notices should not be included in the tilling logic as they will very likely be very short.

18.6 Estimation of the observation time

Even if there are a large proportion of the GRBs that pass our selection criteria, most of them will not be observed due to observational constraint. The actual limit for observation of GBM GRBs is to have observations at a zenith angle lower than 60°, a delay for starting observations of less than 4 h and a dark night.

The observation strategy is applied to the full sample of GRBs observed by GBM on the 13.5 yr of the GBM mission. To make this simple, moon constraints were not taken into account, leading to an overestimation of the observation time. Only the case of pointed observations is presented. The new selection criterion leads to an average of 14.3 GRBs followed per year for an average 46.6 h of observation time per year. The old strategy only allowed following on average 5 GRBs per year with only a slightly better localisation. Also, another interesting point of the new strategy is the increase of low delay observations (Fig. 18.13). Note that during simulation, 30 s of delay was added to the delay of notices to take into account repointing time, time of treatment of the notices, etc...

18.7 Conclusion and perspectives

As seen in this chapter, it is possible to improve the follow-up of GBM GRBs. By using the GRBs also detected by *Swift*/BAT, it was possible to identify a couple of parameters (number of photons, position uncertainty) that works better than the current one for some cases and with similar performance to the actual ones for other. Also, by using these data and choosing wisely the limit value, it is possible to improve either by following the same number of GRBs with better localisation or a larger number of GRBs with a similar localisation.

The value of the selection criteria has been proposed based on the current strategy of LST-1. The results can be used to adapt to any change in this strategy. Using these new selection criteria will not have a major impact on the population of observed GRBs and will allow following more GRBs, including short GRBs and increase the number of short delay follow-ups.

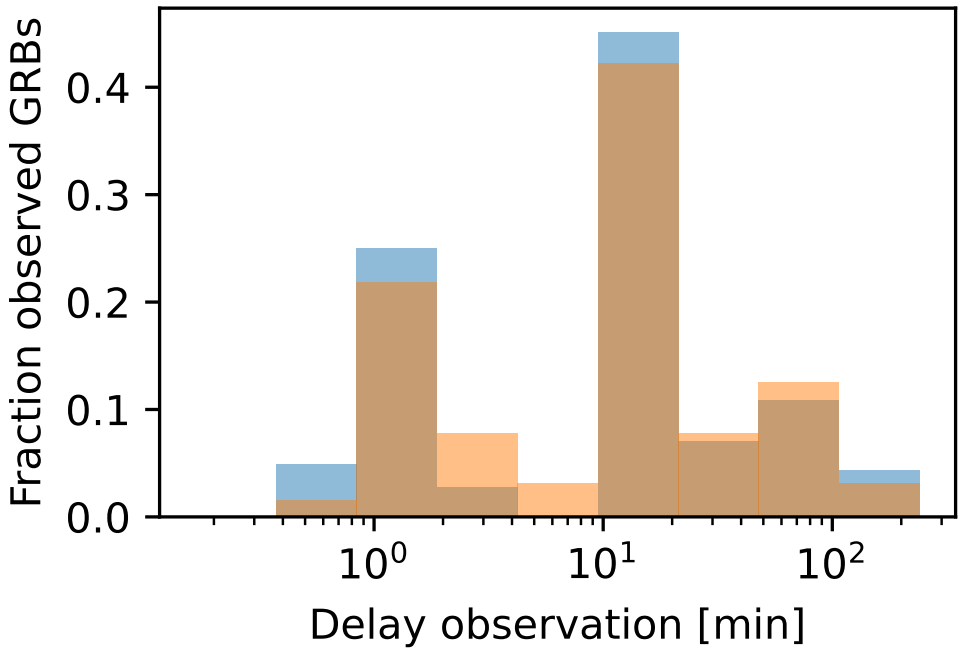

Figure 18.13: Fraction of the GRBs observed with a given delay with new selection criteria (blue) and the old one (orange). The bimodality in the distributions come from the difference of delay between `Ground` and `Final` notices.

Chapter 19

Going further than Li&Ma for GRB detection

Contents

The standard excess and background estimation using ON-OFF technique combined with significance estimation using Li&Ma have proven to be robust for analysing data from IACT instruments. However, Li&Ma does not consider any information from the spectral or temporal distribution, which could allow for uncovering a hidden signal in the background. This is especially true for GRBs, with their large variability following a typical power law shape light curve.

19.1 The canonic GRB light curve

The *Swift* satellite with the XRT instrument made a systematic follow-up of GRBs allowing the determination of numerous light curves of GRBs afterglow in the soft X-Ray band. This has opened a new window and led to a better understanding of these light curves. Among the discoveries, the evidence of a *canonical light curve* for the X-Ray afterglow of long GRBs was one of the most important. The Fig. 19.1 (Zhang et al., 2006; Nousek et al., 2006) show a cartoon of such a typical light curve. The 0 part represents the prompt phase. Then the early afterglow is marked by a fast but short fading phase (part I) followed by a plateau (part II) with a slow fading of the afterglow. Some flares could happen during the plateau (phase V) that could be interpreted as late activity of the central engine (Falcone et al., 2006). The afterglow follows a steeper fading with a typical

temporal index of 1.2 (phase II). In some cases, at a late time, the afterglow fade could accelerate (phase IV).

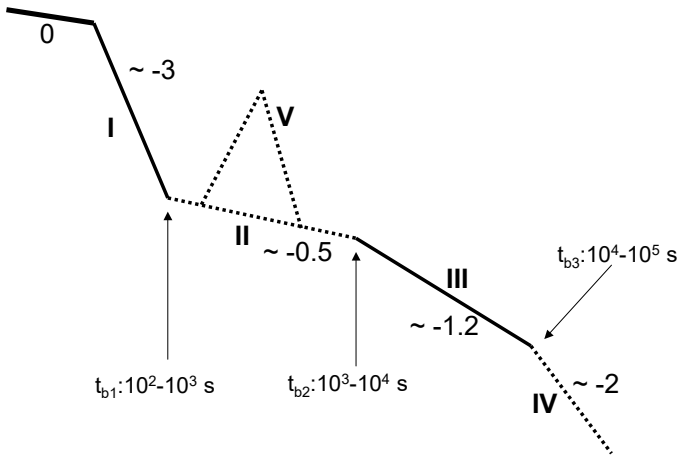

Figure 19.1: Canonical light of the X-Ray afterglow of long GRB seen by *Swift*/XRT. Figure extracted from Zhang et al. (2006)

The observations of GRBs at very high energy (MAGIC Collaboration et al., 2019a; H. E. S. S. Collaboration et al., 2021) have shown similar behaviour between X-Ray and VHE. While the number of events is still low, we could use this information to search for a specific signal shape, as most observations are performed during the afterglow emission.

19.2 Working principles

For Cherenkov experiments, the standard way to make a source detection is by estimating the background and looking for a possible excess. In an analysis of *Fermi*/LAT data, the background is modelled, and a spatial and spectral model is used for the sources. Then to determine the existence of new sources, it is possible to compare the likelihood after fitting the model with and without the source and then take into account spatial and spectral information. This method started to be used in the analysis of IACT data and led to the successful detection of HESS J1702-420 (Abdalla et al., 2021) hidden in the galactic plane. However, it is still uncommon due to the difficulty of the background modelling in these experiments.

GRBs are point-like sources in extragalactic regions. As a consequence, the gain of using spatial information is small, as the background would be mainly constant on the full region across which the signal of the source is spread. Moreover, in the case of a source with a well-known position, we will not be able to gain from the adjustment through a fit of the source position.

As we could drop the spatial information, it decreases the interest in using a background model instead of excess computed from background estimation, as we expect small background variation over time in most cases. Moreover, building an accurate background model at low energy, even more with finely binned temporal information, would be a huge challenge.

So for the proposed algorithm, we will not use a background model but keep the excess and background estimation thanks to ON-OFF methods. The idea of comparing models and selecting the best one based on a likelihood calculation is kept. Instead of comparing a model with background + emission versus background only, it will compare a model with zero emission (aka no source) versus emission from a source.

For this emission model of a source $\phi(E,t)$, two components will be used. A spectral component is described by a simple power law. For most of the low statistics sources detected at VHE, a power law spectral model works quite well. Cherenkov instruments will have the capability to detect a spectral cut-off only for bright GRB, which will be, in any case, detected by Li&Ma analysis. The second component is described by a single temporal power law, more complex behaviour seen earlier only affects early afterglow time. At the end, we have :

$$\phi(E,t) \propto (E^{-\Gamma}) \times (t - t_{\mathrm{ref}})^{\alpha}$$

The algorithm implemented could be expressed as follows:

1. Definition of temporal and spectral binning
2. Multiple OFF background and excess estimation for each temporal and spectral bin
3. Compute the likelihood of a model with zero emission
4. Fit the source model $\phi(E,t)$ to the data with the likelihood maximisation method
5. Compute the p-value using the χ^2 distribution for the number of free parameters in the emission models
6. The significance of the model compared to zero-emission could then be computed with $\sqrt{2}.\mathrm{erf}\,(\mathrm{p}-\mathrm{value})$

The implementation has been made using `gammapy` and `scipy` python libraries. Compared to the algorithm explained above, one thing added to the implementation is the multi-step fit procedure. It could be complex to make the fit converge on many bins so this is performed in three steps. First, the spectral component only uses temporally stacked data. Then the spectral component is frozen, and the temporal component is fitted on the whole data. Then all the components are left free to var, and the fit is rerun again. This procedure helped to minimise the number of non-converging fits.

19.3 Procedure for testing the performances

To test the performances, DL3 files generated by Monte Carlo simulations were used. The simulations performed are the observations of a field view with a GRB-like source. Currently, the model is very simple, with a power law for the spectra and a power law for the light curve. The IRFs used are the `prod 5 IRF` for CTA North (Observatory and Consortium, 2021).

Four observations of a duration of 20 min with an offset angle of 0.7° were simulated. The value of the offset has been chosen based on the IRF and is the largest offset with the same sensitivity as the centre of the FoV at low energies. This type of follow-up of GRBs is typical for most of the IACT experiments on GRBs. The observation delay is between 30 s to 2 h. The reason for focusing on low delay observations is that the observing time simulated is 80 min. If the delay becomes high in front of the observation time, the power law light curve will on the observation window look like a constant light curve without any variation of luminosity. So for a long delay, no considerable improvements are expected from this method.

All the parameters of the emission are randomly peaked for each observation :

- For the temporal index α, between -0.5 and -5.0, allowing to represent the most extreme case seen by XRT
- For the spectral index Γ, between 2.0 and 5.0, to cover any possibilities
- The normalization at 30 GeV and 30 s after the burst time is comprised between 2×10^{-6} to $2 \times 10^{-9}\,\mathrm{cm^{-2}\,s^{-1}\,TeV^{-1}}$. This allows to generation of bright and very faint (below the detection threshold) GRB.

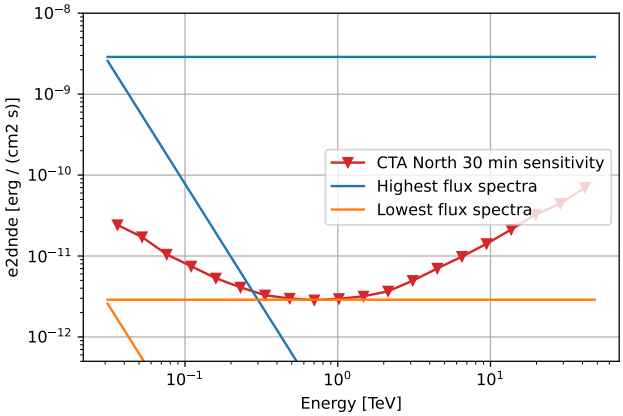

Figure 19.2: The spectra for the highest (blue curve) and lowest (orange curve) simulated flux with the two extreme spectral indexes possible. The sensitivity is the one of CTA for 30 min.

Fig. 19.2 gives a schema of the extreme cases together with the expected CTA sensitivity.

A total of 10,000 simulations have been performed. Each simulation has been analysed with Li&Ma[1], and the method described above. Ten bins per decade for the spectral axis were used. For the temporal axis, several values have been tested with bins duration going from 0.625 min to 20 min. The starting parameters of the model for the fitting procedure are always initialised with the same value (spectral index of 3, temporal index of -1.2).

Due to the vast phase space explored, a significant part of the simulations led to zero photons simulated for the sources ($\sim 55\%$). As these simulations are in practice background only, they will be used to estimate the false alarm rate.

The analysis will also be repeated using different integration times ranging from 10 min to the whole observation time of 80 min. An important drawback of Li&Ma calculation for short in time signals is that a large integration time could lower the significance as the early signal could be hidden in the added background. By design, this should have less impact on the proposed method.

19.4 Results

19.4.1 Number of GRB detections

Figure 19.3 shows the results of the number of sources detected as a function of the integration time for Li&Ma and the proposed method for each time bin tested. At first, it is easy to see that any configuration of the new method performs better than Li&Ma. If we compare the best configuration for Li&Ma to the worst one for the new method, we have a gain of $\sim 15\%$ of detected sources and $\sim 35\%$ for the best configuration. Increasing the integration time does not decrease the number of detected sources, as this is the case for Li&Ma analysis.

The performance of the new method depends on the time binning. A time binning of 1.25 min minutes seems the best to use as it is always among the best performing for any integration time.

Figure 19.4 represents the significance obtained with Li&Ma versus the one obtained with the fit method for the simulations with at least 10 photons from the source. The case where the fit did not converge is represented in orange[2]. They represent close to 10%, showing that still some work would be needed on the fit procedure to improve the performances. These cases were not counted as detection even if they had a high significance. In most cases, a better significance is achieved with the fit method than Li&Ma (point above the x=y black line).

[1] For the Li&Ma analysis, all the events in the given integration window were used.

[2] The significance computed for the case where the fit did not converge corresponds to the one associated with the model parameters for which the fit stop.

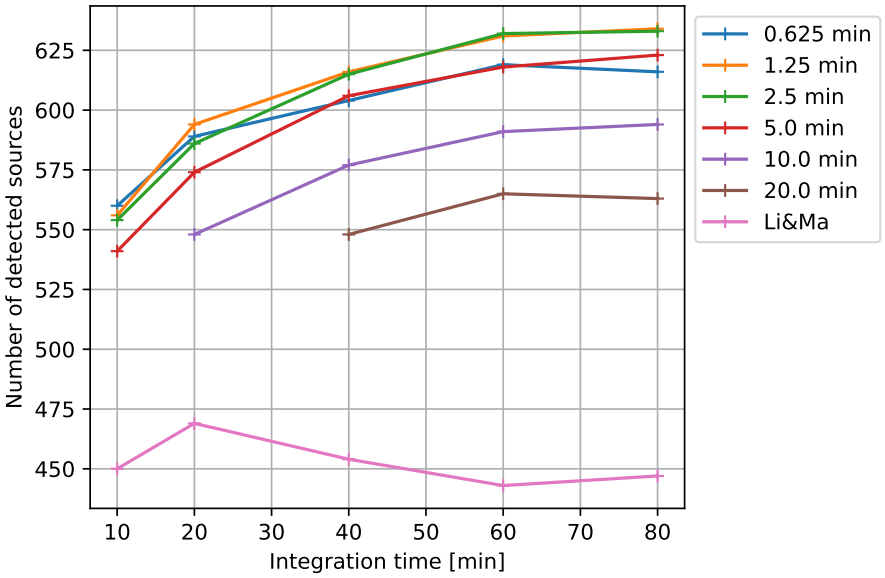

Figure 19.3: Number of sources detected for each Li&Ma and each bin time for the fit method as function of the integration time.

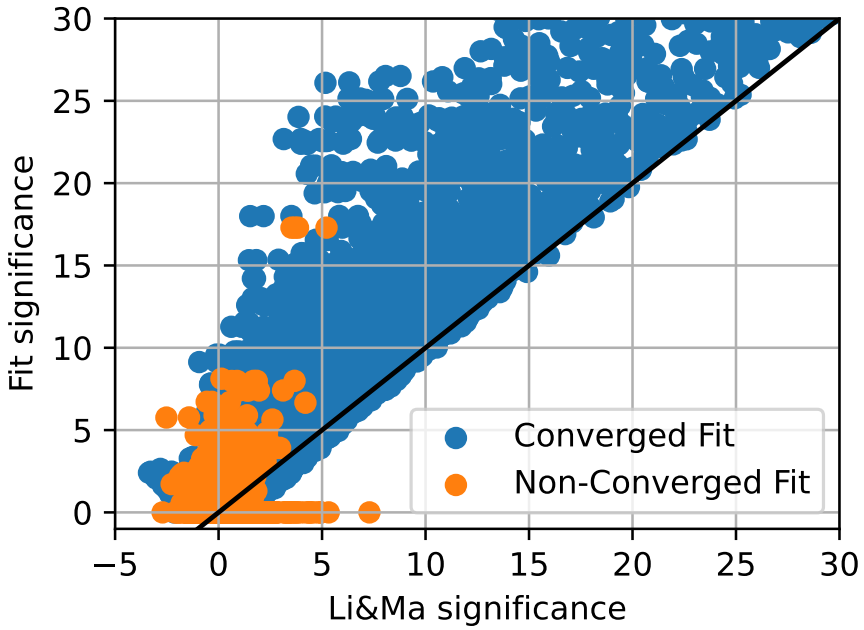

Figure 19.4: Significance obtained for the simulation with at least 10 photons from the source, using the fit method versus the Li&Ma significance for a bin time of 1.25 min. The fits that do not converge are represented in orange.

As mentioned above, there are numerous simulations without any photons simulated from the source, making them background-only simulations. The distribution of the significance of such cases (Fig. 19.5) differs from all the simulations. With a maximum significance of 3.5σ on 5554 simulations, this shows no potential issue with the false detection rate, even if it would need to be

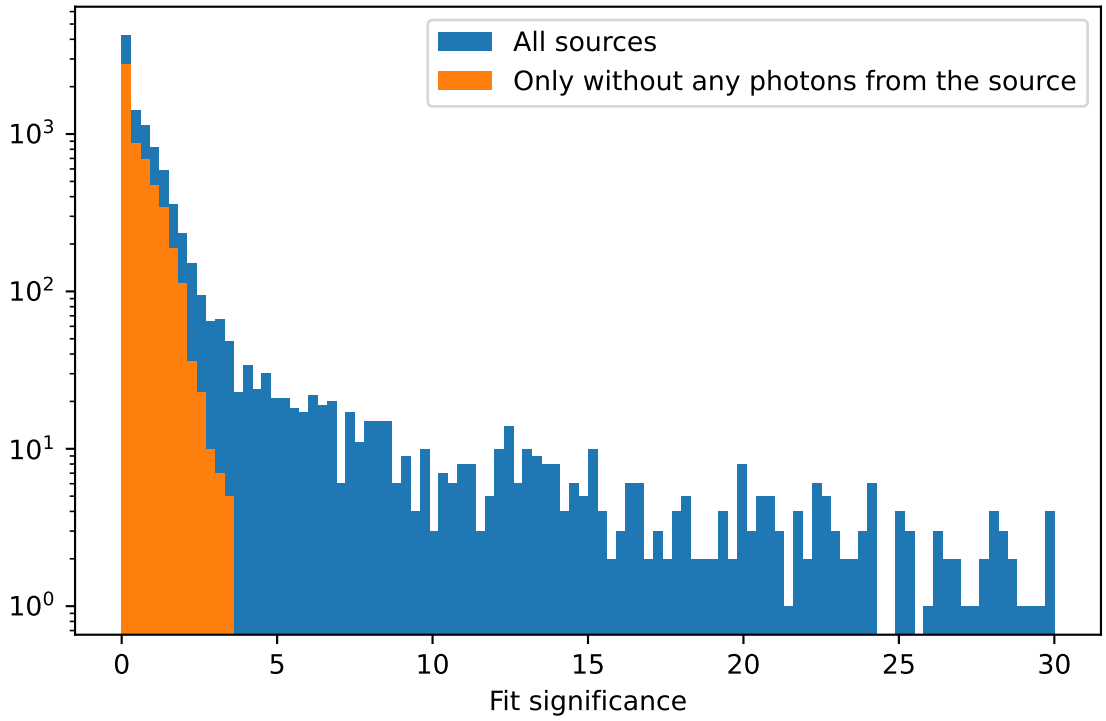

Figure 19.5: Distribution of the significance for all the analyses with the fit method and the only ones without any simulated photons from the sources

confirmed.

19.4.2 Spectral and temporal reconstruction

If we considered the property of the source (simulated spectral and temporal parameters) detected by both methods, we obtained figure 19.6. This figure allows understanding in which condition one of the methods performs better than the other. For Li&Ma, the results of two integration times are used (20 min and 80 min). If the source is detected in at least one of them, it is considered as detected, allowing to increase in the number of detected sources as 21.5% of the sources are detected with only one integration time.

Only 3% of the sources detected by Li&Ma are not detected with the fit method. The fit method detects more sources in nearly every configuration but with a particular excess for sources with a steep light curve and a low observation delay (third panel of the last row). This is not entirely unexpected as the fit method avoids masking this type of signal with the background added by longer integration time. Also, hard GRBs are better detected with the method (second panel of the second row), likely due to the signal at high energy not being masked by the background at low energy, like for Li&Ma.

19.5 Perspectives

The first results obtained are promising, but the simulations used the same spectral and temporal shape as the source model as the one searched by the algorithm. The next step would be to challenge it by adding, for example, a break in the light curves and the EBL absorption effect on the spectra.

The fitting procedure would still benefit from improvement as for $\sim 10\%$ of the source, the fit did not converge.

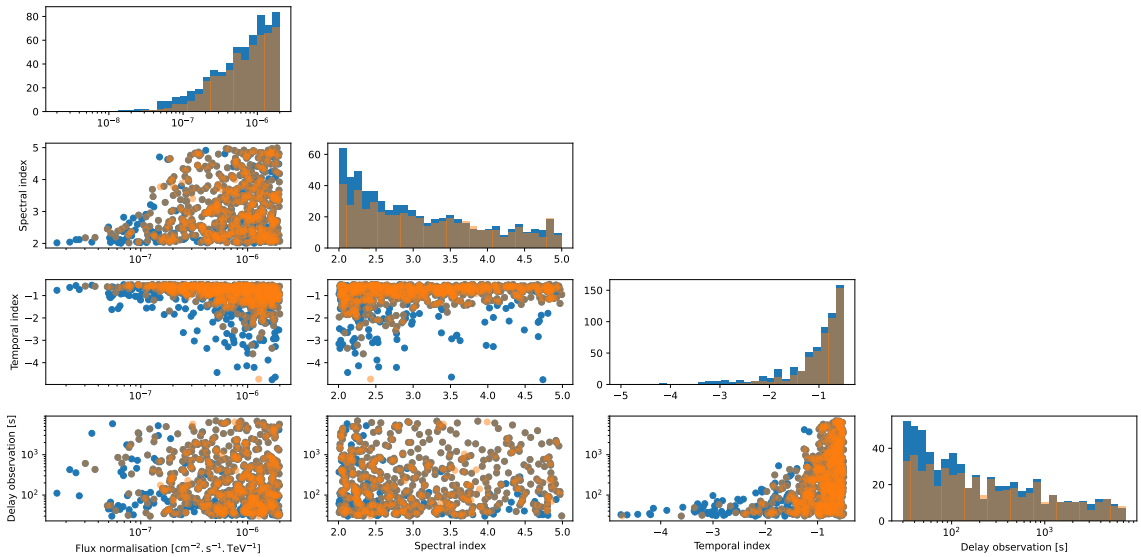

Figure 19.6: Intrinsic and observation properties of the source were detected by both methods (Li&Ma in orange and fit method in blue). For Li&Ma method it is the aggregation of the detection from 20 min and 80 min integration time

It could be worth investigating the use of logarithmic duration temporal binning instead of the fixed duration binning actually used. As seen above, temporal binning has an impact on the performances, so it would likely need to be optimised for each instrument and observation condition to reach the best performance possible.

Other statistical tools have been proposed by some authors to search signals from GRBs (Brun et al., 2020). These tools are more focused on searching the signature of any transient signal compared to the proposed one that takes advantage of the power law light curve of the GRBs afterglow. Comparing their performances on the same dataset could be interesting to see if the proposed method can extract a signal that these tools cannot.

Finally, testing it on real data would be the final step. There are currently not that many GRB candidates with low delay observations in LST, limiting the number of candidate fields of view. In any case, testing the method on data taken on dark patches would be equally important to ensure that no systematical behaviour would cause any false detection.

Chapter 20

A catalogue of Gamma-Ray Burst observations by H.E.S.S.

Contents

Since the first light of the H.E.S.S. telescope, many gamma-ray bursts have been observed. It has been a major program of H.E.S.S. and has conducted to numerous follow-ups. This program finally led to the first detection of a GRB at very high energy with GRB 180720B in 2018 (Abdalla et al., 2019) and, a year later, the detection of GRB 190829A (H. E. S. S. Collaboration et al., 2021). The MAGIC experiment has also run such a program that led to the detection of GRB 190114C (MAGIC Collaboration et al., 2019a) and GRB 201216C (Fukami et al., 2022).

With these four GRBs detected at very high energies in recent years, one of the rising questions is why no detection was achieved before with all these numerous observations performed by several experiments.

To try to answer this question, a reanalysis of all the GRB observations performed by H.E.S.S. from 2003 to 2019 was made and is presented in this work.

20.1 Identification of the observations

20.1.1 Selection of the datasets

The first step was to identify all the observations to analyse. A track of the GRBs observation was kept on internal tools, but as some tool changes happened since the start of the H.E.S.S. experiment, we could not be sure that no information was lost in the process. Also, we wanted to check that no lucky observations of a GRB (observation made without the intent of observing this GRB) were made and not identified at the time.

Consequently, to select these observations, the option of a blind search was used. The overall idea is to crossmatch catalogues of GRBs with the database of all the observation runs performed by H.E.S.S. The studied periods went from the first data that could be analysed with the current software on the 29th of September 2003 to the installation of the NamCam on the telescope CT5

on the 20th of October 2019[1]. A previous catalogue published by H.E.S.S already covered the first years (Aharonian et al., 2009a), but the introduction of template-based reconstruction in the analysis could improve the sensitivity compared to this previous publication.

Five different GRB catalogues were used to search for GRBs from five different experiments, HETE-2 (Vanderspek et al., 2004), *Fermi*/GBM (von Kienlin et al., 2020), *Fermi*/LAT (Ajello et al., 2019), INTEGRAL/ISGRI (Bird et al., 2016), and *Swift*/BAT (Lien et al., 2016). GRBs in multiple catalogues have been kept only once with the most precise localisation available. Then these catalogues need to be crossmatched with the observation database. The *Fermi*/GBM catalogue will be handled differently from the others as the localisation uncertainty is much broader than the field of view of H.E.S.S.

20.1.2 Crossmatch of well-localized GRB

For each GRB presented in the catalogues, a search of corresponding observations runs based on two main criteria was performed:

- a delay of less than 48 h compared to the burst
- a maximum angular distance of 2° between the pointed position and the burst position.

The runs are then clustered following the standard way for GRBs observation in H.E.S.S. If the first run is taken with less than 10 min delay, it will be analysed separately. If there is a hole in the observations of more than 4 h, they are then separated into two analysis clusters.

In total, 71 GRBs with 88 analysis clusters remain after the crossmatch. Most of the GRBs have been detected by *Swift*/BAT with 64 GRBs, and the remaining by HETE 2 (5 GRBs) and *Fermi*/LAT (2 GRBs). Note that this is only information about the most precise trigger instrument, so other instruments have also detected some of the *Swift*/BAT GRBs.

20.1.3 Crossmatch of *Fermi*/GBM GRBs

As mentioned before, for *Fermi*/GBM GRBs, the selection must be handled differently. The uncertainty on the position is large. With the field of view of H.E.S.S., in the best case, one run could cover only up to 30-40% of the uncertainty region.

A first pre-selection is performed by keeping only GRBs with at least one run closer to 20° to the position with less than 24 h delay. This step allowed to removal of most of the GRBs that have no chance of being covered by H.E.S.S., allowing quicker computation for the next step.

The selection is then made using the localisation map from *Fermi*/GBM (Fig. 20.1). This map covers the whole sky and gives the probability of the GRB being in a given direction. It takes into account both statistical and systematic uncertainty. This is important, as the statistical uncertainty varies for the faintest GRBs from more than 30° to 1°. In comparison, the systematic uncertainties typically vary from 2° to 5°, depending notably on the signal and its orientation relative to the spacecraft (Connaughton et al., 2015). This means that for bright GRBs (which are the one mostly followed by H.E.S.S. to have a meaningful localisation compared to the field of view of our instrument), the uncertainty on the position is driven by the systematic.

First only runs with a delay of less than 24 h and a probability to have the GRB in the field of view of more than 1% are kept. The GRB is kept only if all the observation runs selected allow to cover at least 10% of the GBM uncertainty region.

Finally, a clustering algorithm for the observations is run with similar parameters as for well-localized GRB but, to be in the same analysis cluster, runs need to be contiguous spatially also; otherwise, they form different analysis clusters.

This led to a total of 20 GRBs with 26 analysis clusters.

[1] see for example https://www.mpi-hd.mpg.de/hfm/HESS/pages/home/som/2020/10/.

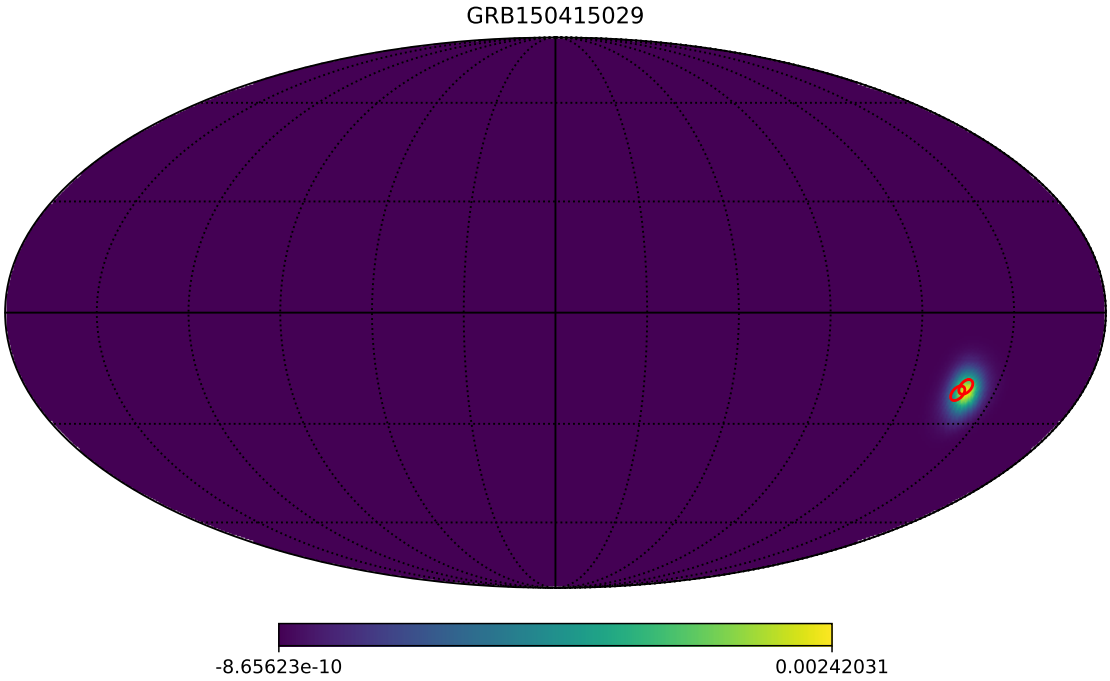

Figure 20.1: Probability map from *Fermi*/GBM for GRB 150415029 with the red circles representing the field of views of the run selected for analysis.

20.1.4 Establishing the final selection list

After this first selection, there were a total of 91 GRBs with 114 analysis clusters. For all these GRBs, a search was performed among the GCN notices for better localisation, a redshift value, or other relevant information. All the follow-up of GBM triggers performed by H.E.S.S. that were not included in this list were also checked for potential precise localisation in the field of view.

Compared to the previous GRB catalogue, two GRBs do not figure in it. These data were taken during the commissioning phase, with each telescope taking data with a Monoscopic trigger. The current analysis software does not support these data. Compared to the internal follow-up database by H.E.S.S., a few GRBs were recovered during this blind search. Also, two GBM alerts benefit from lucky follow-up with data taken on another source (M87 and HESSJ0632+057). Also, several GRBs in the internal database are outside our selection. There are all GBMs follow-ups that did not pass the requirements of the 10% coverage due to either alert with very large uncertainty or follow-up at a position which was not up-to-date at the time of the data taking.

Finally, the GRBs were separated into two different lists, the ones with precise localisation (uncertainty smaller than the ON region) and the ones with large uncertainty. This last one will contain all GBM follow-ups but also *Fermi*/LAT and some of the HETE 2. This separation is due to the need for different analyses. While the ones with precise localisation could be analysed using multiple OFF background estimations, the others need a map to be generated to search for a signal in a broader region.

Our data set comprises 373 runs for a total observation time of 171 hours.

20.2 Quality of the data

Data quality check is an essential step for all the analysis of IACTs and is even more critical for GRBs as there are short observations all grouped on a few hours scale. So any issue with the instrument

or the atmosphere will affect the whole analysis results and not only add a bit of systematic like for analysis on a larger dataset.

For this reason, the standard procedure for analysis of GRBs data in H.E.S.S. is a careful check by two different experts of several aspects detailed below. With a total of 373 runs, the first step was to automatise as much as possible this process. The usual way was to manually check every plot and value directly in the data files. However, this process is slow and not efficient. It is acceptable for a single analysis with a few runs but not for 373 runs. An automatic generator of a PDF report per GRB cluster was created. The document regroups all the information needed for checking data quality. This way, the expert only needs to open this file and get all the information at once.

The data quality check is performed for both analysis chains used in H.E.S.S., there are some data in commons like trigger rate information, but as a lot of the check is linked to the calibration output that is different for each chain, this needs to be done for both.

Then based on the results of the two chains, we could remove one telescope from the analysis or a complete observation run. In a few cases, the data were re-calibrated by calibration experts to solve specific issues.

Finally, the analysis cluster could be redone manually based on what observations remain with which array configuration.

20.2.1 Trigger rate stability

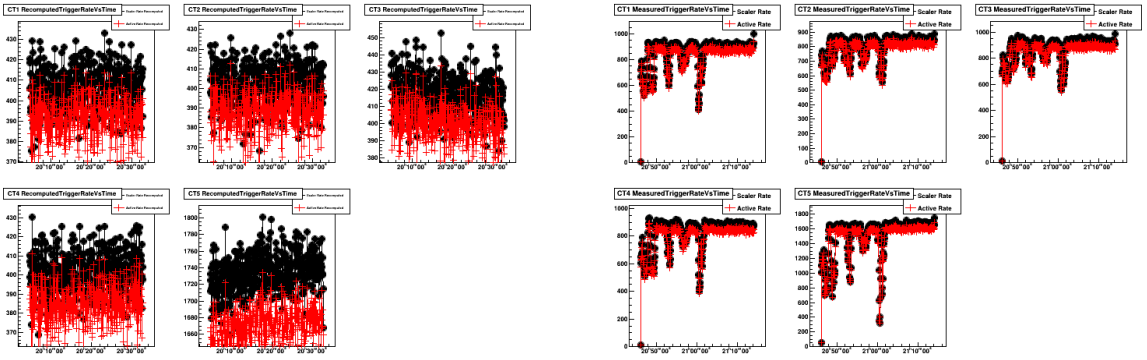

Figure 20.2: Trigger rate per telescope (CT1-5). Left panel, the rate is stable but presents a lot of fluctuations on the right panel.

The trigger rate and its stability across time are essential parameters as there will be a direct indication of the atmosphere state. An unstable trigger rate usually indicates clouds in the field of view. Figure 20.2 presents two cases (good and bad) of the trigger rate for 5 telescopes observations.

The average value of the trigger rate could also point toward a high opacity of the atmosphere. This value is also highly dependent on the zenith angle θ. At the first order, it is linearly dependent on the airmass that could be approximate for not too high zenith angles to be proportional to the inverse of $\cos\theta$.

The trigger rate corrected for the zenith angle needs to be above 100 Hz for CT 1-4 telescopes and above 800 Hz for CT 5. For GRBs, the stability of the trigger rate is determined visually.

20.2.2 Broken pixels and bad pedestals

Broken pixels and bad pedestals are flags that could be given to a pixel at the calibration step to indicate issues with the pixel or the calibration of this pixel. These pixels will be rejected during the analysis if both high-gain and low-gain channels are flagged. Otherwise, only the valid channel will be used. If the proportion of rejected pixels is too high, it will cause issues during the reconstruction step as the showers will not be fully imaged. Figure 20.3 presents two examples of the broken pixels in the camera of CT1.

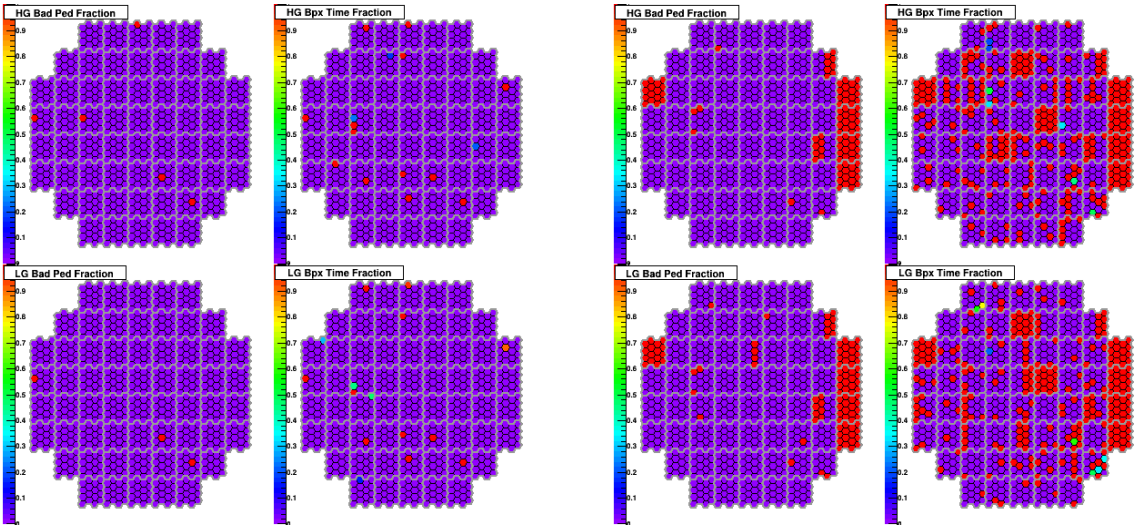

Figure 20.3: Broken pixels maps for CT1 : Left the run can be kept, right, a large fraction of the camera is deactivated and the telescope cannot be kept

The usual threshold is less than 15% of broken pixels for the camera of CT 1-4 telescopes and less than 5% of broken pixels for the camera of CT 5. The lower requirements from CT5 is due to the use of Mono reconstructions that will be more affected by missing pixel.

It is also essential to check the position of the broken pixels. For example, if the 10% of the central pixels of the camera are broken, it will likely cause more issues than 15% on the edges.

20.2.3 Pixel participation

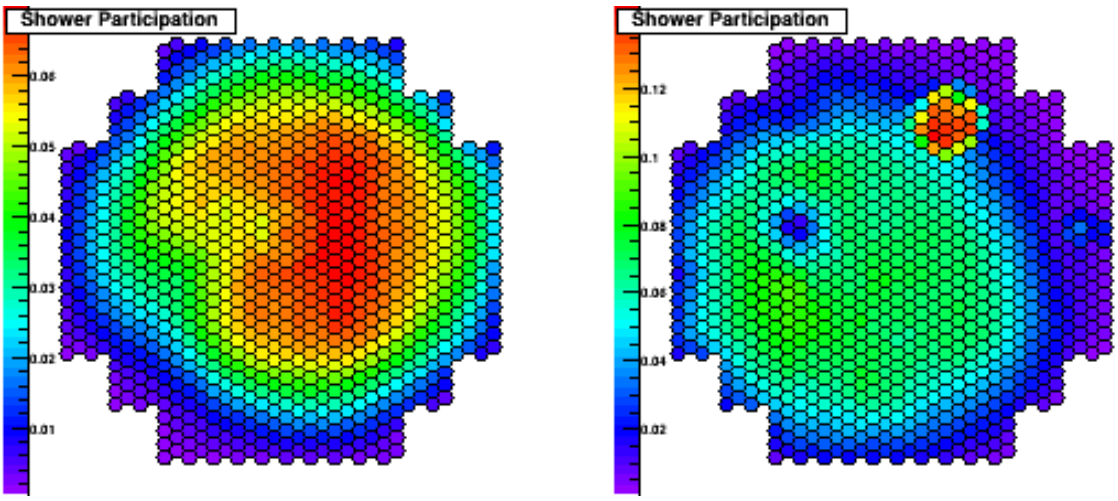

Figure 20.4: A good quality pixel participation plot (left panel) and a bad one with hotspots and holes (right panel). Both are from CT4.

The pixel participation represents the fraction of the participation of a pixel to a trigger. The map of these values across the camera should be somewhat flat, with attenuation close to the edge (left panel of Fig. 20.4). If a pixel or a drawer has low or high participation, the calibration should flag this pixel as broken.

The main reason for these checks is to combine them with the previous ones to be sure that the

calibration step has considered all these issues. If anything is mismatch, it is possible to ask for a re-calibration with manual deactivation of these pixels. The right panel of Fig. 20.4 shows a hotspot that has been investigated during the analysis.

20.2.4 Center of gravity

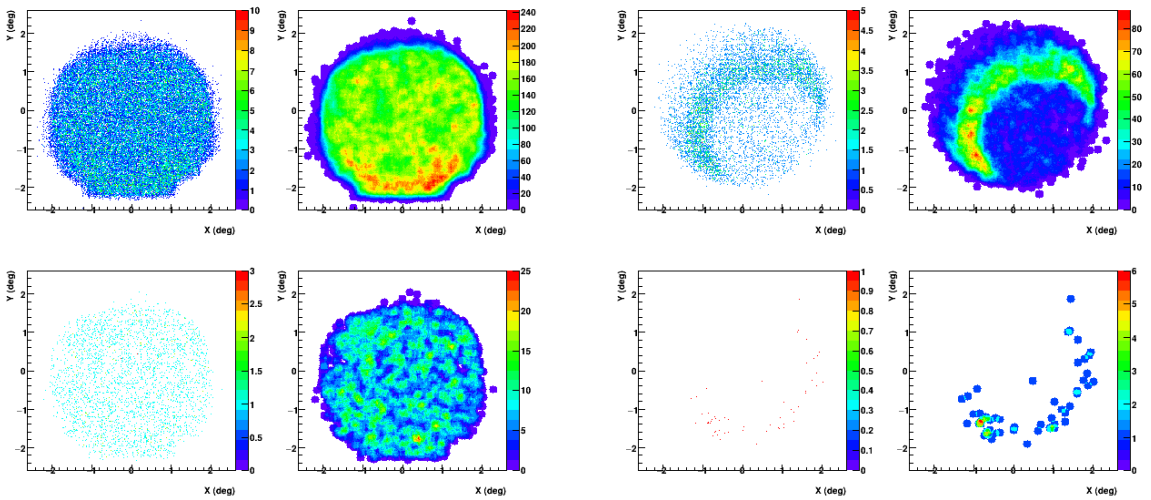

Figure 20.5: COG maps for CT1. The left panel presents a good-quality map while the right panel presents major aberrations.

The distribution of the centre of gravity (COG) of the images is another important parameter. Since most of the events are cosmic rays, this distribution should be relatively flat, with attenuation close to the edges of the camera (Fig. 20.5, left panel). Any bright hotspot could be a hint of issues from the calibration. Holes could be created by dead pixels. It's important to check they are flagged by the calibration in the broken pixel maps. If some severe perturbations are seen, this could be an indication of an issue with the data.

20.2.5 Night Sky Background map

The night sky background (NSB) could cause some issues during the reconstruction, and this is especially true for bright stars in the field of view. It is essential to check that a local high NSB value does not create any hotspots in the COG maps.

20.3 Analysis of the bursts

After data quality, a total of 70 GRBs remain with 86 analysis clusters that can be analysed. The analysis will differ depending on the two categories defined before, GRBs with precise localisation and the ones with large uncertainty. In each case, research of signal will be made, and then spectral constraint will be determined.

All these steps have also been automatised to process all the data in the same way quickly.

20.3.1 Analysis of GRBs with Precise localisation

For these GRBs, the localisation of the burst is good enough for the uncertainty being smaller than the ON region. In this case, a point-like analysis using the GRB position can be performed as for any other type of source.

The reconstruction profile used for these GRBs is H.E.S.S. II Mono[2] if CT 5 data are present. Otherwise, it will be H.E.S.S. I Stereo[3]. Loose cuts will be used each time as there optimised for soft sources, as we expect for GRBs due to EBL absorption.

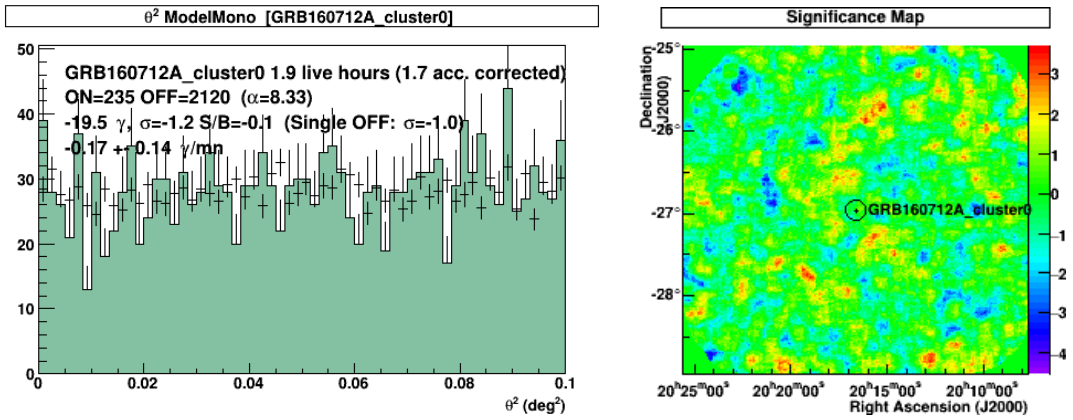

Figure 20.6: Theta square plot (left panel) and significance map (right panel) for GRB 160712A

A multiple OFF background estimation will be run associated with Li&Ma estimator to assess the presence of a signal. A theta square plot will be produced for every analysis (Fig. 20.6, left panel). The integral upper limit, assuming an index of 2.5, starting from the energy threshold of the analysis will then be computed. Also, a significance map using a ring background estimation will be produced. Such a map is presented in figure 20.6, right panel.

20.3.2 Analysis of GRBs with large localisation uncertainties

Running a multiple-off analysis on a specific position does not make sense for GRBs with poor localisation, so only maps will be produced. The reconstruction profile used is either:

- H.E.S.S. II Mono if the localisation uncertainty remains small compared to the field of view
- H.E.S.S. II Stereo[4] profile will be used otherwise as it provides better off-axis performance
- if CT 5 data are not available, we use the H.E.S.S. I Stereo profile.

A ring background estimation will be used to produce a significance map to search for any signal. An integral upper limit map will then be produced.

20.4 Analysis results

The figure 20.8 shows the number of GRBs observed per year. We could see the first period in the early time of H.E.S.S. that was quite active, followed by a small number of observed GRBs and then a ramp-up again after the installation of CT5. 33% of the data include CT 5 data.

As it could be expected, the GRBs observed are dispersed across the whole southern sky (Fig. 20.9). The figure 20.10 shows the evolution of the zenith angle for each observation in function of the delay. There are a few observations with a low delay, and then the observation delay could go up to a day.

[2]Mono reconstruction using only the data from CT 5
[3]Stereo reconstruction using only data from CT 1-4
[4]Stereo reconstruction using data from all the telescopes

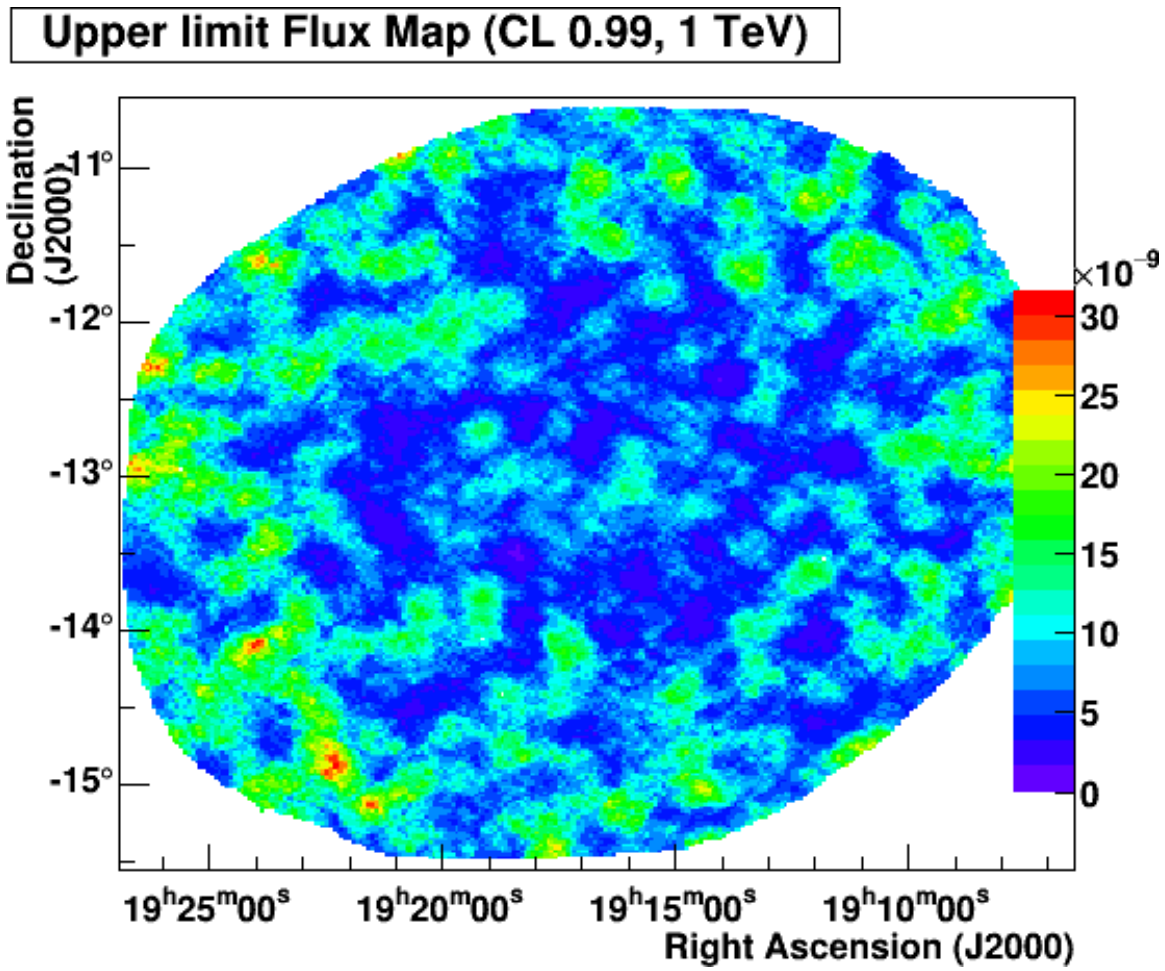

Figure 20.7: Integral upper limit map for GRB 180522607

Table 20.1: Results for the well-localized GRBs

Name	RA J2000	Dec J2000	Configuration	E_{min} [TeV]	Significance	UL [$10^{-8}\,\mathrm{cm}^{-2}\,\mathrm{s}^{-1}$]
GRB 191004B cluster 0	49.2	-39.63	HESSI Stereo	0.38	-0.2	5.66
GRB 191004B cluster 1	49.2	-39.63	HESSI Stereo	0.25	-0.48	1.21
GRB 190821A cluster 0	250.05	-34.0	HESSI Stereo	0.23	-0.34	3.24
GRB 190627A cluster 0	244.82	-5.28	HESSI Stereo	0.38	1.03	8.4
GRB 180613A cluster 0	211.52	-43.07	HESSI Stereo	0.21	-0.29	3.55
GRB 180512A cluster 0	201.93	21.4	HESSII Mono	0.25	0.9	12.01
GRB 180512A cluster 1	201.93	21.4	HESSII Mono	0.31	-1.77	4.4
GRB 180510A cluster 0	276.33	-31.9	HESSI Stereo	0.28	0.64	3.45
GRB 171020A cluster 0	39.24	15.2	HESSI Stereo	0.28	-1.67	1.26
GRB 171020A cluster 1	39.24	15.2	HESSI Stereo	0.51	1.21	1.48
GRB 170531B cluster 0	286.88	-16.41	HESSI Stereo	0.28	0.29	6.03
GRB 170531B cluster 1	286.88	-16.41	HESSII Mono	0.1	-0.24	24.53
GRB 161001A cluster 0	71.91	-57.26	HESSII Mono	0.21	-0.06	66.53
GRB 161001A cluster 1	71.91	-57.26	HESSII Mono	0.17	0.17	7.93
GRB 160712A cluster 0	304.15	-26.95	HESSII Mono	0.11	-1.17	10.56
GRB 150711A cluster 0	221.62	-35.45	HESSII Mono	0.12	-0.6	21.89

Name	RA J2000	Dec J2000	Configuration	E_{min} [TeV]	Significance	UL $[10^{-8}\,\mathrm{cm}^{-2}\,\mathrm{s}^{-1}]$
GRB 150301A cluster 0	244.3	-48.71	HESSII Mono	0.17	1.85	20.68
GRB 141004A cluster 0	76.73	12.81	HESSI Stereo	0.42	-1.59	0.9
GRB 140818B cluster 0	271.13	-1.38	HESSII Mono	0.09	-0.24	34.42
GRB 140818B cluster 1	271.13	-1.38	HESSII Mono	0.1	0.88	23.67
GRB 131202A cluster 0	344.05	-21.66	HESSI Stereo	0.38	0.35	3.45
GRB 131030A cluster 0	345.06	-5.36	HESSII Mono	0.12	1.96	26.63
GRB 131030A cluster 1	345.06	-5.36	HESSII Mono	0.25	1.0	22.41
GRB 130502A cluster 0	138.56	-0.12	HESSI Stereo	0.51	0.19	2.11
GRB 120328A cluster 0	241.61	-39.33	HESSI Stereo	0.23	-0.75	3.6
GRB 110625A cluster 0	286.73	6.75	HESSI Stereo	0.34	1.47	4.93
GRB 100621A cluster 0	315.3	-51.1	HESSI Stereo	0.34	0.02	5.18
GRB 100621A cluster 1	315.3	-51.1	HESSI Stereo	0.38	2.05	4.65
GRB 100418A cluster 0	256.36	11.46	HESSI Stereo	0.76	-0.52	3.31
GRB 091018 cluster 0	32.18	-57.54	HESSI Stereo	0.42	-0.89	0.78
GRB 090201 cluster 0	92.05	-46.59	HESSI Stereo	0.34	-1.25	2.36
GRB 081230 cluster 0	37.33	-25.14	HESSI Stereo	0.83	-1.35	2.45
GRB 081221 cluster 0	15.79	-24.54	HESSI Stereo	0.31	0.1	2.44
GRB 080804 cluster 0	328.66	-53.18	HESSI Stereo	0.31	0.21	6.33
GRB 080804 cluster 1	328.66	-53.18	HESSI Stereo	0.34	-0.18	1.57
GRB 080413A cluster 0	287.29	-27.67	HESSI Stereo	0.23	1.43	11.18
GRB 071003 cluster 0	301.85	10.94	HESSI Stereo	0.56	0.79	1.43
GRB 070920B cluster 0	0.14	-34.81	HESSI Stereo	0.42	-2.59	2.29
GRB 070808 cluster 0	6.76	1.17	HESSI Stereo	0.34	-0.57	1.84
GRB 070724A cluster 0	27.8	-18.59	HESSI Stereo	0.28	0.38	2.99
GRB 070721B cluster 0	33.13	-2.19	HESSI Stereo	0.46	0.36	2.56
GRB 070721A cluster 0	3.16	-28.54	HESSI Stereo	0.34	-0.22	3.68
GRB 070621 cluster 0	323.79	-24.81	HESSI Stereo	0.25	0.53	2.09
GRB 070621 cluster 1	323.79	-24.81	HESSI Stereo	0.42	-1.83	7.46
GRB 070612B cluster 0	261.72	-8.75	HESSI Stereo	0.23	0.26	3.02
GRB 070419B cluster 0	315.7	-31.26	HESSI Stereo	0.62	0.94	4.44
GRB 070209 cluster 0	46.21	-47.37	HESSI Stereo	0.46	0.6	3.54
GRB 061110A cluster 0	336.29	-2.25	HESSI Stereo	0.31	0.11	2.35
GRB 060728 cluster 0	16.64	-41.39	HESSI Stereo	0.28	-0.99	2.08
GRB 060526 cluster 0	232.82	0.28	HESSI Stereo	0.23	0.64	1.65
GRB 060505 cluster 0	331.76	-27.81	HESSI Stereo	0.56	-0.14	4.36
GRB 050801 cluster 0	204.15	-21.92	HESSI Stereo	0.51	-0.68	7.26
GRB 050726 cluster 0	200.05	-32.06	HESSI Stereo	0.46	0.24	2.86
GRB 050607 cluster 0	300.17	9.14	HESSI Stereo	0.31	-0.49	1.73
GRB 160310A cluster 0	98.78	-7.12	HESSI Stereo	0.42	0.74	2.03
GRB 050509 cluster 0	193.22	-44.83	HESSI Stereo	0.25	-0.11	3.59
GRB 041006 cluster 0	13.7	1.23	HESSI Stereo	0.25	-0.67	1.91
GRB 041211 cluster 0	100.8	20.39	HESSI Stereo	2.03	-1.45	3.68
GRB 041211 cluster 1	100.8	20.39	HESSI Stereo	0.51	1.3	2.46
GRB 050209 cluster 0	126.53	19.68	HESSI Stereo	0.76	0.52	1.47

The results of the analysis for the well-localized GRB are given in table 20.1 and the list of poorly localized in table 20.2. No detection has been achieved in the data set.

If we focus on the results of localised GRBs that represent 53 GRBs for 65 analysis clusters. On this whole sample, no signal could be observed. The significance distribution of all these observations is compatible with a pure Poisson noise (Fig. 20.11) with a gaussian fit compatible with a being

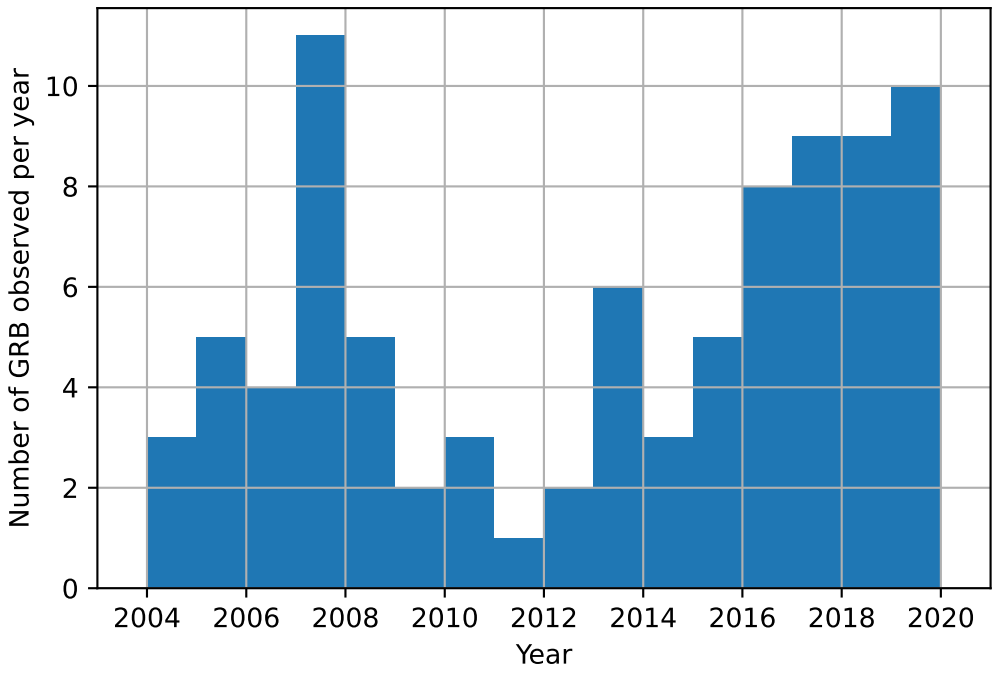

Figure 20.8: Number of GRB observed per year

centred on 0 with a width of 1. This is confirmed by the theta square of all the Mono and Stereo analysis stacked, as no deviation from the background estimation could be seen in Fig. 20.12. This confirms the lack of any signal in the whole dataset but is a good sign of the quality of the background estimation.

Stacking a few events based on their properties and the parameters of the observation is under investigation. However, these parameters are quite scarce, and redshift information is only available for 33% of our sample. Then, finding optimal parameters for stacking is quite complex.

20.5 The *Swift* sample

As a large proportion of the GRBs observed (69%) have been detected and observed by *Swift*. This is then an interesting sample to compare with the sources detected at VHE (all also detected by *Swift*) and the complete population of *Swift* GRBs. *Swift* has two instruments on board: BAT and XRT.

The BAT instrument data presented here comes from the *Swift* GRB table[5]. After discussion with members of the Swift team, experts have informed us that the data on this table might be unreliable and pointed us toward another source of information. This source lacks information for many GRBs in the aggregated data, and further investigations are ongoing to retrieve all the wanted information.

The XRT data come from the *Swift* Burst Analyser (Evans et al., 2010), an automatic pipeline that produces spectra and light curves for GRBs observed by *Swift*/XRT.

[5] https://swift.gsfc.nasa.gov/archive/grb_table/

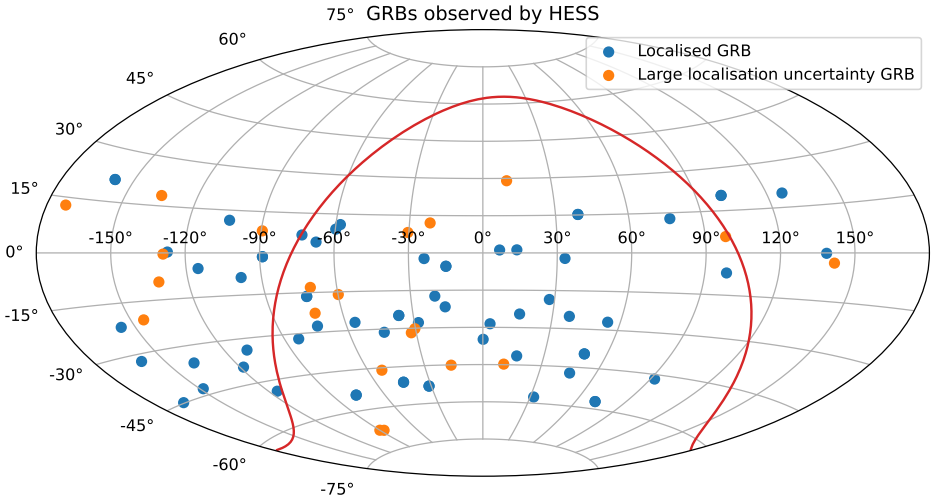

Figure 20.9: Sky map of all the GRBs observed by H.E.S.S.

20.5.1 *Swift*/BAT sample

The *Swift*/BAT instrument provides information about the prompt phase of a GRB. This phase has never been detected at VHE, and none of the GRBs in this list has been observed during this phase, but it could still provide information about the nature of the observed GRB.

Figure 20.13, left panel, show the distribution of the T_{90} duration measured by *Swift*/BAT for all the GRBs observed by the instrument in blue, the ones observed by H.E.S.S. in orange and the four black dashed line represent the ones detected at VHE (both by H.E.S.S. and MAGIC). While the entire *Swift* population and the objects observed by H.E.S.S. do not seem very different in that regard, all the GRBs detected at VHE are long GRBs and two of them have very large T_{90} : GRB 180720B and GRB 190114C.

By looking at the fluence of the GRB shown in the figure 20.13, right panel, it is possible to see that the GRBs detected at VHE were all very bright. In fact, three of those GRBs are brighter than all the other observed GRBs by H.E.S.S. The only one with a brightness similar to the average population of BAT GRBs is GRB 190829A. This GRB was one of the closest ever detected

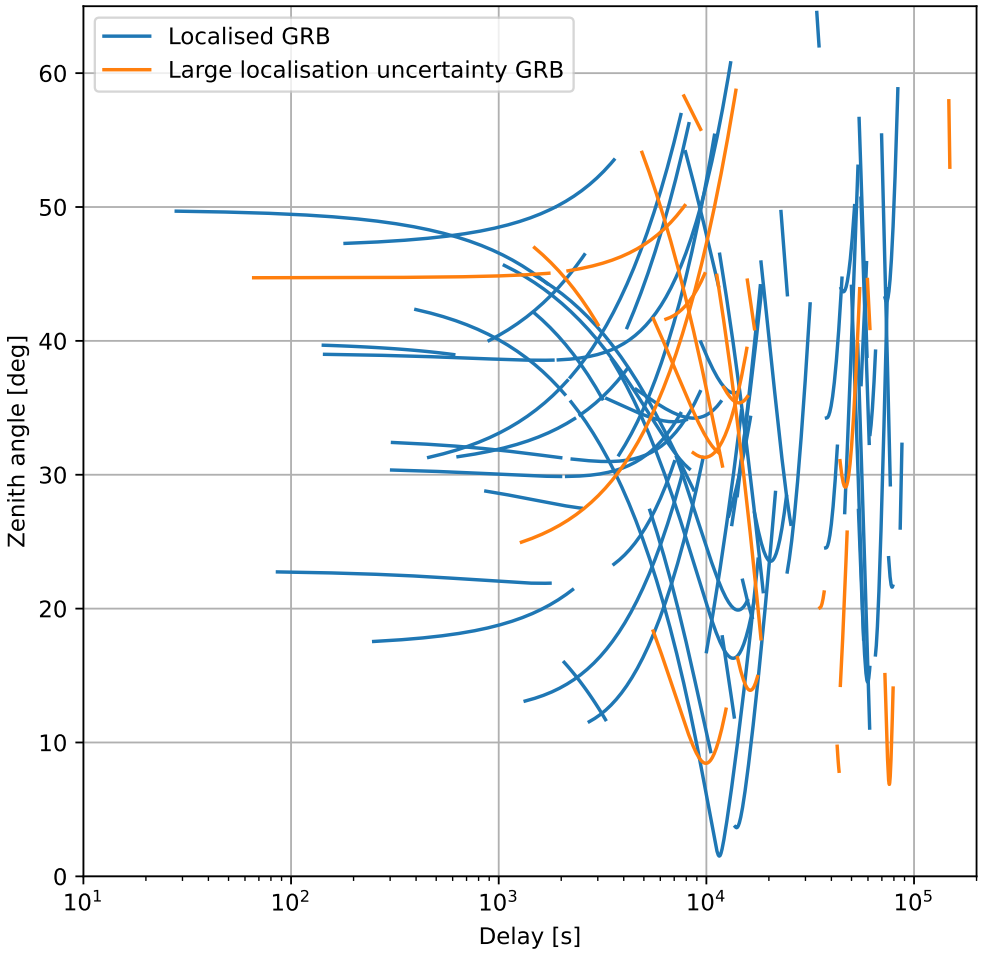

Figure 20.10: Zenith angle of the GRBs observation in function of the delay

(z=0.0785) and, consequently, suffered much less from the EBL absorption that likely helped the detection of this event. Also, this GRB is a candidate for being part of this possible new category of low-luminosity GRBs. It could hint at this category's existence with different properties of emission at VHE. A larger sample of detected GRBs will likely be needed to determine if it sticks out of the typical emission at VHE.

A look at other properties, like the emission's spectral index, has not shown any interesting behaviour and difference compared to the whole population of GRBs detected by *Swift*/BAT.

20.5.2 *Swift*/XRT sample

As mentioned before, the actual detection of GRBs at VHE has shown some correlation of the temporal behaviour between the behaviour at in this energy range and the behaviour seen in X-Ray by *Swift*/XRT. The figure 20.14 shows the light curve of all the GRBs observed by H.E.S.S in light blue. The coloured curves are the GRBs detected at VHE alongside with GRB 130427A, the GRB

Name	RA J2000	Dec J2000	Configuration
GRB 191019A cluster 0	340.02	-17.32	HESSI Stereo
GRB 150428B cluster 0	292.63	4.12	HESSII Mono
GRB 130515A cluster 0	283.44	-54.27	HESSI Stereo
GRB 130515A cluster 1	283.44	-54.27	HESSI Stereo
GRB 180906759 cluster 0	270.0	-67.66	HESSII Stereo
GRB 180906759 cluster 1	273.02	-67.97	HESSII Stereo
GRB 171112868 cluster 0	10.67	-44.76	HESSII Stereo
GRB 170402961 cluster 0	307.19	-45.93	HESSI Stereo
GRB 170826819 cluster 0	327.76	-31.8	HESSII Stereo
GRB 170730133 cluster 1	329.71	-30.22	HESSII Stereo
GRB 190507970 cluster 0	288.36	-22.81	HESSII Stereo
GRB 150422703 cluster 0	215.34	-20.61	HESSII Stereo
GRB 180522607 cluster 0	300.1	-16.03	HESSII Stereo
GRB 180522607 cluster 1	289.17	-13.05	HESSII Stereo
GRB 150127589 cluster 0	141.9	-3.13	HESSI Stereo
GRB 120218276 cluster 0	98.23	5.8	HESSI Stereo
GRB 190306943 cluster 0	231.06	-0.38	HESSI Stereo
GRB 190306943 cluster 1	228.0	-9.3	HESSI Stereo
GRB 160822672 cluster 0	270.48	8.01	HESSII Stereo
GRB 160825799 cluster 0	329.56	8.13	HESSII Mono
GRB 160825799 cluster 1	338.43	12.0	HESSII Mono
GRB 160113398 cluster 0	187.7	12.89	HESSI Stereo
GRB 190727668 cluster 0	224.9	18.28	HESSII Stereo
GRB 180806944 cluster 0	10.48	29.04	HESSII Stereo
GRB 170424A cluster 0	343.7	-45.11	HESSII Mono

Table 20.2: GRB with poor localisation. The position is the centre of the cluster and not the GRB position.

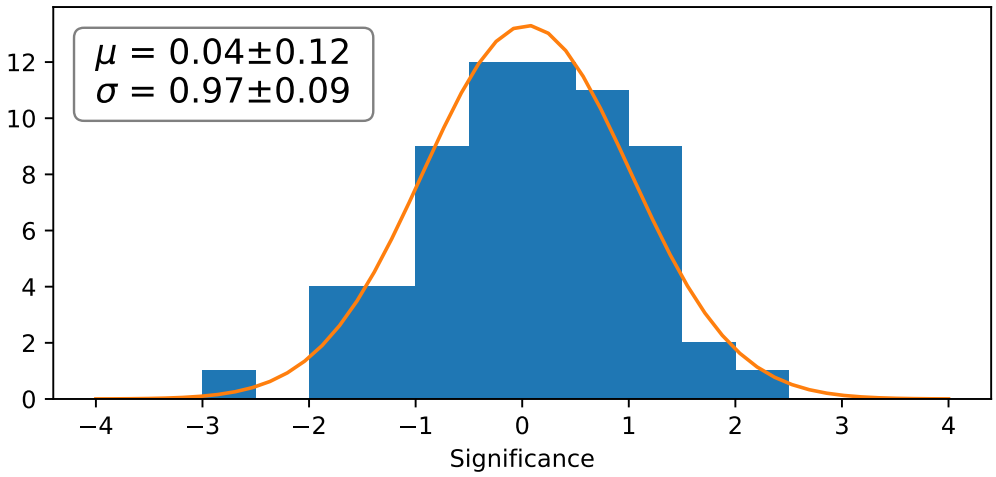

Figure 20.11: Distribution of significance for the GRBs observed by H.E.S.S.

with the highest energy photons (94 GeV) detected by LAT (Ackermann et al., 2014) up until the very recent detection of GRB 221009A.

All the VHE GRBs are among the brightest GRBs seen by *Swift*/XRT. If we select the GRBs

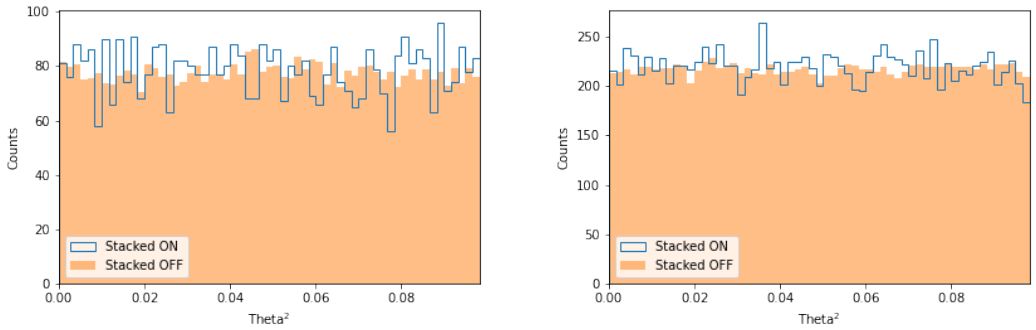

Figure 20.12: Theta square plot of the stacked of all the localised GRBs observed by H.E.S.S. Left is for cluster analyse with CT5 mono and right with the stereo configuration (CT1-4).

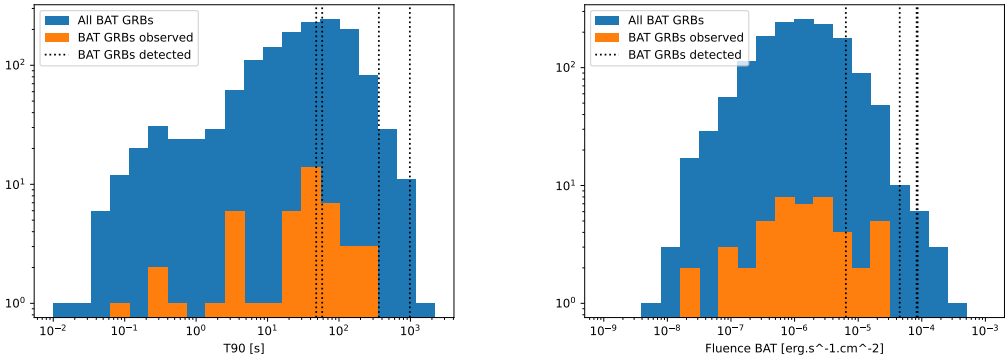

Figure 20.13: T_{90} duration in left and fluence in right for the all the GRBs detected by *Swift*/BAT (blue), GRBs observed by H.E.S.S. (orange) and the ones detected at VHE (dashed lines)

that have a similar brightness during the late afterglow (here defined as $>1\times10^3$ s, above the dotted line in figure 20.14), we have a short list of five GRBs (GRB 070419B, GRB 090201, GRB 100621A, GRB 120328A, GRB 131030A). Three of them do not have any redshift information. We will not consider them for two reasons :

- the average redshift of GRBs detected by *Swift* is around 2 with only 25% of the GRBs with a redshift below 1 (Lien et al., 2016). Any detection of a source with a redshift much superior to 1 is nearly impossible with the energy threshold of H.E.S.S.
- The lack of redshift information makes modelisation and constraint of VHE emission pointless without any detection as it will always be possible to simply increase the redshift to explain the lack of detection.

This leaves as interesting GRBs to investigate: GRB 100621A and GRB 131030A.

If we consider now the GRBs with short observation delay, so observed during their early afterglow phase ($<1\times10^3$ s), by keeping only the bright one (above the dashed line), we have 8 GRBs, with five of them having a redshift measurement, GRB 080804, GRB 100621A, GRB 131030A, GRB 161001A, and GRB 191004B. Two of them are the ones mentioned before for their bright late afterglow.

20.6 A few interesting GRBs

Five GRBs with bright early afterglow and two of them with bright late afterglow and with redshift information have been identified :

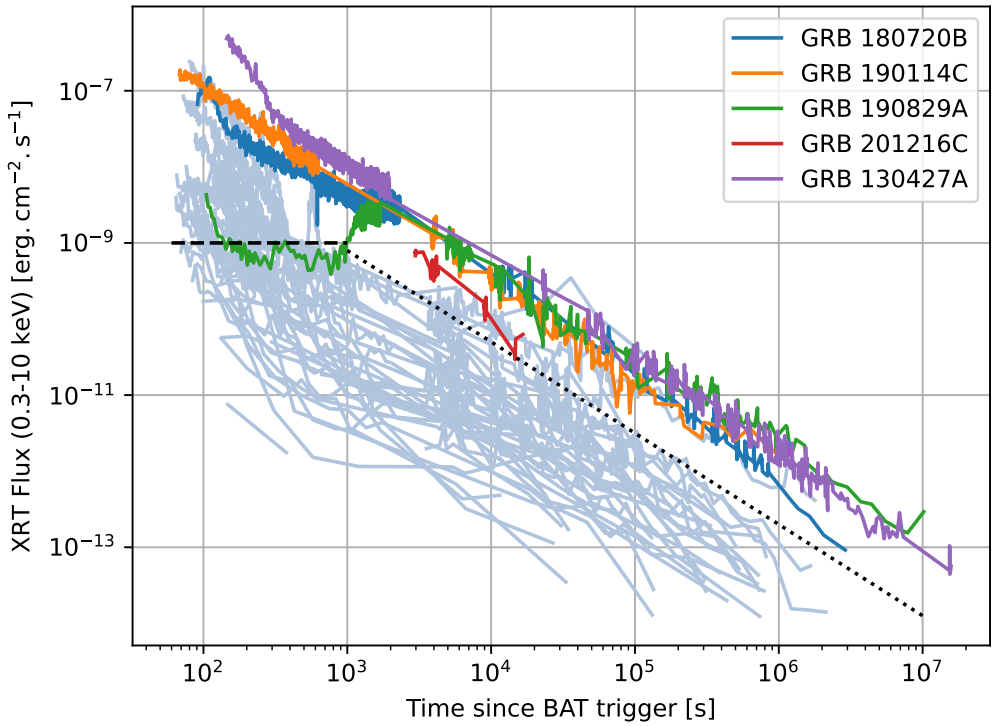

Figure 20.14: Flux of XRT in function of delay since the trigger for the GRBs observed by H.E.S.S. (light blue) and the GRBs detected at VHE and the one detected by LAT the closest to VHE

- GRB 080804 (z = 2.2045)
- GRB 100621A (z = 0.542)
- GRB 131030A (z = 1.263)
- GRB 161001A (z = 0.891)
- GRB 191004B (z = 3.503)

The redshift of all of them is above most of the detected sources at VHE , adding a challenge to detecting such objects. Figure 20.15 give EBL attenuation as a function of the energy for our 5 candidates and the energy threshold of the analysis is shown by dotted lines. We could see that three GRBs have an attenuation close to one order of magnitude at the energy threshold: GRB 100621A, GRB 131030A and GRB 161001A. This is important, but in the case of a bright emission, it may maybe possible to provide significant constraints on them. The two last ones have an already high absorption of several orders of magnitude at their energy threshold, very likely explaining the lack of detection.

This leaves us three GRBs. When looking at their property and compared to the others detected at VHE (Table 20.3), it is possible to see that there are all long GRBs, except for GRB 161001A, which is close to the usual separation limit between short and long GRBs. Even if it is above the 2 s mark, teams from *Swift*/BAT (Markwardt et al., 2016) and Konus-Wind (Frederiks et al., 2016) have both suggested this might be a short GRB based on the temporal and spectral properties.

The BAT fluence of GRB 100621A and GRB 131030A is below the ones detected at VHE (except for GRB 190829A but which was at a very low redshift) but still in the upper end of the sample

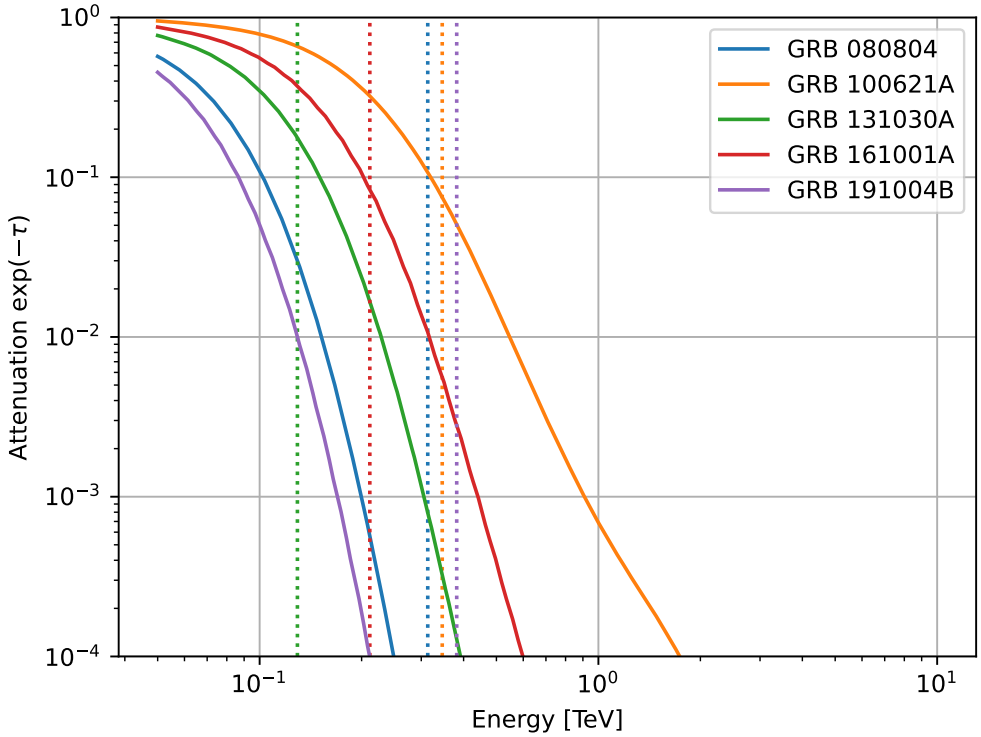

Figure 20.15: Absorption by the EBL in function of the energy for some GRBs. The dotted line represents the energy threshold of the analysis performed by H.E.S.S.

of the GRBs observed by H.E.S.S. On the other hand, GRB 161001A is closer to the centre of the distribution of the fluence measured by Swift/BAT, making it an average GRB in terms of the brightness of the prompt phase.

We will only consider results on the first observation run for each of the three GRBs, the one which has been taken with the lowest delay and so likely the highest flux. With its low delay observations, GRB 190114C observations are the most similar to our three GRBs. We could then test the hypothesis of an emission similar to GRB 190114C (MAGIC Collaboration et al., 2019a). For this, we will use the intrinsic spectra measured by MAGIC alongside with the light curve.

As the observation window has some differences, to correct for it we will use the light curve from MAGIC which has measured a power law shape : $F(t) = F_{ref}\left(\frac{t}{t_{ref}}\right)^{\beta}$ and a temporal index $\beta = -1.60 \pm 0.07$. F_{ref} is the flux at the reference time t_{ref} . The average flux during a time interval is the integral of this function divided by the width of the interval:

$$< F(t) > = \frac{\int_{t_{start}}^{t_{end}} F_{ref}\left(\frac{t}{t_{ref}}\right)^{\beta} dt}{t_{end} - t_{start}}$$

Then defining the reference time t_{ref} at the time at which the flux is equal to the average flux is equivalent to solving this equation :

Name GRB	T90 [s]	BAT Fluence [10^{-7}erg.cm^{-2}]	Redshift
GRB 100621A	63.6	210	0.542
GRB 131030A	41.1	290	1.263
GRB 161001A	2.6	6.7	0.891
GRB 180720B	> 982	860	0.654
GRB 190114C	361.5	830	0.4245
GRB 190829A	58.2	64	0.0785
GRB 201216C	48.0	450	1.1

Table 20.3: Property of the three identified GRBs alongside with the four detected at VHE (in boldface) with the data from the *Swift* GRB table

$$F_{ref} = \frac{\int_{t_{start}}^{t_{end}} F_{ref} \left(\frac{t}{t_{ref}}\right)^{\beta} dt}{t_{end} - t_{start}}$$

$$F_{ref} = \frac{F_{ref}}{{t_{ref}}^{\beta}} \frac{t^{\beta+1}}{(t_{end} - t_{start})(1+\beta)} \Big|_{t=t_{start}}^{t=t_{end}}$$

$$t_{ref} = \left(\frac{{t_{end}}^{\beta+1} - {t_{start}}^{\beta+1}}{(t_{end} - t_{start})(1+\beta)} \right)^{\frac{1}{\beta}}$$

It is possible to determine the time corresponding to the average flux of the new time window in the same way. Then the spectral normalisation is corrected by computing the ratio between the flux at the reference time and the one at the average time of the new time window.

Finally, the spectra were modified to take into account the absorption by the EBL using the model of Domínguez et al. (2011). Differential upper limits at a confidence level of 95% were computed for the H.E.S.S. observations with five bins per decade. The results are shown in the figure 20.16. We could see that H.E.S.S. measurement rejects a GRB 190114C-like spectra for all the GRBs considered. For all the cases, the flux would need to be near one order of magnitude lower to agree with the upper limits determined from the observations.

The figure 20.17 shows the XRT light curve for the three GRBs alongside the one of GRB 19014C. The observation window is also represented. For GRB 100621A and GRB 131030A, the flux is similar in the very early time but decreases much more quickly than GRB 190114C. Consequently, during the observation time, the XRT flux is much lower. If we suppose a similar scaling of the VHE flux, this would then agree with the observations. For GRB 161001A, the XRT flux is always significantly lower than the ones from GRB 190114C.

Further modelisation of the emission of these GRBs would be interesting and also to test the detection method exposed in the chapter 19, as it is particularly efficient at detecting GRBs with short observation delays like the one we are looking at in this section.

20.7 Conclusion

H.E.S.S. has observed a significant number of GRBs during its lifetime. The reanalysis of all the ones not detected previously has shown no hint of any signal across the whole sample.

A look at *Swift* data from XRT and BAT shows that compared to the other GRBs, the ones detected were very bright both during the prompt and the afterglow phase. Also, their redshift was low, with the highest redshift of 1.1 for GRB 201216C. This would be in favour of the main reason for the lack of detection among all the other observed GRBs being simply due to instruments that were not sensitive enough. CTA, with its lower energy threshold and significantly improved sensitivity, will likely lead to more detections.

Three especially interesting GRBs have been identified based on their XRT light curves and redshifts. The observations allow us to reject spectra like GRB 190114C but would be compatible if

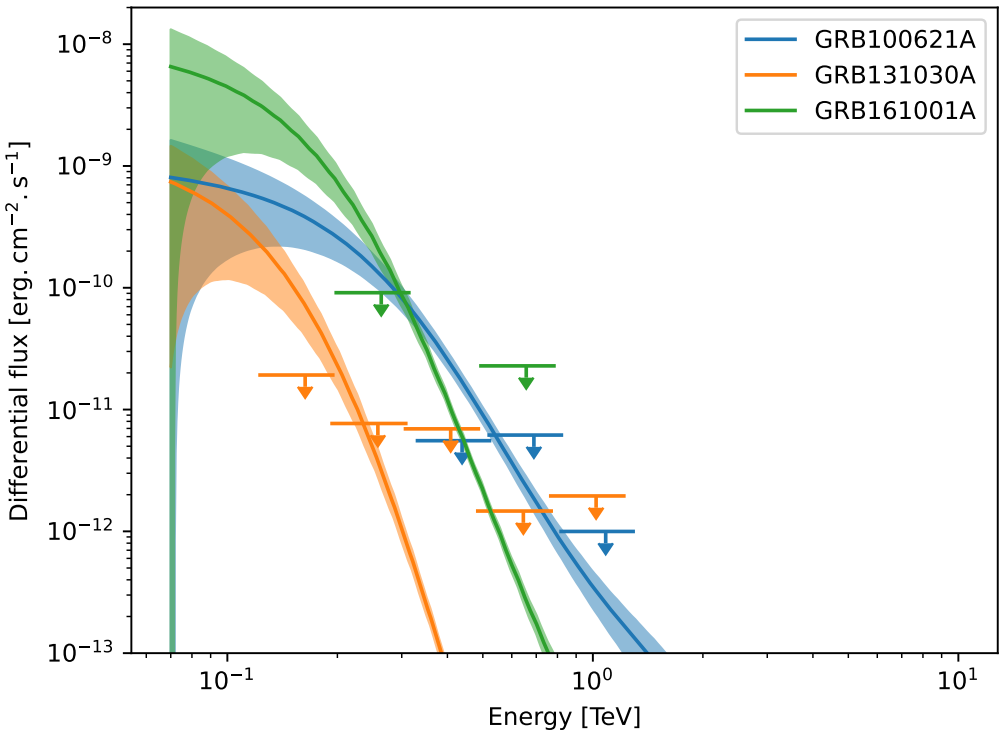

Figure 20.16: Spectra of GRB 190114C rescaled for the time window of each GRBs observation considered and with EBL absorption taken into account. Upper limit are from H.E.S.S. observations.

we suppose an exact scaling of the VHE emission with the XRT light curve. Further modelisation of their emission could be interesting and constrained by the H.E.S.S. observations.

All the GRBs detected at VHE have also been detected by *Fermi*/GBM. Comparing the properties of the GBM GRBs with the one observed by H.E.S.S. with a precise localisation could also bring other insight.

The recent GRB 221009A, which was much brighter than any GRBs observed up to now, especially in *Swift*/XRT (Fig. 20.18), would have let hope for new detection at VHE. LHASSO detected the early time of the GRB (Huang et al., 2022), but no detection has been claimed by any IACT, likely indicating the lack of any detection by any instruments. The GRB exploded on the day of the full moon. So most IACTs were not able to conduct observation on-site, increasing the delay of the observations. Also, due to the very strong moon, the observations took place with serious performance penalties for all instruments. It was only a few nights later that observation with dark nights was possible. However, with the detection of GRB 180720B 10 h after the burst and of GRB 190829A up to 56 h after the burst, we could still have hope for a new detection even maybe a week later if we assume the scaling between XRT and VHE. Understanding the lack of detection will likely be very interesting.

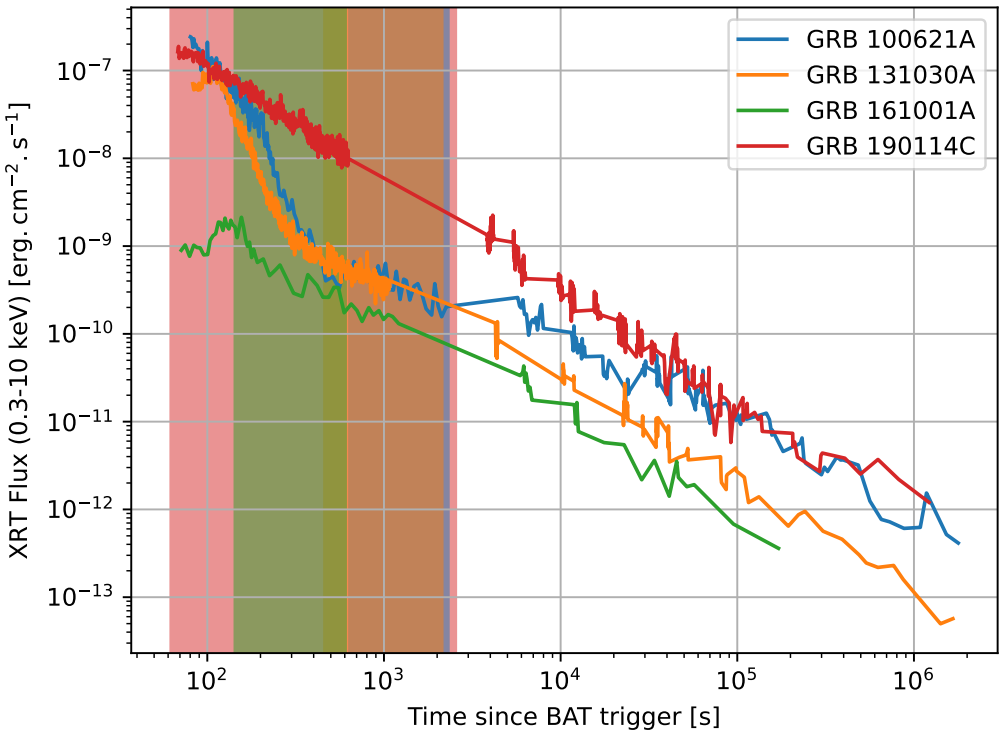

Figure 20.17: Light curve in *Swift*/XRT for the three studied GRBs alongside with the one for GRB 190114C. The time window of observation for each GRB is represented.

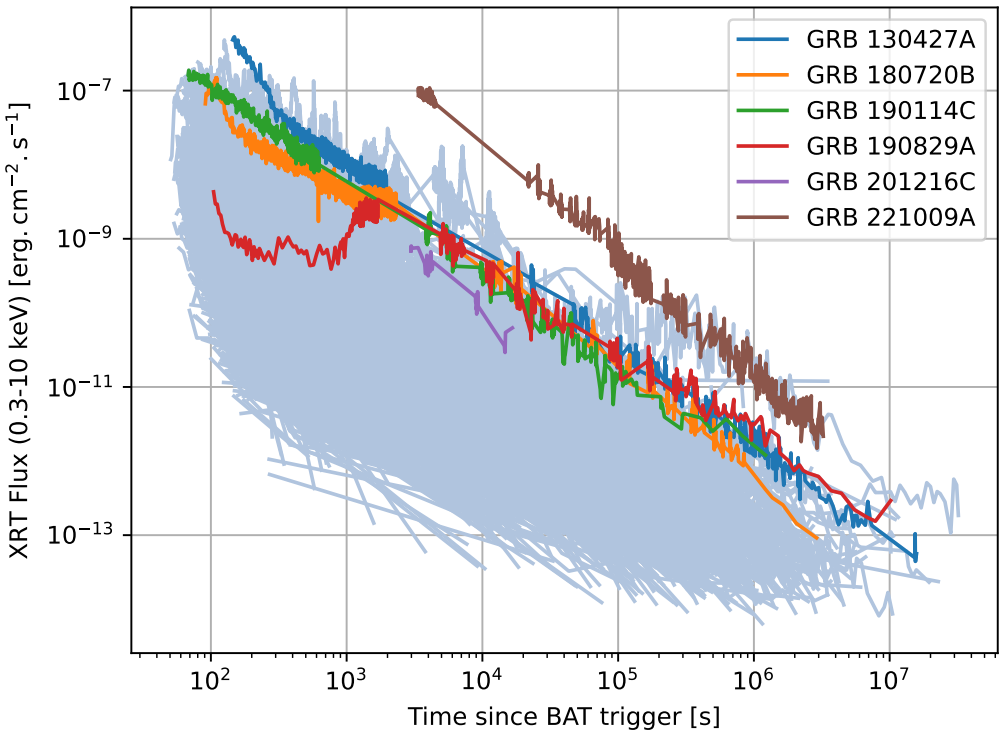

Figure 20.18: Light curve of all the GRBs detected by *Swift*/XRT (light blue) alongside with the interesting GRBs for VHE emission

Chapter 21

Résumé de la partie 5

Contents

21.1 Premiers suivis de sursauts gamma avec LST-1

21.1.1 Observation de sursauts gamma

Le LST-1 est encore en cours de mise en service, mais il a déjà commencé à recueillir des données scientifiques et à mener un programme d'observation sur les sources transitoires telles que les GRB. Le premier suivi d'un GRB a été effectué sur le GRB 201216C dans la nuit du 17 décembre 2020. Depuis, le nombre de GRBs suivis n'a cessé d'augmenter.

J'ai participé à l'établissement des critères d'observations des sursauts gamma. Le nombre d'heures d'observation demandé étant encore faible, ceux-ci permettent le suivi dans de nombreux cas et sont probablement amenés à être révisés dans le futur. Ils incluent dans la stratégie le suivi de l'essentiel des instruments de détection de GRB actuels.

Au moment de l'écriture de ces lignes, 22 sursauts ont été observé par LST-1. La position de ceux-ci est visible dans la figure 21.1. Le nombre total d'observations n'est pas aussi élevé qu'espéré

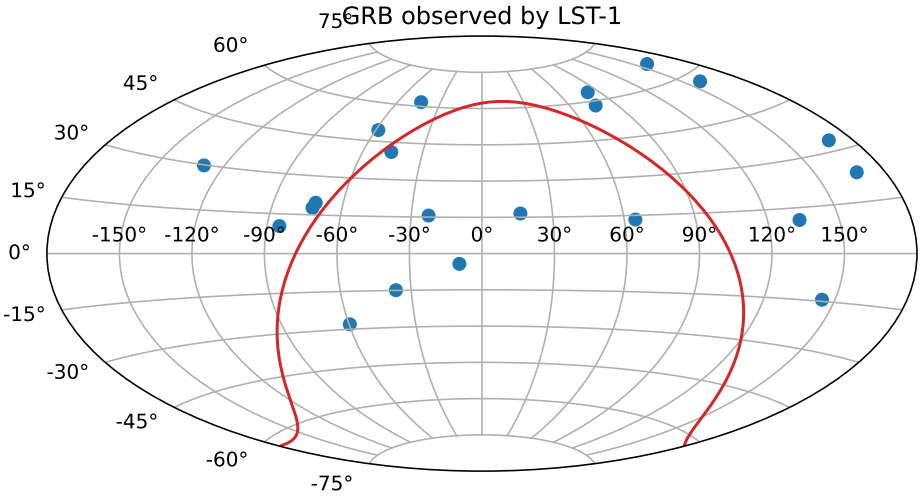

Figure 21.1: Position dans le ciel des GRBs observés par LST-1

du fait des activités de test de l'instrument ainsi que l'arrêt des opérations du fait de l'éruption volcanique ayant eu lieu sur l'île de La Palma.

21.1.2 Analyse de quelques sursauts

21.1.2.1 GRB 210511B

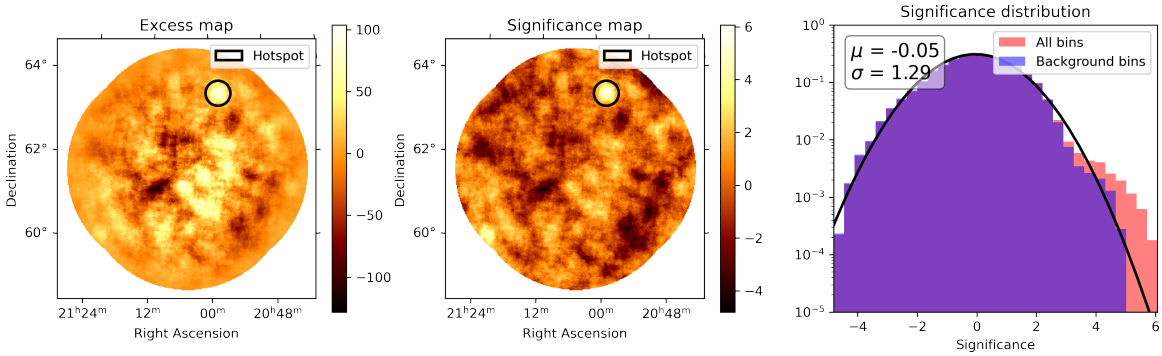

Figure 21.2: Carte d'excès (panneau de gauche), carte de significance (panneau central) et distribution de la significance (panneau de droite) pour les observations du GRB 210511B pour une énergie comprise entre 50 GeV et 190 GeV, le cercle en noir est le point chaud identifié.

GRB 210511B a été initialement détecté par *Fermi*/GBM et suivi par LST-1 avec 16h de délai. Au moment des observations, la position comportait une grande incertitude. Les analyses ont révélé un point chaud à basse énergie dans les cartes (Fig. 21.2). La position mesurée est RA = $(314.471 \pm 0.017_{stat})°$ et Dec = $(63.250 \pm 0.010_{stat})°$. Les dernières informations de localisation du GRB excluent celui-ci comme une explication de ce point chaud. Aucune contrepartie crédible n'a été trouvée ni aucune explication du fait de l'instrument (problème de calibration, étoile dans le champs de vue, ...). Du fait de sa significance tout juste au-dessus du seuil de détection, il est toujours incertain que celui-ci correspondent à un réel signal et une ré-analyse avec des coupures plus optimisées permettra probablement d'aider à répondre à cette question.

21.1.2.2 GRB 210704A

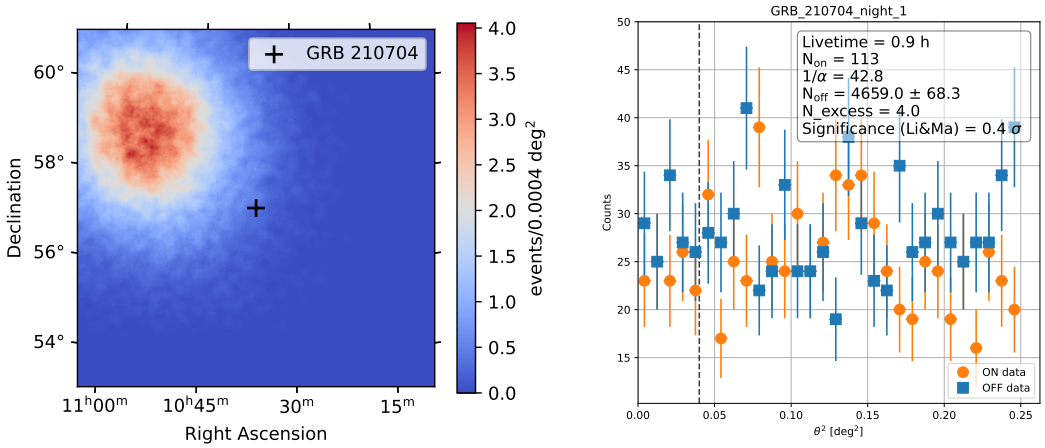

Figure 21.3: Résultats de l'analyse des observations du GRB 210407A avec sur le panneau de gauche les cartes de comptage et sur le panneau de droite le tracé du théta2 représentant l'excès en fonction de la distance angulaire carrée par rapport à la position de la source.

De la même manière que GRB 210511B, GRB 210704A a été détecté par *Fermi*/GBM avec une large incertitude sur la localisation. Après les observations effectué par LST-1, une localisation précise fournie par *Swift*/XRT est arrivée, celle-ci se situait au bord du champs de vue. Cependant, une analyse a pu être effectuée (Fig. 21.3) et n'a mené à aucune détection. Toutefois, des observations sur le Crabe dans des conditions similaires ont montré une sensibilité très faible, ne permettant pas ainsi de contraindre l'émission à très haute énergie de ce GRB.

21.2 Améliorer les critères de sélection pour le suivi des GBM

21.2.1 Les alertes envoyé par textitFermi/GBM

Le Gamma-ray Burst Monitor (GBM) à bord du satellite *Fermi* a détecté un grand nombre de sursauts gamma, et est plus sensible aux GRB courts que Swift/BAT. Leur suivi représente donc un certain intérêt, cependant, le suivi des alertes GBM est complexe en raison de la grande incertitude sur la position. Afin d'optimiser leur suivi de ces alertes, les instruments Cherenkov pour le suivi utilisent des critères de sélection basés sur la significance du GRB et l'incertitude de position en ayant optimisé indépendamment chaque paramètre.

Il existe quatre types d'alertes envoyées par GBM: GBM_Alert, GBM_Flight_Position, GBM_Ground_Position, et GBM_Final. Les derniers type d'alerte fournissent des positions plus précises, mais avec un délai plus large que les précédentes.

21.2.2 Optimisation de la sélection

La première étape a été de sélectionner les GRB également détectés par Swift/BAT, qui fournit ainsi une position précise de référence. Ensuite ont été étudiés les paramètres corrélés à la précision de la localisation fourni par GBM. Puis une optimisation en tenant compte de ces paramètres a été effectuée afin de pouvoir choisir les GRBs les mieux localisés et ce pour chaque type d'alerte. Finalement, deux couples de paramètres on été retenus : soit l'utilisation du nombre de photon et de l'incertitude sur la position, soit l'utilisation de la significance et de l'incertitude sur la position. La figure 21.5 représente la fraction de GRBs suffisamment bien localisés pour être situés dans le

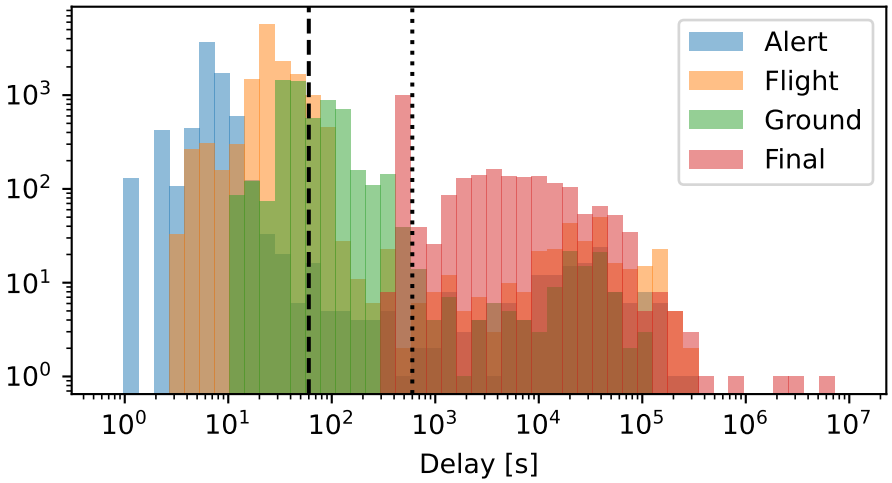

Figure 21.4: Distribution du délai pour chaque type d'alerte envoyé par l'instrument GBM. La ligne en tiret représente la minute de retard, tandis que la ligne en pointillé correspond à dix minutes de retard. Cette figure a été réalisée à partir de ~ 30000 alertes envoyées par *Fermi*/GBM sur 13.5 yr pour un total de 7874 événements.

	`Flight`	`Ground`	`Final`
Position uncertainty	$<13.4^\circ$	$<3.1^\circ$	$<4.5^\circ$
Significance	$> 13\sigma$	$> 18.5\sigma$	
Number of photons			> 185

Table 21.1: Critère de sélection obtenus pour des observations en mode pointés

champ de vue par rapport à la fraction de GRBs conservés par les critères de sélection. On peut ainsi voir que l'on peut observer plus de GRBs avec la même qualité de localisation ou autant avec une meilleure qualité de localisation en utilisant ces nouveaux critères.

Les critères obtenus pour les observations avec un seul pointé sont présentés dans le tableau 21.1 et ceux pour le cas avec une stratégie à plusieurs pointés sont présentés dans le chapitre 18.

21.2.3 Proposition d'une nouvelle stratégie de suivi

Sur la base des résultats mentionnés précédemment, il est possible de proposer cette procédure de suivi :

1. À la réception d'alerte de type `Alert`, aucune action à effectuer.

2. À la réception d'une alerte de type `Flight`, si les critères de sélection sont remplis, commencer les observations sur les coordonnées indiquées. Pour de nouvelles alertes `Flight`, ne pas mettre à jour le pointage.

3. À la réception d'une alerte de type `Ground`, si les observations ont déjà commencé avec une alerte `Flight`, arrêter l'observation en cours et changer de pointage pour les nouvelles coordonnées. Sinon, tester les critères de sélection et ne commencer les observations que s'ils sont remplis. Tant qu'aucune alerte `Final` n'est reçue, mettre à jour la position basée uniquement sur la dernière alerte `Ground` au début d'une nouvelle séquence d'observation.

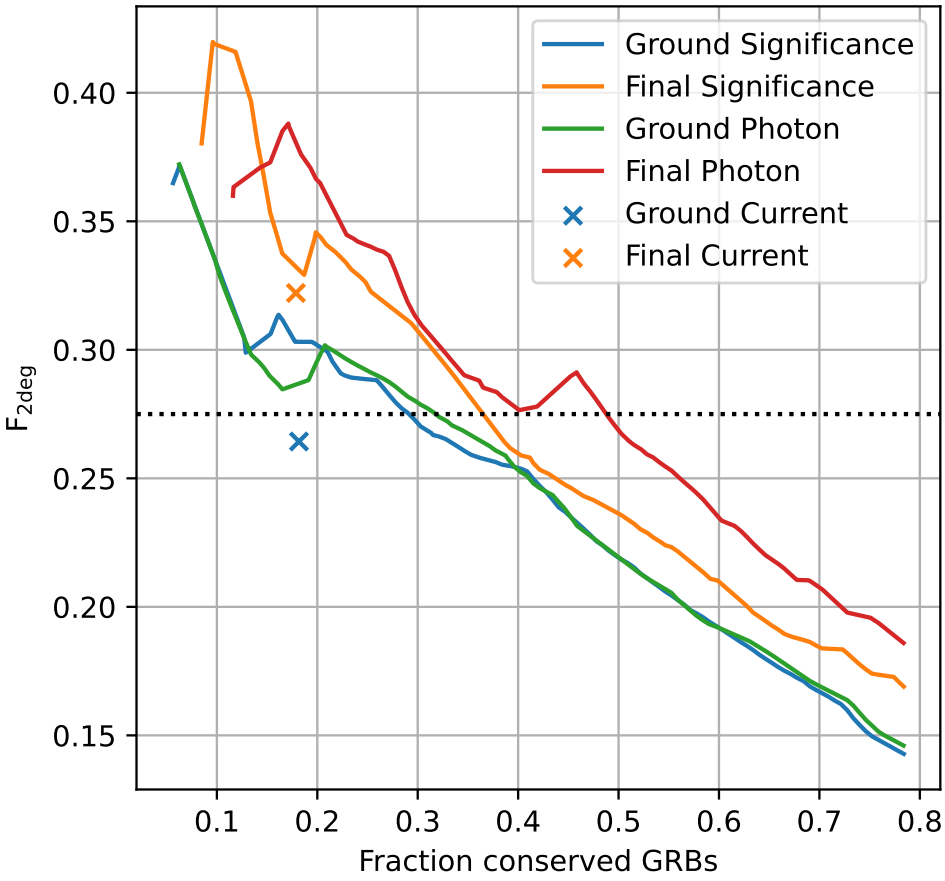

Figure 21.5: Fraction des GRBs localisés à moins de 2° de la position réelle en fonction de la fraction de GRBs passant les critères de sélection pour les notifications `Ground` et `Final`. Pour chaque type, la croix représente les critères de sélection actuels, la courbe de significance, les critères d'optimisation utilisant comme paramètres la significance et l'incertitude de position, et la courbe des photons, les critères d'optimisation utilisant comme paramètres le nombre de photons et l'incertitude de position. Les lignes pointillées représentent la cible choisie pour la fraction de confinement.

4. À la réception d'une alerte de type `Final`, si les observations ont déjà commencé avec une alerte `Flight` ou `Ground`, attendre la fin de l'observation en cours avant de mettre à jour le pointage. Sinon, commencer les observations si le GRB répond aux critères de sélection.

5. S'il n'y a pas d'alerte `Ground` ou `Final` après une séquence d'observation basée sur une alerte `Flight`, arrêter les observations.

Le choix de ne pas mettre à jour à chaque nouvelle alerte vise à éviter une large fraction de temps à déplacer le télescope et ainsi manquer les observations à faible délai. Pour certains GRB, en quelques minutes, il est possible de recevoir plus de dix alertes `Flight` et `Ground`.

21.2.4 Evolution des critères de sélection pour le tiling

Il a ainsi été montré qu'il est possible d'améliorer la sélection des alertes *Fermi*/GBM, augmentant ainsi les chances que le GRB soit dans le champ de vue. Une approche simpliste a été proposée pour étendre ces critères à des observations avec tiling. Il serait cependant intéressant de reproduire cette étude mais en utilisant le logiciel planifiant ces observations afin d'être sûr que cela se traduit dans la pratique.

21.3 Au-delà de Li&Ma pour la détection de GRB

La méthode standard de calcul d'excès et d'estimation du fond en utilisant la technique ON-OFF combinée avec l'estimation de la significance selon Li&Ma s'est révélée robuste pour l'analyse des données provenant d'instruments IACT. Cependant, Li&Ma ne prend pas en compte les informations provenant de la distribution spectrale ou temporelle des événements, ce qui pourrait permettre de mettre en évidence un signal caché dans le fond. Cela est particulièrement vrai pour les sursauts gamma, avec leur grande variabilité temporelle suivant une courbe de lumière typique en forme de loi de puissance.

21.3.1 Principe de fonctionnement

La méthode est inspirée des analyses dites 3D utilisée depuis récemment pour l'analyse de certain champs galactiques complexes. Un modèle d'émission est ajusté sur les données et sa vraisemblance est comparée à celle d'un modèle d'émission nulle. Une différence majeure est un binning temporel et spectrale à la place du binning spatial et spectral. Cela permet ainsi de garder les méthodes traditionnelles d'estimation du fond tout en évitant ainsi le point épineux des modèle de fond.

21.3.2 Procédure de test des performances

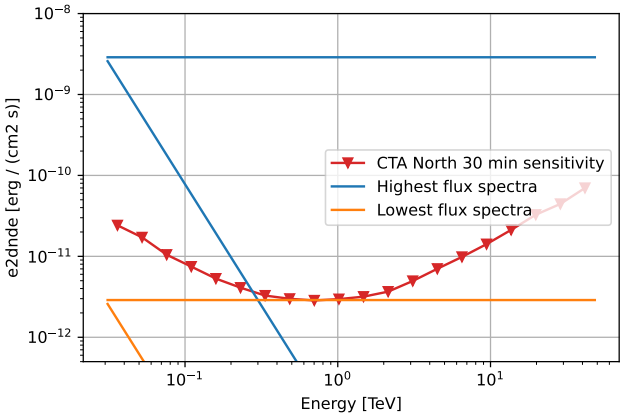

Figure 21.6: Les spectres avec les deux indices spectraux les plus extrêmes simulés pour les flux les plus élevés (courbe bleue) et les plus bas (courbe orange). La sensibilité est celle de CTA pour 30 min.

Afin de tester les performances, nous avons simulé de nombreuses observations de CTA avec des signaux ressemblant à des GRB (spectre et courbe de lumière en loi de puissance). Afin d'identifier les points forts et faibles, plusieurs paramètres sont laissés libres, tels que le délai des observations, l'indice spectral et l'indice temporelle ainsi que le flux. Sur la figure 21.6 sont représentés les spectres les plus extrêmes simulés et comparés à la sensibilité obtenue pour 30 min d'observation avec le site

Nord de CTA, celui utilisé pour les simulations. La nouvelle méthode proposée ainsi qu'une analyse standard utilisant Li&Ma sont effectuée pour différent temps d'intégration sur ces simulations.

21.4 Résultats

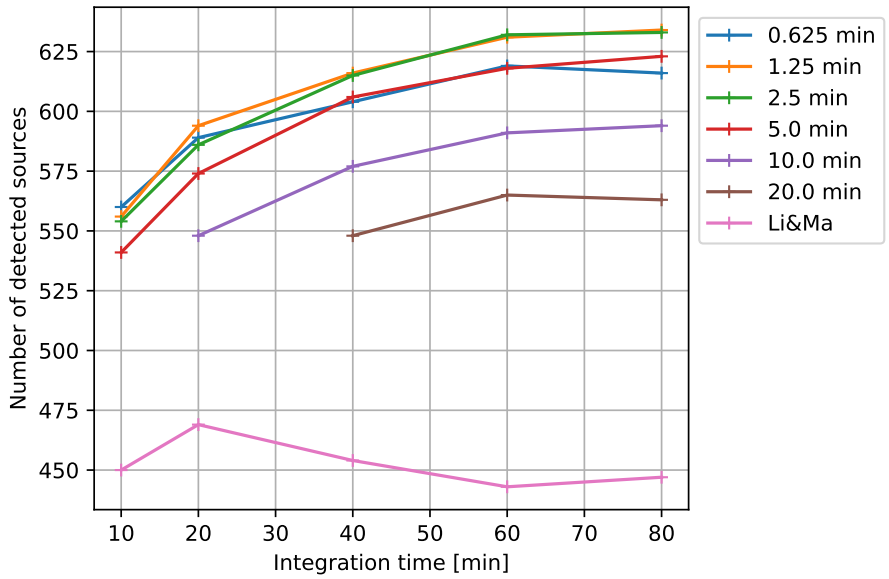

Figure 21.7: Nombre de sources détectées pour Li&Ma et chaque taille de bin temporelle pour la méthode d'ajustement en fonction du temps d'intégration.

Il est possible de visualiser le nombre de sources détectées avec chaque méthode sur la figure 21.7. On peut ainsi constater que la nouvelle méthode surpasse Li&Ma avec un gain jusqu'à 35% dans la meilleure configuration. Un autre avantage de cette nouvelle méthode est qu'augmenter le temps d'intégration par ajustement ne réduit pas la significance pour les GRBs avec la plus forte décroissance temporelle comme c'est le cas avec Li&Ma, simplifiant ainsi l'analyse car il n'est pas pertinent d'optimiser ce critère.

L'essentiel des gains est observé sur les GRBs ayant soit un spectre dur, soit un délai d'observation faible ou encore une forte décroissance temporelle. Si le premier est relativement peu utile dans le cas des GRBs, les deux autres peuvent potentiellement aider à en détecter de nouveau.

21.5 Perspectives

Ces premiers résultats sont encourageant et permettent de détecter de nombreuses sources qui ne l'auraient pas été par Li&Ma. Cependant, la forme spectrale et temporelle simulée et recherchée sont identiques. Il serait intéressant d'étudier l'impact de différences dans celles-ci sur la capacité de l'algorithme à détecter des sources. Il serait également intéressant de tester cela sur des données réelles afin de vérifier si ce gain de performance est reproduit, mais aussi que la méthode ne produit pas des fausses détections.

21.6 Le catalogue des observations de sursaut gamma de H.E.S.S.

Depuis les premières observations du réseau de télescopes H.E.S.S., de nombreux sursauts gamma ont été observés. Il s'agit d'un programme majeur de H.E.S.S. qui a donné lieu à de nombreux suivis. Ce programme a finalement conduit à la première détection d'un sursaut gamma à très haute énergie avec GRB 180720B en 2018 (Abdalla et al., 2019) et, un an plus tard, à la détection de GRB 190829A (H. E. S. S. Collaboration et al., 2021). L'expérience MAGIC a également mené un tel programme qui a abouti à la détection de GRB 190114C (MAGIC Collaboration et al., 2019a) et GRB 201216C (Fukami et al., 2022).

Avec ces quatre GRBs détectés à très haute énergie au cours des dernières années, l'une des questions émergentes est de comprendre pourquoi aucune détection n'avait été réalisée par le passé malgré ces nombreuses observations effectuées par plusieurs expériences.

Pour tenter de répondre à cette question, une réanalyse de toutes les observations de GRBs effectuées par H.E.S.S. de 2003 à 2019 a été réalisée et est ici présentée.

21.6.1 Sélection des données

Afin d'être sûr de n'oublier aucune observations, la base de données des observations a été comparée aux catalogues GRB de cinq instruments principaux (HETE-2 (Vanderspek et al., 2004), *Fermi*/GBM (von Kienlin et al., 2020), *Fermi*/LAT (Ajello et al., 2019), INTEGRAL/ISGRI (Bird et al., 2016), et *Swift*/BAT (Lien et al., 2016)).

Cela a permis ainsi d'identifier 91 GRBs, dont 2 qui ont été observés par chance par H.E.S.S. et où le suivi n'était pas intentionnel. La qualité des données a ensuite été vérifiée manuellement avec attention, menant à l'élimination d'un certain nombre d'observations.

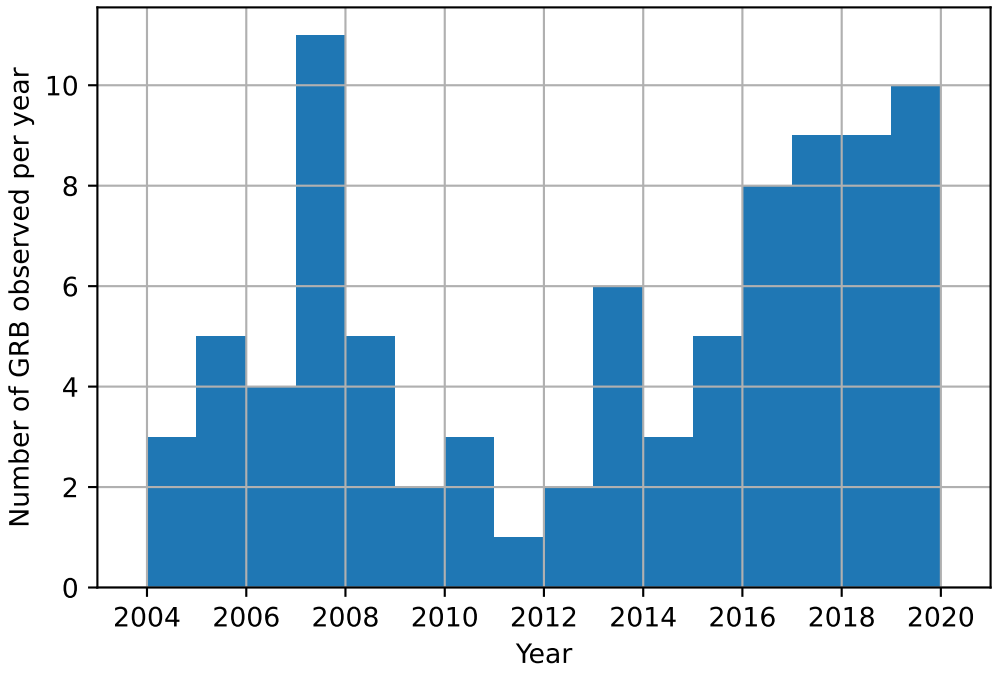

Figure 21.8: Nombre de GRB observés par an

Après ce filtrage, il reste 70 GRBs dans le datasets à analyser. Les observations sont réparties

sur l'ensemble des années, mais avec des variations principalement dues à l'évolution des critères d'observations (Fig. 21.8).

21.6.2 Analyse des données et résultats

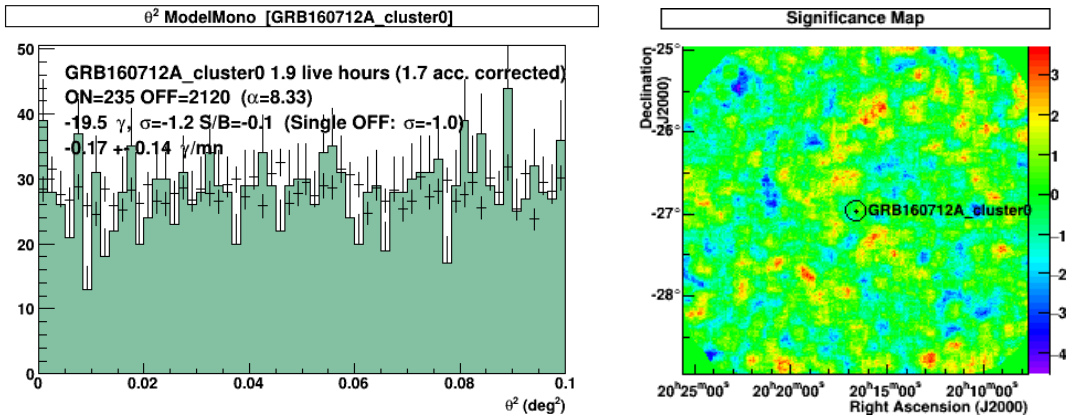

Figure 21.9: Graphique de Theta carré (panneau de gauche) et carte de significance (panneau de droite) pour le GRB 160712A

L'ensemble de ces données a été analysé avec les méthodes standard d'analyse de GRB définies dans H.E.S.S. Aucun signal dû à un GRB n'a pu être identifié. En vue de la publication de l'ensemble des résultats, des cartes de significance et des theta carré (Fig; 21.9) ainsi que les limites supérieures ont été calculées pour l'émission à très haute énergie.

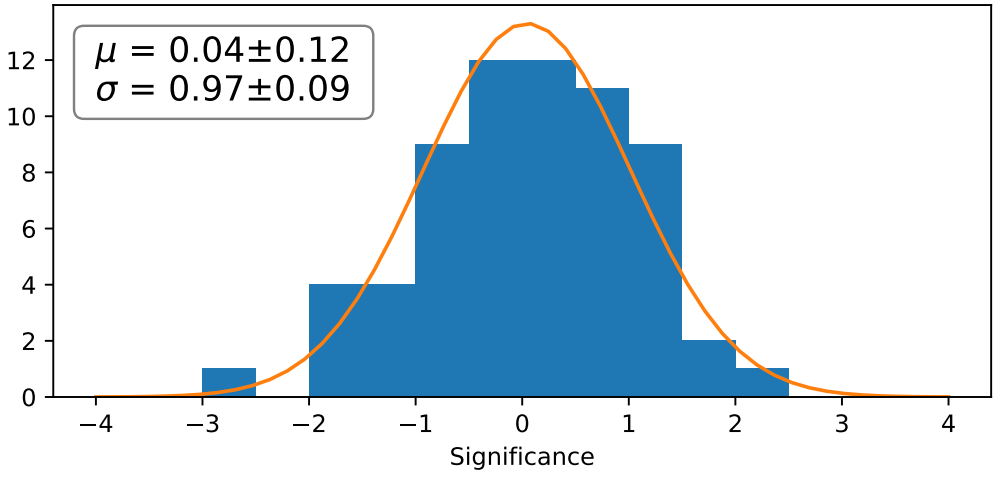

Figure 21.10: Distribution de la significance pour les GRBs observés par H.E.S.S.

Quand on regarde la distribution de la significance des GRBs avec une bonne localisation observé par H.E.S.S. (Fig 21.10), on peut constater que celle-ci est bien ajustée par une loi normale compatible avec une moyenne de 0 et un écart type de 1. Cela est la distribution attendue dans le cas où l'ensemble des observations ne contient aucun signal. Confirmant ainsi les résultats de l'analyse individuelle.

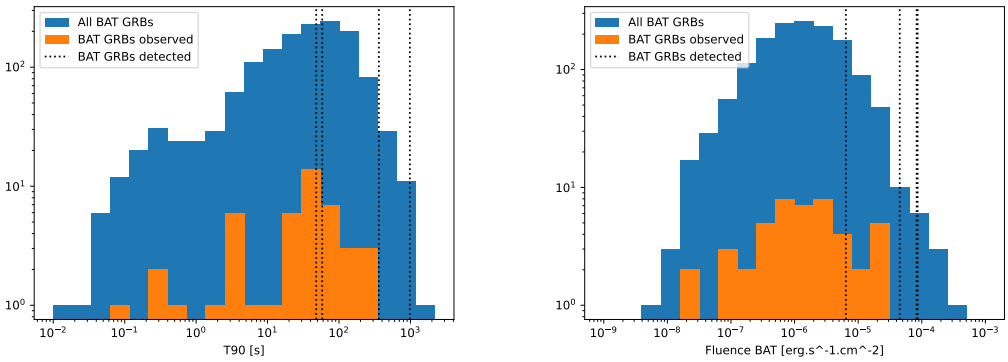

Figure 21.11: T_{90} à gauche et fluence à droite pour tous les GRB détectés par *Swift*/BAT (en bleu), les GRB observés par H.E.S.S. (en orange) et ceux détectés en VHE (lignes pointillées).)

21.6.3 Analyse de population avec les GRBs détectés par *Swift*/BAT

Parmi les GRBs avec une bonne localisation, une large portion a été détectée par *Swift*/BAT, ce qui permet ainsi de comparer les propriétés de la phase prompte des GRBs observés et des GRBs détectés à très haute énergie (Fig. 20.13). La seule déviation significative observée est sur la fluence, les GRBs détectés étant plus brillant que les autres observés.

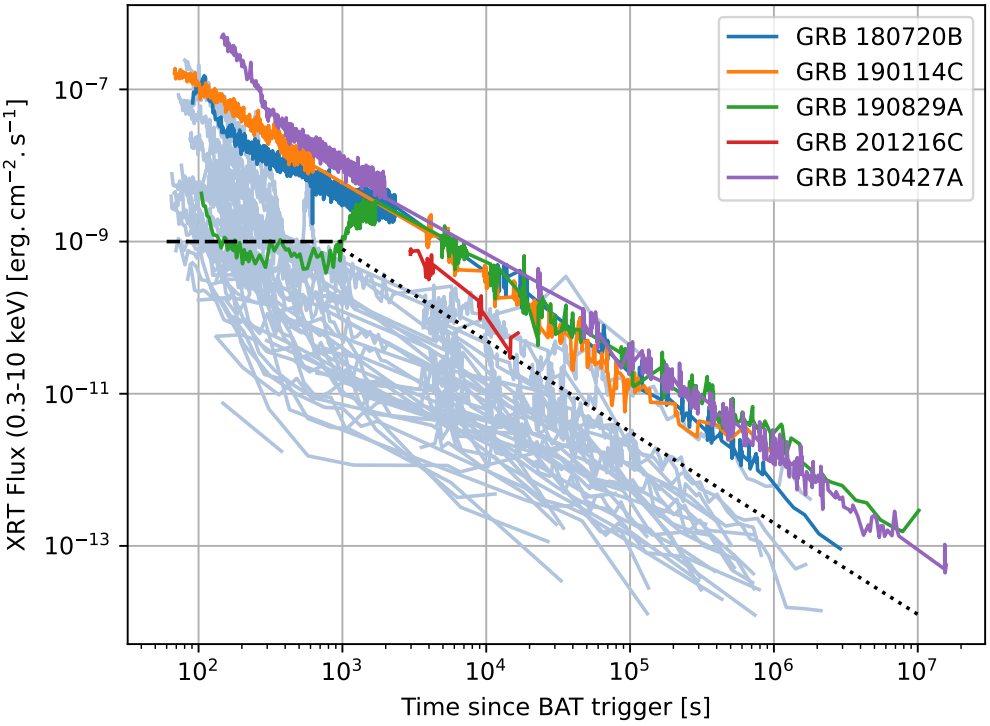

Figure 21.12: Flux mesuré par XRT en fonction du délai depuis la détection pour les GRB observés par H.E.S.S. (en bleu clair) et les GRB détectés en VHE ainsi que celui détecté par LAT le plus proche des très hautes énergies.

On peut également regarder les propriétés de la phase de rémanence à l'aide des données *Swift*/XRT qui a effectué un suivi de l'ensemble de ces GRBs. On peut également constater que seulement les GRBs les plus brillants on été détectés (Fig. 21.12).

21.6.4 Conclusion

H.E.S.S. a observé un nombre significatif de GRB au cours de son existence. La réanalyse de tous ceux qui n'avaient pas été détectés précédemment n'a montré aucun indice de signal à travers l'ensemble de l'échantillon.

Un regard sur les données de *Swift* montre que, comparé aux autres GRB, ceux qui ont été détectés étaient très brillants, à la fois pendant la phase prompte et la phase de rémanence. Cela semble indiquer que la raison principale du manque de détection parmi tous les autres GRB observés étant simplement dû à des instruments qui n'étaient pas assez sensibles. CTA, avec son seuil d'énergie inférieur et une sensibilité nettement améliorée, conduira probablement à plus de détections.

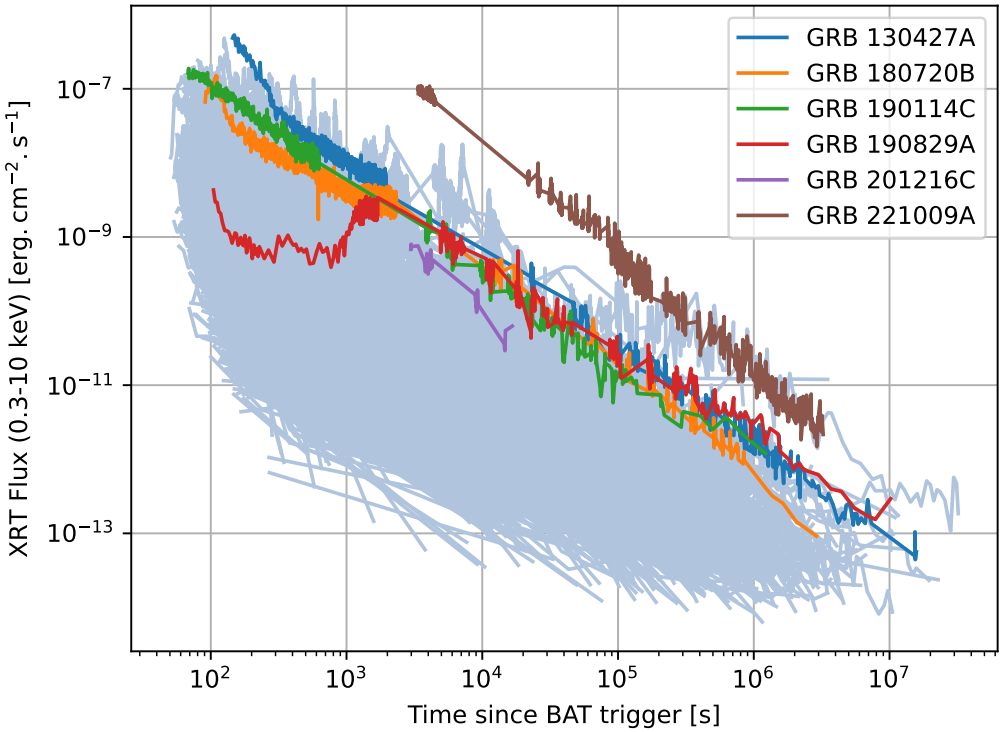

Figure 21.13: Courbe de lumière de tous les GRB détectés par *Swift*/XRT (en bleu clair) aux côtés des GRB intéressants pour l'émission VHE

Le récent GRB 221009A, qui était beaucoup plus brillant que tous les GRB observés jusqu'à présent, en particulier dans *Swift*/XRT (Fig. 21.13), aurait pu laisser espérer une nouvelle détection en VHE. LHASSO a détecté un signal en provenance du GRB peu de temps après la détection par *Fermi*/GBM, mais aucune détection n'a été revendiquée par aucun IACT, indiquant probablement l'absence de détection par tout instrument. Le GRB a eu lieu le jour de la pleine lune. Ainsi, la plupart des IACT n'ont pas pu effectuer d'observation immédiatement, augmentant le délai des observations. De plus, en raison de la lune très forte, les observations ont eu lieu avec de sérieuses pénalités de performance pour tous les instruments. Ce n'est que quelques nuits plus tard que l'observation dans de bonnes conditions a été possible. Cependant, avec la détection du GRB

180720B 10 heures après le sursaut et du GRB 190829A jusqu'à 56 heures après le sursaut, nous aurions pu encore espérer une nouvelle détection même peut-être une semaine plus tard si nous supposons une relation d'intensité entre l'émission en X et à très haute énergie. Comprendre la raison du manque de détection nous apprendra probablement de nombreux détails sur les GRBs.

Part VI

Conclusion

Chapter 22

Conclusion

Since their first detection, gamma-ray bursts have been extensively studied by many instruments across all of the electromagnetic spectrum. Observations have proven their extragalactic origin and their high luminosity. The flux evolution with time is also studied. In X-ray, such a canonical light-curve has been proposed by more recent experiments. But despite this, many unknowns remain about those enigmatic events. Among the main questions, we can mention especially their emission process at the highest energies, the acceleration mechanism, or whether they are sources contributing significantly to UHE cosmic-rays.

One of the major recent discoveries was their emission in the VHE range and that such emission can last for several days. As always with the first detection, it brought maybe more questions than answers, and the limited number of bursts detected at VHE does not permit any conclusion. Detecting more would help get a better view of the overall properties of VHE emission, and this is one of the goals of the future generation of VHE instruments.

The Cherenkov Telescope Array (CTA) is the next-generation instrument for VHE astronomy. The improved sensitivity and lower energy threshold compared to the current experiments will be very useful for detecting GRBs. The arrays will be made up of several types of telescopes. Among them, the Large-Sized Telescopes (LST) will provide sensitivity at low energies with their large reflector. Such size allows them to catch the faint light of showers created by low-energy (tens of GeV) photons. The LSTs can also re-point in less than 30 seconds anywhere in the sky, making them great instruments for observing GRBs.

A light-structure design has been used to allow these fast repointing capabilities. One of the drawbacks is the significant deformation of the structure, which needs to be taken into account in order to have an accurate pointing of the telescope. Such deformation can be measured and taken into account online while the telescope is pointing. Such measurement system, called the `Bending Model`, has been developed in order to provide an online correction of those systematic effects.

The `Bending Model` interact with several subsystems of the telescope to perform measurement of the mispointing and compute a model will observation across the sky. It has been tested on the prototype LST-1, which is currently under commissioning in La Palma. With their design, LSTs telescopes will help detect more GRBs, but to try to improve their abilities even further, some possibilities were explored in this thesis. Among them, testing the performance on observation data of the deep learning model $\gamma -$ PhysNet, the optimisation of cut selection based on integral sensitivity or a new statistical method to search for GRB signal in the data. All of these have shown potential for improving the number of detections.

Some instruments providing GRBs alerts localise GRBs poorly. Among them, the *Fermi*/GBM instrument is an important contributor to the number of detected GRBs. The search for selection criteria that would improve the overall localisation of the observed GRBs was performed and resulted in a significant improvement in the chance of observing the real GRB position. Finally, one of the main interrogations remains whether or not GRBs detected at VHE have different properties. The GRB catalogue of H.E.S.S. attempts to answer this, but no evident specific properties could be highlighted. However, the detected bursts were brighter than the ones not detected, likely indicating

that failed attempts at detection were caused by the GRB not being bright enough to be detected by our instruments with their current sensitivity. CTA will be able to test this hypothesis further, hopefully leading to a better understanding of GRBs.

Chapter 23

Conclusion (en Français)

Depuis leur première détection, les sursauts gamma ont été largement étudiés par de nombreux instruments à travers tout le spectre électromagnétique. Les observations ont pu prouver leur origine extragalactique et leur haute luminosité. L'évolution du flux dans le temps a également été étudiée. Dans les rayons X, une courbe de lumière canonique a été proposée par des expériences plus récentes. Cependant, de nombreuses inconnues subsistent sur ces événements énigmatiques. Parmi les principales questions, on peut mentionner leur processus d'émission aux énergies les plus élevées, le mécanisme d'accélération, ou s'ils sont des sources contribuant significativement aux rayons cosmiques UHE.

Une des découvertes majeures récentes a été leur émission dans la gamme des rayons gamma de très haute énergie (VHE) et que cette émission peut durer plusieurs jours. Comme toujours avec la première détection, cela a peut-être soulevé plus de questions que de réponses et le nombre limité de sursauts détectés à très haute énergie ne permet pas de tirer de conclusion facilement. En détecter plus aiderait à mieux comprendre les propriétés globales de l'émission VHE et c'est l'un des objectifs de la future génération d'instruments.

Cherenkov Telescope Array (CTA) est le prochain instrument de pointe pour l'astronomie VHE. La sensibilité améliorée et le seuil d'énergie inférieur par rapport aux expériences actuelles seront très utiles pour détecter les GRB. Les réseaux seront composés de plusieurs types de télescopes. Parmi eux, les Large-Sized Telescopes (LST) offriront une sensibilité à basses énergies avec leur grand réflecteur. Une telle taille leur permet de capter la faible lumière des douches créées par les photons de faible énergie (dizaines de GeV). Les LST peuvent également se repositionner en moins de 30 secondes n'importe où dans le ciel, ce qui en fait d'excellents instruments pour observer les GRB.

Pour permettre ces capacités de repositionnement rapide, une conception de structure légère a été utilisée. L'un des inconvénients est la déformation significative de la structure, qui doit être prise en compte pour avoir un pointage précis du télescope. Une telle déformation peut être mesurée et prise en compte durant les mouvements du télescopes. Un tel système, appelé `Bending Model`, a été développée pour fournir une correction en ligne de ces effets systématiques.

Le `Bending Model` interagit avec plusieurs sous-systèmes du télescope pour effectuer des mesures de l'erreur sur le pointé et calculer un modèle avec des observations à travers le ciel. Il a été testé sur le prototype LST-1, actuellement en phase de mise en service à La Palma.

De par leur conception, les télescopes LST aideront à détecter plus de GRB, mais pour essayer d'améliorer encore leurs capacités, certaines possibilités ont été explorées dans cette thèse. Parmi elles, tester la performance sur des données d'observation du modèle d'apprentissage profond $\gamma -$ PhysNet, l'optimisation de la sélection des coupures basée sur la sensibilité intégrée ou une nouvelle méthode statistique pour rechercher le signal provenant d'un GRB dans les données. Tous ces éléments ont montré un potentiel pour améliorer le nombre de détections.

Certains instruments fournissant des alertes GRB mais localisent mal ces événements. Parmi eux, le *Fermi*/GBM détecte une part importante de l'ensemble des GRBs détectés. La recherche de critères de sélection qui amélioreraient la localisation globale des GRB observés a été effectuée et a

abouti à une amélioration significative de la chance d'observer la position réelle du GRB.

Enfin, l'une des principales interrogations reste de savoir si les GRB détectés à VHE ont des propriétés différentes. Le catalogue GRB de H.E.S.S. tente de répondre à cette question, mais aucune propriété spécifique évidente n'a pu être mise en évidence. Cependant, les sursauts détectés étaient plus brillants que ceux non détectés, indiquant probablement que les tentatives de détections échouées étaient dues au fait que le GRB n'était pas assez brillant pour être détecté par nos instruments avec leur sensibilité actuelle. CTA pourra tester davantage cette hypothèse, menant, espérons-le, à une meilleure compréhension des sursaut gamma.

Bibliography

Aab, A., Abreu, P., Aglietta, M., et al. (2018). An Indication of Anisotropy in Arrival Directions of Ultra-high-energy Cosmic Rays through Comparison to the Flux Pattern of Extragalactic Gamma-Ray Sources. *Astrophysical Journal, Letters*, 853(2):L29.

Aartsen, M. G., Ackermann, M., Adams, J., et al. (2018). Astrophysical neutrinos and cosmic rays observed by IceCube. *Advances in Space Research*, 62(10):2902–2930.

Abbott, B. P., Abbott, R., Abbott, T. D., et al. (2017). Multi-messenger Observations of a Binary Neutron Star Merger. *Astrophysical Journal, Letters*, 848(2):L12.

Abbott, R., Abbott, T. D., Abraham, S., et al. (2021). Observation of Gravitational Waves from Two Neutron Star-Black Hole Coalescences. *Astrophysical Journal, Letters*, 915(1):L5.

Abdalla, H., Adam, R., Aharonian, F., et al. (2019). A very-high-energy component deep in the γ-ray burst afterglow. *Nature*, 575(7783):464–467.

Abdalla, H., Aharonian, F., Ait Benkhali, F., et al. (2021). Evidence of 100 TeV γ-ray emission from HESS J1702-420: A new PeVatron candidate. *Astronomy and Astrophysics*, 653:A152.

Abdo, A. A., Ackermann, M., Arimoto, M., et al. (2009). Fermi Observations of High-Energy Gamma-Ray Emission from GRB 080916C. *Science*, 323(5922):1688.

Abdollahi, S., Acero, F., Ackermann, M., et al. (2020). Fermi Large Area Telescope Fourth Source Catalog. *Astrophysical Journal, Supplement*, 247(1):33.

Abdollahi, S., Acero, F., Ackermann, M., et al. (2020). Fermi large area telescope fourth source catalog. *The Astrophysical Journal Supplement Series*, 247(1):33.

Abraham, J., Abreu, P., Aglietta, M., et al. (2008). Observation of the Suppression of the Flux of Cosmic Rays above $4{\times}10^{19}$eV. *Physical Review Letters*, 101(6):061101.

Abreu, P., Aglietta, M., Albury, J. M., et al. (2022a). Arrival Directions of Cosmic Rays above 32 EeV from Phase One of the Pierre Auger Observatory. *Astrophysical Journal*, 935(2):170.

Abreu, P., Aglietta, M., Albury, J. M., et al. (2022b). A Search for Photons with Energies Above 2 $\times$ 10^{17} eV Using Hybrid Data from the Low-Energy Extensions of the Pierre Auger Observatory. *Astrophysical Journal*, 933(2):125.

Acciari, V. A., Ansoldi, S., Antonelli, L. A., et al. (2022). Proton acceleration in thermonuclear nova explosions revealed by gamma rays. *Nature Astronomy*, 6:689–697.

Acciari, V. A., Arlen, T., Aune, T., et al. (2014). Observation of Markarian 421 in TeV gamma rays over a 14-year time span. *Astroparticle Physics*, 54:1–10.

Ackermann, M., Ajello, M., Asano, K., et al. (2014). Fermi-LAT Observations of the Gamma-Ray Burst GRB 130427A. *Science*, 343(6166):42–47.

Aharonian, F., Akhperjanian, A. G., Barres de Almeida, U., et al. (2009a). HESS observations of γ-ray bursts in 2003-2007. *Astronomy and Astrophysics*, 495(2):505–512.

Aharonian, F., Akhperjanian, A. G., Barres DeAlmeida, U., et al. (2009b). HESS Observations of the Prompt and Afterglow Phases of GRB 060602B. *Astrophysical Journal*, 690(2):1068–1073.

Aharonian, F., Akhperjanian, A. G., Bazer-Bachi, A. R., et al. (2006). Observations of the Crab nebula with HESS. *Astronomy and Astrophysics*, 457(3):899–915.

Ahumada, T., Singer, L. P., Anand, S., et al. (2021). Discovery and confirmation of the shortest gamma-ray burst from a collapsar. *Nature Astronomy*, 5:917–927.

Ajello, M., Arimoto, M., Axelsson, M., et al. (2019). A Decade of Gamma-Ray Bursts Observed by Fermi-LAT: The Second GRB Catalog. *Astrophysical Journal*, 878(1):52.

Albert, A., Alfaro, R., Alvarez, C., et al. (2020). 3hwc: The third HAWC catalog of very-high-energy gamma-ray sources. *The Astrophysical Journal*, 905(1):76.

Aliu, E., Anderhub, H., Antonelli, L. A., et al. (2008). Observation of Pulsed γ-Rays Above 25 GeV from the Crab Pulsar with MAGIC. *Science*, 322(5905):1221.

Amelino-Camelia, G., Ellis, J., Mavromatos, N. E., Nanopoulos, D. V., and Sarkar, S. (1998). Tests of quantum gravity from observations of γ-ray bursts. *Nature*, 393(6687):763–765.

Amenomori, M., Bao, Y. W., Bi, X. J., et al. (2019). First detection of photons with energy beyond 100 tev from an astrophysical source. *Phys. Rev. Lett.*, 123:051101.

Anderson, C. D. (1933). The positive electron. *Phys. Rev.*, 43:491–494.

Ashkar, H., Brun, F., Füßling, M., et al. (2021). The H.E.S.S. gravitational wave rapid follow-up program. *Journal of Cosmology and Astroparticle Physics*, 2021(3):045.

Astropy Collaboration, Price-Whelan, A. M., Lim, P. L., et al. (2022). The Astropy Project: Sustaining and Growing a Community-oriented Open-source Project and the Latest Major Release (v5.0) of the Core Package. *Astrophysical Journal*, 935(2):167.

Atkins, R., Benbow, W., Berley, D., et al. (2004). TeV Gamma-Ray Survey of the Northern Hemisphere Sky Using the Milagro Observatory. *Astrophysical Journal*, 608(2):680–685.

Auger, P., Ehrenfest, P., Maze, R., Daudin, J., and Fréon, R. A. (1939). Extensive cosmic-ray showers. *Rev. Mod. Phys.*, 11:288–291.

Barbier-Brossat, M. and Figon, P. (2000). Catalogue général de vitesses radiales moyennes pour les étoiles galactiques. Mean radial velocities catalog of galactic stars. *Astrophysics and Space Science*, 142:217–223.

Barthelmy, S. D., Cline, T. L., Gehrels, N., et al. (1994). BACODINE: The Real-Time BATSE Gamma-Ray Burst Coordinates Distribution Network. In Fishman, G. J., editor, *Gamma-Ray Bursts*, volume 307 of *American Institute of Physics Conference Series*, page 643.

Becquerel, H. (1896). Sur les radiations émises par phosphorescence. In *Comptes rendu de l'académie des sciences*, pages 420–421.

Berretta, A., Longo, F., Axelsson, M., et al. (2021). GRB 210704A: Fermi-LAT detection. *GRB Coordinates Network*, 30375:1.

Bird, A. J., Bazzano, A., Malizia, A., et al. (2016). The IBIS Soft Gamma-Ray Sky after 1000 Integral Orbits. *Astrophysical Journal, Supplement*, 223(1):15.

Bissaldi, E., Meegan, C., and Fermi GBM Team (2021). GRB 210511B: Fermi GBM observation. *GRB Coordinates Network*, 29996:1.

Blumenthal, G. R. and Gould, R. J. (1970). Bremsstrahlung, Synchrotron Radiation, and Compton Scattering of High-Energy Electrons Traversing Dilute Gases. *Reviews of Modern Physics*, 42(2):237–271.

Boër, M., Gendre, B., and Stratta, G. (2015). Are Ultra-long Gamma-Ray Bursts Different? *Astrophysical Journal*, 800(1):16.

Bromberg, O., Nakar, E., and Piran, T. (2011). Are Low-luminosity Gamma-Ray Bursts Generated by Relativistic Jets? *Astrophysical Journal, Letters*, 739(2):L55.

Brun, F. (2011). *Sources ténues ou transitoires dans les régions centrales de la Galaxie avec H. E. S. S. : application à l'étude de la région du vestige de supernova W49B.* PhD thesis. Thèse de doctorat dirigée par Naurois, Mathieu de Particules. Noyaux. Cosmos Paris 6 2011.

Brun, F., Piel, Q., de Naurois, M., and Bernhard, S. (2020). Analysis methods to search for transient events in ground-based very high energy γ-ray astronomy. *Astroparticle Physics*, 118:102429.

Cao, Z., Aharonian, F. A., An, Q., et al. (2021). Ultrahigh-energy photons up to 1.4 petaelectronvolts from 12 γ-ray Galactic sources. *Nature*, 594(7861):33–36.

Cavallo, G. and Rees, M. J. (1978). A qualitative study of cosmic fireballs and gamma -ray bursts. *Monthly Notices of the Royal Astronomical Society*, 183:359–365.

Chevalier, J. (2017). *Active galactic nuclei population study at TeV with the H.E.S.S. telescopes and variability studies of the blazar PKS 2155-304 with SSC modelling.* Theses, Université Grenoble Alpes.

Chiozzi, G., Gustafsson, B., Jeram, B., et al. (2002). CORBA-based Common Software for the ALMA project. In Lewis, H., editor, *Advanced Telescope and Instrumentation Control Software II*, volume 4848 of *Society of Photo-Optical Instrumentation Engineers (SPIE) Conference Series*, pages 43–54.

Chudakov, A. (1989). VHE and UHE gamma ray astronomy: history and problems. In *Cosmic Gamma Rays, Neutrinos, and Related Astrophysics*, pages 163–182. Springer.

Chudakov, A., Dadykin, V., Zatsepin, V., and Nesterova, N. (1964). A search for photons with energy 10^{13} eV from local sources of cosmic radiation. In *Proc. PN Lebedev Phys. Inst*, volume 26, page 118.

Clay, J. (1927). Penetrating radiation. In *Proceedings of the royal academy of sciences Amsterdam*, volume 30, pages 1115–1127.

Cline, T. L. (1961). Search for high-energy cosmic gamma rays. *Phys. Rev. Lett.*, 7:109–112.

Collaboration, H. (2018). H.E.S.S. first public test data release. For terms of use, see README.txt and hess_dl3_dr1.pdf.

Connaughton, V., Briggs, M. S., Goldstein, A., et al. (2015). Localization of Gamma-Ray Bursts Using the Fermi Gamma-Ray Burst Monitor. *Astrophysical Journal, Supplement*, 216(2):32.

CTA-LST Project, T., Abe, H., Aguasca, A., et al. (2022a). Analysis of the Cherenkov Telescope Array first Large Size Telescope real data using convolutional neural networks. In *37th International Cosmic Ray Conference*, page 703.

CTA-LST Project, T., Abe, H., Aguasca, A., et al. (2022b). First follow-up of transient events with the CTA Large Size Telescope prototype. In *37th International Cosmic Ray Conference*, page 838.

Cucchiara, A., Levan, A. J., Fox, D. B., et al. (2011). A Photometric Redshift of z ~9.4 for GRB 090429B. *Astrophysical Journal*, 736(1):7.

D'Ai, A., Kennea, J. A., Tohuvavohu, A., et al. (2021). GRB 210704A: Swift-XRT afterglow detection. *GRB Coordinates Network*, 30379:1.

Daigne, F. and Mochkovitch, R. (2007). The low-luminosity tail of the GRB distribution: the case of GRB 980425. *Astronomy and Astrophysics*, 465(1):1–8.

Daum, A., Hermann, G., Heß, M., et al. (1997). First results on the performance of the hegra iact array. *Astroparticle Physics*, 8(1):1–11.

de Naurois, M. (2012). *Very High Energy astronomy from H.E.S.S. to CTA. Opening of a new astronomical window on the non-thermal Universe*. Habilitation à diriger des recherches, Université Pierre et Marie Curie - Paris VI.

de Naurois, M. and Mazin, D. (2015). Ground-based detectors in very-high-energy gamma-ray astronomy. *Comptes Rendus Physique*, 16(6-7):610–627.

de Naurois, M. and Rolland, L. (2009). A high performance likelihood reconstruction of γ-rays for imaging atmospheric Cherenkov telescopes. *Astroparticle Physics*, 32(5):231–252.

de Ugarte Postigo, A., Izzo, L., Pugliese, G., et al. (2022). GRB 221009A: Redshift from X-shooter/VLT. *GRB Coordinates Network*, 32648:1.

Deil, C., Zanin, R., Lefaucheur, J., et al. (2021). Gammapy - A prototype for the CTA science tools. In *35th International Cosmic Ray Conference (ICRC2017)*, volume 301 of *International Cosmic Ray Conference*, page 766.

Dembinski, H. and et al., P. O. (2020). scikit-hep/iminuit.

Di Sciascio, G. (2022). Measurement of energy spectrum and elemental composition of pev cosmic rays: Open problems and prospects. *Applied Sciences*, 12(2).

Diehl, R., Dupraz, C., Bennett, K., et al. (1995). COMPTEL observations of Galactic $\hat{2}6\hat{A}l$ emission. *Astronomy and Astrophysics*, 298:445.

Diehl, R., Halloin, H., Kretschmer, K., et al. (2006). Radioactive ^{26}Al from massive stars in the Galaxy. *Nature*, 439(7072):45–47.

Dole, H., Lagache, G., Puget, J. L., et al. (2006). The cosmic infrared background resolved by Spitzer. Contributions of mid-infrared galaxies to the far-infrared background. *Astronomy and Astrophysics*, 451(2):417–429.

Domínguez, A., Primack, J. R., Rosario, D. J., et al. (2011). Extragalactic background light inferred from AEGIS galaxy-SED-type fractions. *Monthly Notices of the Royal Astronomical Society*, 410(4):2556–2578.

Evans, P. A., Willingale, R., Osborne, J. P., et al. (2010). The Swift Burst Analyser. I. BAT and XRT spectral and flux evolution of gamma ray bursts. *Astronomy and Astrophysics*, 519:A102.

Falcone, A. D., Burrows, D. N., Lazzati, D., et al. (2006). The Giant X-Ray Flare of GRB 050502B: Evidence for Late-Time Internal Engine Activity. *Astrophysical Journal*, 641(2):1010–1017.

Feldman, G. J. and Cousins, R. D. (1998). Unified approach to the classical statistical analysis of small signals. *Physical Review D*, 57(7):3873–3889.

Fermi, E. (1949). On the Origin of the Cosmic Radiation. *Physical Review*, 75(8):1169–1174.

Fermi, E. (1954). Galactic Magnetic Fields and the Origin of Cosmic Radiation. *Astrophysical Journal*, 119:1.

Fermi-LAT Collaboration, Ajello, M., Atwood, W. B., et al. (2021). High-energy emission from a magnetar giant flare in the Sculptor galaxy. *Nature Astronomy*, 5:385–391.

Fichtel, C. E., Hartman, R. C., Kniffen, D. A., et al. (1975). High-energy gamma-ray results from the second Small Astronomy Satellite. *Astrophysical Journal*, 198:163–182.

Frail, D. A., Kulkarni, S. R., Nicastro, L., Feroci, M., and Taylor, G. B. (1997). The radio afterglow from the γ-ray burst of 8 May 1997. *Nature*, 389(6648):261–263.

Franceschini, A. (2021). Photon-Photon Interactions and the Opacity of the Universe in Gamma Rays. *Universe*, 7(5):146.

Frederiks, D., Golenetskii, S., Aptekar, R., et al. (2016). Konus-Wind observation of GRB 161001A (short/hard ?). *GRB Coordinates Network*, 19977:1.

Frontera, F., Costa, E., Piro, L., et al. (1998). Spectral Properties of the Prompt X-Ray Emission and Afterglow from the Gamma-Ray Burst of 1997 February 28. *Astrophysical Journal, Letters*, 493(2):L67–L70.

Fruchter, A. S., Pian, E., Thorsett, S. E., et al. (1999). The Fading Optical Counterpart of GRB 970228, 6 Months and 1 Year Later. *Astrophysical Journal*, 516(2):683–692.

Fukami, S., Berti, A., Loporchio, S., et al. (2022). Very-high-energy gamma-ray emission from GRB 201216C detected by MAGIC. In *37th International Cosmic Ray Conference. 12-23 July 2021. Berlin*, page 788.

Gaia Collaboration, Brown, A. G. A., Vallenari, A., et al. (2018). Gaia Data Release 2. Summary of the contents and survey properties. *Astronomy and Astrophysics*, 616:A1.

Galama, T. J., Vreeswijk, P. M., van Paradijs, J., et al. (1998). An unusual supernova in the error box of the γ-ray burst of 25 April 1998. *Nature*, 395(6703):670–672.

Gallant, Y. A. (2002). Particle Acceleration at Relativistic Shocks. In Guthmann, A. W., Georganopoulos, M., Marcowith, A., and Manolakou, K., editors, *Relativistic Flows in Astrophysics*, volume 589, page 24.

Gehrels, N., Sarazin, C. L., O'Brien, P. T., et al. (2005). A short γ-ray burst apparently associated with an elliptical galaxy at redshift z = 0.225. *Nature*, 437(7060):851–854.

Gendre, B., Stratta, G., Atteia, J. L., et al. (2013). The Ultra-long Gamma-Ray Burst 111209A: The Collapse of a Blue Supergiant? *Astrophysical Journal*, 766(1):30.

Gomboc, A. (2012). Unveiling the secrets of gamma ray bursts. *Contemporary Physics*, 53(4):339–355.

Gould, R. J. and Schréder, G. P. (1967). Opacity of the Universe to High-Energy Photons. *Physical Review*, 155(5):1408–1411.

Greisen, E. W. and Calabretta, M. R. (2002). Representations of world coordinates in FITS. *Astronomy and Astrophysics*, 395:1061–1075.

Greisen, K. (1966). End to the Cosmic-Ray Spectrum? *Physical Review Letters*, 16(17):748–750.

Guetta, D. and Della Valle, M. (2007). On the Rates of Gamma-Ray Bursts and Type Ib/c Supernovae. *Astrophysical Journal, Letters*, 657(2):L73–L76.

Guha, A. and Nicholson, P. (2022). GRB221009A: Ionospheric disturbance observed in India. *GRB Coordinates Network*, 32745:1.

H. E. S. S. Collaboration, Abdalla, H., Aharonian, F., et al. (2021). Revealing x-ray and gamma ray temporal and spectral similarities in the GRB 190829A afterglow. *Science*, 372(6546):1081–1085.

H. E. S. S. Collaboration, Aharonian, F., Ait Benkhali, F., et al. (2022). Time-resolved hadronic particle acceleration in the recurrent nova RS Ophiuchi. *Science*, 376(6588):77–80.

Harris, M. J., Knödlseder, J., Jean, P., et al. (2005). Detection of γ-ray lines from interstellar ^{60}Fe by the high resolution spectrometer SPI. *Astronomy and Astrophysics*, 433(3):L49–L52.

Harrison, F. A., Craig, W. W., Christensen, F. E., et al. (2013). The Nuclear Spectroscopic Telescope Array (NuSTAR) High-energy X-Ray Mission. *Astrophysical Journal*, 770(2):103.

Hartman, R. C., Bertsch, D. L., Bloom, S. D., et al. (1999). The Third EGRET Catalog of High-Energy Gamma-Ray Sources. *Astrophysical Journal, Supplement*, 123(1):79–202.

Hayashida, M., Noda, K., Teshima, M., et al. (2015). The Optical system for the Large Size Telescope of the Cherenkov Telescope Array. In *34th International Cosmic Ray Conference (ICRC2015)*, volume 34 of *International Cosmic Ray Conference*, page 927.

Hayes, L. A. and Gallagher, P. T. (2022). A Significant Sudden Ionospheric Disturbance Associated with Gamma-Ray Burst GRB 221009A. *Research Notes of the American Astronomical Society*, 6(10):222.

He, K., Zhang, X., Ren, S., and Sun, J. (2016). Deep residual learning for image recognition. In *2016 IEEE Conference on Computer Vision and Pattern Recognition (CVPR)*, pages 770–778.

Hess, V. F. (1912). Observations in low level radiation during seven free balloon flights. *Phys. Zeit*, 13:1084–1091.

Hewish, A., Bell, S. J., Pilkington, J. D. H., Scott, P. F., and Collins, R. A. (1968). Observation of a Rapidly Pulsating Radio Source. *Nature*, 217(5130):709–713.

Hillas, A. M. (1984). The Origin of Ultra-High-Energy Cosmic Rays. *Annual Review of Astronomy and Astrophysics*, 22:425–444.

Hillas, A. M. (1985). Cerenkov Light Images of EAS Produced by Primary Gamma Rays and by Nuclei. In *19th International Cosmic Ray Conference (ICRC19), Volume 3*, volume 3 of *International Cosmic Ray Conference*, page 445.

Hirata, K., Kajita, T., Koshiba, M., et al. (1987). Observation of a neutrino burst from the supernova SN1987A. *Physical Review Letters*, 58(14):1490–1493.

Hirata, K. S., Kajita, T., Kifune, T., et al. (1989). Observation of ^{8}B solar neutrinos in the Kamiokande-II detector. *Physical Review Letters*, 63(1):16–19.

Hjorth, J., Sollerman, J., Møller, P., et al. (2003). A very energetic supernova associated with the γ-ray burst of 29 March 2003. *Nature*, 423(6942):847–850.

Huang, Y., Hu, S., Chen, S., et al. (2022). LHAASO observed GRB 221009A with more than 5000 VHE photons up to around 18 TeV. *GRB Coordinates Network*, 32677:1.

Hurley, K., Dingus, B. L., Mukherjee, R., et al. (1995). Detection of a γ-ray burst of very long duration and very high energy. *Nature*, 374(6517):94.

Hurley, K., Ipn, Mitrofanov, I. G., et al. (2021). IPN triangulation of GRB 210511B. *GRB Coordinates Network*, 30002:1.

IceCube Collaboration, Aartsen, M. G., Ackermann, M., et al. (2018). Multimessenger observations of a flaring blazar coincident with high-energy neutrino IceCube-170922A. *Science*, 361(6398):eaat1378.

Jacquemont, M. (2020). *Cherenkov image analysis with deep multi-task learning from single-telescope data*. Theses, Université Savoie Mont Blanc.

Jacquemont, M., Vuillaume, T., Benoit, A., Maurin, G., and Lambert, P. (2021a). Deep learning for astrophysics, understanding the impact of attention on variability induced by parameter initialization. In Del Bimbo, A., Cucchiara, R., Sclaroff, S., et al., editors, *Pattern Recognition. ICPR International Workshops and Challenges*, pages 174–188, Cham. Springer International Publishing.

Jacquemont, M., Vuillaume, T., Benoit, A., Maurin, G., Lambert, P., and Lamanna, G. (2021b). First Full-Event Reconstruction from Imaging Atmospheric Cherenkov Telescope Real Data with Deep Learning. In *International Conference on Content-Based Multimedia Indexing (CBMI)*, page 6 p., Lille, France. IEEE.

James, F. and Roos, M. (1975). Minuit - a system for function minimization and analysis of the parameter errors and correlations. *Computer Physics Communications*, 10(6):343–367.

James, F. and Roos, M. (1975). Minuit: A System for Function Minimization and Analysis of the Parameter Errors and Correlations. *Comput. Phys. Commun.*, 10:343–367.

Kangas, T. and Fruchter, A. S. (2021). The Late-time Radio Behavior of Gamma-ray Burst Afterglows: Testing the Standard Model. *Astrophysical Journal*, 911(1):14.

Kashlinsky, A., Arendt, R. G., Mather, J., and Moseley, S. H. (2005). Tracing the first stars with fluctuations of the cosmic infrared background. *Nature*, 438(7064):45–50.

Klebesadel, R., Evans, W. D., Laros, J. G., et al. (1982). A catalog of gamma-ray bursts with Earth crossing times. *Astrophysical Journal, Letters*, 259:L51–L56.

Klebesadel, R. W., Strong, I. B., and Olson, R. A. (1973). Observations of Gamma-Ray Bursts of Cosmic Origin. *Astrophysical Journal, Letters*, 182:L85.

Knoll, G. F. (2010). *Radiation detection and measurement*. John Wiley & Sons.

Kobayashi, Y., Okumura, A., Cassol, F., et al. (2021). Camera Calibration of the CTA-LST prototype. In *37th International Cosmic Ray Conference*, volume ICRC2021, page 720, Berlin, Germany.

Kouveliotou, C., Meegan, C. A., Fishman, G. J., et al. (1993). Identification of Two Classes of Gamma-Ray Bursts. *Astrophysical Journal, Letters*, 413:L101.

Kraushaar, W. L. and Clark, G. W. (1962). Search for Primary Cosmic Gamma Rays with the Satellite Explorer XI. *Physical Review Letters*, 8(3):106–109.

Kraushaar, W. L., Clark, G. W., Garmire, G. P., et al. (1972). High-Energy Cosmic Gamma-Ray Observations from the OSO-3 Satellite. *Astrophysical Journal*, 177:341.

Le Bohec, S., Degrange, B., Punch, M., et al. (1998). A new analysis method for very high definition imaging atmospheric Cherenkov telescopes as applied to the CAT telescope. *Nuclear Instruments and Methods in Physics Research A*, 416(2):425–437.

Leprince-Ringuet, L. and Auger, P. (1934). étude par la méthode des coincidences de la variation du rayonnement cosmique suivant la latitude. *J. Phys. Radium*, 5(5):193–198.

Lesage, S., Veres, P., Roberts, O. J., Burns, E., Bissaldi, E., and Fermi GBM Team (2022). GRB 221009A: Fermi GBM observation. *GRB Coordinates Network*, 32642:1.

Levan, A. J., Tanvir, N. R., Starling, R. L. C., et al. (2014). A New Population of Ultra-long Duration Gamma-Ray Bursts. *Astrophysical Journal*, 781(1):13.

Li, T. P. and Ma, Y. Q. (1983). Analysis methods for results in gamma-ray astronomy. *Astrophysical Journal*, 272:317–324.

Li, Y., Wen, X., Sun, X., et al. (2020). The GECAM and its payload. *Scientia Sinica Physica, Mechanica & Astronomica*, 50(12):129508.

Liang, E., Zhang, B., Virgili, F., and Dai, Z. G. (2007). Low-Luminosity Gamma-Ray Bursts as a Unique Population: Luminosity Function, Local Rate, and Beaming Factor. *Astrophysical Journal*, 662(2):1111–1118.

Lien, A., Sakamoto, T., Barthelmy, S. D., et al. (2016). The Third Swift Burst Alert Telescope Gamma-Ray Burst Catalog. *Astrophysical Journal*, 829(1):7.

Longair, M. S. (2011). *High Energy Astrophysics*.

Longo, F., Berti, A., Bosnjak, Z., et al. (2022). Upper limits on the very high energy emission from GRBs observed by MAGIC. In *37th International Cosmic Ray Conference. 12-23 July 2021. Berlin*, page 820.

Lopez-Coto, R., Vuillaume, T., Moralejo, A., et al. (2022). cta-observatory/cta-lstchain: v0.9.9 - 2022-10-25.

Ma, X.-H., Bi, Y.-J., Cao, Z., et al. (2022). Chapter 1 LHAASO Instruments and Detector technology. *Chinese Physics C*, 46(3):030001.

MAGIC Collaboration, Acciari, V. A., Ansoldi, S., et al. (2019a). Teraelectronvolt emission from the γ-ray burst GRB 190114C. *Nature*, 575(7783):455–458.

MAGIC Collaboration, Acciari, V. A., Ansoldi, S., et al. (2019b). Observation of inverse Compton emission from a long γ-ray burst. *Nature*, 575(7783):459–463.

Malacaria, C., Meegan, C., and Fermi GBM Team (2021). GRB 210704A: Fermi GBM detection. *GRB Coordinates Network*, 30380:1.

Markwardt, C. B., Barthelmy, S. D., Cummings, J. R., et al. (2016). GRB 161001A, Swift-BAT refined analysis (likely a short GRB). *GRB Coordinates Network*, 19974:1.

Meegan, C., Lichti, G., Bhat, P. N., et al. (2009). The Fermi Gamma-ray Burst Monitor. *Astrophysical Journal*, 702(1):791–804.

Meegan, C. A., Fishman, G. J., Wilson, R. B., et al. (1992). Spatial distribution of γ-ray bursts observed by BATSE. *Nature*, 355(6356):143–145.

Meszaros, P. and Rees, M. J. (1993). Relativistic Fireballs and Their Impact on External Matter: Models for Cosmological Gamma-Ray Bursts. *Astrophysical Journal*, 405:278.

Metzger, M. R., Djorgovski, S. G., Kulkarni, S. R., et al. (1997). Spectral constraints on the redshift of the optical counterpart to the γ-ray burst of 8 May 1997. *Nature*, 387(6636):878–880.

Monet, D. G., Levine, S. E., Canzian, B., et al. (2003). The USNO-B Catalog. *Astronomical Journal*, 125(2):984–993.

Nakar, E. and Sari, R. (2012). Relativistic Shock Breakouts—A Variety of Gamma-Ray Flares: From Low-luminosity Gamma-Ray Bursts to Type Ia Supernovae. *Astrophysical Journal*, 747(2):88.

Neddermeyer, S. H. and Anderson, C. D. (1937). Note on the nature of cosmic-ray particles. *Phys. Rev.*, 51:884–886.

Nelder, J. A. and Mead, R. (1965). A Simplex Method for Function Minimization. *The Computer Journal*, 7(4):308–313.

Nigro, C., Hassan, T., and Olivera-Nieto, L. (2021). Evolution of data formats in very-high-energy gamma-ray astronomy. *Universe*, 7(10).

Nousek, J. A., Kouveliotou, C., Grupe, D., et al. (2006). Evidence for a Canonical Gamma-Ray Burst Afterglow Light Curve in the Swift XRT Data. *Astrophysical Journal*, 642(1):389–400.

Nöthe, M., Kosack, K., Nickel, L., and Peresano, M. (2021a). Prototype open event reconstruction pipeline for the cherenkov telescope array. In *Proceedings, 37th International Cosmic Ray Conference*, volume 395.

Nöthe, M., Peresano, M., Sitarek, J., et al. (2021b). cta-observatory/pyirf: v0.5.0.

Observatory, C. T. A. and Consortium, C. T. A. (2016). CTAO Instrument Response Functions - version prod3b-v2.

Observatory, C. T. A. and Consortium, C. T. A. (2021). CTAO Instrument Response Functions - prod5 version v0.1.

Okumura, A., Dang, T. V., Ono, S., et al. (2017). Prototyping hexagonal light concentrators using high-reflectance specular films for the Large-Sized Telescopes of the Cherenkov Telescope Array. *Journal of Instrumentation*, 12(12):P12008.

P., G., J., H., Kobayashi, Y., et al. (2020). Low-level correction procedures for DRS4. *Internal communication*.

Paciesas, W. S., Meegan, C. A., Pendleton, G. N., et al. (1999). The Fourth BATSE Gamma-Ray Burst Catalog (Revised). *Astrophysical Journal, Supplement*, 122(2):465–495.

Paciesas, W. S., Pendleton, G. N., Lestrade, J. P., et al. (1989). Performance of the large-area detectors for the Burst and Transient Source Experiment on the Gamma Ray Observatory. In Hailey, C. J. and Siegmund, O. H. W., editors, *EUV, X-Ray, and Gamma-Ray Instrumentation for Astronomy and Atomic Physics*, volume 1159 of *Society of Photo-Optical Instrumentation Engineers (SPIE) Conference Series*, pages 156–0.

Parsons, R. D. and Hinton, J. A. (2014). A Monte Carlo template based analysis for air-Cherenkov arrays. *Astroparticle Physics*, 56:26–34.

Parsons, R. D. and Ohm, S. (2020). Background rejection in atmospheric Cherenkov telescopes using recurrent convolutional neural networks. *European Physical Journal C*, 80(5):363.

Particle Data Group, Workman, R. L., Burkert, V. D., et al. (2022). Review of Particle Physics. *Progress of Theoretical and Experimental Physics*, 2022(8). 083C01.

Perryman, M. A. C., Lindegren, L., Kovalevsky, J., et al. (1997). The HIPPARCOS Catalogue. *Astronomy and Astrophysics*, 323:L49–L52.

Piron, F. (2016). Gamma-ray bursts at high and very high energies. *Comptes Rendus Physique*, 17(6):617–631. Gamma-ray astronomy / Astronomie des rayons gamma - Volume 2.

Piron, F., Djannati-Atai, A., Punch, M., et al. (2001). Temporal and spectral gamma-ray properties of ¡ASTROBJ¿Mkn 421¡/ASTROBJ¿ above 250 GeV from CAT observations between 1996 and 2000. *Astronomy and Astrophysics*, 374:895–906.

Preece, R. D., Briggs, M. S., Mallozzi, R. S., Pendleton, G. N., Paciesas, W. S., and Band, D. L. (2000). The BATSE Gamma-Ray Burst Spectral Catalog. I. High Time Resolution Spectroscopy of Bright Bursts Using High Energy Resolution Data. *Astrophysical Journal, Supplement*, 126(1):19–36.

Publication, E. S., editor (1997). *The HIPPARCOS and TYCHO catalogues. Astrometric and photometric star catalogues derived from the ESA HIPPARCOS Space Astrometry Mission*, volume 1200 of *ESA Special Publication*.

Punch, M., Akerlof, C. W., Cawley, M. F., et al. (1992). Detection of TeV photons from the active galaxy Markarian 421. *Nature*, 358(6386):477–478.

Purcell, W. R., Cheng, L. X., Dixon, D. D., et al. (1997). OSSE Mapping of Galactic 511 keV Positron Annihilation Line Emission. *Astrophysical Journal*, 491(2):725–748.

Rees, M. J. and Meszaros, P. (1994). Unsteady Outflow Models for Cosmological Gamma-Ray Bursts. *Astrophysical Journal, Letters*, 430:L93.

Renaud, M., Vink, J., Decourchelle, A., et al. (2006). The Signature of ^{44}Ti in Cassiopeia A Revealed by IBIS/ISGRI on INTEGRAL. *Astrophysical Journal, Letters*, 647(1):L41–L44.

Rybicki, G. B. and Lightman, A. P. (1979). *Radiative processes in astrophysics*.

Salafia, O. S., Ravasio, M. E., Yang, J., et al. (2022). Multiwavelength View of the Close-by GRB 190829A Sheds Light on Gamma-Ray Burst Physics. *Astrophysical Journal, Letters*, 931(2):L19.

Salvaterra, R., Della Valle, M., Campana, S., et al. (2009). GRB090423 at a redshift of z˜8.1. *Nature*, 461(7268):1258–1260.

Schneid, E. J., Bertsch, D. L., Fichtel, C. E., et al. (1992). EGRET detection of high energy gamma rays from the gamma-ray burst of 3 May 1991. *Astronomy and Astrophysics*, 255:L13.

Serna-Franco, J., Alfaro, R., Audehm, J., et al. (2022). Simulations Performance of a 55 Imaging Air-Cherenkov Telescopes HAWC's Eye at High Altitude. In *37th International Cosmic Ray Conference. 12-23 July 2021. Berlin*, page 765.

Sobol', I. (1967). On the distribution of points in a cube and the approximate evaluation of integrals. *USSR Computational Mathematics and Mathematical Physics*, 7(4):86–112.

Sommer, M., Bertsch, D. L., Dingus, B. L., et al. (1994). High-Energy Gamma Rays from the Intense 1993 January 31 Gamma-Ray Burst. *Astrophysical Journal, Letters*, 422:L63.

Stecker, F. W., Puget, J. L., and Fazio, G. G. (1977). The cosmic far-infrared background at high galactic latitudes. *Astrophysical Journal, Letters*, 214:L51–L55.

Su, M., Slatyer, T. R., and Finkbeiner, D. P. (2010). Giant Gamma-ray Bubbles from Fermi-LAT: Active Galactic Nucleus Activity or Bipolar Galactic Wind? *Astrophysical Journal*, 724(2):1044–1082.

Svinkin, D., Frederiks, D., Hurley, K., et al. (2021). A bright γ-ray flare interpreted as a giant magnetar flare in NGC 253. *Nature*, 589(7841):211–213.

Swanenburg, B. N., Bennett, K., Bignami, G. F., et al. (1981). Second COS-B catalogue of high-energy gamma-ray sources. *Astrophysical Journal, Letters*, 243:L69–L73.

Swanenburg, B. N., Bennett, K., Bignami, G. F., et al. (1978). COS B observation of high-energy γ radiation from 3C273. *Nature*, 275(5678):298.

Terasawa, T., Tanaka, Y. T., Takei, Y., et al. (2005). Repeated injections of energy in the first 600ms of the giant flare of SGR1806 - 20. *Nature*, 434(7037):1110–1111.

The Pierre Auger Collaboration, Aab, A., Abreu, P., et al. (2017). Observation of a large-scale anisotropy in the arrival directions of cosmic rays above 8 × 10¡sup¿18¡/sup¿ ev. *Science*, 357(6357):1266–1270.

Troja, E., van Eerten, H., Ryan, G., et al. (2019). A year in the life of GW 170817: the rise and fall of a structured jet from a binary neutron star merger. *Monthly Notices of the Royal Astronomical Society*, 489(2):1919–1926.

van Paradijs, J., Groot, P. J., Galama, T., et al. (1997). Transient optical emission from the error box of the γ-ray burst of 28 February 1997. *Nature*, 386(6626):686–689.

Vanderspek, R., Dullighan, A., Butler, N., et al. (2004). The HETE-2 Burst Catalog. In Fenimore, E. and Galassi, M., editors, *Gamma-Ray Bursts: 30 Years of Discovery*, volume 727 of *American Institute of Physics Conference Series*, pages 57–60.

Veres, P., Burns, E., Bissaldi, E., Lesage, S., Roberts, O., and Fermi GBM Team (2022). GRB 221009A: Fermi GBM detection of an extraordinarily bright GRB. *GRB Coordinates Network*, 32636:1.

Virtanen, P., Gommers, R., Oliphant, T. E., et al. (2020). SciPy 1.0: Fundamental Algorithms for Scientific Computing in Python. *Nature Methods*, 17:261–272.

von Kienlin, A., Meegan, C. A., Paciesas, W. S., et al. (2020). The Fourth Fermi-GBM Gamma-Ray Burst Catalog: A Decade of Data. *Astrophysical Journal*, 893(1):46.

Wagner, S., Rani, B., and H. E. S. S. Collaboration (2021). Enhanced HE and VHE gamma-ray activity from the FSRQ PKS 0346-27. *The Astronomer's Telegram*, 15020:1.

Wakely, S. P. and Horan, D. (2008). TeVCat: An online catalog for Very High Energy Gamma-Ray Astronomy. In *International Cosmic Ray Conference*, volume 3 of *International Cosmic Ray Conference*, pages 1341–1344.

Walter, R., Rodriguez, J., Foschini, L., et al. (2003). INTEGRAL discovery of a bright highly obscured galactic X-ray binary source IGR J16318-4848. *Astronomy and Astrophysics*, 411:L427–L432.

Weekes, T. C., Cawley, M. F., Fegan, D. J., et al. (1989). Observation of TeV Gamma Rays from the Crab Nebula Using the Atmospheric Cerenkov Imaging Technique. *Astrophysical Journal*, 342:379.

Wolter, H. (1952). Spiegelsysteme streifenden Einfalls als abbildende Optiken für Röntgenstrahlen. *Annalen der Physik*, 445(1):94–114.

Wulf, T. (1910). Observations on the radiation of high penetration power on the Eiffel tower. *Physikalische Zeitschrschift*, 11:811.

Zatsepin, G. T. and Chudakov, A. E. (1961). On the methods for searching local sources of high energy photons. *Zhur. Eksptl'. i Teoret. Fiz.*, 41.

Zatsepin, G. T. and Kuz'min, V. A. (1966). Upper Limit of the Spectrum of Cosmic Rays. *Soviet Journal of Experimental and Theoretical Physics Letters*, 4:78.

Zhang, B. (2011). Open questions in GRB physics. *Comptes Rendus Physique*, 12:206–225.

Zhang, B., Fan, Y. Z., Dyks, J., et al. (2006). Physical Processes Shaping Gamma-Ray Burst X-Ray Afterglow Light Curves: Theoretical Implications from the Swift X-Ray Telescope Observations. *Astrophysical Journal*, 642(1):354–370.